Czech Technical University in Prague
Faculty of Nuclear Sciences and Physical Engineering

Doctoral Thesis

2013 **Miroslav Myška**

Czech Technical University in Prague
Faculty of Nuclear Sciences and Physical Engineering

Double Parton Scattering Contribution to the Same-Sign W Boson Pair Production at ATLAS

Doctoral Thesis

by

Miroslav Myška

Department of Physics
Academical Year: 2012/2013
Advisor: RNDr. Pavel Staroba, CSc.

Dedicated to Martina

Double Parton Scattering Contribution to the Same-Sign W Boson Pair Production at ATLAS

Miroslav Myška

Abstract

This thesis investigates the feasibility of the double parton scattering measurement in high-energy proton-proton collisions using the ATLAS detector. In these processes, two or more distinct parton interactions proceed simultaneously in a single proton-proton collision at hard scales. The multiple parton interaction phenomenon is especially important for the exploration of the transverse structure of the colliding protons.

The process under study is the production of a pair of W bosons with the same electric charge, where both gauge bosons decay to a muon and an appropriate neutrino. Since the cross section is expected to be very small, this thesis focus on the description of the kinematic differences between the signal and background processes using the Monte Carlo simulations of proton-proton collisions at $\sqrt{s} = 14$ TeV. The fiducial region found is considered to be the most suitable for the signal measurement.

This thesis concludes that the LO cross section for the production of same-sign muon pairs in the studied fiducial region is 8.7 fb, which also includes 1.1 fb of the signal process cross section. Therefore, the fraction of the double parton scattering events is expected to be around 13%. This implies that the integrated luminosity necessary for the signal significance of 5 standard deviations above the physics background is about 150 fb^{-1}.

Keywords: LHC, ATLAS, Proton-Proton Collisions, Lepton Production, Double Parton Scattering, Monte Carlo Simulations

Příspěvek dvojitého partonového rozptylu k produkci páru stejně nabitých W bosonů v experimentu ATLAS

Miroslav Myška

Abstrakt

Tato práce zkoumá měřitelnost dvojitého partonového rozptylu ve vysokoenergetických srážkách protonů pomocí detektoru ATLAS. V těchto procesech probíhají dvě nebo více různých tvrdých partonových interakcí současně v jediné protonové srážce. Studium násobných partonových srážek je důležité především pro výzkum příčné struktury srážejících se protonů.

Zkoumaným procesem je produkce páru W bosonů se stejným elektrickým nábojem. Oba kalibrační bosony se rozpadají na mion a odpovídající neutrino. Jelikož se předpokládá velmi malý účinný průřez, tato práce se zaměřuje na popis kinematických rozdílů mezi signálním a pozad'ovými procesy pomocí Monte Carlo simulací protonových srážek při $\sqrt{s} = 14$ TeV. Nalezená kinematická oblast se jeví jako vhodná pro měření daného procesu.

Práce uzavírá, že účinný průřez pro produkci stejně nabitých mionových párů ve studované kinematické oblasti je v nejnižším řádu 8.7 fb. Podíl signálního procesu tvoří 13%, tedy 1.1 fb. Z toho vyplývá, že integrovaná luminosita nutná k dosažení významnosti signálu alespoň 5 standardních odchylek nad pozadím je přibližně 150 fb^{-1}.

Klíčová slova: LHC, ATLAS, Proton-Protonové Srážky, Produkce Leptonů, Dvojitý Partonový Rozptyl, Monte Carlo Simulace

Acknowledgement

I have met many interesting people during the long time of my post-graduate studies who have influenced me and my understanding of particle physics. It is impossible to express here my gratitude to all of them, as well as I cannot list all the people from the ATLAS collaboration, who partially participate in any ATLAS-related research.

Above of all, I would like to thank my supervisor Pavel Staroba for his guidance and advices through all these years. Our discussions significantly contributed to shape my insight to the field of particle physics.

I am grateful to the Marie Curie Initial Training Network (MCnet), in which I had an honor to shortly participate and where I have learned a lot about the Monte Carlo programs and physics beyond them. My thanks go primarily to Stefan Gieseke, Michael H. Seymour, Andrew Buckley and Andrzej Siódmok.

I would like to acknowledge the ATLAS team leader Igor Jex from the Czech Technical University in Prague. I am indebted to him for his continuous support.

Many thanks belong to my colleagues and university fellows Oldřich Kepka, Vojtěch Juránek, Jan Čepila, Michal Nyklíček, Jiří Král and Miroslav Krůs, who always had time to dispute the physics with me and helped me especially with the technicalities and software issues.

Last but not least, I would like to thank my parents Eliška Myšková and Miroslav Myška and to my dearest partner Martina Kyseláková for their love and support throughout all my life. Without these ingredients, I am sure I would never finish this thesis neither anything else valuable.

Thank you.

Declaration:

I declare that the presented results are original, except where explicit reference is given, and that I have completed this thesis myself.

Miroslav Myška

Contents

1 Introduction **1**

2 Multiple Parton Interactions **3**
2.1 Underlying event . . . 4
2.2 Double parton scattering . . . 5
2.3 Poisson model . . . 6
2.4 Effective cross section . . . 10
2.5 Hadron matter distribution . . . 12
2.6 Eikonal model . . . 15
2.7 Herwig++ . . . 17

3 Double Parton Scattering Measurements **19**
3.1 The AFS measurement of 4-jets production . . . 20
3.2 The UA2 measurement of 4-jets production . . . 22
3.3 The CDF measurement of 4-jets production . . . 24
3.4 The CDF measurement of γ + 3 jets production . . . 27
3.5 The D0 measurement of γ + 3(2) jets production . . . 32

4 Further DPS Studies **36**
4.1 γ^*/Z/W + jets . . . 36
4.2 $b\bar{b}$ + H/W/Z . . . 39
4.3 Vector boson pair . . . 41
4.4 Meson pair . . . 44

5 Effective Cross Section Correction **46**
5.1 Parton level correction . . . 47
5.2 Hadron level correction . . . 49
5.3 $\mathcal{R}$ factor . . . 50
5.4 Triple parton scattering removal uncertainty . . . 51
5.5 Estimation of the correction factor f . . . 52
5.6 Result . . . 56

6 The Large Hadron Collider and the ATLAS detector **57**
6.1 The Large Hadron Collider . . . 57
6.2 The ATLAS detector . . . 59

6.2.1 Inner detector . . . 60
6.2.2 Calorimeter . . . 61
6.2.3 Muon spectrometer . . . 61
6.2.4 Trigger . . . 63
6.2.5 Detector response simulation . . . 63

7 Double Parton Scattering at ATLAS **64**
7.1 γ + 3 jets . . . 64
7.2 4 jets . . . 65
7.3 W + 2 jets . . . 67
7.4 ll + 2 jets . . . 71

8 Physics Objects **72**
8.1 Muons . . . 72
8.1.1 Muons at ATLAS . . . 72
8.1.2 Primary vertex . . . 74
8.2 Jets . . . 75
8.2.1 Ideal algorithm properties . . . 76
8.2.2 Cone algorithms: PxCone and CDF JetClue . . . 77
8.2.3 Sequential recombination algorithm: anti-k_t . . . 78
8.2.4 Jets at ATLAS . . . 80

9 Analysis of the Same-Sign Muon Pairs **83**
9.1 Double parton scattering signal generation . . . 86
9.2 Single parton scattering background estimation . . . 91
9.2.1 SPS di-boson production . . . 92
9.2.2 SPS $t\bar{t}$ production . . . 94
9.3 Event selection . . . 96
9.4 Background suppression . . . 98
9.4.1 Lepton analysis . . . 98
9.4.2 Jet analysis . . . 105
9.5 Final selection . . . 114
9.6 Further di-boson background suppression . . . 116
9.7 Cross section measurement . . . 124
9.8 Data reconstruction efficiency for $\mu^+\mu^+$ production at $\sqrt{s} = 14$ TeV . . . 127
9.9 Generalization to the same-sign di-muon production in pp collisions at $\sqrt{s} = 7$ and 14 TeV . . . 129

10 Summary and Conclusions **135**

A σ_{eff} Analysis Results **137**
A.1 Intrinsic k_T dependence . . . 137
A.2 Jet algorithm dependence . . . 139
A.3 PDF dependence . . . 141
A.4 Order of α_S dependence . . . 142

B Steering of the Generation **143**
B.1 Common settings of Herwig++ 143
B.2 DPS $W^+W^+ \to \mu^+\mu^+$ generation in Herwig++ 144
B.3 Di-boson ME's hadronization in Herwig++ 145
B.4 $t\bar{t} \to \mu^+\mu^+$ generation in Herwig++ 146

C Missing Transverse Energy **147**

D B - tagging **148**

E Analysis Plots **149**

References **154**

1 Introduction

The purpose of this thesis is to study the double parton scattering, i. e. the process in which at least two different parton interactions occur simultaneously in a single hadron-hadron collision. The primary goal is to decide if this mechanism is able to provide two independent hard electroweak interactions in the same proton-proton collision at LHC energies and if this process would be measurable by the ATLAS detector.

The topic of multiple parton interactions (MPI), which is a general term for an arbitrary number of parton interactions occurring in one hadron-hadron collision, is quite old and has been under development almost hand in hand with the formulation of parton model itself in 70's of the 20th century. The first experimental evidences for the existence of MPI, even slightly indirect, have been brought not long afterwards since the acceleration technology started to turn its attention from lepton to hadron colliders. One of the most important measurements that provided important constrains for Monte Carlo models [1] was made by the UA5 collaboration at CERN's SPS collider in 80's [2]. The advantage of this detector, e.g. in comparison to contemporary Tevatron experiments, was the large pseudorapidity acceptance, approximately $|\eta| < 5$. The number of observed tracks with respect to their transverse momentum would be very difficult to explain without the inclusion of the MPI phenomenon.

The first directly aimed measurement of double parton scattering (DPS) was performed at ISR in CERN by the AFS collaboration [3]. The measurement is described in details in Chapter 3. Let's only mention that the measured final state was formed by 4-jet system and that the assumption of independence of simultaneous parton processes leads to the extraction of the appropriate cross section. The comparison of the DPS cross section for 4-jet production and the cross section for the single parton scattering (SPS) production of 2-jet allowed the estimation of the DPS scaling factor. The measurement of this scaling factor has been performed several times up to these days but the results always indicated the strong influence of parton correlations inside the hadron [4].

This dissertation begins with the short overview of the development of the MPI cross section evaluation, see Chapter 2. Attention was paid to preserve the internal consistency of symbolism used despite that the nomenclature in the literature is not unified and may sometimes be the source of a confusion. It should be emphasized that theoretical models for the description of MPI do not go beyond the Standard Model (SM) even though they work with the generalization of the common prescription for the internal hadron structure.

The question of internal parton distributions in the transverse space and parton

correlations in momentum, color or even spin is still open. Its answering will require a large number of very precise measurements. Measurements of DPS performed up to now are described in Chapter 3. These measurements were restricted to deal with 4-jet systems or with a direct photon production associated with 3 jets. It is very desirable to investigate a much wider spectra of processes in the future in addition to the existing measurements. The double Drell-Yan process [5–7], whether for two neutral bosons or in the form of same-sign W pair production as suggested in this study, has been soon recognized as a very promising process for the investigation of internal parton dynamics. Chapter 4 sets this particular study into the context of other theoretical studies suggested to be realized at LHC experiments.

Chapter 5 reinterprets the CDF measurement and suggests the correction, which should be applied on the CDF result in order to calculate the theoretically more convenient scaling factor for DPS processes. The result of this analysis was published in [**?**] and the obtained scaling factor is used in the further analysis of the process under study.

The experimental part of the thesis begins with the short description of the LHC accelerator and the ATLAS detector, see Chapter 6. An overview of the DPS measurements planned by the ATLAS collaboration is presented in Chapter 7. Chapter 8 contains the definitions of the studied physics objects with respect to the ATLAS detector and explains the basic terminology used.

Chapter 9 contains the whole analysis. It starts from the description of the signal process, discusses the physics background processes which are taken into consideration and lists all the computational tools used including the Monte Carlo generators and ATLAS software. Since the cross section of the studied signal process is small, the analysis explores very carefully the signal event topology in comparison to the background processes. This thesis proposes several kinematical selections for the suppression of the dominant background but the signal always forms only the small fraction of the whole studied data sample. However, the thesis finds the DPS production of two same-sign muons measurable for a long period of data taking by the ATLAS detector.

Chapter 10 summarizes the impact of this thesis and points out the main results reached.

2 Multiple Parton Interactions

In the Standard Model, hadrons are described as composite objects assembled from elementary particles called partons which cannot be directly detected, since they are confined in bound states, and which are modeled as point-like particles. These partons are further classified as quarks, particles with a half-integer spin and with one of six flavors, and gluons, intermediate particles of the strong force with an integer spin. The key point is that all partons carry a color quantum charge and thus they may interact with each other. With the increasing energy of the whole system, a hadron becomes a very dense object not far from being considered as a cloud of partons. According to the quantum number conservation laws, there are few sum rules that must be obeyed by any description of the internal hadron structure. One of them is the conservation of number of base flavor quarks called valence quarks. All other partons evolved from these valence quarks, whether quarks, antiquarks or gluons, are labeled as sea partons.

Assuming that the hadron is accelerated and collides with another hadron, the parton model [8] assigns a fraction x of the hadron's longitudinal momentum to a parton which interacts with a parton from the other hadron, while the remaining part of the hadron decays according to its energy. Parton distribution functions (PDFs) in the leading order of their perturbative expansion describe the probability of finding a parton with the desired flavor and fractional momentum in the given hadron and for the given scale of the interaction.

In the scattering theory, the cross section $\sigma_S(s)$ for the interaction of the hadron h_1 with the hadron h_2 at the given energy of collision $\sqrt{s}$, where only single parton interaction takes place, can be expressed as a convolution of the PDFs ($f_h^i(x)$) and the parton level cross section ($\hat{\sigma}$):

$$\sigma_S(s) = \sum_{i,j} \int dx_1 dx_2 f_{h_1}^i(x_1) f_{h_2}^j(x_2) \int_{(p_T^{min})^2} dp_T^2 \frac{d\hat{\sigma}^{ij}(x_1, x_2, s, p_T)}{dp_T^2}, \tag{2.1}$$

where indices i and j go over the parton flavors. The validity of such a convolution (factorization) is not intuitive and had to be proven to be right for specific processes separately. Here, an infrared divergent parton level cross section is assumed and thus the integration threshold p_T^{min} for the minimum allowed transverse momentum of the secondary partons was introduced in order to satisfy that the perturbative expansion can be used for its calculation. So far, the symbol of the factorization scale is avoided since both PDFs would have the same one.

2.1 Underlying event

With the development of hadron accelerators and with the exploring of hadron collisions at higher and higher energies, the explanation of the long set of final state particles has become more and more problematic. First of all, with the increasing energy of the collision, interacting partons with the same x carry the larger energy and thus the probability of the emission of a sufficiently hard parton from the initial- or final-state of the interaction also increases.

All the particle activity in the final state except the high transverse momentum (p_T) secondaries coming from the hard interaction is generally called as an Underlying Event (UE) [9]. Figure 2.1 sketches a hadron-hadron collision, where the red lines represents the hard QCD $2 \rightarrow 2$ interaction producing two high-p_T (hard) products oriented almost back-to-back to each other. The large number of low-p_T (soft) particles is represented by several lines going in more forward direction and which stem from the initial- or final-state radiation or from the decay of hadron remnants. Moreover, the figure shows another interaction point, which produces mostly soft or semi-hard particles indistinguishable from the other parts of the UE.

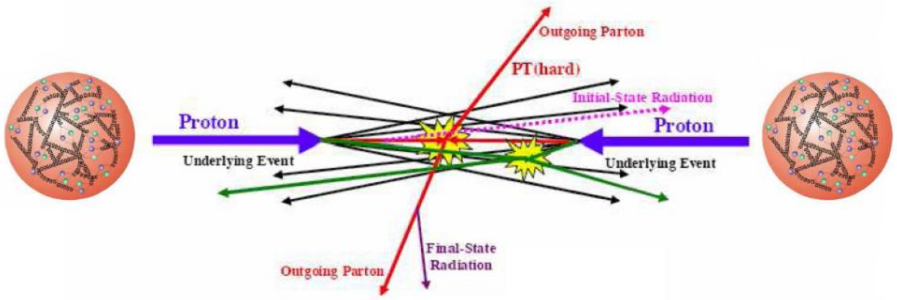

Figure 2.1: The sketch of a proton-proton collision with one hard parton interaction and one additional soft parton interaction contributing to the underlying event [10].

The increasing energy of the accelerated hadron is also consumed to produce more and more virtual sea partons which form a sizable flux of point-like particles able to interact with partons inside the other hadron accelerated in the opposite direction. Therefore, the possibility of occurrence of more than one parton-parton interaction in the same hadron-hadron collision significantly increases. The influence of these so called Multiple Parton Interactions (MPI) can be studied either using precise detectors able to reconstruct individual tracks of charged particles with p_T down to few hundreds of MeV or by measuring total deposited energy in the calorimeter.

The measurement of the UE has obtained almost united form, see for instance the CDF analysis [11]. In most of analyses, the distributions of average number of charged particles and the average scalar p_T sum of all tracks are measured with respect to the direction of the hardest reconstructed jet. Particles with azimuthal angle $\phi_{particle}$ closer to the azimuthal angle of the leading jet $\phi_{1^{st}jet}$ than 60° are defined to be *toward* to the hardest jet and particles with the $\Delta\phi = \phi_{particle} - \phi_{1^{st}jet} > 120°$ are labeled as going

away from the hardest jet. The remaining area of the detector is called the *transverse* region. This region is especially sensitive to the underlying event and the distributions measured for these particles are very suitable to constrain the theoretical UE models within Monte Carlo generators. Data from the Tevatron as well as LHC measurements of UE and minimum bias events strongly supports the importance of the MPI. The description of the hadron activity in detectors cannot be explained just through the higher order radiation or even when incorporating a diffraction.

The existence of the MPI is also supported by the measurements of the inclusive cross section for the production of low-p_T di-jets. The number of di-jets increases significantly with the decreasing minimal transverse momentum required for the jets. QCD calculations of the total and inclusive cross section e.g. in [12] show an interesting trend, where the measured inclusive cross section exceeds the perturbatively calculated one already at $\sqrt{s} \sim 1$ TeV and its extrapolation towards higher energies even exceeds the calculated total cross section. This effect, often referred as the unitarity violation, can be even more serious when incorporating processes with the pomeron exchange, see e.g. [13,14]. The unitarity is then preserved by the assumption that the MPI contributes to the inclusive cross section σ^{incl} according to the average number of parton interactions $< n(s) >$ for the given collision and energy, while the inelastic cross section σ^{inel}, defined for at least one desired interaction in the event, remains the part of the total cross section. Mathematically, this relation can be expressed as

$$\sigma_S^{incl} =< n(s) > \sigma_S^{inel}. \tag{2.2}$$

2.2 Double parton scattering

So far, the multiple parton scattering was discussed in the context of soft and semi-hard QCD processes, which create the unavoidable background to all processes studied at contemporary hadron accelerators. However, as the fractional longitudinal momenta of partons acting in these MPI processes decrease with the increasing energy of hadron collisions, when one assumes the fixed invariant mass of the products of the parton interaction, the chance of occurrence of at least two hard parton interactions in the same hadron collision rises according to the standard parton distribution functions. The simplest case of MPI process, where two of the parton interactions are hard enough to be clearly identified in the detector, is called Double Parton Scattering (DPS). Using this definition, one has to realize that the true number of parton interactions remains hidden and the soft part of the MPI is treated inclusively, even when one deals with the exclusive DPS cross section.

There are many papers, e.g. [15–21], dealing with the DPS as a contribution to the multi-jet final state and also several papers exploring other types of processes, e.g. [5–7, 22–25]. A selection of relevant studies for the LHC is summarized in Chapter 4. The first direct measurement of the DPS process was done at CERN's ISR for 4 jet final state. The results of this and other experiments measuring the DPS are described in Chapter 3.

Generally speaking, there are two kinds of the DPS processes, as shown in Fig. 2.2. In one case, all parton processes proceed completely independent on each other

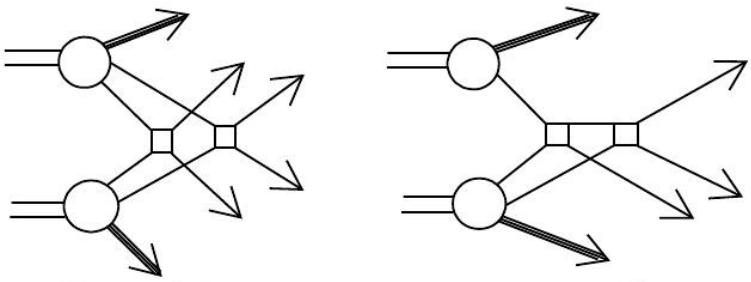

Figure 2.2: Schematic picture of two kinds of double parton scattering processes. Left: two disconnected $2 \to 2$ parton processes. Right: one parton process $2 \to 2$ followed by a rescattering of one of the secondaries with another parton inside the opposite hadron.

and always one parton from the first hadron interacts with one parton from the second hadron. The question of the independence of the soft multiple parton interactions will probably be never fully answered, however, the presence of interconnecting color strings among internal lines in the two hard interactions in the DPS process is assumed to be negligible or at least to have a negligible effect. The CDF collaboration did not find any evidence for the correlations between the two interactions [26].

In the second case, the DPS process may be described as a pair of successive interactions of one parton from the first hadron with two partons from the second hadron, i.e. as the rescattering. The cross sections for the rescattering process of type QCD 3 $\to$ 3 is evaluated e.g. in Ref. [27]. The authors state that rescattering is suppressed, in comparison with the disconnected DPS process of type QCD $4 \to 4$, but it still can create a non-negligible fraction of the soft UE [28]. Nowadays, the UE model in the Pythia [29] generator incorporates the calculation of these rescattering processes and estimates that about half of all minimum bias events measured at the LHC contain at least one parton rescattering.

Since the rate of the hard parton rescatterings is sizable only in heavy ion collisions and is suppressed in the proton-proton collisions, only the disconnected (independent) multiple parton scattering will be taken into consideration in this dissertation.

2.3 Poisson model

Even though the multiple parton interactions are expected to be independent of each other and momenta of secondary products are assumed to be uncorrelated, the same cannot be easily assumed for the interacting partons inside the hadron. Therefore, the generalization of Eq. (2.1) to the case of MPI contains new and completely unknown distribution functions, $\tilde{\Gamma}_{h_i}(x_i)$, reflecting the dynamics of many-parton system inside the hadron and representing the density of partons in hadron h_i which carry a fraction x_i of the hadron longitudinal momenta. The inclusive cross section from (2.2) which can

exceed the total cross section can be symbolically written as

$$\sigma_S^{incl}(s) = \int dx_1 dx_2 \tilde{\Gamma}_{h_1}(x_1)\tilde{\Gamma}_{h_2}(x_2) \int_{(p_T^{min})^2} dp_T^2 \frac{d\hat{\sigma}(x_1, x_2, s, p_T)}{dp_T^2}, \tag{2.3}$$

This phenomenological form of the inclusive cross section has to be further developed to be calculable. Models for these complex distributions are discussed later but let's assume that this cross section is known and can be used as a starting point for the evaluation of the simple Poisson model for the description of MPI.

The Poisson model is meant to be as general as possible. The main assumption is that characteristics of the parton flux, which is dependent on the longitudinal parton momentum and on the parton's position in the hadron in the transverse space, can be factorized. The general distribution of interacting parton matter $\tilde{\Gamma}_{h_i}(x_i)$, where the partons positioning in the transverse space is integrated over the size of the hadron, can be expressed as

$$\tilde{\Gamma}_{h_i}(x_i) = \int d^2\beta' \Gamma_{h_i}(x_i) g(\beta'), \tag{2.4}$$

where function g is the parton distribution function in the transverse space. The two-dimensional variable β' is the vector pointing from the hadron center to the interacting parton of the given hadron, see Fig. 2.3. For the simplification of the notation, the dependence of the transverse distribution on the flavor of partons is avoided, however, the general validity of the Poisson model is not affected. The inclusion of the flavor dependence for the transverse distributions is discussed separately in Section 2.4

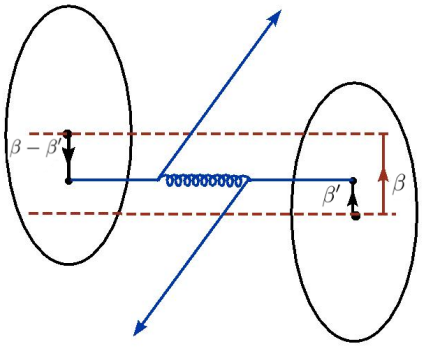

Figure 2.3: A sketch of the SPS in a hadron-hadron collision with the impact parameter β. Distances of interacting partons from the appropriate hadron center in the transverse space are β' and $\beta - \beta'$.

Under the assumption of the factorizability of the longitudinal and transverse dependences of general distributions $\tilde{\Gamma}$, one can reformulate the inclusive cross section

$$\sigma_S^{incl} = \int dx_1 dx_2 \int d^2\beta \int d^2\beta' \Gamma_{h_1}(x_1) g(\beta') \Gamma_{h_2}(x_2) g(\beta - \beta') \int_{(p_T^{min})^2} dp_T^2 \frac{d\hat{\sigma}(x_1, x_2, s, p_T)}{dp_T^2}, \tag{2.5}$$

where the variable β is the impact parameter of the hadron collision defined as the vector between the centers of the two hadrons in the transverse space. After performing the integration over β', the cross section becomes

$$\sigma_S^{incl} = \int dx_1 dx_2 \int d^2\beta \Gamma_{h_1}(x_1)\Gamma_{h_2}(x_2)A(\beta) \int_{(p_T^{min})^2} dp_T^2 \frac{d\hat{\sigma}(x_1, x_2, s, p_T)}{dp_T^2}, \tag{2.6}$$

where the function $A(\beta)$ defined as

$$A(\beta) = \int d^2\beta' g(\beta')g(\beta - \beta') \tag{2.7}$$

characterizes the overlap of the two colliding hadrons for the given impact parameter. This function has to be normalized to one when integrating over the whole size of hadron in the transverse space

$$\int d^2\beta A(\beta) = 1, \tag{2.8}$$

since it may not affect the product of the parton densities and the inclusive cross section for single parton process is then simply

$$\sigma_S^{incl} = \int dx_1 dx_2 \int \Gamma_{h_1}(x_1)\Gamma_{h_2}(x_2) \int_{(p_T^{min})^2} dp_T^2 \frac{d\hat{\sigma}(x_1, x_2, s, p_T)}{dp_T^2}. \tag{2.9}$$

However, if one aims to evaluate the inclusive cross section for the double parton scattering, the derivation analogous to the single parton scattering leads to the non-trivial dependence of the cross section on the overlap function $A(\beta)$:

$$\begin{aligned}
\sigma_D^{incl} &= \frac{1}{2!} \int d^2\beta \int dx_1 dx_1' \Gamma_{h_1}(x_1)\Gamma_{h_2}(x_1')A(\beta) \int_{(p_T^{min})^2} dp_T^2 \frac{d\hat{\sigma}(x_1, x_1', s, p_T)}{dp_T^2} \times \\
&\quad \times \int dx_2 dx_2' \Gamma_{h_1}(x_2)\Gamma_{h_2}(x_2')A(\beta) \int_{(p_T^{min})^2} dp_T^2 \frac{d\hat{\sigma}(x_2, x_2', s, p_T)}{dp_T^2} = \\
&= \int d^2\beta \frac{1}{2!} \left(A(\beta) \int dx dx' \Gamma_{h_1}(x)\Gamma_{h_2}(x') \int_{(p_T^{min})^2} dp_T^2 \frac{d\hat{\sigma}(x, x', s, p_T)}{dp_T^2} \right)^2 = \\
&= \int d^2\beta \frac{1}{2!} \left(A(\beta)\sigma_S^{incl} \right)^2 .
\end{aligned} \tag{2.10}$$

Here, the inclusive meaning of the many-parton distribution $\Gamma_h(x)$ as a flux of partons is used to express both interactions separately. The integration of the overlap function squared is commonly defined as the inverse value of the effective cross section σ_{eff}

$$\int d^2\beta (A(\beta))^2 = \frac{1}{\sigma_{eff}} \tag{2.11}$$

and the inclusive cross section for double parton scattering becomes

$$\sigma_D^{incl} = \frac{1}{2} \frac{\sigma_S^2}{\sigma_{eff}}. \tag{2.12}$$

The σ_{eff} then reflects all the unknown correlations among the partons in the transverse space. The one half in (2.10) is a combinatorial factor prohibiting the double counting in the cross section since two indistinguishable parton processes are assumed. The expression for the inclusive cross section for disconnected N-tuple parton scattering is given by a straightforward generalization:

$$\sigma_N^{incl} = \int d^2\beta \frac{1}{N!} \left(A(\beta)\sigma_S^{incl}\right)^N . \tag{2.13}$$

Since the overlap function has the dimension of the inverse barn, the dimensionless base of the integrand in (2.13), $A(\beta)\sigma_S^{incl}$, can be used to evaluate the mean number of parton interactions in the given hadron-hadron collision with the given impact parameter:

$$< n(\beta, s) >= A(\beta)\sigma_S^{incl}. \tag{2.14}$$

Since these parton interactions are assumed to be uncorrelated, they obey Poissonian statistics:

$$P_k(\beta) = \frac{(< n(\beta, s) >)^k}{k!} e^{-<n(\beta,s)>} = \frac{(A(\beta)\sigma_S^{incl})^k}{k!} e^{-A(\beta)\sigma_S^{incl}}, \tag{2.15}$$

which describes the distribution of the probability of having exactly k parton interactions in the hadron collision. This distribution is the main building block of most of the models describing MPI.

Using the probability distribution, one can directly express all the cross sections of interest. The exclusive cross section describes the cross section for hadron collision with exactly N parton interactions :

$$\sigma_N^{excl} = \int d^2\beta P_N(\beta) = \int d^2\beta \frac{(A(\beta)\sigma_S^{incl})^N}{N!} e^{-A(\beta)\sigma_S^{incl}}, \tag{2.16}$$

where the exponential function has the meaning of the suppression factor, which ensures that no additional parton interaction of the same type can be present in the collision.

The regularized inelastic cross section, which describes the cross section for hadron-hadron collisions where at least N parton interactions take place, is

$$\sigma_N^{inel} = \int d^2\beta \sum_{k=N}^{\infty} P_k(\beta). \tag{2.17}$$

The inelastic cross section for the most interesting case of single parton scattering, where sum goes from $N = 1$ to infinity, becomes

$$\sigma_S^{inel} = \int d^2\beta \sum_{k=1}^{\infty} P_k(\beta) = \int d^2\beta \left(1 - e^{-A(\beta)\sigma_S^{incl}}\right). \tag{2.18}$$

On the other hand, the inclusive cross section counts how many desired secondaries, e.g. di-jets, are in the final state and may exceed the total cross section. The inclusive

cross section for N-tuple parton scattering is proportional to the Nth moment of the Poisson distribution:

$$\begin{aligned}\sigma_N^{incl} &= \int d^2\beta \sum_{k=N}^{\infty} \binom{k}{N} P_k(\beta) = \int d^2\beta \sum_{k=N}^{\infty} \frac{k(k-1)\dots(k-N-1)}{N!} P_k(\beta) = \\ &= \int d^2\beta \frac{(A(\beta)\sigma_S^{incl})^N}{N!} e^{-A(\beta)\sigma_S^{incl}} \sum_{k=N}^{\infty} \frac{(A(\beta)\sigma_S^{incl})^{k-N}}{(k-N)!} = \\ &= \int d^2\beta \frac{(A(\beta)\sigma_S^{incl})^N}{N!}, \end{aligned} \tag{2.19}$$

which is identical to (2.13). This relation of inclusive cross section to the moment of the Poisson distribution leads to the expression of the mean number of parton interactions n using the inclusive SPS cross sections and to the expression of its dispersion using the inclusive DPS cross section. These relations are:

$$< n > \sigma_S^{inel} = \int d^2\beta \sum_{k=1}^{\infty} \frac{k(A(\beta)\sigma_S^{incl})^k}{k!} e^{-A(\beta)\sigma_S^{incl}} = \int d^2\beta A(\beta)\sigma_S^{incl} = \sigma_S^{incl} \tag{2.20}$$

$$\begin{aligned}\frac{< n(n-1) >}{2}\sigma_S^{inel} &= \frac{1}{2}\int d^2\beta \sum_{k=2}^{\infty} \frac{k(k-1)(A(\beta)\sigma_S^{incl})^k}{k!} e^{-A(\beta)\sigma_S^{incl}} = \\ &= \frac{1}{2}\int d^2\beta \left(A(\beta)\sigma_S^{incl}\right)^2 = \sigma_D^{incl}. \end{aligned} \tag{2.21}$$

Relation (2.20) reproduces the input interpretation of the the inclusive cross section in Eq. (2.2) and therefore has a more general validity than just for the simplest Poisson model [30].

So far, the model dealt with a single type of the parton process, motivated by the obvious dominance of the QCD $2 \to 2$ process over the other processes that may have a measurable chance to occur in multiple parton scattering. However, the generalization to several types of independent processes is simple and naturally extends the Poisson model. The probability distributions for the individual process types (2.15) depend on the appropriate inclusive cross section. For instance, the inelastic cross section for the hadron collision with at least l parton interactions of type a and at least m interactions of the distinct type b is

$$\sigma_{l+m}^{inel}(\sigma_a^{incl}, \sigma_b^{incl}) = \int d^2\beta \frac{(A(\beta)\sigma_a^{incl})^l}{l!} e^{-A(\beta)\sigma_a^{incl}} \frac{(A(\beta)\sigma_b^{incl})^m}{m!} e^{-A(\beta)\sigma_b^{incl}}. \tag{2.22}$$

2.4 Effective cross section

Considering Eq. (2.12) for the inclusive double parton scattering

$$\sigma_D^{incl} = \frac{1}{1+\delta_{ab}} \frac{\sigma_a \sigma_b}{\sigma_{eff}} \tag{2.23}$$

but now allowing any two parton processes a and b. If the processes are identical, the double counting is prohibited by the non-zero value of the delta function and vice versa, if the two processes are distinguishable, the whole combinatorial factor is equal to one. In this notation, the product of the two inclusive SPS cross sections σ_a and σ_b is divided by the effective area, here called effective cross section σ_{eff}, characterizing the effect of the internal correlations among partons in the transverse space.

This scaling of the inclusive DPS cross section is widely accepted as a reasonable approximation, whether this scale factor is called effective cross section [31] or not. For instance, authors of [32] express the denominator in (2.23) as an area πR^2 . The radius R could be calculated via the transverse gluon radius of the nucleon. The meaning of the scaling denominator remains the same, i.e. to quantifies the effect of the internal parton correlations with respect to the simple product of SPS cross sections σ_a and σ_b.

The first intuitive expectations, like in [18], estimated the effective cross section to be similar in size to the total hadron-hadron cross section. This approximation may be slightly improved by the evaluation of the σ_{eff} using relations (2.20) and (2.21) for the mean number of parton interactions and its dispersion:

$$\sigma_{eff} = \frac{< n >^2}{< n(n-1) >} \sigma_S^{inel}. \tag{2.24}$$

This relation implies that if the number of parton interactions would be Poissonian also after the integration over the impact parameter of the hadron collision, the effective cross section would be almost equal to the inclusive cross section for having at least one parton interaction of the given type. However, the real parton interactions are expected to have a larger dispersion as compared with the Poissonian one and thus the effective cross section should be smaller than the inelastic cross section. The smaller the effective cross section is measured the larger is the effect of parton correlations. Measurements, which are described in Section 3, found σ_{eff} to be of order of 10 mb. It proves that parton correlations have a non-negligible effect indeed.

In the formalism used in this thesis, the effective cross section σ_{eff} is defined to be independent on the process as well as independent on the energy of the collision. The latter is usually considered as a good approximation even though the similar dependence on the energy is expected as for the total cross section and some papers already work on the evaluation of the σ_{eff} in dependence on the fractional momenta of partons [33–35]. The former property can be, however, reviewed and the dependence of σ_{eff} on the process may be introduced. Namely, the dependence of the overlap function $A(\beta)$ on different flavors of the interacting partons is considered in [4, 36]:

$$A(\beta) \to \sum_{ij} A_j^i(\beta), \tag{2.25}$$

where indices i and j stand for the flavors of the interacting partons in the given parton interaction. In the case of the double parton scattering, the inclusive cross section (2.23) becomes

$$\sigma_D^{incl} = \frac{1}{1+\delta_{ab}} \sum_{ijkl} \int d^2\beta A_j^i(\beta) A_l^k(\beta) \sigma_{ij,a} \sigma_{kl,b}, \tag{2.26}$$

where the second interaction is between parton flavors k and l. The formalism summing over the parton flavors will appear to be more convenient after introducing the simple factorization model for the so far general distributions $\Gamma_{h_i}(x_i)$ in Section 2.5. The integration over the impact parameter β in (2.26) leads to

$$\sigma_D^{incl} = \frac{1}{1+\delta_{ab}} \sum_{ijkl} \Theta_{kl}^{ij} \sigma_{ij,a} \sigma_{kl,b}, \tag{2.27}$$

where

$$\Theta_{kl}^{ij} = \int d^2\beta A_j^i(\beta) A_l^k(\beta) \tag{2.28}$$

are geometrical coefficients characterizing differences in the scaling of different types of DPS processes. One can compare it to general case with no parton flavor dependence considered in (2.11). It is almost impossible to measure the geometrical coefficients for all individual flavors of partons but it might be possible to distinguish at least contributions based on the classification of partons as valence (v) and sea (s). The scale factors $1/\Theta_{kl}^{ij}$ are calculated in Ref. [4] for all the double-combinations in terms of ss, vs, vv parton interactions. These scale factors significantly differ from the smallest one of 12.4 mb for ss-ss double parton process to the largest one of 67.4 mb for vv-vv process.

In addition, one could take a look at the multiple parton scattering and its scaling factor as a short generalization of this section. The inclusive cross section (2.13) for $N > 2$ could be rewritten as

$$\sigma_N^{incl} = \frac{1}{N!} \frac{(\sigma_S^{incl})^N}{\sigma_{N,eff}^{N-1}} \tag{2.29}$$

where the scaling factor $\sigma_{N,eff}$ has a dimension of a cross section and depends on the number of parton interactions. It is defined similarly to effective cross section for the double parton scattering as

$$\frac{1}{\sigma_{N,eff}^{N-1}} = \int d^2\beta (A(\beta))^N. \tag{2.30}$$

The work in Ref. [24] uses the Gauss distribution to model the transverse distribution function $g(\beta')$:

$$g(\beta') = \frac{1}{2\pi\kappa^2} e^{\frac{\beta^2}{2\kappa^2}} \tag{2.31}$$

and evaluates $\sigma_{N,eff}$ as

$$\sigma_{N,eff} = N^{N/(N-1)}(4\pi\kappa^2). \tag{2.32}$$

One can note that this scaling factor slightly decreases with the increasing number of parton interactions.

2.5 Hadron matter distribution

In Eq. (2.3), the flux of interacting partons is symbolically written as an unknown function $\tilde{\Gamma}_{h_i}(x_i)$. This section brings an overview of models which offer more-or-less

simplified description of internal hadron matter through different distribution functions. For the simplification of the notation, the double parton scattering will be considered in the following.

The most general description of the double parton distribution function can be found in the covariant QCD [37–39], where the light-cone reference system is designed with a special aim to cover a wide range of processes including soft QCD and diffraction physics. For instance, the effective cross section can be expressed as a ratio of the generalized double parton distribution function (dGPD) $F(y_1, y_2, Q_1^2, Q_2^2, \Delta)$ and the product of the corresponding structure functions $F(y_i, Q_i^2)$ [40]:

$$\frac{1}{\sigma_{eff}} = \int \frac{d^2\Delta}{(2\pi)^2} \frac{F(y_1, y_2, Q_1^2, Q_2^2, -\Delta) F(y_1', y_2', Q_1^2, Q_2^2, \Delta)}{F(y_1, Q_1^2) F(y_2, Q_2^2) F(y_1', Q_1^2) F(y_2', Q_2^2)}. \tag{2.33}$$

Here, y_i are light-cone momentum fractions of the given parton and Δ is a two-dimensional vector given by the Fourier conjugation of the transverse distance between the interacting partons in the same hadron. For the first time in the text, the two scales Q_1^2 and Q_2^2 of the parton interactions are involved in the notation. The advantage of this general approach is that one can study all correlation effects packed in the single function. Besides correlations of partons momenta, also correlations of spin and color can be further studied, see e.g. [41, 42]. On the other hand, the specific disadvantage of this description of the hadron structure is its non-correspondence with the standard single parton distribution functions (PDFs).

Thus, the following discussion will move towards the simplest possible model, where all parts of the generalized distributions are factorized and one can use the convolution of known PDFs in calculations. As already done above, the first step is to approximate the generalized double distributions as a convolution of two functions: one describing the longitudinal part and one representing the transverse part of the general distribution, as indicated in (2.4). Moreover, one can split the distributions according to parton flavors and get the generalized distribution as a sum over all combinations of the two flavors of the interacting partons. Indices i and j are used for one parton interaction, indices k and l are used for the second interaction. The symbolical expression (2.10) can now be rewritten to

$$\sigma_D^{incl} = \frac{1}{1+\delta_{ab}} \int dx_1 dx_2 dx_1' dx_2' \sum_{ijkl} D_{h_1}^{ik}(x_1, x_2, Q_1^2, Q_2^2) D_{h_2}^{jl}(x_1', x_2', Q_1^2, Q_2^2) \times$$
$$\times \int_{(p_T^{min})^2} dp_T^2 \frac{d\sigma_a^{ij}(x_1, x_1', s, p_T)}{dp_T^2} \int_{(p_T^{min})^2} dp_T^2 \frac{d\sigma_b^{kl}(x_2, x_2', s, p_T)}{dp_T^2} \int d^2\beta (A(\beta))^2, \tag{2.34}$$

where the product of two symbolic distributions $\Gamma_{h_1}(x_1) \times \Gamma_{h_1}(x_2)$ is replaced by the double parton distribution function (dPDF) $D_{h_1}^{ik}(x_1, x_2)$. This function takes into account longitudinal momentum correlations while correlations in the transverse space are factorized out and confined in the overlap function. Several theoretical studies [22, 43–46] argue that longitudinal momentum correlations in the double parton scattering do exist and could have a substantial effect, especially at higher scales Q_i^2. These studies elaborate the formalism of the evolution equation for the dPDFs, the double DGLAP

equation, and the appropriate momentum and number sum rules which the dPDFs have to obey. Moreover, the set of LO dPDFs for the special case of equal scales $Q_1^2 = Q_2^2 = Q^2$ (the GS09 dPDFs [47]) was prepared to be included to calculations.

For most processes, the further factorization of dPDF as a convolution of two single parton distribution functions is a good approximation, since the sea quark and gluon distributions dominate at low x. In theoretical studies, different forms of quasi-factorization have been suggested. The most general form can be written as

$$D_h^{ik}(x_1, x_2, Q^2) = f_h^i(x_1, Q^2) f_h^k(x_2, Q^2) \Theta(1 - x_1 - x_2)(1 - x_1 - x_2)^r, \qquad r = 0, 1, 2 \quad (2.35)$$

where Θ is Heaviside function controlling that the total parton longitudinal momentum does not exceed the hadron's momentum. The sort of ad-hoc factor $(1 - x_1 - x_2)^r$ is designed to suppress contributions from high-x interactions. Authors of [48] study the kinematics of secondary leptons in the DPS same-sign W pair production at matrix element level and compare the factorized distributions for $r = 0$, 1, and 2 against the GS09 dPDF. Their results cannot be easily summarized. Some distributions favor $r = 1$ and some indicates that this type of correlation is not the exactly desired one. Older work [18] also tested the above factorization for $r = 1$ against the factorization of the form

$$D_h^{ik}(x_1, x_2, Q^2) = f_h^i(x_1, Q^2) f_h^k(x_2/(1 - x_1), Q^2). \quad (2.36)$$

They found their results to be insensitive to the choice of the factorization.

There is also more sophisticated approach using the quasi-factorization of the dPDF. For instance, authors of [22] split the solutions of the double DGLAP equation into the fully factorized form (2.35) with $r = 0$ for small scales Q^2, while they suggest additional correlation factors to it for larger scales:

$$D_h^{ik}(x_1, x_2, Q^2) = f_h^i(x_1, Q^2) f_h^k(x_2, Q^2) \Theta(1 - x_1 - x_2) + C_h^{ik}(x_1, x_2, Q^2). \quad (2.37)$$

They express the last term, $C_h^{ik}(x_1, x_2, Q^2)$, as a nontrivial function of the standard PDFs, which is not repeated here. However, they find the effect of this term as negligible for $x < 0.1$.

The assumption of low-x processes leads therefore to the simplest expression of the double parton distribution using the full factorization as

$$D_h^{ik}(x_1, x_2, Q^2) = f_h^i(x_1, Q^2) f_h^k(x_2, Q^2), \quad (2.38)$$

where neither correlations nor momentum conservation are present.

The last unknown function is the transverse distribution $g(\beta')$ introduced already in (2.4). Throughout papers [1, 49–51], three types of distributions are considered:

- Solid disc model:

  $$g(\beta') = Const. \text{ for } |\beta'| < R_h \text{ and } g(\beta') = 0 \text{ for } |\beta'| > R_h \quad (2.39)$$

  where R_h is the radius of the sphere.

- Gaussian model:

$$g(\beta') \propto e^{-\frac{\beta'^2}{A^2}} \tag{2.40}$$

with parameter A representing the width of the distribution.

- Exponential model:

$$g(\beta') \propto \int dz e^{-\frac{\vec{r}}{B}} \tag{2.41}$$

where the transverse distribution is formally given as an integral over the longitudinal coordinate z from the distribution of three-dimensional radius r. The distribution is generally parametrized by a factor B. It is also convenient [52] to display the transverse distribution in Fourier-transform representation with parameter D as

$$g(\beta') \propto \int d^2k \frac{e^{ik\beta'}}{(1+\frac{k^2}{D^2})^2}. \tag{2.42}$$

The transverse distributions are directly connected with the overlap function $A(\beta)$ via (2.7) whose integral over the impact parameter gives the effective cross sections, see (2.11). Experimental values of this scale factor for mostly proton-antiproton collision were found to be several times ($\sim 4\times$) smaller than the appropriate inelastic cross sections. This fact points towards the approximative picture of the internal proton structure, where the hard core of the proton is compressed into much smaller volume ($r \sim 0.5$ fm) than is the expected size of proton ($r \sim 1$ fm) from the measurements of the total cross section. This findings favor the picture where the hadron matter is distributed according to Gaussian- or exponential-like function with dense core and thin surroundings. This interpretation stems from the known fact that the harder the single parton interaction is the more it is biased towards the central collision, where the overlap of the colliding hadrons is large, and the probability of multiple parton interactions is enhanced. Moreover, the DPS cross section (2.23) can be interpreted as a product of one SPS cross section and the conditional probability of happening of the second interaction given that the first interaction happens. It implies that the conditional probability should be enhanced by a smaller scaling denominator σ_{eff} than the mentioned σ_{tot}.

2.6 Eikonal model

Since the signature of MPI lies primarily in the production of low-p_T particles (i.e. in the measurement of minimum bias and UE), the theoretical description has to be expanded also below the previously defined minimum transverse momentum cut p_T^{min}. This cut-off in the integration of the differential cross section as a function of the transverse momentum of outgoing particles was required in order to satisfy that the parton-level cross section can be calculated using the perturbative expansion. One of the possible descriptions connecting perturbative and non-perturbative scatterings is provided by the dual parton model [53–55]. Another method is to use simple extrapolations of the shapes

of the transverse momentum distributions calculated perturbatively below the pre-set p_T^{min}. For instance, one of the most important distributions is the transverse momentum of QCD jets. Even general purpose Monte Carlo generators of hadron-hadron events, e.g. Herwig++ [56], may not be complete in its description of the forward and diffraction physics and thus rely on the extrapolations.

The optical theorem is build on the unitarity of the S-matrix and relates the total cross section, which theoretically includes all the possible known as well as yet unknown processes, to the imaginary part of the elastic scattering amplitude $A(s)$:

$$\sigma^{tot} = \frac{1}{s} Im\left(A(s)\right). \tag{2.43}$$

The amplitude $A(s)$ can be expressed in terms of the eikonal function $\chi(\beta, s)$ as the Fourier transform in the impact parameter space as

$$A(s) = 2is \int d^2\beta \left(1 - e^{-\chi(\beta,s)}\right) e^{iq\beta}, \tag{2.44}$$

where q is the transverse component of momentum transfer in the c.m. system. Thus, the elastic and total cross sections can be written as

$$\sigma^{el} = \int d^2\beta \left|1 - e^{-\chi(\beta,s)}\right|^2, \tag{2.45}$$

$$\sigma^{tot} = 2 \int d^2\beta \left(1 - e^{-\chi(\beta,s)}\right). \tag{2.46}$$

The inelastic part of the total cross section is then given by the subtraction of the elastic component

$$\sigma^{inel} = \sigma^{tot} - \sigma^{el} = \int d^2\beta \left(1 - e^{-2\chi(\beta,s)}\right) \tag{2.47}$$

An important cross check between the generally valid eikonal model and the previous Poisson model is the comparison of the two inelastic cross sections (2.47) and (2.18). One can immediately see that the eikonal function for inelastic processes can be modeled using the overlap function as

$$\chi(\beta, s) = \frac{1}{2} A(\beta) \sigma_S^{incl}. \tag{2.48}$$

Since both overlap function and σ_S^{incl} were previously defined for the hard processes, i.e. depending on the cut-off p_T^{min}, one can suggest the generalization of the eikonal function from being restricted to inelastic processes to all processes contributing to total cross section:

$$\chi_{tot}(\beta, s) = \chi_{hard}(\beta, s) + \chi_{soft}(\beta, s) = \frac{1}{2} A_{hard}(\beta) \sigma_{hard}^{incl} + \frac{1}{2} A_{soft}(\beta) \sigma_{soft}^{incl}, \tag{2.49}$$

where $\sigma_S^{incl} = \sigma_{hard}^{incl}$. This means that the hard and soft multiple parton interactions could be described by the independent Poisson distribution, both having their own overlap distribution. Underlying event modeling in general-purpose Monte Carlo generators

reflects such separation and introduce two components of their transverse momentum distribution.

Pythia can be set to generate MPI processes in several ways [50]. One of the most important settings is to use the sum of two Gauss distributions for the $g(\beta')$ distribution, where the hard and soft component are characterized via the different width-like parameters. This transverse distribution is often referred as the double Gauss model. Herwig++ also uses two transverse distributions which contain the hard- or the soft-process related parameter. Unlike Pythia, Herwig++ uses the exponential model for the transverse distributions motivated by the formula for classical electromagnetic form factor. Since this thesis uses Herwig++ generator in the analysis part, its underlying event modeling is summarized separately in the next section. Generally speaking, both double Gauss model and double electromagnetic form factor model were fitted to experimental data, mostly from Tevatron experiments, and tuned their parameters. One can see, that parameters of the transverse distributions show the same relation. The parameters for the soft part of the distribution correspond to the profile of the hadron, which is less dense but wider in the transverse space, while the hard parts of the distributions favor more dense and smaller transverse profile of the hadron. This hadron matter picture is often called as a hot spot model.

2.7 Herwig++

The underlying event modeling based on the eikonal model used in Herwig++ program is nicely described in several papers [57–61]. Here, only a very brief summary is provided with connection to the above general theoretical considerations. This model is build on the assumption that individual parton interactions are independent, i.e. the distribution of number of interactions obeys the Poisson distribution. The model also assumes that the distribution of partons in one hadron factorizes with respect to the impact parameter β and fractional longitudinal momentum dependences. Herwig++ calculates at its start-up the mean number of parton interactions according to the pre-set matrix elements required according to (2.14). The necessary inclusive cross section for the evaluation of the mean number of interactions can be calculated via

$$\sigma_S^{incl} = \sum_{ij} \int dx_1 dx_2 f_{h_1}^i(x_1, Q^2) f_{h_2}^j(x_2, Q^2) \int_{(p_T^{min})^2} dp_T^2 \frac{\hat{\sigma}^{ij}(x_1, x_2, s, p_T)}{dp_T^2}. \tag{2.50}$$

The overlap function is given by (2.7), where the transverse distribution is chosen to be the same as the electromagnetic form factor:

$$g(\beta') = \frac{1}{(2\pi)^2} \int d^2k \frac{e^{ik\beta'}}{\left(1 + \frac{k^2}{\mu^2}\right)^2}, \tag{2.51}$$

where the parameter μ has the meaning of the inverse hadron radius. The integral (2.7) then yields [62]

$$A(\beta) = \frac{\mu^2}{96\pi} (\mu\beta)^3 K_3(\mu\beta), \tag{2.52}$$

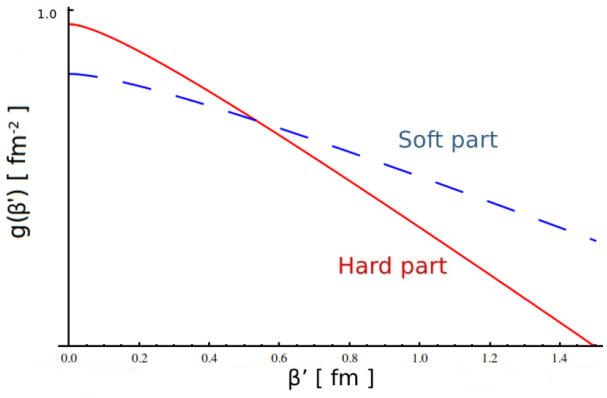

Figure 2.4: Distribution of partons in the transverse space $g(\beta')$ for the hard (red) and soft (blue) hadron overlap in the logarithmic scale, where the β' is the two-dimensional vector between the parton and the center of the hadron in the transverse space. The distribution of partons participating in hard interactions is more central than the distribution for partons exhibiting in soft interactions.

where the $K_3(\mu\beta)$ is the modified Bessel function of the third kind.

The underlying event model in Herwig++ also contains the extension given by the eikonal function (2.49). Evaluation of the overlap function for the soft processes $A_{soft}(\beta)$ is given by the same expression as the hard overlap, only using the different parameter μ. They can be distinguished by an appropriate subscript as μ_h and μ_s. While the parameter μ_s is calculated with respect to the total cross section and carefully tuned, the μ_h is considered mostly as a free parameter ready to be further tuned according to the new energies of the LHC collisions. So far, the model is capable to describe the whole spectrum of UE and minimum bias data from the Tevatron. The values recommended for the LHC energies in Herwig++ 2.5.1 are

$$\mu_h^2 = 1.35 \text{ GeV}^2, \qquad \mu_s^2 \simeq 0.43 \text{ GeV}^2 \tag{2.53}$$

Transverse momentum distributions for modeling of the hard and soft overlap functions for these two values of μ parameter are shown in Fig. 2.4.

For completeness, the value of the transverse momentum threshold set between the perturbative and non-perturbative approaches in the given version of Herwig++ is:

$$p_T^{min} = 3.16 \text{ GeV}. \tag{2.54}$$

3 Double Parton Scattering Measurements

In this section, five measurements of double parton scattering are briefly described in order to demonstrate the experimental point of view and also to set the double parton scattering processes into context of physics and detector background, which is mostly dominant. In all cases, special kinematical region had to be probed and new MPI-sensitive variables were found in order to measure an approximate value of the effective cross section, σ_{eff}, or at least to set a most probable constraints on its value. All experiments modeled DPS process as a composition of completely uncorrelated parton interactions and mostly no constraints are placed on parton correlations. Thus, the σ_{eff} is always extracted using a simple formula

$$\sigma_{DPS} = \frac{1}{1+\delta_{ab}} \frac{\sigma_a \sigma_b}{\sigma_{eff}}. \tag{3.1}$$

Experiment	$\sqrt{s}$ [GeV]	Final state	Base selections	σ_{eff} [mb]
AFS (pp) [3]	63	4jets	$E_T^j > 4$ GeV, $\lvert\eta^j\rvert < 0.9$	~ 5
UA2 ($p\bar{p}$) [63]	630	4jets	$E_T^j > 15$ GeV, $\lvert\eta^j\rvert < 2.0$	> 8.3
CDF ($p\bar{p}$) [64]	1800	4jets	$p_T^j > 25$ GeV, $\lvert\eta^j\rvert < 3.5$	$12.1^{+10.7}_{-5.4}$
CDF ($p\bar{p}$) [26]	1800	γ + 3 jets	$E_T^j > 5$ GeV, $\lvert\eta^j\rvert < 4.2$ $E_T^\gamma > 16$ GeV, $\lvert\eta^\gamma\rvert < 0.9$	$14.5 \pm 1.7^{+1.7}_{-2.3}$
D0 ($p\bar{p}$) [49]	1960	γ + 3 jets	$p_T^j > 15$ GeV, $\lvert\eta^j\rvert < 3.0$ $p_T^\gamma > 60$ GeV, $\lvert\eta^\gamma\rvert < 2.5$	$16.4 \pm 0.3 \pm 2.3$

Table 3.1: Quick overview of the measurements of σ_{eff} performed up to now. Only very brief sketch of the fiducial region is given and the reader is referred to appropriate sections.

Up to now, only four experiments reported their results for the σ_{eff} measurement. At first, only QCD process of 4-jets production was studied as a probe of the higher order process and perturbative calculations and brought a first hints towards a new physics, within the Standard Model. With higher energy, Tevatron experiments obtained first reasonably accurate measurements of DPS 4-jets production and extended the investigation also to electroweak sector by searching for a direct photon accompanied by 3 jets in the final state. Abbreviated experimental conditions and the main results, the σ_{eff}

scale factors, are summarized in Table 3.1. Experiments are described in more detail in the individual sections. A special attention is paid to the methodology of the DPS process simulation and one can compare the evolution of tools and Monte Carlo models at least on the basic level. A significant space is also dedicated to the CDF $\gamma + 3$ jets measurement, which is a unique for its substantial independence on the theoretical models.

3.1 The AFS measurement of 4-jets production

The Axial Field Spectrometer (AFS) collaboration, signed as the experiment R807 and active in between years 1977 - 1982, studied high transverse energy flow phenomena in proton-proton and proton-antiproton collisions at $\sqrt{s} = 63$ GeV at the Intersecting Storage Rings (ISR) in the European Organization for Nuclear Research (CERN) in Geneva. Among other studies concerning multi-jet productions, the impact of the multiple parton scattering was measured [3] as the very first probe of this predicted phenomenon. The measurement demonstrated that the selected 4-jets events are more probably produced via double parton scattering than via $2 \to$ n QCD process, where at least double gluon bremsstrahlung accompany $2 \to 2$ QCD parton scattering, see Fig. 3.1. Specifically, the proton-proton collision events of the integrated luminosity of 10 pb^{-1} were analyzed for the measurement of the double parton scattering (DPS) and the double bremsstrahlung (DBS) fractions within the selected 4-jets events.

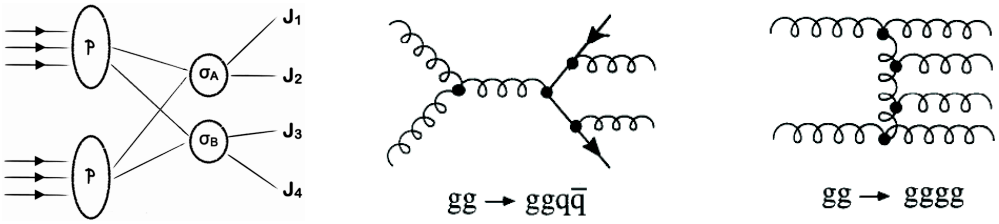

Figure 3.1: Four jet production in proton-proton interaction. A schematic diagram for double parton scattering (left plot) and two examples of double gluon bremsstrahlung (two right plots).

At first, the kinematics of DPS and DBS events were studied using Isajet [65] Monte Carlo generator of pp collisions. Using a simulation of the detector, MC events were analyzed in the same way as the measured data and hence their direct comparison is possible. Both DBS and DPS processes are calculated at the lowest order. The gluon radiations are added to the DBS process within initial- and final-state parton cascades. Gluon bremsstrahlung is not allowed in the case of DPS events. However, the more realistic jet E_T spectra are obtained by adjusting an intrinsic transverse momenta to both 2-jets systems in the same event. The two mechanisms of 4-jets production can be characterized by the momentum imbalance (I)

$$I = \frac{1}{2}(\vec{p}_{T1}^{\,2} + \vec{p}_{T2}^{\,2}), \tag{3.2}$$

where 2-jets pairs with $\vec{p}_{T1,2}$ are formed in order to find the best combination for pair-wise balanced 4 jets. The combination with the minimal imbalance is selected. The motivation is to emphasize the DPS process, where both pairs of outgoing partons are perfectly balanced in $\vec{p}_T$ at the lowest order, while the DBS exhibits a non-zero imbalance even at parton level.

Figure 3.2 shows an example momentum imbalance distributions for 4-jets events selected from real as well as Monte Carlo data. Selected events contain 4 jets satisfying the following selection:

$$\begin{aligned} \sum_{j=1}^{4} E_T^j &\geq 25 \text{ GeV}, \\ E_T^j &\geq 4 \text{ GeV}, \\ |\eta| &< 0.9, \\ \omega^{ij} &\geq 55^\circ. \end{aligned}$$

The ω^{ij} is the inter-jet angle for any pair of jets from the 4-jets system. The data distribution embodies a significant abundance of events in comparison to the DBS events from Monte Carlo and the DPS fraction fills the difference very well. The amount of the DPS events within the measured sample is extracted to be

$$f_{DPS} = (55 \pm 14)\%. \tag{3.3}$$

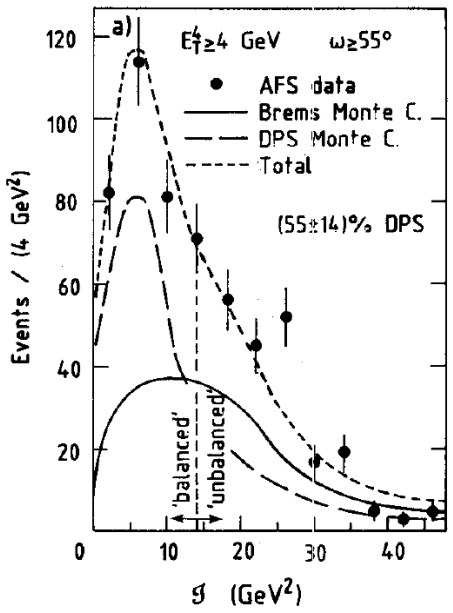

Figure 3.2: The jet-pairs momentum imbalance distribution for 4-jets production. DPS and DBS Monte Carlo data together fit the data very well. The fraction of DPS events in the data was found to be (55±14)% [3].

Moreover, the fraction of DPS events can be studied in two regions according to the minimal value of the momentum imbalance I. Events with $I < 14$ GeV are considered as balanced and contain approximately 66% of DPS events. The complementary region, where $I \geq 14$ GeV, has the fraction of DPS events around 40%. The fraction of DPS events within a given 4-jets selection increases when the minimum jet p_T is increased to 5 GeV. On the contrary, the DPS fraction slightly decreases when the minimal inter-jet angle ω^{ij} is increased to 65°. Results are corrected for all possible sources of background events, including the double proton interactions (pile-up), which was estimated to be around 5%).

The AFS measurement uses the above described method of f_{DPS} extraction for estimation of the MPI scale factor, nowadays called as effective cross section, σ_{eff}. The method consists in comparison of the measured and calculated yield ratio for DPS 4-jets and QCD 2-jets processes:

$$R_{DPS\ 4j/SPS\ 2j} = \frac{N_{DPS\ 4jets}}{N_{SPS\ 2jets}}. \tag{3.4}$$

Measuring of the ratio of two cross sections has an advantage of being insensitive to the jet energy scale calibration and other sources of systematic uncertainty.

The experimental value of $R^{exp}_{DPS\ 4j/SPS\ 2j}$ is obtained from data, on which the appropriate cuts are applied to both 4- and 2-jets events. Total jet E_T has to be in the interval 28 - 30 GeV and the minimal E_T of each jet pair in 4-jets system is set to 1/3 of the total jet E_T. The number of DPS 4 jets events is then gained just by multiplying of f_{DPS} and number of all 4 jets events. The final $R^{exp}_{DPS\ 4j/SPS\ 2j}$ is corrected to parton level and is of value

$$R^{exp}_{DPS\ 4j/SPS\ 2j} = 6\% \pm 1.5\%\ \text{(stat.)} \pm 2.2\%\ \text{(syst.)}. \tag{3.5}$$

In the theoretical description, the DPS process is considered to be a composition of two QCD 2-jets productions, where the available energy for the second interaction is reduced according to the energy of the first di-jets process. Authors calculated appropriate matrix elements in leading order and multiply their SPS result by K factor equal 2. In the DPS case, K^2 is taken as the total multiplication factor for transition to next-to-leading order. One can express the theoretical $R^{teor}_{DPS\ 4j/SPS\ 2j}$ in the abbreviated form as

$$R^{teor}_{DPS\ 4j/SPS\ 2j} = \frac{K\sigma^{LO}_{2j}}{\frac{K^2}{2\sigma_{eff}}\sigma^{LO}_{2j}\sigma'^{LO}_{2j}}, \tag{3.6}$$

where the kinematical difference between the two parton processes in the denominator is indicated by apostrophe.

Eventually, the comparison of the experimental ratio and the LO calculations leads to σ_{eff} determination:

$$\sigma_{eff} \approx 5\ \text{mb}. \tag{3.7}$$

3.2 The UA2 measurement of 4-jets production

The Underground Area 2 (UA2) Collaboration was investigating proton-antiproton interactions at $\sqrt{s} = 630$ GeV. The detector was situated at the Super-Proton-Synchrotron (SPS) accelerator ring at CERN. The collaboration was working during the years 1978 - 1992 and its main goal, together with the experiment UA1, was a discovery of the electroweak bosons W and Z. In the years 1988 and 1989, after the detector upgrade, the collaboration also turned its attention to QCD multi-jet production analysis and to the multiple parton scattering investigation [63]. The sample of 9947 4-jets events was extracted, which corresponds to an integrated luminosity $\mathcal{L}$ of 7.6 pb^{-1}. The UA2 4-jets event selection contains 4 jets arranged in the descending order by their transverse energy from the first hardest jet and all jets have to satisfy

$$E^j_T > 15\ \text{GeV}, \qquad |\eta^j| < 2,$$

while the fifth jet E_T has to be below 10 GeV, if found. The 4-jets system has to carry at least 40% of the total transverse energy deposited in the whole calorimeter ($|\eta| < 3$). Moreover, a maximal missing transverse energy of 20 GeV is required in order to select events well contained in the calorimeter.

As described in the preceding section, the 4-jets final state can be produced via DPS or DBS mechanism, see Fig 3.1. UA2 collaboration used the KS [66] and the BGK [67] programs for the QCD multi-jet event generation, where the matrix element calculation is completely implemented for the desired order of α_s^4 at the tree level. The DPS events were generated using the modified Pythia [68], where the production of two QCD $2 \rightarrow 2$ parton interactions in one event was possible. The matrix element divergences were avoided by retaining only events, where outgoing partons have transverse energy at least 12 GeV and their space separation is greater than 30°. Both Monte Carlo productions were simulated for the detector acceptance and response.

The fraction of DPS events within the measured 4-jets sample was extrapolated from the comparison of the data and both Monte Carlo samples. The problem of normalization of Monte Carlo DPS and DBS distributions was solved by re-normalizing both sets to unity. The true numbers of events are gained from the best fit of the weighted combination of these two distributions to the measured data. The transverse momentum imbalance S defined as

$$S = \sqrt{\frac{1}{2}\left(\frac{|\vec{p}_T^{\,i} + \vec{p}_T^{\,j}|^2}{|\vec{p}_T^{\,i}| + |\vec{p}_T^{\,j}|} + \frac{|\vec{p}_T^{\,k} + \vec{p}_T^{\,l}|^2}{|\vec{p}_T^{\,k}| + |\vec{p}_T^{\,l}|}\right)} \tag{3.8}$$

was found to be the most sensitive variable for detecting a possible signal from double parton scattering. Only the smallest value of S is considered from the three possibilities corresponding to the three permutations of jet pairs, where indices i, j, k, l represents the four hardest jets. The distribution of the logarithm of imbalance S is shown in Fig. 3.3. Left plot demonstrates the kinematical differences between DPS and DBS for the normalized $\log(S)$ distributions and compares them to the measured data. The distributions behave very similarly to the imbalance I defined by the AFS collaboration, see Eq.(3.2). The DPS imbalance is smeared around the zero value, while the DBS exhibits a significant shift towards the larger values. One can also see, that the shape of the QCD multi-jet production model describes the shape of the data very well and that the fraction of DPS events lies within the range of few percent.

The final number of DPS 4-jets events, N_{DPS}, is extracted to be 755 ± 109 using a minimum χ^2/NDF value, which is a function of the DPS event fraction. However, these events contain also their indistinguishable partners coming from the multiple hadron interactions and not from MPI. Number of background events, N_b, was estimated to be 60 ± 40. The overall efficiency factor ϵ for the analysis cuts, trigger and jet reconstruction efficiencies and other effects is found to be (18.8 ± 5.5)% and so the total production cross section can be finally calculated:

$$\sigma_{DPS} = \frac{N_{DPS} - N_b}{L \cdot \epsilon} = 0.49 \pm 0.20 \text{ nb}. \tag{3.9}$$

This result implies that the double parton scattering cross section can be constrained as $\sigma_{DPS} < 0.82$ nb at 95% confidence level. Considering that UA2 collaboration measured also the 2-jets production cross section, the simple formula 3.1 relating DPS production rate and its scale denominator leads to the reported limit on the effective cross section:

$$\sigma_{eff} > 8.3 \text{ mb at } 95\% \text{ CL}. \tag{3.10}$$

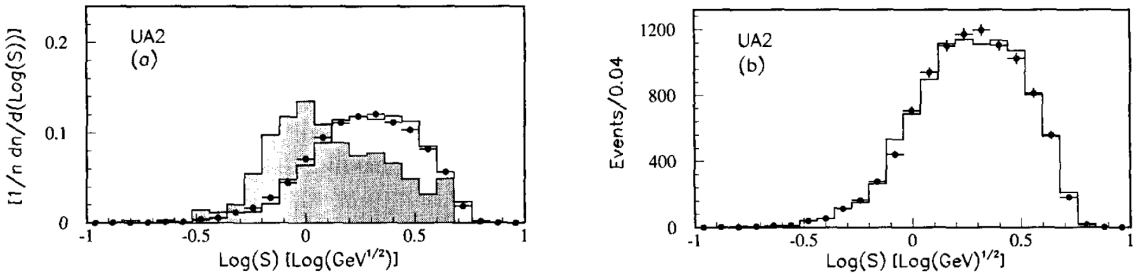

Figure 3.3: (a) Log(S) distributions for the 4-jets data (points), DPS (hatched histogram) and DBS (solid line) Monte Carlo events [63]. All histograms are normalized to unity. (b) The comparison of the data points to the best fit distribution combining both Monte Carlo models [63].

3.3 The CDF measurement of 4-jets production

The last measurement of the double parton scattering contribution to the 4-jets events up to now was performed by the Collider Detector at Fermilab (CDF) Collaboration at the Fermi National Accelerator Laboratory (Fermilab). For this measurement [64], data of integrated luminosity $\mathcal{L}$ of 325 nb^{-1} were collected during the years 1988 - 1989 of the Tevatron accelerator run. Proton-antiproton collisions at $\sqrt{s} = 1.8$ TeV were studied. At first, the topology of 4-jets events was investigated in order to search for DPS. All four individual jet p_T spectra and six inter-jet angles between each jet pair are in good agreement with the theoretical predictions for leading order QCD calculation of double bremsstrahlung process and only a small space is left for the possible DPS contribution to the studied 4-jets events. The Papageno [69] program with an approximate matrix element of Kunszt and Stirling [70] was used to model the theoretical predictions. Monte Carlo matrix element generation was followed by the fast parton level detector simulation in order to produce more realistic and smooth global jet quantities that can be compared to the measured data. Parton level cuts on minimal transverse momentum ($p_T^{parton} > 18$ GeV) and pseudorapidity ($|\eta| < 4.0$) of all outgoing partons and their spatial separation $\Delta R > 0.8$ were set for the purpose of avoiding the singularities inherent in the matrix element calculation.

The investigated final state consisted of four jets reconstructed in the CDF calorimeters. Jet cone clustering algorithm similar to the CDFJetClu, described in Sec. 8.2.2, was used with size R = 0.7. The fiducial region of the 4-jets event selection was defined with respect to the detector geometry and trigger efficiency. Only events with one reconstructed vertex were accepted and its position along the beam axis was restricted to be $|z_{vtx}| < 60$ cm. Even though, small fraction of double interactions (pile-up events), where vertex detector was not able to distinguish the two interaction points, remains in the sample but was found to be negligible as the double parton scattering background. Most of the double proton interactions proceed as a combination of one DBS event and one minimum bias event, while the combination of two di-jet events was estimated to be negligible. Therefore, the pile-up kinematics exhibit more like the DBS and not like

the DPS. Furthermore, the 4 jets have to satisfy:

$$p_T^j > 25 \text{ GeV}, \qquad |\eta^j| < 3.5, \qquad \Delta R^{jj} > 1.0, \qquad \sum_{4\ jets} p_T > 140 \text{ GeV}. \tag{3.11}$$

The remaining 4-jets event sample of size $N_{tot} = 2213$ is analyzed in order to find a fraction of DPS events against the DBP events:

$$R = \frac{N_{DPS}}{N_{DBS}}. \tag{3.12}$$

Jets were paired according to the minimal transverse momentum imbalance

$$S = \sqrt{\frac{1}{2}\left(\frac{|\vec{p}_T^{\,i} + \vec{p}_T^{\,j}|^2}{\sqrt{|\vec{p}_T^{\,i}| + |\vec{p}_T^{\,j}|}} + \frac{|\vec{p}_T^{\,k} + \vec{p}_T^{\,l}|^2}{\sqrt{|\vec{p}_T^{\,k}| + |\vec{p}_T^{\,l}|}}\right)} \tag{3.13}$$

evaluated for all three possible combinations of jet pairings. This variable is very similar to the UA2 definition in Eq. (3.8). Even more suitable variable, Δ_S, reflecting the DPS and DBS kinematical differences was found. The Δ_S is defined as the azimuthal angle between the two di-jets paired according to the minimal S. The dynamics of DBS prefer configurations where the gluons are emitted close to the original parton direction and therefore the Δ_S tends to peak at maximal angle $\Delta_S \sim \pi$. On the contrary, the DPS processes are modeled as two completely independent di-jet productions and thus the Δ_S gives a uniform distribution in the interval 0-π. Therefore, the signal dominant region corresponds to the low S and low Δ_S values. Figure 3.4 demonstrates both distributions and compares measured data points with pure QCD DBS Monte Carlo prediction and with an admixture of DBS and DPS Monte Carlo events. The ratios R of the resulting admixture are obtained from the individual minimal χ^2/NDF fit of Monte Carlo mix to the data for the appropriate characteristics and are given in the plot.

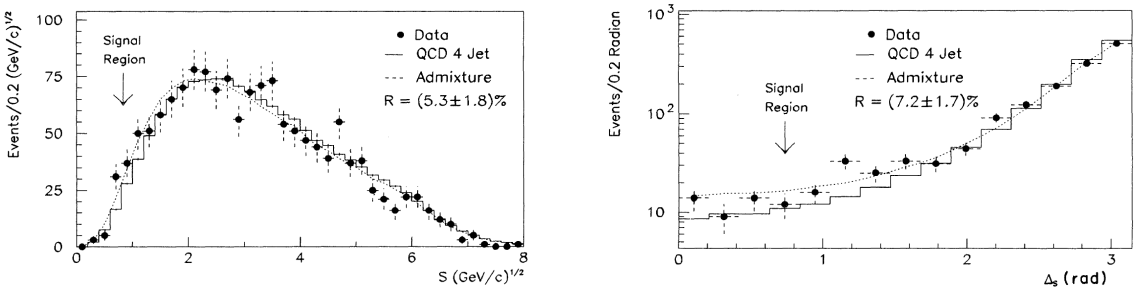

Figure 3.4: Transverse momentum imbalance S (left) and di-jet pair azimuthal angle Δ_S (right) distributions of 4-jets events paired according to the minimal S [64]. Cut p_T < 15 GeV is placed on the 5^{th} hardest jet in the event.

The results of the analysis were found to be very sensitive to the choice of the suppression p_T cut applied on the 5^{th} hardest jet in the event. Both S and Δ_S variables were

studied in dependence on the maximal transverse momentum allowed for the 5^{th} jet, P_{T5}. Figure 3.5 shows the dependence of the fraction R on the P_{T5} cut. The presence of the fifth jet creates a depletion of DPS events in the signal region for S and an enhancement in the signal region for Δ_S. The intersection of the two distributions leads to the final value 13.2 GeV of the P_{T5} cut. The combined fit to S and Δ_S is performed using an admixture of the normalized shapes for DPS and DBS processes. The final fraction of DPS events over DBS events is found to be

$$R = 0.054 \pm 0.013(\text{stat})^{+0.010}_{-0.015}(\text{syst}) \qquad (3.14)$$

which leads to the 2.7σ significance of the double parton scattering signal.

The determination of the DPS production cross section is based on the measured fraction R and only the event selection, A^{cuts}_{DPS}, and trigger, A^{trig}_{DPS}, efficiencies are needed in addition. Their values, same as their uncertainties, were obtained using Monte Carlo simulations and are

$$\begin{aligned} A^{cuts}_{DPS} &= (6.5 \pm 0.9) \cdot 10^{-3}, \\ A^{trig}_{DPS} &= 0.85 \pm 0.10. \end{aligned}$$

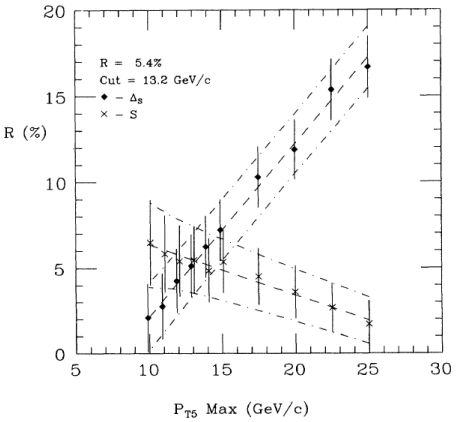

Figure 3.5: Double parton scattering event fraction R for the S and Δ_S variables as a function of the p_T cut applied on the 5^{th} hardest jet [64].

Since the DPS fraction R is defined with respect to the number of DBS events and not to the total number of all 4-jets events ($N_{tot} = N_{DPS} + N_{DBS}$), small arithmetics is needed to express the double parton cross section:

$$\sigma_{DPS} = \frac{N_{DPS}}{L \cdot A^{cuts}_{DPS} \cdot A^{trig}_{DPS}} = \frac{R}{R+1} \, \frac{N_{tot}}{L \cdot A^{cuts}_{DPS} \cdot A^{trig}_{DPS}} \qquad (3.15)$$

Values for all the variables can be found in the text and thus one can get easily the final result

$$\sigma_{DPS} = 63^{+32}_{-28} \text{ nb}. \qquad (3.16)$$

The calculation of the effective cross section, σ_{eff}, takes the reached DPS production cross section and compares it with the calculated SPS di-jet cross section at leading order

$$\sigma_{di-jet} = 39 \ \mu\text{b} \ \pm \ 20\% \qquad (3.17)$$

according to the formula 3.1. The result with the combined uncertainty is

$$\sigma_{eff} = 12.1^{+10.7}_{-5.4}\text{mb}. \qquad (3.18)$$

The appropriate 95% confidence interval was evaluated to

$$4.1 < \sigma_{eff} < 41 \text{ mb (95\% CL)} \qquad (3.19)$$

and can be compared with the UA2 result (3.10).

3.4 The CDF measurement of γ + 3 jets production

In the year 1997, the CDF Collaboration published other results of the double parton scattering measurement in $p\bar{p}$ collisions at $\sqrt{s} = 1.8$ TeV [26]. This time, they analyzed final states consisting of direct photon followed by exactly 3 jets. This channel was used for obvious advantage that the presence of a photon is very helpful for distinguishing the individual parton interactions from each other.

The detector signal for the photon was not distinguished against the neutral meson signatures (multiple photons from meson decay) like π^0 and thus both possibilities were considered in the final state. The data were collected during the years 1992 and 1993 and formed the total integrated luminosity of 16 pb^{-1}. The aim of the measurement was to obtain the factor σ_{eff} for double parton scattering normalization without reference to theoretical calculations or without reliance on Monte Carlo description of their final state.

Double parton scattering contribution to the γ + 3 jets final state may be classified according to the number of jets coming from the individual parton interactions. Figure 3.6 illustrates two main possibilities. The first one is formed by the production of γ + 1 jet system coming from the first scatter and followed by a di-jet production as the second parton interaction. The second type of DPS process is a composition of γ + 2 jets production (1. scatter) and a di-jet production (2. scatter), where only one jet is observed while the second is not reconstructed or fall outside the acceptance region. The case of γ + 0 jets production (1. scatter) followed by a 3-jet production (2. scatter), e.g. through the gluon radiation from the di-jet production, is highly suppressed. Suppression of the γ + 0 jets production is given by the fact that cross section of the photon Drell-Yan production decreases significantly with the rise of the energy of interaction and that the dominant process for the photon production is the QCD Compton scattering, where photon is produced in association with a parton. At the leading order, this final state photon and parton are back-to-back oriented and balanced in p_T. Therefore the chance of finding an parton interaction producing only photon without additional jet was neglected.

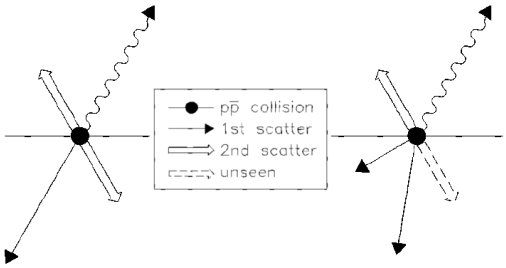

Figure 3.6: Two possible γ + 3 jets double parton production combinations. Left: DP process consisting of γ + 1 jet production followed by di-jet production. Right: DP process formed by γ + 2 jets production followed by di-jet production, where one jet is outside the allowed kinematic range or not reconstructed [26].

For the same reason, the highest number of parton interactions within one proton-

antiproton collision producing $\gamma + 3$ jets is limited to three. Such a case is called a triple parton scattering, where photon + 1 jet come from the first parton interaction and the two other parton interactions produce one observed jet each. This triple parton scattering will be discussed later and its removal from the CDF data will be the reason for the σ_{eff} re-evaluation, see Chapter 5. Authors of [26] provide an exclusive double parton scattering cross section measurement, where two and only two parton scatterings are allowed. However, this definition is slightly inconvenient because the final state production should always be considered in the inclusive manner. One can hardly distinguish the true number of parton interactions per one hadron-hadron collision. To summarize all the points, the DPS cross section (3.1) can be rewritten more precisely as

$$\sigma_{DPS}^{excl} = \frac{(\sigma_{\gamma+0jet}\sigma_{3jets}) + \sigma_{\gamma+1jet}\sigma_{2jets} + \sigma_{\gamma+2jets}\sigma_{1jet}}{\sigma_{eff(CDF)}}, \tag{3.20}$$

For this study, the background process is the single parton scattering production of prompt photon accompanied by 3 jets from gluon bremsstrahlung and is further signed as $\mathcal{Q}$ as a reference to QCD radiations.

The "two-data-set" method for the background suppression was used together with several kinematic variables sensitive to DPS. This method will be described later.

The detector-dependent physics objects, photon and jets, discussed above are defined using the inclusive photon trigger with no jet requirement and by applying certain offline selection. Hadron component of the survived events were clustered using unspecified cone algorithm of radius 0.7, probably the CDF JetClu [71] or a similar one. Different cuts were applied on different jets according to their transverse energy. Let's mark them in decreasing order of E_T as j_1, j_2, and j_3. Events having at least one photon and three and only three jets satisfying:

$$\begin{aligned} E_T^{\gamma} &> 16 \text{ GeV}, \quad E_T^{j} > 5 \text{ GeV}, \quad E_T^{j_2,j_3} < 7 \text{ GeV}, \\ |\eta^{\gamma}| &< 0.9, \quad \Delta R^{\gamma j} > 0.8, \\ |\eta^{j}| &< 4.2, \quad \Delta R^{jj} > 0.7, \end{aligned}$$

were accepted. The requirement of low jet E_T threshold was studied and the value of 5 GeV was found to be high enough to detect only real jet production and to filter instrumental effects off. One should point out that the jet acceptance region was taken here according to the maximal plug and forward calorimeters coverage. On the other hand, σ_{eff} extraction was based on the measurement of the collision vertex (or vertices) along the beam line using the time projection chambers (VTX) and thus the acceptance region for track jets was only $|\eta| < 1.3$. This η-acceptance limitation was used for pile-up measurement and the final result had to be corrected to the acceptance ratio for 1 VTX and 2 VTX data sets. This and similar technical details will not be fully discussed here. The final selection contained 13747 of 1 VTX events and 4904 of 2 VTX events. The aim of this chapter is to summarize variables used for double parton scattering identification and to describe the main features of the σ_{eff} extraction method.

The σ_{eff} extraction method is motivated by sizable uncertainties coming from the theoretical calculations of production rates for the discussed parton processes. Authors

therefore turn to comparison of single- and double-vertex data that belong to the double parton (DP) processes and to the double hadron interactions (DI) within the same beam crossing. The latter case may be interpreted also as the pile-up events. Both production rates can be estimated in the case of the non-single-diffractive (NSD) inelastic $p\bar{p}$ collision cross section measurement, where one divide recorded data into two categories (DP and DI) according to the number of interaction vertices. The number of DP events in the data sample with one NSD collision is

$$N_{DP} = \left(\frac{\sigma_a \sigma_b}{\sigma_{eff}\sigma_{NSD}}\right) N_c(1). \tag{3.21}$$

Similarly, the number of DI events in the data with two NSD collisions can be expressed as

$$N_{DI} = 2\left(\frac{\sigma_a}{\sigma_{NSD}}\right)\left(\frac{\sigma_b}{\sigma_{NSD}}\right) N_c(2), \tag{3.22}$$

where the factor 2 is combinatorial. Processes a and b in DI case can be ordered in two ways with respect to two hadron collisions unlike the DP process. $N_c(1)$ and $N_c(2)$ correspond to the numbers of beam crossings with one and two NSD collisions, respectively. The ratio of (3.22) and (3.21) solve easily for σ_{eff}:

$$\sigma_{eff} = \left(\frac{N_{DI}}{N_{DP}}\right)\left(\frac{N_c(1)}{2N_c(2)}\right)\sigma_{NSD}. \tag{3.23}$$

At the detector level, formula has to be rewritten to the form

$$\sigma_{eff} = \left(\frac{N_{DI}}{N_{DP}}\right)\left(\frac{A_{DP}}{A_{DI}}\right) R_c \sigma_{NSD}, \tag{3.24}$$

where the acceptance ratio for DP and DI events was added and the ratio of beam-crossing numbers has to be replaced by the R_c factor depending on pile-up size and appropriate efficiencies. These two factors were evaluated as

$$\begin{aligned} \frac{A_{DP}}{A_{DI}} &= 0.958, \\ R_c &= 2.06 \pm 0.02^{+0.01}_{-0.13}. \end{aligned}$$

The non-single-diffractive cross section σ_{NSD} is known from other CDF measurement [72]

$$\sigma_{NSD} = (50.9 \pm 1.5) \text{ mb}. \tag{3.25}$$

The rest of this section describes the main aspects of the "two-data-set" method for determination of numbers of DP and DI events and summarizes the results. The two-data-set method consist in creating two differently populated data samples for both DP and DI categories. The motivation is to compare signal-rich and signal-poor samples and thus subtract the appropriate background.

More specifically, the number of DP events N_{DP} was determined using the comparison of two data sets (marked as A and B) gained by application of similar but different

cuts on measured data. Sample B differs from the A only by requiring higher transverse energies for the second and third jet: $7 < E_T^{j_2,j_3} < 9$ GeV. All other cuts are the same as for the sample A, which are summarized above. The unknown fraction of DP events in the sample A is signed as f_{DP}^A and, similarly, the fraction of DP events in sample B is marked as f_{DP}^B. After that, one can express distribution of any measured variable, denoted as $\mathcal{A}$, for the sample A and for each bin i as:

$$\mathcal{A}_i = (1 - f_{DP}^A)\mathcal{Q}_i + f_{DP}^A \mathcal{M}_i^A, \tag{3.26}$$

where $\mathcal{Q}$ represents QCD single parton (SP) background distribution and $\mathcal{M}$ is the distribution for special combination of "MIX" events. This "MIX" data sample is the key point of the whole analysis and represents the very characteristic behavior of DP events. Events from inclusive gamma trigger were combined with minimum bias data, where at least one jet was required, and the A selection cuts were applied afterwards.

The similar steps may be done for the selection B, where the same variable as for sample A has distribution $\mathcal{B}$ and assuming that shapes of the background distributions in the two data sets A and B are the same. One can write it bin by bin as

$$\mathcal{B}_i = (1 - f_{DP}^B)\mathcal{Q}_i + f_{DP}^B \mathcal{M}_i^B. \tag{3.27}$$

All distributions $\mathcal{A}$, $\mathcal{B}$, $\mathcal{M}^A$ and $\mathcal{M}^A$ are normalized to unit area. The background contribution Q may be completely eliminated by suitable combination of data sets $A - kB$, where k becomes equal to $(1 - f_{DP}^A)/(1 - f_{DP}^B)$. $\mathcal{A}_i - k\mathcal{B}_i$ can be thus expresses as

$$\mathcal{A}_i - \left(\frac{1 - f_{DP}^A}{1 - C f_{DP}^A}\right)\mathcal{B}_i = f_{DP}^A \mathcal{M}_i^A - \left(\frac{C f_{DP}^A (1 - f_{DP}^A)}{1 - C f_{DP}^A}\right)\mathcal{M}_i^B. \tag{3.28}$$

The ratio of signal fractions $C \equiv f_{DP}^B / f_{DP}^A$ is known parameter which can be obtained from data assuming that both selections A and B contain such a fraction of DP events that correspond to the fraction of MIX DP events after the given selection. One can formally write $N_A^{MIX} = \lambda N_A^{DP}$ and simultaneously $N_B^{MIX} = \lambda N_B^{DP}$. This assumption is supported by the fact that the MIX data samples well describe the DP kinematics. Therefore, the C parameter is determined without true knowledge of the actual amount of DP events in data as

$$C \equiv \frac{f_{DP}^B}{f_{DP}^A} \equiv \frac{N_B^{DP}}{N_B^{DATA}} \frac{N_A^{DATA}}{N_A^{DP}} = \frac{\lambda N_B^{DP}}{N_B^{DATA}} \frac{N_A^{DATA}}{\lambda N_A^{DP}} = \frac{N_B^{MIX}}{N_B^{DATA}} \frac{N_A^{DATA}}{N_A^{MIX}}. \tag{3.29}$$

The value of this fraction was found to be 0.660 ± 0.002.

Equation (3.28) serves as a χ^2 test over all bins of the four plots, $\mathcal{A}$, $\mathcal{B}$, $\mathcal{M}^A$, and $\mathcal{M}^B$, with a single free parameter f_{DP}^A. Four observables were found to have the strongest selection power to distinguish the double and single parton scatterings. These are three angles ϕ_i between the photon and always one jet. The fourth distinguishing variable, ΔS, is the azimuthal angle between the $\vec{p}_T$ vectors of the minimum-S pairs, analogously to Δ_S for the CDF 4-jets measurement. The observable S represents the significance of

pairwise momentum imbalance of all possible pair combinations of $\gamma + 3$ jets:

$$S = \sqrt{\frac{1}{2}\left(\frac{|\vec{p}_T(\gamma, j_i)|}{\delta p_T(\gamma, j_i)}\right)^2 + \left(\frac{|\vec{p}_T(j_k, j_l)|}{\delta p_T(j_k, j_l)}\right)^2}, \tag{3.30}$$

where $\vec{p}_T(X, Y)$ are transverse momenta vectors of the γ-jet and jet-jet pairs with corresponding uncertainties δp_T. The uncertainties are calculated as root-mean-squared values of the $|\vec{p}_T(X, Y)|$. As an example, the normalized ΔS distributions for individual selections as well as for their subtraction are shown in Fig. 3.7.

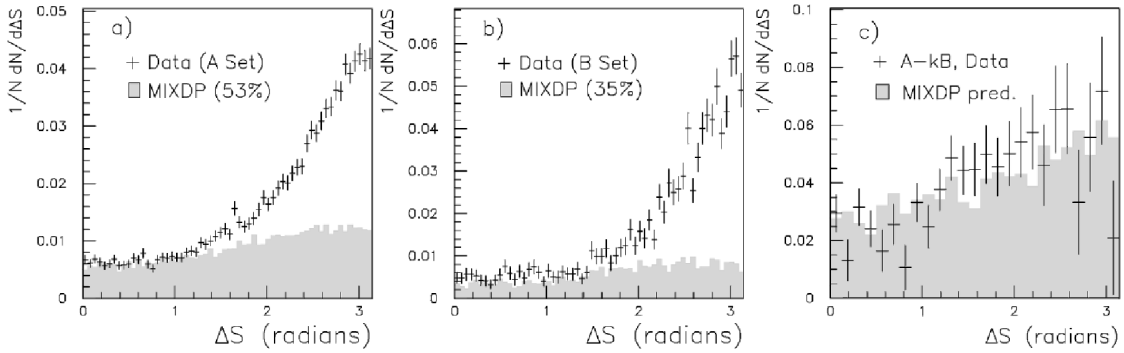

Figure 3.7: Partial results for the two-data-set fit to the ΔS distribution alone. ΔS variable was found to have a greatest sensitivity to double parton scattering. (a) Distributions for the A selection, data and MIX data sets. MIX data were normalized using f_{DP}^A. (b) The same for the B selection. MIX distribution was normalized using $C \times f_{DP}^A$. (c) $A - kB$ combination of two data sets in order to eliminate the SP background [26].

Finally, the result of the simultaneous fit to all four variables with minimal χ^2/NDF yields the fraction of (inclusive) DPS events within the studied 1VTX data sample:

$$f_{DP} = 0.526 \pm 0.025(\text{stat}) \pm 0.009(\text{syst}). \tag{3.31}$$

The number of DP events in the data sample is acquired without any Monte Carlo simulations and is perfectly independent on the theory. There is only one correction that we have to take into account. The DPS cross section (3.20) was considered to be exclusive in the number of parton interactions. Therefore, one has to subtract the estimated number of triple parton (TP) interaction events from the data. This fraction was found to be

$$f_{TP} = 17^{+4}_{-8}\%. \tag{3.32}$$

As already mentioned, this signal suppression will be the source of the further correction on the DPS normalization factor $\sigma_{eff(CDF)}$.

The second unknown variable in the (3.24) is the number of double interactions. The precise vertex detector was used to measure the jet origin in the z coordinate going along the beam axis. Four different areas of Δz between the three jets were defined and the ΔS distribution was investigated. Using the very similar two-data-set technique, the final fraction of DI events in 2VTX data was found to be

$$f_{DI} = 0.177 \pm 0.019(\text{stat}) \pm 0.018(\text{syst}). \tag{3.33}$$

Eventually, implementing all the evaluated factors together leads to the final result

$$\sigma_{eff(CDF)} = (14.5 \pm 1.7^{+1.7}_{-2.3}) \text{ mb}. \tag{3.34}$$

Furthermore, no evidence for $\sigma_{eff(CDF)}$ dependence on Feynman x was found. Also, no kinematic correlations between the two hard parton scatterings were observed.

3.5 The D0 measurement of γ + 3(2) jets production

In the year 2010, the D0 Collaboration at Fermilab reported its results of the double parton scattering investigation in $\gamma + 3$ jets events in proton-antiproton collisions at $\sqrt{s}$ = 1.96 TeV [49]. In comparison to the previous measurement of the same final state by the CDF [26], the D0 collaboration had much higher statistics at the disposal and at even slightly larger energy of hadron collisions. The analyzed event sample corresponds to the integrated luminosity of 1.02 fb^{-1}. The higher statistics of events allow the usage of higher transverse momentum cuts. Especially the direct photon cuts result in a significantly higher photon purity than in the CDF analysis.

The method of the effective cross section extraction is completely analogous to the CDF one and thus only the different kinematic region is further described. The event selection searches for an isolated high-p_T photon satisfying

$$(60 < p_T^{\gamma} < 80) \text{ GeV}, \qquad |y^{\gamma}| < 1.0 \text{ or } 1.5 < |y^{\gamma}| < 2.5 \tag{3.35}$$

followed by at least three jets reconstructed by the iterative midpoint cone algorithm [73] with cone radius R = 0.7 from the calorimeter towers covering the region $|y| < 3.0$. The final jets are p_T ordered where the first jet $j1$ is the hardest jet in the event. Due to the large statistics, the phase space was divided into 3 disjoint intervals according to the second- and third-jet transverse momentum:

$$(15 < p_T^{j2,j3} < 20) \text{ GeV}, \qquad (20 < p_T^{j2,j3} < 25) \text{ GeV}, \qquad (25 < p_T^{j2,j3} < 30) \text{ GeV}. \tag{3.36}$$

The hardest jet cut $p_T^{j1} > 25$ GeV remains the same in all three bins. For the better comparison to the theory, jet transverse momenta are corrected to the particle level. All analyzed objects are required to be separated in the $\eta - \phi$ plane by R = 0.7. Moreover, the maximal missing transverse energy of $0.7 p_T^{\gamma}$ is demanded in order to suppress the cosmic radiation background and the contribution from W boson decays in the lepton channel that might produce a fake photon.

Analysis is based on the CDF's model of DPS events construction using a combination of two 1 VTX events, one with a direct photon production and one for di-jet production. Two-data-sets method, or also called template method, combines DPS rich and DPS poor data sets according to a slightly different cuts and search for kinematical variables sensitive to the DPS event topology. In the D0 study, three generally different pairings of the four final state objects, γ and 3 jets, are used according to the minimal imbalances S_X. The index X represents three different ways how to calculate the appropriate imbalance. One momentum imbalance was previously used by CDF (3.30),

here denoted as S_{p_T}, and two new transverse momentum and azimuth angle imbalances are defined

$$S_{p'_T} = \sqrt{\frac{1}{2}\left(\frac{|\vec{p}_T(\gamma, j_i)|}{|\vec{p}_T(\gamma)| + |\vec{p}_T(j_i)|}\right)^2 + \left(\frac{|\vec{p}_T(j_k, j_l)|}{|\vec{p}_T(j_k)| + |\vec{p}_T(j_l)|}\right)^2}, \tag{3.37}$$

$$S_\phi = \sqrt{\frac{1}{2}\left(\frac{\Delta\phi(\gamma, j_i)}{\delta\phi(\gamma, j_i)}\right)^2 + \left(\frac{\Delta\phi(j_k, j_l)}{\delta\phi(j_k, j_l)}\right)^2}. \tag{3.38}$$

There is only one variable ΔS, defined as

$$\Delta S = \Delta\phi(\vec{p}_T(\gamma, j_i),\ \vec{p}_T(j_k, j_l)), \tag{3.39}$$

which is used for the final fit and the extraction of the DPS event fraction within the investigated data sample. However, this variable depends on the choice of the $\gamma + 3$ jets pairing. The final fit is performed at three different distributions of ΔS_X corresponding to the three minimal S_X pairings, where ΔS_{p_T}, $\Delta S_{p'_T}$ and ΔS_ϕ are distinguished. Results of the fit for the three ΔS_X distributions and for three different regions of the $P_T^{j2,j3}$ are shown in Fig. 3.8 as well as in Table 3.2. There is one significant difference in comparison to the CDF analysis. The D0 retained triple parton events in the DP sample and thus they perform an inclusive double parton scattering measurement.

Other components necessary for the σ_{eff} measurement, see Eq. (3.24), are briefly summarized. The fraction of double interactions within the investigated sample, f_{DI}, was found to be in the range between 0.094 and 0.189 depending on the $p_T^{j2,j3}$ cut, see Table 3.2 for details. The same method as described in the CDF $\gamma + 3$ jets measurement was used. Considering that the detector related efficiencies and other corrections were extracted in the detailed analysis, the last unknown variable is the non-single-diffractive cross section, σ_{NSD}, for the proton-antiproton interactions at $\sqrt{s} = 1.96$ TeV.

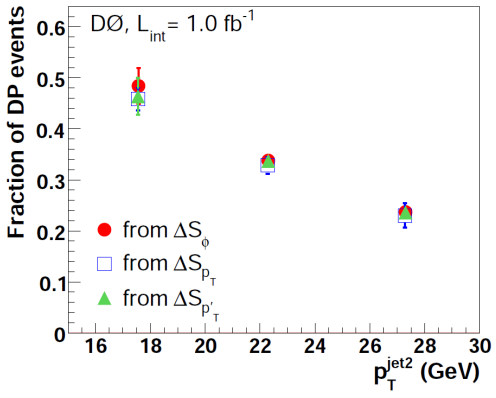

Figure 3.8: Fractions of DP events obtained from individual fits to ΔS_{p_T}, $\Delta S_{p'_T}$ and ΔS_ϕ distributions in the three bins of second hardest jet transverse momentum [49].

D0 study estimates its value from the known inelastic cross section measured and from an extrapolation of single- and double-diffractive cross sections measured at $\sqrt{s} = 1.8$ TeV. The σ_{NSD} for $\sqrt{s} = 1.96$ TeV was found to be

$$\sigma_{NSD} = 44.76 \pm 2.89 \text{ mb}. \tag{3.40}$$

Except the three individual values for effective cross section σ_{eff} calculated for three $p_T^{j2,j3}$ regions and written in Table 3.2, the D0 also reports the average value of σ_{eff} covering the whole studied kinematical region:

$$\sigma_{eff} = 16.4 \pm 0.3(\text{stat}) \pm 2.3(\text{syst}) \text{ mb}. \tag{3.41}$$

$p_T^{j2,j3}$ [GeV]	N_{tot}^{1VTX}	f_{DP}	N_{tot}^{2VTX}	f_{DI}	σ_{eff} [mb]
15 - 20	2182	0.466±0.041	2026	0.189±0.029	18.2±3.8
20 - 25	3475	0.334±0.023	2792	0.137±0.027	16.3±3.7
25 - 30	3220	0.235±0.027	2309	0.094±0.025	13.9±4.5

Table 3.2: Summary of the event numbers and an appropriate DP and DI event fractions in the studied samples for three different regions of $p_T^{j2,j3}$. The resulting effective cross sections for individual settings are in the last column.

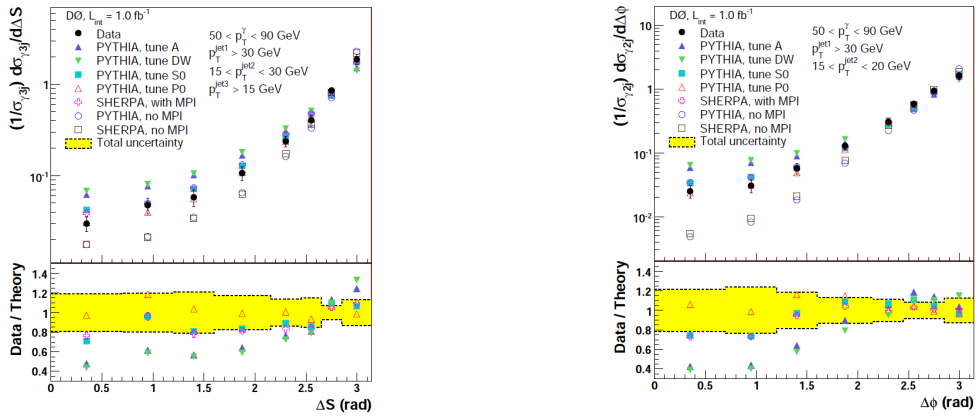

Figure 3.9: Normalized differential cross section as a function of the azimuthal angle between pre-defined transverse momenta in γ + 3 jets (left) and γ + 2 jets (right). Kinematical cuts used are specified in the plots [49].

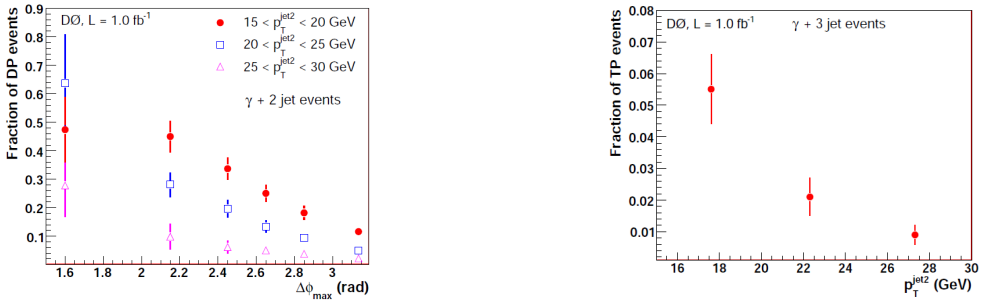

Figure 3.10: Left: fraction of DP events with total uncertainties in γ + 2 jet events as a function of the maximum $\Delta\phi$ between the γ-$j1$ pair and the second jet. Three regions of p_T^{j2} are studied in the correspondence to (3.36). Right: fraction of TP events with total uncertainties in γ + 3 jet events in three $p_T^{j2,j3}$ bins. Event sample definition corresponds to the previous measurement [49].

One year later, in the 2011, D0 published an extension of their original study described above. This time, they investigated azimuthal correlations in the γ + 3 jets and γ + 2 jets events [74]. The differential cross sections for the angle in the transverse

plane to the beam direction between the $\vec{p}_T$ of γ-jet and jet-jet pairs are compared with the Monte Carlo predictions. Photon and 3 jets are paired according to their transverse momenta, i.e. the first pair is formed by photon and the leading jet, the second pair is created by the second and third hardest jets. In the case of $\gamma + 2$ jets, the second pair is substituted only by the second jet. A wide variety of result numbers and distributions can be represented e.g. by ΔS (for $\gamma + 3$ jets) and $\Delta\phi$ (for $\gamma + 2$ jets) distributions in Fig. 3.9. ΔS is the same variable as defined in (3.39), while the $\Delta\phi$ substitutes the azimuth angle imbalance for the $\gamma + 2$ jets case and is defined as

$$\Delta\phi = \Delta\phi(\vec{p}_T(\gamma, j_1),\ \vec{p}_T(j_2)). \tag{3.42}$$

Notice, that only one p_T^{j2} bin is shown in the right plot in Fig. 3.9, while the lack of $\gamma + 3$ jets events prohibits to split the sample in the same way as the $\gamma + 2$ jets sample. The comparison is made against several tunes for Pythia and Sherpa [75] generators and the main purpose of this extensive study is to provide enough of information for the further tunes and improvements of the MPI models for these Monte Carlo programs.

Moreover, D0 estimated fractions of triple parton (TP) scattering events within $\gamma + 3$ jets data sample and DP event fraction in the $\gamma + 2$ jets sample. In the previous study, these TP events were part of the DP fraction and now their contribution is taken apart. Mean values of the appropriate fractions with their uncertainties are shown in Fig. 3.10.

4 Further DPS Studies

The goal of this chapter is to bring a comprehensive overview of processes, where multiple parton scattering may be a significant contribution or form physics background at parton level. All final states described below are considered for the proton-proton collisions at the LHC energies and were studied at theoretical level using direct calculation or Monte Carlo event generation. Studies involving kinematical specifics connected to the ATLAS detector and containing detector-simulated or real data are separated in Chapter 7.

The list of the studied processes serves as a demonstration of the importance of this phenomena, especially in the context of the hadron matter spatial distribution. Any process itself cannot fully describe parton-parton correlations inside the hadron (proton in the case of LHC), since the different processes probe generally different interacting partons. Thus, the range of the investigated processes is desired to be as wide as possible. All the complementary informations have to be collected and will serve for the testing of the theoretical models. The following list excludes studies concerning general 4-jet production, where no particular predictions were provided. Four categories are distinguished for a better systematization of the final states: vector boson followed by jets, $b\bar{b}$ associated with scalar or vector boson, vector boson pair and meson pair.

4.1 γ^*/Z/W + jets

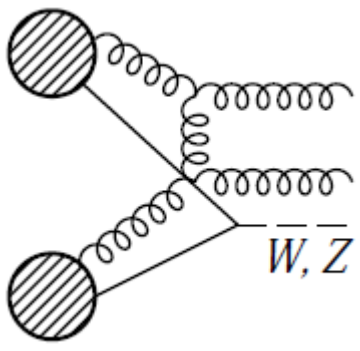

Figure 4.1: Example diagram for the DPS production of W/Z + 2 jets.

The process of direct photon + 3-jet production, which became popular at the Tevatron [26, 49], was also studied for the LHC energies of 7, 10 and 14 TeV [23]. The author shows a strong dependence of the MPI γ + 3 jets signal yield on the transverse momentum of the photon and concludes that single photon trigger at 80 GeV would suppress most of the signal and the MPI contribution would be at the per cent level. However, the MPI fraction increases to 5-10 % if the lower p_T threshold of 30 GeV is considered. Thus, the MPI measurement for γ + 3 jets final state is predicted to depend drastically on the trigger strategies but can be performed in principle.

A more significant measurement is proposed to search for opposite-charge same-flavor lepton pairs whose invariant mass is around the Z boson value,

see Fig 4.1. The study in Ref. [23] models the DPS events by combining parton level events from the matrix element generator MadEvent [76] and compares them to single parton scattering processes with the same final state. Possibilities of Z + 2/3/4-jet productions are considered at $\sqrt{s} = 7$, 10 and 14 TeV. The SPS processes are produced using the CTEQ6L1 [77] parton distribution function. DPS events are obtained combining at random one event from each of the reaction. DPS events can be re-weighted by the appropriate ratio of parton distribution functions and coupling constants in order to gain results corresponding also to other PDF choices, MRST2008LO [78] and GS09 [44, 47]. Therefore, one can compare fully factorized model of two-parton distribution function using convolution of single-parton distribution functions against the partially factorized model represented by the two-parton distribution function GS09. The effective cross section for the MPI cross section calculation is taken to be 12 mb.

A wide range of results can be found in [23]. Presented cross sections depend on three distribution functions, on three collision energies, on three jet separation cuts and also on the number of jets following the lepton pair. However, the general conclusion can be made. The signal to background ratio rises with energy approximately from 10 to 20 per cent. The DPS contribution to Z + 3 jets is the lowest one, which is clearly resulting from the parton level character of the investigated events. The differences for the parton distribution functions used are between 30 and 90 %, where the difference is lower for the processes with lower order in α_S. The absolute cross sections for the DPS Z + jets events are of order of 1 pb and therefore this channel is assumed to be measurable even within the first LHC data. An example of the final cross sections for Z + 2 jets is shown in Table 4.1. These results are in a good agreement with the predictions achieved earlier in [79] for Z + 2/3-jet production at Tevatron energies, where the value of 15.4 mb was taken for the σ_{eff}.

σ [pb]	7 TeV			10 TeV			14 TeV		
	CTEQ	MSTW	GS09	CTEQ	MSTW	GS09	CTEQ	MSTW	GS09
SPS	16.56	18.88		30.63	35.15		52.65	60.70	
DPS	1.88	2.61	2.66	4.80	6.35	6.68	11.27	14.37	15.50
S/B	0.11	0.14		0.16	0.18		0.21	0.24	

Table 4.1: Z($\mu\mu$) + 2-jet production cross sections in pb. Kinematical cuts reasonably follow general CMS and ATLAS acceptances.

A more detailed kinematical analysis was performed only for the case of Z + 4-jet production at $\sqrt{s} = 14$ TeV [24], where also the triple parton scattering was taken into account and its contribution was assumed to be 20 times lover than the double parton fraction. The single parton scattering background was reduced using $\Delta R > 0.5$ cuts for jet-jet and jet-lepton distances in $\eta - \phi$ plane, by $|\Delta\eta(j_f j_b)| > 3.8$ separation condition placed on the most forward and most backward jets in the event and using the cut on maximal angle among jets $|\Delta\phi(jj)| > 0.9\pi$, see Fig 4.2. These cuts reflect parton level behavior of independent parton interactions, where outgoing partons/jets are back-to-back oriented. The resulting signal-to-background ratio is close to 0.18 and

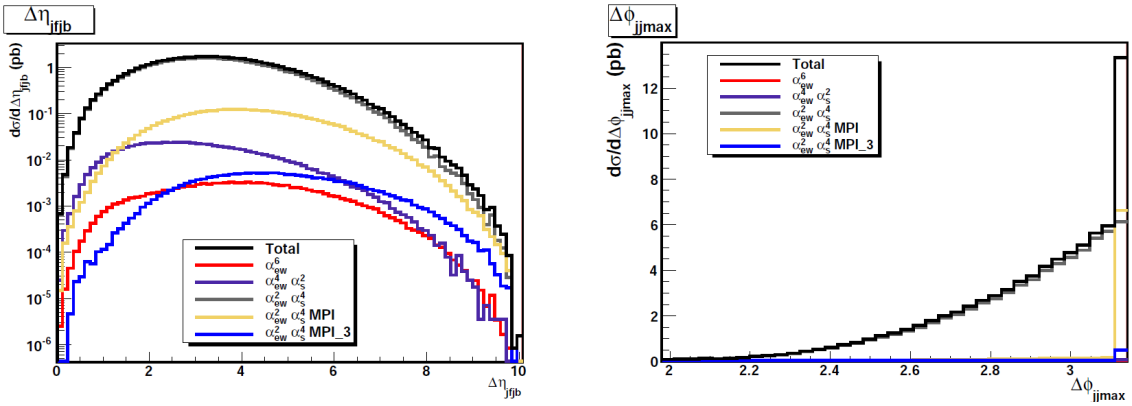

Figure 4.2: Distributions of $\Delta\eta$ separation between the most forward and the most backward jet (left) and distributions of largest $\Delta\phi$ separation between jet pairs (right) for different contributions (according to the types of vertices needed) to Z + 4-jet production. Z boson is assumed to decay leptonically.

the cross section for MPI signal production is predicted to be around 260 fb. Therefore, it appears measurable even for the 1 fb^{-1} of 14 TeV data.

W + jets production, see Fig 4.1, is very similar to the neutral boson + jets production, where the invariant mass of the lepton pair is loosened and therefore the ambiguity of the measurement rises. The price of the lover purity of the signal is balanced by the higher production cross section. Both processes are of the same importance since they probe different pairs of partons. Neutral bosons are created from same-flavor quark-antiquark pairs while the W bosons are mostly produced via $u\bar{d}$ and $d\bar{u}$ interactions. On the contrary, these Drell-Yan annihilations are followed by the QCD di-jet production probing mostly the gluon component of hadron.

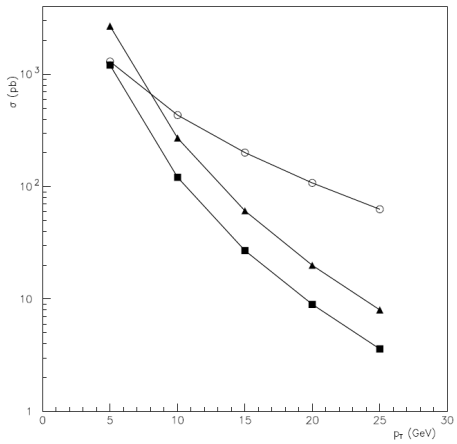

Figure 4.3: Cross section for W + 2-jet production as a function of the jet transverse momentum threshold for SPS higher order QCD (circles), DPS (triangles) and multiple hadron interactions (squares) [79].

At first, one can take a look at the transverse momentum of jets accompanying the W boson and compare the behavior of QCD higher order radiations against partons from double parton interactions. Figure 4.3 shows cross sections for W + 2-jet production as a function of the jet p_T threshold. Double parton scattering and multiple hadron interactions exhibit much steeper decrease than the QCD contribution. One can expect the same behavior of the additional jets for the Z boson production. This behavior can be used for the enhancement or reduction of the DPS in the data sample, as was used e.g. in [26].

Further predictions for the DPS W + jets production were done for the Tevatron energy [80], where the parton level production cross section was estimated to 10 pb, and for the LHC energy [25]. The latter study considers double parton scattering W + 4-jet production as a background for the $t\bar{t}$ production in the semi-leptonic decay channel, where no b-tagging is considered. One charged lepton and four jets were analyzed in order to quantify the individual contributions from single, double and triple parton scattering at the parton level. The cross section for the DPS events was normalized using the value of 14.5 mb for the σ_{eff}. In order to enhance the DPS fraction, the same cuts on $\Delta\eta(j_f j_b)$ and $\Delta\phi(jj)$ as in the case of Z + jets [24] were applied, as mentioned above. Moreover, no jet triplet was allowed to have invariant mass close to the top mass. The final inclusive DPS cross section was estimated to 2.8 pb, which creates 17% of the total W + 4-jet production cross section.

4.2 $b\bar{b}$ + H/W/Z

The Higgs boson production investigation is without any doubt the flagship of the LHC experiments. The question of the importance of the multiple parton scattering has been studied in several papers, e.g. [81–85], where the associated production of $b\bar{b}$ with either a vector or a scalar boson is of the main interest, since the $b\bar{b}$ decay channel is one of the most promising for the Higgs measurement.

In the Standard Model (SM) of particle interactions, the coupling constant for the H$b\bar{b}$ vertex is small, despite the large bottom quark mass, while e.g. the MSSM model offers a significant enhancement. Therefore, observation of the abundance of SPS events producing $b\bar{b}$ + H could bring new physics hints. On the other hand, double parton scattering contributes to the final state through two independent parton processes, one producing Higgs boson and one producing $b\bar{b}$ pair, similarly to Fig. 4.1. The SPS H + $b\bar{b}$ signal can be reached through the radiation of a Higgs scalar boson from the initial or final state lines, for instance like in left plot in Fig. 4.4. The study in [83] calculates NLO SM SPS contribution and compares it to the fully factorized model of DPS, where the σ_{eff} is taken to be 14.5 mb. The two cross sections are comparable and around 1 pb for Higgs mass around 126 GeV.

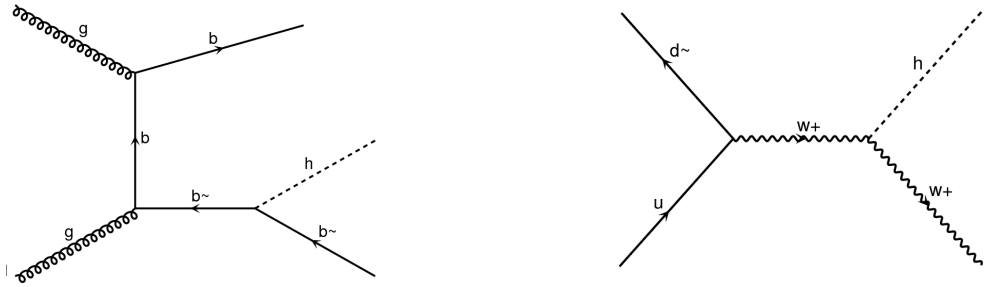

Figure 4.4: Left: One of the possible SPS diagrams producing Higgs boson in association with $b\bar{b}$ pair. Right: Example SPS diagram for Higgs boson production in association with W boson.

The measurement of the production of Higgs boson associated with any vector boson (either W or Z), see e.g. right plot in Fig. 4.4, is an effective way of how to reduce QCD background that would normally overwhelm the Drell-Yan production of the Higgs boson decaying hadronically. For the Higgs mass around 126 GeV, the most important decay channel is the $b\bar{b}$ creation. From the experimental point of view, the most promising is to search for one isolated lepton coming from W decay and the $b\bar{b}$ pair. Background created by the double parton scattering was studied in [81,82,85]. In principle, both W and Z vector bosons can be searched for in association with the Higgs boson, as studied in [84].

Theoretical calculations [84,85] estimate the production cross sections for DPS background to W/Z + $b\bar{b}$ for $\sigma_{eff} = 12.0$ mb and conclude that the DPS contribution produce a sizable background to SPS Higgs production. In order to suppress this DPS background, or oppositely to enhance it, kinematical variables sensitive to the event topology are studied with an optimistically looking strength to distinguish the origin of the given final state. Similarly to the case of 4 jets and γ + jets measurements described in Chapter 3, angular and transverse momentum sensitive variables are used in order to quantify the back-to-back orientation of the appropriate pairs of outgoing particles and jets. A parton level study for 7 TeV p-p interactions [81] evaluates $S_{p'_T}$ transverse momentum imbalance defined in Eq. (3.37) and the azimuthal angle between outgoing pairs $\Delta\phi$ for the DPS W + $b\bar{b}$ signal and sum of SPS processes creating physics background to it, see Fig. 4.5. The pairing of the final state particles is based on the reconstruction of the neutrino p_T from the missing transverse energy and therefore one pair is lepton + its neutrino and the second pair corresponds to two b-jets. The most problematic background, the SPS $t\bar{t}$ production, is highly suppressed by the cut on maximum missing transverse energy of 45 GeV.

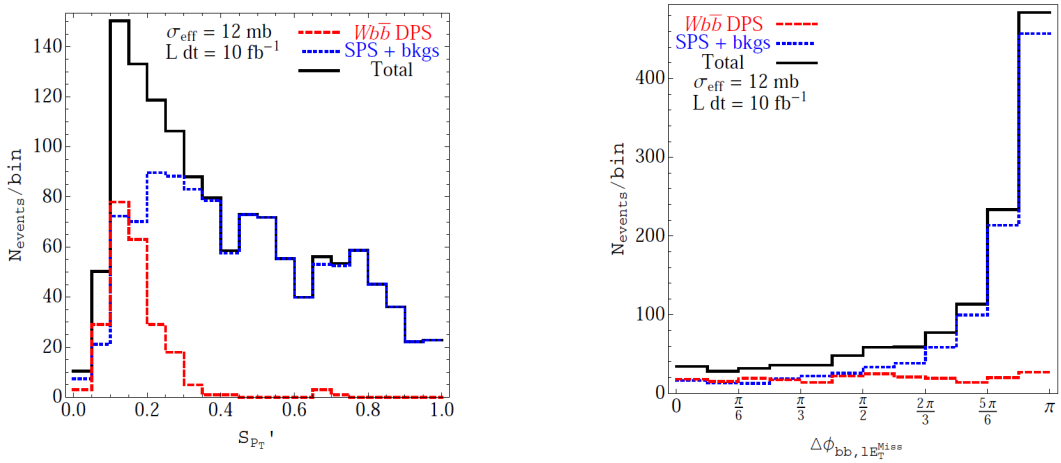

Figure 4.5: Distributions of $S_{p'_T}$ (left) and $\Delta\phi$ (right) for DPS and SPS productions of W + $b\bar{b}$.

The shape of the transverse momentum imbalance $S_{p'_T}$ is remarkably different for SPS and DPS processes. The DPS signal peaks for the lower values of $S_{p'_T}$ and thus the DPS selection cut is chosen to $0 < S_{p'_T} < 0.25$. On the other hand, the azimuthal

angle between the final pairs tend to be close to the maximum value of π for the DPS signal. The DPS selection is restricted to events, where $\Delta\phi < 3/4\ \pi$. The production cross section for DPS events was normalized using $\sigma_{eff} = 12.0$ mb. The final selection is expected to have a statistical significance in the range $S/\sqrt{B} \sim 12$ - 15. A similar study in Ref. [82] uses artificial neural network for DPS and SPS separation and concludes that DPS fraction could be within 4 - 8 per cent with respect to the SPS W + 2-jet production, where the invariant mass of the jet pair has to be in the range (115 - 150) GeV.

4.3 Vector boson pair

Generally, a multiple weak boson production is an important component of the Standard Model and its precise measurement became one of the main goals of the LHC physics programs. A more precise tuning of SM free parameters or even signs of new physics depend on the ability to determine all the possible physics background processes. If the component coming from the multiple parton scattering does or does not play a negligible role remains an open question. Theoretical work [86] compares production cross sections for almost all charge combinations of two, three and four weak gauge bosons (with no branching ratios) for both single and double parton scattering processes in proton-proton collisions at $\sqrt{s} = 14$ TeV. In the latter category, the author used a fully factorized model for double parton distribution function and the value of $\sigma_{eff} = 14.5$ mb. Reported rates are evaluated at leading order and thus the three and especially four boson productions are only rough estimates. Still, one can observe very strong dominance of SPS processes over the DPS ones for three and four gauge boson productions. DPS production rates of ZZ and oppositely charged WW are smaller by two orders of magnitude than the SPS contributions. Only the DPS production of same sign W pair is comparable to its SPS counterpart, since the SPS production requires additional two jets in its lowest order and thus is suppressed in comparison to the opposite-sign W pair production.

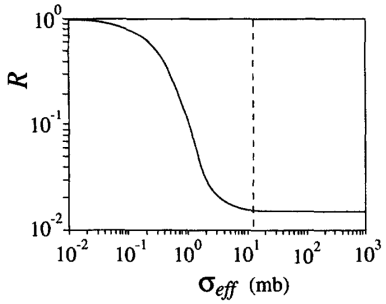

Figure 4.6: The ratio R of the same-sign and opposite-sign W pair production rates as a function of the σ_{eff}.

If one could measure precisely any charge combination of the W pair production, the yield ratio between same-sign and opposite-sign pairs

$$R = \frac{\sigma^{SPS}_{W^+W^+} + \sigma^{DPS}_{W^+W^+} + \sigma^{SPS}_{W^-W^-} + \sigma^{DPS}_{W^-W^-}}{\sigma^{SPS}_{W^+W^-} + \sigma^{DPS}_{W^+W^-}} \quad (4.1)$$

would be a useful characteristic that might be tested for DPS models. The ratio is calculated in [87] for a wide range of the σ_{eff}, see Fig. 4.6. However, the ratio looks sensitive to the σ_{eff} only in the range between 0.1 and 10 mb. The plateau for the higher values indicates no determination power for this ratio.

A special case should be highlighted. The opposite-sign W pair production associated with at least two additional jets is one of the important channels for the Higgs boson observation

at ATLAS [88]. As pointed out above, DPS does not contribute to the pure di-lepton final state but it shows up that the case with the additional jets might be much more contaminated by this DPS background. The study in [24] calculates all SPS and DPS cross sections for $\mu^+\mu^- jj$ production and uses similar cuts as in [88]. The event selection is designed to suppress the most serious background, the $t\bar{t}$ production, requiring some minimal di-jet invariant mass and minimal rapidity (or pseudo-rapidity) between the two jets. The event selection in [24] contains cuts

$$|\eta_{jj}| > 4.2, \qquad M_{jj} > 600 \text{ GeV}, \tag{4.2}$$

which are very similar to cuts in [88], and finds that DPS fraction is negligible.

Since the DPS contribution to this final state can be easily filtered off, one has to search for a process with minimal SPS competing background and search for kinematical selection, which could enhance the DPS chances to be observed. The same-sign W pair production is very promising in this context and is the subject of this thesis. Detailed description and discussion is moved to the Sec. 9.1. Here, only few remarks concerning previous studies are given. Papers [24, 89] compare DPS only against the SPS WW + 2-jet production and thus the conclusions are exaggeratedly optimistic. There is only one work [48] dealing with all the main physics background processes but only at the parton level. In order to model more realistically p_T spectra of the outgoing leptons, the authors introduce p_T smearing for the W boson, which would have a zero p_T without the higher order radiations. Jets that would accompany the lepton pair in the real high energy collision are not analyzed. This study provides very valuable hints and suggestions for the further investigation, especially in the direction of the multi-body parton distribution function modeling. Their predictions are made using both fully factorized and semi-factorized double PDFs. The former model uses the single PDF MRST2008LO and also introduces some trivial parton correlations to final double parton distribution function:

$$D^{ab}(x_1, x_2) = f^a(x_1) f^b(x_2) \Theta(1 - x_1 - x_2)(1 - x_1 - x_2)^n, \qquad n \;=\; 0,\; 1,\; 2. \tag{4.3}$$

The Heaviside function Θ controls the longitudinal momentum conservation, while the polynomial function behind it artificially suppress events, where interacting partons would have the sum of their momenta close to one. Models for $n = 0,\, 1,\, 2$ ($\text{MSTW}_{0,1,2}$) are kinematically compared to the semi-factorized double PDF GS09. Figure 4.7 shows distributions of lepton pseudorapidity and the pseudorapidity asymmetry, defined for two leptons l_1 and l_2 as:

$$a_{\eta_l} = \frac{\sigma(\eta_{l_1} \cdot \eta_{l_2} < 0) - \sigma(\eta_{l_1} \cdot \eta_{l_2} > 0)}{\sigma(\eta_{l_1} \cdot \eta_{l_2} < 0) + \sigma(\eta_{l_1} \cdot \eta_{l_2} > 0)}. \tag{4.4}$$

One can see that the higher rapidities are probed the higher effect of correlations in longitudinal momenta is visible, since different models for double PDFs include different amount of correlations.

In conclusion from [48], same-sign WW parton level analysis indicates a general measurability of the DPS process in comparison to the physics background. SPS WZ

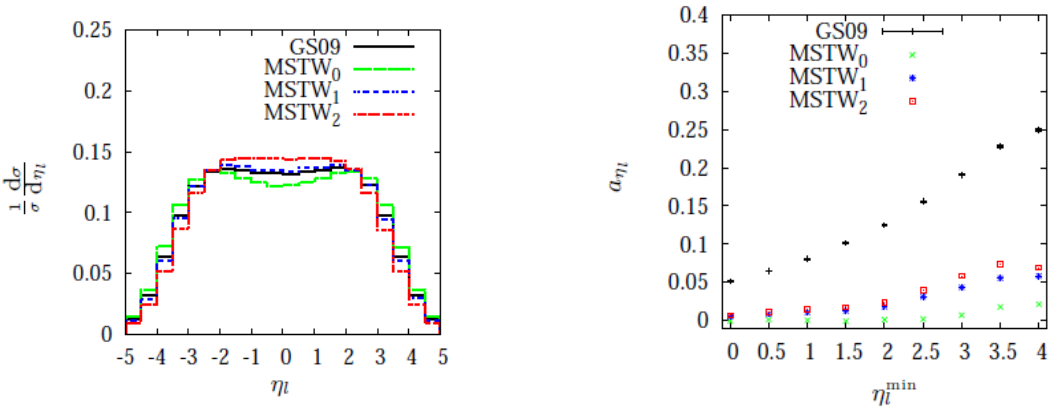

Figure 4.7: Lepton pseudorapidity (left) and the appropriate asymmetry (right) for p-p collisions at $\sqrt{s} = 14$ TeV for four different models for double PDF. No cuts are applied.

pair production creates the most serious background that oversizes the DPS signal by factor of 6 (for l^+l^+) and of 8 (for l^-l^-). $\sigma_{eff} = 14.5$ mb was used for the DPS cross section normalization.

Predictions for the second type of double Drell-Yan process, the DPS γ^*/Z pair production, also attracts interest. Theoretically, two pairs of oppositely charged leptons with the same flavor and with the invariant mass around the Z boson value is very attractive from the experimental point of view, since one can easily pair the four lepton final state and so separate the two independent Drell-Yan Z boson creations. Unfortunately, such a DPS production cross section would be too low and therefore one has to turn his attention towards lower values of the lepton pair invariant mass. The inclusion of the virtual photon production into the double Drell-Yan process rises not only the signal cross section but magnifies the list of the possible physics background processes and also increases the ambiguity in the lepton pairings.

The study in [90] ignores the background created by a coincident creation of four leptons, e.g. in simple QCD process with huge underlying cross section, and compares DPS only to SPS di-boson production. Even though, their results exhibit a strong complications in the definition of the lepton pairings and generally in the process identification. At parton level (PL), the transverse momentum imbalance

$$S = \frac{1}{2}\left(\frac{|\vec{p}_T^{\,\mu_1^+} + \vec{p}_T^{\,\mu_1^-}|}{|\vec{p}_T^{\,\mu_1^+}| + |\vec{p}_T^{\,\mu_1^-}|} + \frac{|\vec{p}_T^{\,\mu_2^+} + \vec{p}_T^{\,\mu_2^-}|}{|\vec{p}_T^{\,\mu_2^+}| + |\vec{p}_T^{\,\mu_2^-}|}\right) \tag{4.5}$$

serves as a perfect tool in distinguishing the SPS and DPS contributions, see the solid line in Fig. 4.8. However, the modeling of the parton shower (PS) and the intrinsic parton k_T smearing, signed in Fig. 4.8 as σ, has a drastic effect on the S distributions. The perfect zero imbalance gets smeared over almost the whole region between 0 and 1. The remaining differences between SPS and DPS are not very convictive. More powerful variables are the transverse momenta of the outgoing leptons, which are lower for DPS than for SPS, and angular correlation sensitive variables, like the azimuth angle

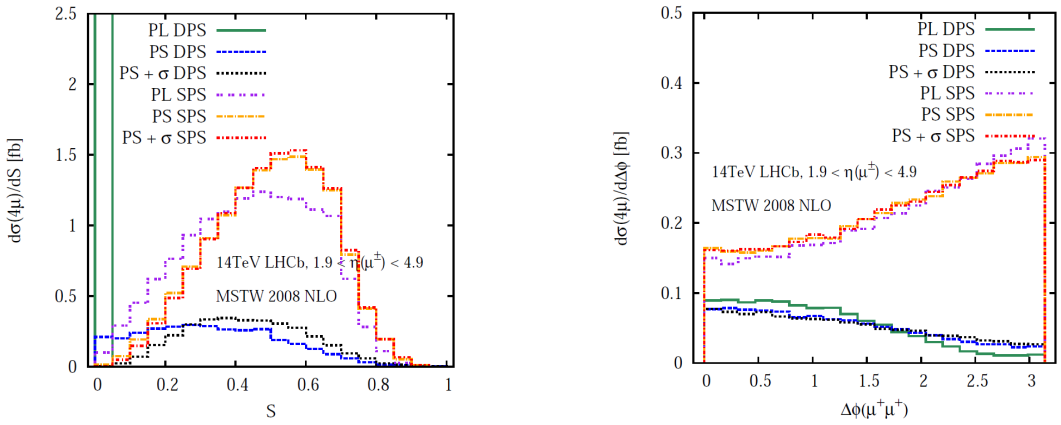

Figure 4.8: Left: distributions of the transverse momentum imbalance S for the four muon final state produced via DPS and SPS process. Right: distributions of the angle between the two μ^+ in the transverse plane. Both plots show three levels of transverse momentum modeling for both processes. Proton-proton interactions at 14 TeV were considered.

between the same-sign leptons. The former character of DPS events favors experiments, where detectors are capable to detect low p_T leptons, like LHCb. The angular correlation between the two γ^*/Z's in SPS process induce a bigger angular separation of the outgoing same-sign leptons in the transverse plane, $\Delta\phi$, see Fig. 4.8. The expected flat distribution of $\Delta\phi$ for DPS process is affected by the kinematical selection and tend to be shifted towards the smaller angular separation. In summary, double Drell-Yan production of two neutral vector bosons can be measurable at low p_T detectors, like LHCb, but very problematic at ATLAS.

4.4 Meson pair

Similarly to the double Drell-Yan process, the four lepton final state can also be studied as a signal for double meson production, e.g. pp $\rightarrow$ J/ψ + J/ψ + X. Lepton pairing becomes much more definite for the known invariant mass and no transverse momentum imbalance is needed. Recently, the LHCb collaboration published results of single [91] and double [92] J/ψ measurement. They observe a strong disagreement of double J/ψ data with the SM SPS expectations. Studies like [90, 93–96] comment the LHCb data and add DPS estimation to SPS predictions to explain the event abundance. Numerically, the measured double J/ψ production cross section is 5.6$\pm$1.1$\pm$1.2 nb, while the SPS component is evaluated approximately to 4 nb and the DPS contribution is predicted to be around 2 nb. Besides the production rates, also kinematics of SPS and DPS components seems to be complementary and could fit the data well. Invariant mass distribution of the J/ψ pair from [93] indicate very significant fraction of the DPS events in the measured data, see left plot in Fig. 4.9. The mass distribution for SPS events peaks at too low values, while the DPS distribution is wider and peaks at higher

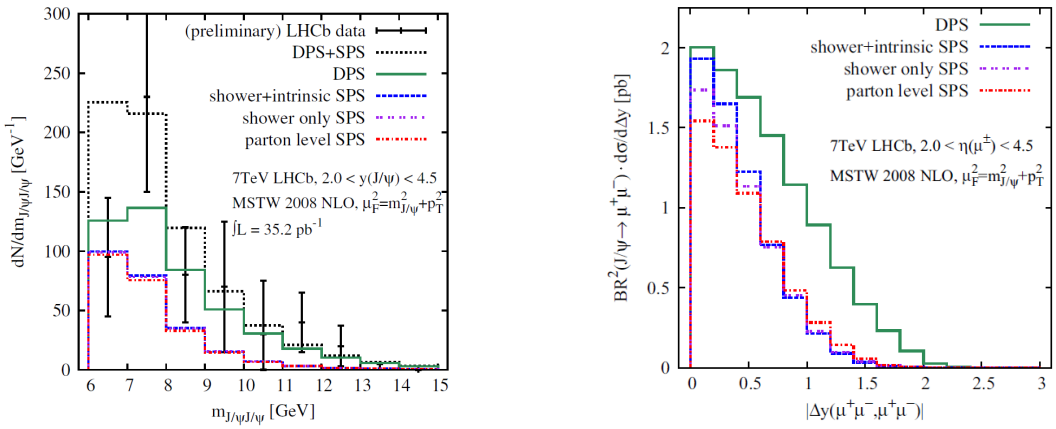

Figure 4.9: Invariant mass distribution (left) and rapidity separation (right) for $J/\psi \to \mu^+\mu^-$ pair.

values. Even though the data points have large uncertainties, the combined SPS and DPS distribution fits the data quiet well. However, the further diagnostics of the measured data and identification of the DPS fraction might be problematic. SPS process produces much more angularly correlated meson pairs than the DPS process and thus the difference in their rapidity should be generally smaller. Right plot in 4.9 compares SPS and DPS distributions of $|\Delta y|$ between the two lepton (muon) pairs.

The authors of [94, 96] do not follow the effort for the SPS and DPS identification and rather search for slightly different processes, where the SPS or DPS component would be suppressed in principle. At the preliminary level, the authors argue that the production of two different quarkonia resonances is highly suppressed for SPS processes, while the two independent productions in DPS are not affected by the change of the final state. Therefore, the productions of $J/\psi + \chi_c$, $J/\psi\ \Upsilon$ and $\chi_b\chi_c$ are suggested for even better DPS measurement than the J/ψ pair production.

Other MPI studies probe low p_T regions, whether they investigate neutral pion pair production at RHIC [97], J/ψ production associated with open charm hadron or double open charm hadron production at LHCb [98] or just QCD $c\bar{c}$ [99] and $b\bar{b}$ [100] pair production for proton-proton collisions.

The incoming LHC era will hopefully bring enough information for all of these processes that the final sum of our knowledge will truly provide a new picture of the hadron matter.

5 Effective Cross Section Correction

All measurements of the DPS described in Chapter 3 aimed for the estimation of the value of the effective cross section, σ_{eff}, which was defined to scale the inclusive DPS cross sections for any two parton interactions independent on each other, see Eq. (3.1). CDF's measurement of the direct photon production in association with three jets from the year 1997 [26], described in details in Section 3.4, was better than any that came before it. Their method avoided almost all reliance on a Monte Carlo modeling of their final states and on theoretically calculated cross sections. The importance of this measurement is underlined by the fact that almost all the analysis predicting DPS measurements for the LHC era described in Chapter 4 use the CDF's result

$$\sigma_{eff(CDF)} = (14.5 \pm 1.7(\text{stat.})^{+1.7}_{-2.3}(\text{syst.}))\ \text{mb}. \tag{5.1}$$

There are few exceptions, since some analyses try to reflect the dependence of σ_{eff} on the energy of the hadron collision.

This chapter points out that CDF used a non-standard definition of the σ_{eff}, in which the left-hand-side of Eq. (3.1) corresponds to the cross section for exactly two scatters, rather than the more conventional definition, in which it corresponds to the inclusive two-scatter cross section [101]. This transition was done when CDF excluded the estimated $17^{+40}_{-8}\%$ of the triple parton scattering events from their measurement. Their definition of the σ_{eff} can be written in terms of the appropriate final state selection:

$$\sigma^{ex}_{\gamma+3jets;2} = \frac{\sigma_{\gamma+1jet}\sigma_{2jets} + \sigma_{\gamma+2jets}\sigma_{1jet}}{\sigma_{eff(CDF)}}. \tag{5.2}$$

Here, same as in the rest of the chapter, number of required scatters is explicitly denoted using semi-colon and the appropriate number after the final state declaration in the subscript. The inclusive and exclusive cross sections are also clearly distinguished by the superscript. Cross sections with no indices are the standard inclusive single parton scattering cross sections, e.g. $\sigma^{in}_{\gamma+1jet;1} = \sigma_{\gamma+1jet}$.

The work in Ref. [102] from the year 1999 was the first one, where the need of the correction from one definition of the σ_{eff} to the other was highlighted. The authors correctly noted that the exclusive value of the $\sigma_{eff(CDF)}$ should be regarded as an upper bound on the value related to an inclusive measurement. In the 2007 study [30], the author suggests a correction based on the parton level picture of the interaction and evaluates the σ_{eff} to be roughly 11 mb.

This chapter recapitulates the parton level analysis in details, see Section 5.1, where the exclusive double and triple parton scattering cross sections are expressed in terms of σ_{eff} and $\sigma_{eff(CDF)}$ in order to demonstrate the transition between exclusive and inclusive measurements. Section 5.2 argues that this parton level correction is too oversimplified, since CDF was not able to count the number of scatters in the event, and that the indirectness of CDF's measurement in identifying double and triple scatters requires more sophisticated analysis. Section 5.3 estimates the theoretical value σ_{eff} from the overlap function for two colliding hadrons in the given model. Section 5.4 revises the method of the $\sigma_{eff(CDF)}$ extraction with the aimed at reducing its experimental uncertainty. The analysis of the Monte Carlo data necessary for the evaluation of the final correction is described in Section 5.5. The result for the correct σ_{eff} value is given in the last section of this chapter.

5.1 Parton level correction

The evaluation of the parton level correction is the starting point for the further specification. In this model, analysis of the $\gamma + 3$ jets final state is simplified to the description of the double parton scattering event as a composition of independent parton processes of two types. First type, let's note it as process a, corresponds to the direct photon production, while the second type, process b, is any QCD $2 \to 2$ process. At this stage, one does not count how many jets are detected from which process. The process is considered as present in the event, when at least one jet can be detected. Experimental analysis implies that inclusive double parton scattering producing $\gamma + 3$ jets consists of one process of type a and one process of type b, or consists of one process of type a and two processes of type b. The former process is the exclusive double parton scattering and the latter process is the triple parton scattering. This classification is the salient point of the oversimplification stemming from the parton level picture, in which one has the ability to distinguish how many processes of type b are present in the event. The final correction for σ_{eff} then rises from the comparison between the exclusive cross sections for double and triple parton scattering. This ratio

$$\frac{\sigma^{ex}_{ab;3}}{\sigma^{ex}_{ab;2}} = \frac{17}{83}. \tag{5.3}$$

is the key information available from the CDF measurement besides the value of the $\sigma_{eff(CDF)}$.

The general expression of the exclusive multi parton scattering cross section arises from the simple statistical approach, where the dependence of the parton distribution functions on the hadron impact parameter and longitudinal momentum fraction factorizes. In this model, the Poisson distribution describes the probability of having exactly n parton scatterings of the type a and exactly m parton scatterings of the type b, at the given hadron collision impact parameter β. The parameter of this Poisson distribution is the mean number of the given parton interactions. According to the eikonal model, the average number of parton scatterings of type a can be expressed as a convolution of single parton interaction cross section, σ_a, and the hadron-hadron overlap function, $A(\beta)$.

Specifically, the cross section for exactly one scattering of type a and one interaction of type b can be expressed as

$$\sigma_{ab;2}^{ex} = \sigma_a \sigma_b \int d^2\beta \left(A(\beta)\right)^2 e^{-(\sigma_a+\sigma_b)A(\beta)} = \frac{\sigma_a \sigma_b}{\sigma_{eff(CDF)}}. \tag{5.4}$$

One can immediately see the inconvenience of such a definition of effective cross section

$$\sigma_{eff(CDF)} = \frac{1}{\int d^2\beta \left(A(\beta)\right)^2 e^{-(\sigma_a+\sigma_b)A(\beta)}}, \tag{5.5}$$

which clearly depends on the investigated processes. On the other hand, the appropriate inclusive double parton scattering cross section is

$$\sigma_{ab;2}^{in} = \sigma_a \sigma_b \int d^2\beta \left(A(\beta)\right)^2 = \frac{\sigma_a \sigma_b}{\sigma_{eff}}, \tag{5.6}$$

where the integrand does not contain the exponential factor and depends only on the hadron overlap function. Inverse value of this integral is therefore more convenient definition of the measurable effective cross section:

$$\sigma_{eff} = \frac{1}{\int d^2\beta \left(A(\beta)\right)^2}. \tag{5.7}$$

One may note that the two scale factors (5.5) and (5.7) become identical for rare processes with small cross sections. However, the γ + jets measurement is not the case and the exponential factor plays the non-negligible correction role.

In the following, two notation simplifications are made. First, the cross section for direct photon production can be neglected in addition with the QCD scattering, i.e. $\sigma_a + \sigma_b \approx \sigma_b$. Second, since the maximal number of parton scatterings in the CDF analysis is three, the expansion of the exponential factors is always in the appropriate accuracy, i.e. to the third order of the overlap function.

With the given accuracy and using the definition of the inclusive effective cross section (5.7), one can rewrite the exclusive double parton scattering cross section for one process of type a and one process of type b to

$$\sigma_{ab;2}^{ex} = \sigma_a \sigma_b \int d^2\beta \left(A(\beta)\right)^2 \left(1 - \sigma_b A(\beta)\right) = \frac{\sigma_a \sigma_b}{\sigma_{eff}} - \mathcal{R}\frac{\sigma_a \sigma_b^2}{\sigma_{eff}^2}, \tag{5.8}$$

where

$$\mathcal{R} \equiv \frac{\int d^2\beta \left(A(\beta)\right)^3}{\left[\int d^2\beta \left(A(\beta)\right)^2\right]^2}. \tag{5.9}$$

The discussion about the factor $\mathcal{R}$ is moved to Section 5.3. Here, one can evaluate it using the exclusive triple parton scattering cross section for one process of type a and two processes of type b

$$\sigma_{ab;3}^{ex} = \frac{1}{2}\sigma_a \sigma_b^2 \int d^2\beta \left(A(\beta)\right)^3 = \frac{1}{2}\sigma_a \sigma_b^2 \frac{\mathcal{R}}{\sigma_{eff}^2}, \tag{5.10}$$

as

$$\mathcal{R} = \frac{2\sigma_{eff}^2 \sigma_{ab;3}^{ex}}{\sigma_a \sigma_b^2}. \tag{5.11}$$

So far, a and b processes are the same for double and triple parton scattering and the insertion of (5.11) into (5.8) leads to

$$\sigma_{ab;2}^{ex} = \frac{\sigma_a \sigma_b}{\sigma_{eff}} - 2\sigma_{ab;3}^{ex}. \tag{5.12}$$

Cross sections for a and b processes in the first term can be replaced using the $\sigma_{eff(CDF)}$ definition (5.5) and one gets the final relation between the two effective cross sections:

$$\sigma_{eff(CDF)} = \sigma_{eff} \left(1 + 2\frac{\sigma_{ab;3}^{ex}}{\sigma_{ab;2}^{ex}} \right). \tag{5.13}$$

This relation completely reproduces the result of [30]. Numerically it leads to

$$\sigma_{eff} \approx \frac{\sigma_{eff(CDF)}}{1.14} = 10.3 \text{ mb}. \tag{5.14}$$

5.2 Hadron level correction

At this point, one has to switch from the parton level description to hadron level using the event definition of CDF, since the real experiment cannot distinguish the true number of scatters. In order to calculate the same quantities as before, one has to analyze all possible single parton scattering processes, which in double or triple combination can form the final state of $\gamma + 3$ jets. According to the CDF paper, double parton scattering can proceed in two ways. Prompt photon is followed by 2 jets coming from the same scatter in roughly 75% of double parton events while the the third jet comes form the second scatter. In the rest of 25% of the event sample, the photon creation produces only one jet and the two remaining jets come form the second scatter. On the other hand, the triple parton scattering may proceed only in one combination, where each scatter produces exactly one jet in the measured kinematic region.

With the same accuracy as in the parton level case, exclusive double and triple parton scattering production rates are

$$\begin{aligned} \sigma_{\gamma+3jets;2}^{ex} = \int d^2\beta [& (\sigma_{\gamma+1jet} A(\beta)) (\sigma_{2jets} A(\beta)) + \\ & + (\sigma_{\gamma+2jets} A(\beta)) (\sigma_{1jet} A(\beta))] (1 - \sigma_{jets} A(\beta)), \end{aligned} \tag{5.15}$$

$$\sigma_{\gamma+3jets;3}^{ex} = \frac{1}{2!} \int d^2\beta \left[(\sigma_{\gamma+1jet} A(\beta)) (\sigma_{1jet} A(\beta)) (\sigma_{1jet} A(\beta)) \right]. \tag{5.16}$$

Note that the exponential factor for suppressing further jet production from additional scatters is changed to $-\sigma_{jets} A(\beta)$, where σ_{jets} is the inclusive cross section for production of at least one jet with $\mathrm{E}_T > 5$ GeV.

The procedure described below is completely analogous to the parton level case. The $\mathcal{R}$ factor is evaluated from (5.16):

$$\mathcal{R} = \frac{2\sigma_{eff}^2 \sigma^{ex}_{\gamma+3jets;3}}{\sigma_{\gamma+1jet}\sigma_{1jet}^2}. \tag{5.17}$$

Exclusive double parton scattering cross section (5.15) then becomes

$$\sigma^{ex}_{\gamma+3jets;2} = \frac{\sigma_{\gamma+1jet}\sigma_{2jets} + \sigma_{\gamma+2jets}\sigma_{1jet}}{\sigma_{eff}} - 2\frac{\sigma_{\gamma+1jet}\sigma_{2jets} + \sigma_{\gamma+2jets}\sigma_{1jet}}{\sigma_{\gamma+1jet}\sigma_{1jet}}\frac{\sigma_{jets}}{\sigma_{1jet}}\sigma^{ex}_{\gamma+3jets;3}, \tag{5.18}$$

where the first term is again rewritten using the CDF's definition of effective cross section. This time, all subprocesses are specified according to their final state:

$$\sigma^{ex}_{\gamma+3jets;2} = \frac{\sigma_{\gamma+1jet}\sigma_{2jets} + \sigma_{\gamma+2jets}\sigma_{1jet}}{\sigma_{eff(CDF)}}. \tag{5.19}$$

Putting everything together yields the relation corrected to the event definition:

$$\sigma_{eff(CDF)} \approx \sigma_{eff}\left(1 + 2\frac{\sigma^{ex}_{\gamma+3jets;3}}{\sigma^{ex}_{\gamma+3jets;2}} \times \frac{\sigma_{\gamma+1jet}\sigma_{2jets} + \sigma_{\gamma+2jets}\sigma_{1jet}}{\sigma_{\gamma+1jet}\sigma_{1jet}} \times \frac{\sigma_{jets}}{\sigma_{1jet}}\right) \tag{5.20}$$

$$= \sigma_{eff}\left(1 + 2\frac{\sigma^{ex}_{\gamma+3jets;3}}{\sigma^{ex}_{\gamma+3jets;2}}\left(\frac{\sigma_{2jets}}{\sigma_{1jet}} + \frac{\sigma_{\gamma+2jets}}{\sigma_{\gamma+1jet}}\right)\frac{\sigma_{jets}}{\sigma_{1jet}}\right) \tag{5.21}$$

$$= \sigma_{eff}\left(1 + 2\frac{\sigma^{ex}_{\gamma+3jets;3}}{\sigma^{ex}_{\gamma+3jets;2}} f\right) \tag{5.22}$$

where f is the correction factor characterizing the difference between the parton and hadron level corrections

$$f = \left(\frac{\sigma_{2jet}}{\sigma_{1jet}} + \frac{\sigma_{\gamma+2jets}}{\sigma_{\gamma+1jet}}\right)\frac{\sigma_{jets}}{\sigma_{1jet}} \tag{5.23}$$

In general, the first component of the new correction factor f is expected to be smaller than unity, while the second component is expected to be larger than unity. Thus the direction of the overall effect is not straightforward.

The required cross sections cannot be extracted from the CDF paper alone, however, the cross sections are closely related and paired into ratios, where they can be better predicted. In further, a Monte Carlo generation is used to extract the cross sections and to make an estimate of their uncertainty.

5.3 $\mathcal{R}$ factor

A short comment on the previously defined $\mathcal{R}$ factor (5.9) is in order here since its physics relevance is very interesting. The direct comparison of the inclusive effective cross section (5.7) and the CDF effective cross section (5.5) can be obtained using the

substitution of σ_{jets} instead of the σ_b and by expansion of the exponent with the same accuracy as before. With a little arithmetic one obtains:

$$\begin{aligned}\sigma_{eff(CDF)} &\approx \frac{1}{\int d^2\beta (A(\beta))^2(1-\sigma_{jets}A(\beta))} = \\ &= \sigma_{eff} + \frac{\int d^2\beta \sigma_{jets}(A(\beta))^3}{\int d^2\beta (A(\beta))^2 \left[\int d^2\beta (A(\beta))^2 - \int d^2\beta \sigma_{jets}(A(\beta))^3\right]} \approx \\ &\approx \sigma_{eff} + \frac{\int d^2\beta (A(\beta))^3}{\left[\int d^2\beta (A(\beta))^2\right]^2}\ \sigma_{jets}, \end{aligned} \tag{5.24}$$

which is

$$\sigma_{eff(CDF)} \approx \sigma_{eff} + \mathcal{R}\sigma_{jets}. \tag{5.25}$$

The coefficient $\mathcal{R}$ was expressed in the previous sections from the known ratio of triple and double parton scattering production rates. However, the coefficient $\mathcal{R}$ can be also calculated numerically as a function of the overlap function, which depends on the transverse parton distributions $g(\beta')$ integrated over the hadron radius

$$A(\beta) = \int d^2\beta' g(\beta')g(\beta - \beta') \tag{5.26}$$

It is also interesting to note that the value of the $\mathcal{R}$ parameter depends only on the shape of the overlap function and not on its size. Four types of transverse parton distributions were tested and the results are in the increasing order for the coefficient $\mathcal{R}$: a 'black disc' type ($\mathcal{R} = 1.26$), a Gaussian distribution ($\mathcal{R} = 1.33$), the electromagnetic form factor as used in Herwig++ [56] ($\mathcal{R} = 1.46$), and an exponential distribution ($\mathcal{R} = 1.78$). However, the unknown value of σ_{jets} prohibits the feedback extraction of any constraints from the CDF measurement and any Monte Carlo dependent absolute value would be very inaccurate.

5.4 Triple parton scattering removal uncertainty

The last step towards the final form of our correction is motivated by an effort to suppress the systematic error of the effective cross section. CDF reports that the triple parton event fraction is $17^{+40}_{-8}\%$. Such a large uncertainty is then propagated to the final systematic error in the evaluation of the effective cross section $\sigma_{eff(CDF)}$. This one of the biggest contributions to the systematic error can be avoided by revising CDF's procedure. Therefore, the next step is to define a new CDF effective cross section, $\hat{\sigma}_{eff(CDF)}$, which would correspond to the CDF's measurement, if the estimation of the fraction of the triple parton scattering events would not be used for correcting the final number of searched DPS events.

For a brief revision of CDF's measurement, let's recapitulate the formula (3.24):

$$\sigma_{eff(CDF)} = \frac{N_{DI}}{N_{DP}} \left(\frac{A_{DP}}{A_{DI}}\right) R_C \sigma_{NSD}, \tag{5.27}$$

where main numbers are:

$$\begin{aligned} N_{DI} &= 1060 \pm 110 \pm 110, \\ N_{DP} &= N_{DP+TP} \times R_{DP} \\ &= 7360 \pm 360^{+720}_{-380}, \\ N_{DP+TP} &= 8865 \pm 430 \pm 150, \\ R_{DP} &= 0.83 \pm 0^{+0.08}_{-0.04}. \end{aligned}$$

Here, N_{DI} stands for the number of double hadron interactions (DI), identified using vertex detector, N_{DP} is the number of pure exclusive double parton scattering (DP) events. R_{DP} is the fraction of DP events within all MPI events N_{DP+TP}. The other parameters in (5.27) are explained in Section 3.4. Our new effective cross section is defined

$$\hat{\sigma}_{eff(CDF)} = \frac{N_{DI}}{N_{DP+TP}} \left(\frac{A_{DP}}{A_{DI}} \right) R_C \sigma_{NSD} = \frac{N_{DP}}{N_{DP+TP}} \sigma_{eff(CDF)} \tag{5.28}$$

and its value

$$\hat{\sigma}_{eff(CDF)} = (12.0 \pm 1.4(\text{stat.})^{+1.3}_{-1.5}(\text{syst.})) \text{ mb}. \tag{5.29}$$

carries a smaller systematic error than the original value (5.1).

The inclusive effective cross section can be obtained by adding $\sigma^{ex}_{\gamma+3jets;3}$ to both sides of Eq. (5.18) and one gets

$$\begin{aligned} \sigma^{ex}_{\gamma+3jets;2} + \sigma^{ex}_{\gamma+3jets;3} = & \frac{\sigma_{\gamma+1jet}\sigma_{2jets} + \sigma_{\gamma+2jets}\sigma_{1jet}}{\sigma_{eff}} - \\ & - \sigma^{ex}_{\gamma+3jets;3} \left[2 \frac{\sigma_{\gamma+1jet}\sigma_{2jets} + \sigma_{\gamma+2jets}\sigma_{1jet}}{\sigma_{\gamma+1jet}\sigma_{1jet}} \frac{\sigma_{jets}}{\sigma_{1jet}} - 1 \right]. \end{aligned} \tag{5.30}$$

Using the definition of $\hat{\sigma}_{eff(CDF)}$

$$\sigma^{ex}_{\gamma+3jets;2} + \sigma^{ex}_{\gamma+3jets;3} = \frac{\sigma_{\gamma+1jet}\sigma_{2jets} + \sigma_{\gamma+2jets}\sigma_{1jet}}{\hat{\sigma}_{eff(CDF)}} \tag{5.31}$$

one obtains the final form of the correction:

$$\hat{\sigma}_{eff(CDF)} = \sigma_{eff} \left(1 + \frac{\sigma^{ex}_{\gamma+3jets;3}}{\sigma^{ex}_{\gamma+3jets;2} + \sigma^{ex}_{\gamma+3jets;3}} [2f - 1] \right) \tag{5.32}$$

5.5 Estimation of the correction factor f

The three ratios in the correction factor (5.23) are not known from the CDF measurement and have to be calculated using Monte Carlo programs including the full shower and hadronization steps, since the generation should model the real event as tight as possible. Since the analyzed jets are produced with relatively low transverse energy, three generators, Herwig++ 2.5.2 [56, 103], Herwig 6.510 [104, 105] and Pythia 6.4.26 [29] are used in order to quantify the theoretical uncertainty with respect to their settings. Several features were found to have a non-negligible effect on the appropriate cross sections

and were studied in more detail. These are the order of α_S, the width of the Gauss distribution of the intrinsic k_T of the interacting partons, the matrix element transverse momentum cuts and the parton distribution function. In addition, the influence of the jet clustering algorithm was also under the study. Since the ratio (5.3) has an uncertainty of $\sim {}^{+30}_{-50}\%$, an uncertainty of the correction factor f, see Eq. (5.22), that multiply it of order 20% or less would be ample, leaving the result for the effective cross section dominated by the experimental uncertainties. It would be unreasonable to aim for a significantly higher accuracy than this, since $\alpha_S(5\text{ GeV}) \sim 0.2$ and this analysis relies on the leading order Monte Carlo generators.

According to the CDF analysis, jet cuts depend on the order of jet in the event with respect to its transverse energy. The fact that the leading jet could be above or below the 7 GeV, while the two trailing jets have to be below this threshold, induces an additional correlation between the two scatters, in principle. The sum over the two divisions of the jet origin between the two scatters should be extended to include a sum over all assignments of the leading jet between the two scatters, and whether it is above or below 7 GeV. However, the part of the cross section coming from events in which the leading jet comes from the QCD scattering and not from the photon production was found to be tiny, about 1.5%. Moreover, it is about the same fraction in the numerator and the denominator for the appropriate ratio, so neglecting these events really has a negligible effect. Therefore, the highest E_T jet in γ + jets is required to be above 5 GeV and all other jets to be between 5 GeV and 7 GeV.

In order to compare all three generators, the analysis of all events is performed using Rivet 1.7.0 analysis tool [106]. All particles in the final state with $|\eta| < 4.2$ are taken for the jet formation with no minimal p_T required. In the case of the analysis of the γ + jets events, the hardest photon was excluded from the jet clustering. CDF E_T cuts are applied on the final jets. Jet algorithms used are CDFJetClu [71], PxCone [107] and anti-k$_t$ [108] as implemented in FastJet 2.4.2 [109, 110]. Algorithms were chosen to follow the development of the jet algorithms from the IR unsafe cone algorithm CDFJetClu, used by the CDF collaboration, through the slightly IR safer mid-point cone algorithm PxCone, till the IR safe anti-k$_t$ algorithm, which belong to the family of sequential recombination jet algorithms and produce also jets in the shape of cones. All jet algorithm settings were kept default, except the minimal transverse energy required for the clustered protojets in the PxCone algorithm. This threshold was changed from the default value of 0.5 GeV to 0.1 GeV, see Fig. 8.3. If not stated otherwise, the CDFJetClu algorithm was used for the jet clustering. Only events where the direct photon satisfies CDF's cuts on transverse momenta, pseudorapidity and photon-jet isolation are accepted.

Since all the final states are supposed to be produced only by single parton interaction, the MPI modeling was turned off for all the generators. All other options were kept at their default values, except the one under study and explicitly stated in the tables. Both processes were generated in two separate parts, a Soft and a Hard, according to the matrix element $\hat{p}_T$ cuts so one can observe the migration of events due to the shower and hadronization procedures. For the jets production (photon + jets production, respectively) cross sections the Hard part is defined with $\hat{p}_T > 2$ GeV ($\hat{p}_T > 10$ GeV) and

the Soft part with $0.5 < \hat{p}_T < 2$ GeV ($5.0 < \hat{p}_T < 10$ GeV). Cuts differ only for the Pythia Soft run, since the default setting of Pythia does not produce any events with $\hat{p}_T < 1.0$ GeV. The lower value of 0.5 was investigated but an enormous increase of cross sections exhibiting the problem of the QCD infra red divergence forced the analysis to be a little inconsistent. However, the contribution to 5 GeV jets from events with parton p_T in between 0.5 and 1.0 GeV is expected to be very small.

The obtained cross sections, their ratios and values of the correction factor for each generator with its default settings are presented in Table 5.1. Statistical errors are negligible since the studied statistics of MC data allows much accurate cross section estimation than the original CDF measurement of few thousands of events. The first observation is that the γ + jets sample for $p_{T\gamma} > 16$ GeV is well behaved: there is almost no migration from hard processes below 10 GeV. For the QCD scattering cross sections, however, a significant amount of migration from below 2 GeV can be seen. One can conclude that these events are somewhat less likely to be well modeled, which is also reflected by significantly different cross sections obtained from different generators. Nevertheless, the amount of migration is similar in each of these cross sections, therefore the mis-modeling cancels to some extent in their ratios and hence the correction factor is reasonably predicted. This is particularly evident when comparing the correction factors obtained from Herwig++ and Pythia. Despite significant differences in the cross sections, the values of the correction factors are very close. The reason why this coefficient is different in the case of Herwig will be explained later in this section.

	Herwig++			Herwig			Pythia		
σ [mb]	Hard	Soft	Sum	Hard	Soft	Sum	Hard	Soft	Sum
σ_{1jet}	9.16	3.16	12.32	5.33	6.61	11.94	6.93	2.51	9.44
σ_{2jets}	0.62	0.15	0.77	0.54	0.70	1.24	0.72	0.00	0.72
σ_{jets}	13.87	3.70	17.57	8.72	8.31	17.03	10.54	2.52	13.06
σ [nb]									
$\sigma_{\gamma+1jet}$	5.66	0.03	5.69	3.41	0.16	3.57	4.47	0.08	4.55
$\sigma_{\gamma+2jets}$	1.46	0.01	1.47	1.02	0.04	1.06	1.05	0.07	1.22
$\frac{\sigma_{2jets}}{\sigma_{1jet}}$	0.063			0.103			0.076		
$\frac{\sigma_{jets}}{\sigma_{1jet}}$	1.426			1.426			1.383		
$\frac{\sigma_{\gamma+2jets}}{\sigma_{\gamma+1jet}}$	0.258			0.300			0.246		
f	0.458			0.575			0.445		
$f_{avg.}$	0.493								

Table 5.1: The calculated cross-sections, their ratios and values of the correction factor for the default settings of each generator Herwig++, Herwig, and Pythia.

Table 5.1 already started to address the question how the results depend on the Monte Carlo modeling by using three different event generators with their default settings. In the following, the other sources of systematic uncertainty is explored using one of the generators, Herwig++. Its default settings is changed in order to determine how the details of the generation affect the results. The most important effects for this study

are the order of α_S (1-loop and 2-loops), width of the Gauss distribution of the intrinsic transverse momentum k_T (we studied three values 0, 1 and 2 GeV) of the interacting partons, and the parton distribution functions (MRST98 [111], CTEQ6L1 [77] and MRST LO** [112]). In addition, since CDF did its studies at calorimeter level and this study is at particle level, three different jet algorithms mentioned above (CDFJetClu, PxCone and anti-k$_t$) are applied in the analysis to see how dependent are the results on these fine details.

More results are included in Appendix A. Here, only the values of the f factor for each above mentioned effect are provided. Results for the different PDFs and two different orders of α_S are shown in Table 5.2. One can see that the impact of the PDF on the result is small. Similarly, the order of α_S has only little effect on the f factor.

PDF	MRST98	CTEQ6L1	MRST LO**	α_S	1-loop	2-loops
f	0.477	0.447	0.458	f	0.476	0.458

Table 5.2: The correction factors obtained using Herwig++ with three different PDF sets MRST98, CTEQ6L1 and MRST LO** (default in Herwig++) and two different orders of α_S, 1-loop and 2-loops (default in Herwig++).

Jet clustering algorithms have a little increased influence on the outcome, see Table 5.3, but this uncertainty is still small in relation to the uncertainty stemming from the different Monte Carlo models used.

Jet algorithm	CDFJetClu	PxCone	anti-k$_t$
f	0.458	0.512	0.525

Table 5.3: The correction factors obtained using Herwig++ with three different jet algorithms PxCone, anti-k$_t$ and CDFJetClu (used in the CDF analysis).

By far, the dominant effect is due to intrinsic k_T modeling, therefore its influence was studied using all three generators, see Table 5.4. This effect is also responsible for what one can see in Table 5.1. Results obtained using default settings of Pythia and Herwig++ are very similar. This is because the intrinsic momentum in both generators was tuned to experimental data and have by default similar value $k_T \sim 2$ GeV, while in Herwig it was not tuned to the data and by default is equal to 0 GeV. Therefore, in this respect results from Herwig++ and Pythia should be trusted more than from Herwig. Table 5.4 shows that all generators provide similar value of f for the same k_T value.

f	$k_T = 0.0$ GeV	$k_T = 1.0$ GeV	$k_T = 2.0$ GeV
Herwig++	0.648	0.582	0.465
Herwig	0.575	0.619	0.564
Pythia	0.620	0.590	0.445

Table 5.4: The correction factors obtained using three generators and three different values of intrinsic k_T.

In summary, the average value of f obtained from three different event generators with their default settings is taken as an estimate of the final value of the correction factor. The standard deviation of the estimation is taken as a half of the difference between the maximum and minimum value of f caused by the effects studied in this section. The final result is

$$f_{avg.} = 0.49 \pm 0.10(\text{syst.}). \tag{5.33}$$

It indeed carries the uncertainty around 20% as expected from the estimation of α_S.

As a simple cross-check, one can note that the reached cross sections correspond to the very similar distribution of γ + 3 jets events according to their origin. Prompt photon is followed by 2 jets coming from the same scatter in about 80% of our events using Herwig++, 74% using Herwig and 76% using Pythia, while the the third jet comes from the second scatter. The experimental value was quoted as $\approx 75\%$ [26]. Considering the inherent uncertainties in jet physics at 5 GeV, the fact that this analysis works at particle level and CDF's analysis works at uncorrected detector level, and the desired accuracy of the final correction factor, one can consider this to be very good agreement.

5.6 Result

Given that the correction factor $f_{avg.}$ was found to be 0.49 ± 0.10, the factor in square brackets in (5.32), $2f$ - 1, turns out to be very close to zero indicating that the difference between inclusive measurement and the true inclusive cross section for double parton scattering is very small. The uncertainty on the triple-scattering event fraction $0.17^{+0.04}_{-0.08}$ can be neglected with respect to the uncertainty of the factor $2f_{avg.}$ - 1. Our final result for the effective cross section is

$$\sigma_{eff} = (12.0 \pm 1.3(\text{stat.})^{+1.3}_{-1.5}(\text{syst.}))\ \text{mb}. \tag{5.34}$$

It is worth noting that both statistical and systematic uncertainties have decreased, since the additional uncertainty of our correction factor is much smaller than the avoided uncertainty stemming from the triple scattering removal done originally by CDF (5.1).

6 The Large Hadron Collider and the ATLAS detector

6.1 The Large Hadron Collider

The Large Hadron Collider (LHC) [113–117] is the world-largest particle accelerator built to date. It is located at CERN (European Organization for Nuclear Research) on the Swiss-French border near the city of Geneva in Switzerland. The accelerator can be classified as a ring proton-proton (ion-ion) synchrotron and is installed in the 26.7 km long tunnel at a depth of 50 - 175 m underground, which previously hosted the Large Electron Positron (LEP) collider. The LHC machine consists of two accelerating pipes, each serving for the acceleration of and independent beam of particles to the same energy but in opposite directions. At points, where the two beam pipes are guided through each other, the particles are focused to collide.

The accelerator uses the super-conducting technology for operating magnets, which provide the magnetic field of around 8 T to bend the trajectory of circulating particles to keep them on the orbit. These dipole magnets are made from NbTi cables which have to be cooled down to 1.9 K by super-fluid liquid helium. The whole LHC machine contains 1232 of dipole magnets. In addition, there are many multi-pole magnets used to focus the beams close to the collision points. The protons are accelerated when passing through the radio-frequency cavities at one point of the ring.

The LHC is designed to accelerate primarily protons of energy of 450 GeV up to 7 TeV simultaneously in the two opposite directions (in the separate pipes going along to each other) and collide them. Since the two colliding particles are identical, the total designed energy of a proton-proton system at an interaction point, $\sqrt{s}$, is 14 TeV. The LHC is also capable to accelerate heavy ions, e.g. Pb^{82+}, and collide them at the center-of-mass energy 5.5 TeV per nucleon pair.

The protons are injected into the LHC in bunches, with a maximum bunch size of roughly 10^{11} protons (N). One LHC beam fill consists maximally of 2808 bunches in each direction (n_b). These bunches orbit the ring with a frequency of 11 kHz (f_{rev}) and may collide at four points of the beam crossings, around which detectors were built for measuring of the products of the interactions. These detectors are called CMS [119], ATLAS [120], ALICE [121] and LHCb [122]. At each of the interaction point, bunches collides with each other at a frequency of 40 MHz. The flux of protons

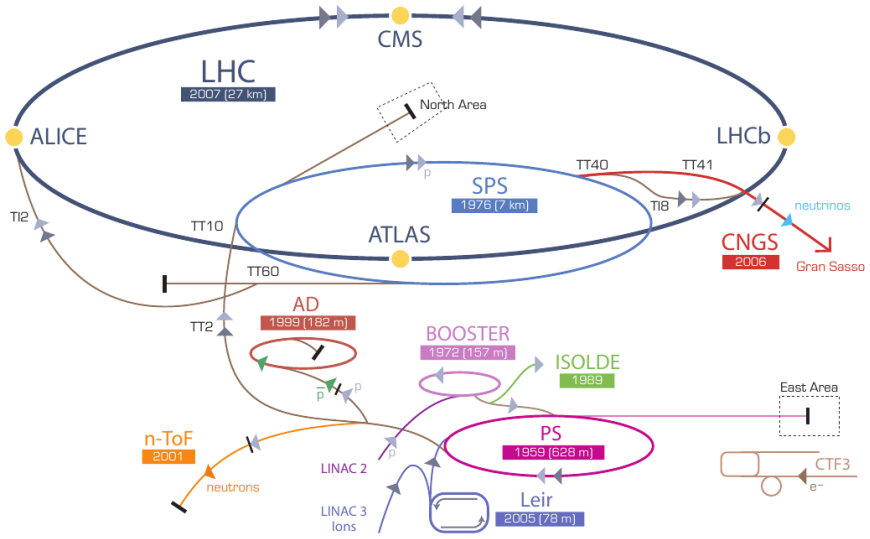

Figure 6.1: The CERN accelerator cascade [118]. The picture is not in scale.

can be characterized by a quantity known as luminosity $\mathcal{L}$, which is defined as

$$\mathcal{L} = \frac{f_{rev} n_b N^2}{A}, \tag{6.1}$$

where A is the cross-sectional area of the beam at a collision point and depends on the transverse horizontal and vertical spread of the proton bunches. The maximal instantaneous luminosity is designed to 10^{34} cm^{-2}s^{-1}, which is about 30 times higher than the Tevatron's luminosity. The instantaneous luminosity decreases in time due to the collisions and beam losses during the circulation in the LHC ring. The luminosity integrated over the data-taking period then characterize the size of the explored data.

The LHC ring is actually the last component of the complex cascade of the linear and ring accelerators which deliver the 450 GeV protons into the LHC machine. Figure 6.1 shows the most important links in the chain for the proton (ion) beam production. The protons start their journey in the linear accelerator Linac2, in which they reach an energy of 50 MeV. The protons travel further though three circular accelerators. These are in order the Proton Synchrotron Booster (1.4 GeV), The Proton Synchrotron (PS) (25 GeV) and the Super Proton Synchrotron (SPS), where the energy of the protons increases up to 450 GeV which is the injection energy of the LHC.

The operation of the LHC has begun in September 2008 with a successful circulation of its first proton bunches, but then the operation was stopped for more than a year [123]. The first proton-proton collisions were recorded by ATLAS on November 23 in 2009. During the first LHC run in the years 2010 - 2012, the energy and the luminosity were increased. The total size of recorded data by the ATLAS experiment is 27.0 fb^{-1} at the date of December 17 for a short-term shut down in 2013.

6.2 The ATLAS detector

One of the detectors build at the LHC interaction points is the ATLAS detector (A Toroidal LHC ApparatuS) [120, 124]. ATLAS is a general-purpose detector designed to combine all the classic components of modern detectors (silicon trackers, calorimeters and muon spectrometer) and to embody a very good performance in all the directions. Each detector subsystem is composed of a barrel and two endcap parts. All the active components of the detector are briefly described in the following sub-sections.

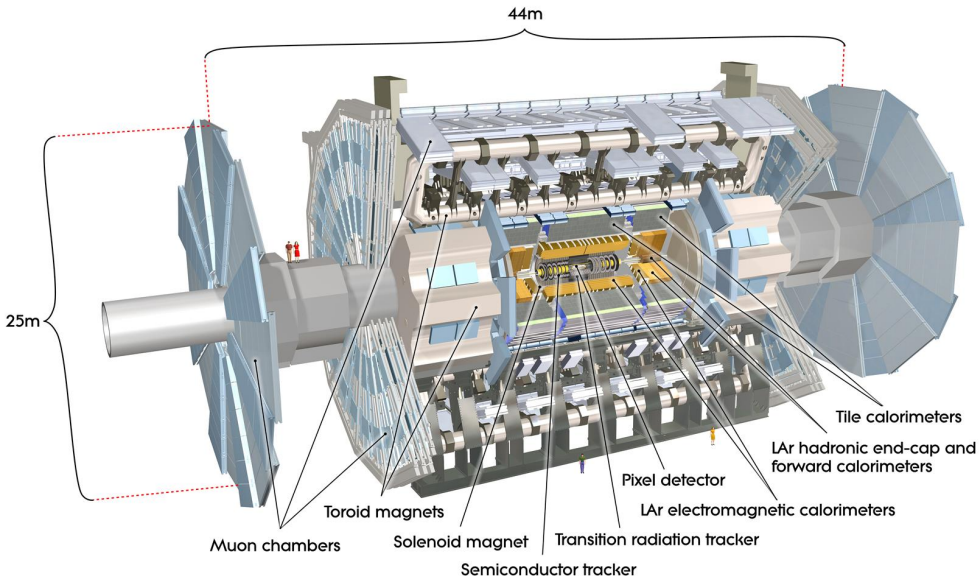

Figure 6.2: The ATLAS detector [125]. The inner-most layers belong to the inner tracker, and include both silicon and straw tube sensors. Inner detector is surrounded by the electromagnetic and hadronic calorimeters. The large air-core toroids and muon spectrometer create the outer envelope of the detector.

The cartoon of the detector is shown in Fig. 6.2. It has a shape of a cylinder laid on its side with length of 42 m and radius of 11 m. The axis of the cylinder goes in the middle of the LHC beam pipe. The interaction point in the middle of the detector is also the origin of the Cartesian right-handed coordinate system. The x-axis points to the center of the LHC ring, the z-axis follows the beam direction and the y-axis goes upwards. The azimuthal angle ϕ is measured as usual around the beam axis, and the polar angle Θ is the angle from the beam axis. The coordinate system determines the definition of the transverse momentum and the pseudorapidity:

$$p_T = p\sin(\Theta), \qquad \eta = -\ln\tan(\Theta/2). \tag{6.2}$$

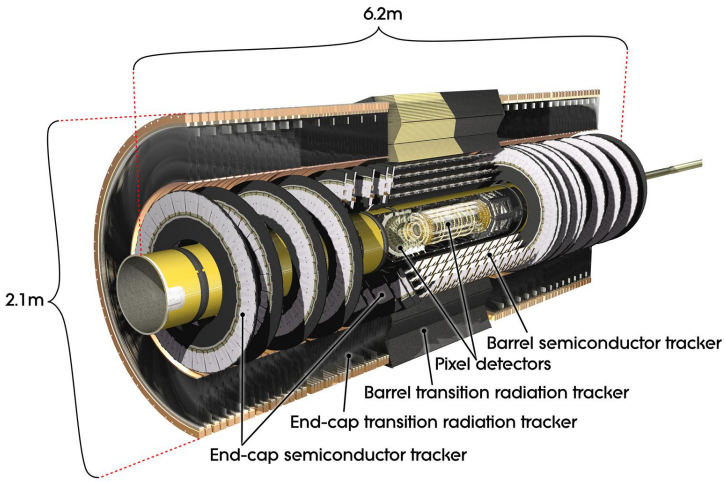

Figure 6.3: The inner tracking system of the ATLAS detector [125]. Detecting elements in the barrel are arranged axially, while those in the endcap are arranged radially.

6.2.1 Inner detector

The interaction point is closely surrounded by the inner detector, see Fig. 6.3. The inner detector provides a precise track measurement for charged particles with $|\eta| < 2.5$. The most inner part is made up from high-resolution silicon pixel sensors, the second part is made up from silicon micro-strip detector called Semi-Conductor Tracker (SCT). The silicon detectors are followed by the Transition Radiation Trackers (TRT) towards the outer radii, which is capable to discriminate the pions and electrons. This part is composed by straw-tube detectors based on the induction and detection of the transition radiation initiated by the passing charged particle. The whole inner detector is surrounded by a thin superconducting solenoid providing a 2 T magnetic field.

The pixel detector has three layers in both barrel and endcap regions. The very first layer is integrated to the beryllium beam pipe and is called the B-layer. The pixel sensors contain about 80 million of pixels, whose dimensions are 50×400 μm. The intrinsic accuracy in R - ϕ plane is about 10 μm and an intrinsic z (R) accuracy is 115 μm in the barrel (endcap).

The SCT detector has four layers in the barrel part and nine in the endcap part. The strips of the silicon sensors are 12 cm in length, with a pitch of 80 μm. The total number of strips is slightly over 6 millions.

The TRT detector is formed by about 350,000 of straw-like tubes working like a gas detector with a diameter of 4 mm and a length of 1.4 m (in the barrel part) or 0.35 m (in the endcap part). These straws are oriented along the beam pipe in the barrel part and perpendicularly to the beam in the endcap part.

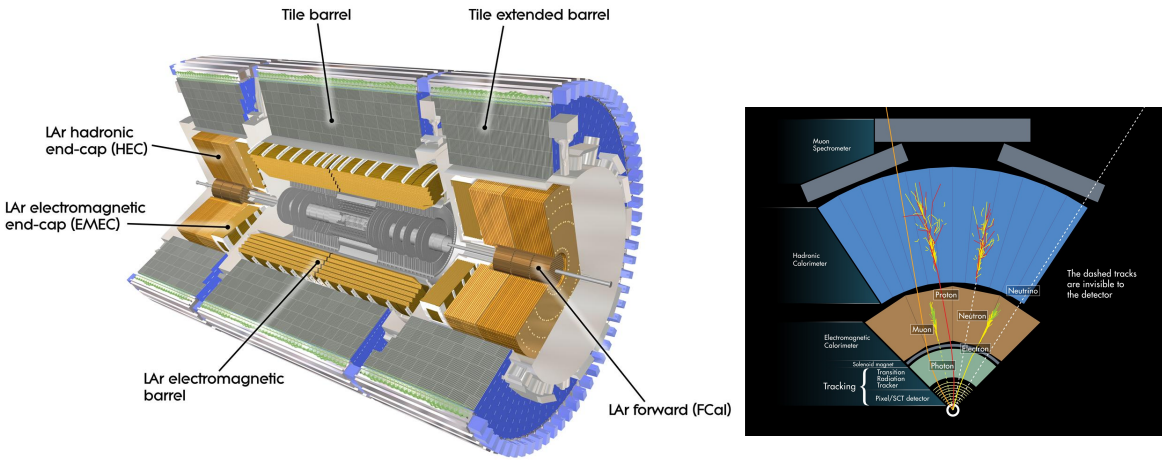

Figure 6.4: Left: The ATLAS calorimeter system. Right: A transverse cut of the whole ATLAS detector with the emphasized EM and hadron showers [125].

6.2.2 Calorimeter

The second part of the ATLAS detector is the calorimeter system, which covers the pseudorapidity range $|\eta| < 4.9$. Calorimeters serve as a partially active medium for the evolution of the electromagnetic and hadronic showers induced by the primary particle, as sketched in Fig. 6.4.

The electromagnetic (EM) section is a high granularity liquid-argon and lead calorimeter with excellent energy and position resolution. It covers the pseudorapidity range $|\eta| < 3.2$. Two different technologies are used for the hadronic calorimetry. First, the tile calorimeter with steel plates alternating with scintillator tiles covers the barrel region ($|\eta| < 1.7$). Two endcap detectors use liquid-argon scintillators together with copper plates and extend the calorimeter coverage region to $|\eta| < 3.2$. Furthermore, forward calorimeters instrumented with liquid-argon/copper and liquid-argon/tungsten detectors provide electromagnetic and hadronic energy measurements in $3.1 < |\eta| < 4.9$ region. The liquid-argon calorimeter is generally more radiation hard and thus it suits better to the regions close to the beam pipe.

6.2.3 Muon spectrometer

The outermost part of the ATLAS detector is the giant muon spectrometer consisting of four types of muon chambers laid out according to Fig. 6.5. Muon chambers can be divided to precise track detectors, Monitored Drift Tubes (MDT) and Cathode Strip Chambers (CSC), and to fast trigger chambers, Resistive Plate Chambers (RPC) and Thin Gap Chambers (TGC). Even though the high-precision tracking chambers reach up to $|\eta| < 2.7$, the trigger chambers are restricted only to $|\eta| < 2.4$. The trigger chambers of the muon system provide fast information on muon tracks traversing the detector, allowing the L1 trigger logic to recognize their multiplicity and approximate energy range. The whole spectrometer is built with three large superconducting toroid

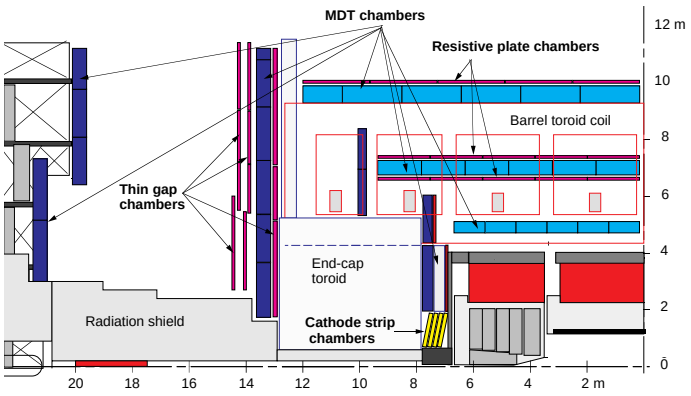

Figure 6.5: Overview of the ATLAS muon spectrometer [126].

magnets arranged with an eight-fold azimuthal coil symmetry. Its magnetic field is not uniform and the bending power varies between 1 and 7.5 Teslameters.

The largest part of the muon spectrometer is formed by the MDT chambers. There are total of 1150 MDT chambers in the whole detector which could cover an area of 5500 m^2. The size of the chamber varies according to its position in the detector, but the general layout can be described as in Fig. 6.6. The aluminium frame houses four optical alignment rays which monitor the internal geometry of the chamber. Three or four layers of drift tubes are attached to the frame on both sides. The tubes are made of aluminium, have diameter of 30 mm and serve as cathodes. Gold-plated tungsten wire in the middle serves as an anode. The tube works as a gas detector in which the passing muon induce the creation of a electron-ion pair which drift towards the electrodes. The total number of these tubes in the ATLAS muon spectrometer is 354,000.

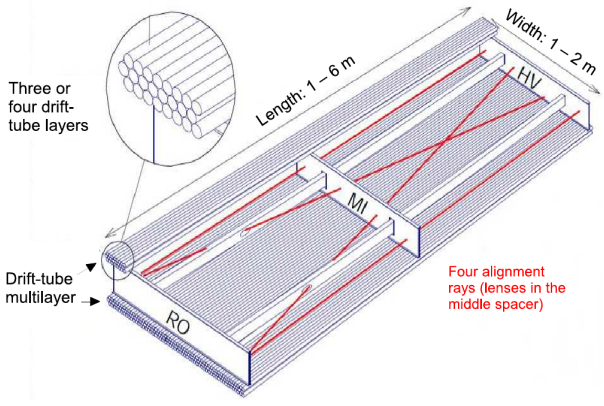

Figure 6.6: Mechanical structure of a MDT chamber [120].

Since the limit for safe operation of the MDT chambers is at counting rates of about 150 Hz/cm^2, the more radiation hard CSC chambers are used in the first layer of the endcap part of the detector. Their operation is considered safe up to counting rate of

about 1000 Hz/cm^2, which is higher than the rate expected in the range of the muon spectrometer covering $|\eta| < 2.7$. The CSC chambers are multi-wire proportional gas chambers, from which the signal is measured from the charge induced in the cathode strips. The technology allows for fast signal readout, with a time resolution of 7 ns. The CSC chambers have 30,700 readout channels.

6.2.4 Trigger

A three level trigger system [120] selects detected events to be recorded for further offline analysis. Its purpose is to reduce the actual rate of collisions to approximately 200 events per second before data transfer to storage unit. The Level-1 trigger uses a limited amount of the total detector information to make a decision in less than 2.5 μs and reduces the rate to about 75 kHz. L1 trigger defines the region-of-interest according to the triggered object. The Level-2 trigger selections use all the available detector data, at full granularity and precision, within the selected region-of-interest and reduce the output rate to approximately 3.5 kHz. The highest level of the trigger system, the event filter (EF), is based on standard ATLAS event reconstruction and offline analysis applications with an average event processing time of the order of four seconds. The final output rate of the whole EF computing farm is about 200 Hz with an event size of approximately 1.3 megabyte.

6.2.5 Detector response simulation

A reasonable prediction based on the Monte Carlo event generators should be supported by the detector response simulation. The ATLAS simulation [127] infrastructure accommodates many event generation programs, combines the Geant4 [128] simulation of the response of the individual sub-detectors and provides also the simulation of trigger decisions. The simulation chain is divided into three steps. At first, hits in the detector are simulated in order to treat the pre-generated event same as if it would be a real event. Each particle is propagated through the full ATLAS detector as implemented in the Geant4. The second step is digitalization of the energy deposited in the sensitive regions of the detector into voltages and currents. The last step is the reconstruction, where the detector output is transformed into raw particle physics objects, like tracks and energy clusters. The large-scale production of events for ATLAS physics and performance studies requires to be run on the LHC Computing Grid.

7 Double Parton Scattering at ATLAS

7.1 $\gamma + 3$ jets

The most precise measurements of double parton scattering were performed at the Tevatron experiments using a direct photon production accompanied by 3 jets, see Fig. 3.6, whether in the inclusive or exclusive manner. The importance of these measurements was demonstrated in Chapters 3 and 5, where the description of the method of effective cross section extraction took a significant space. The first logical step is to accommodate this method also for the ATLAS measurement and preserve the continuity of the MPI energy scale dependence investigation. Unfortunately, there is only small progress done so far and the question of feasibility of a $\gamma + 3$ jets measurement using the ATLAS detector stays open.

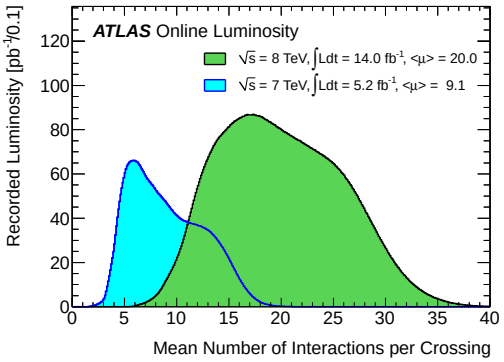

Figure 7.1: The luminosity-weighted distribution of the mean number of proton-proton interactions per crossing for the 2011 and part of 2012 data with the mean value $< \mu >$. More details can be found in [129].

There is no doubt that this channel is important and should be carefully investigated but the CDF's method is very problematic at the first sight. The goal, to stay as little model dependent as possible, will have to be reviewed. Briefly, the suggestion is to compare production rates of DPS events with one interaction vertex and double proton interaction events with two vertices. However, the LHC provides much higher luminosity than the Tevatron. Therefore, the method based on the very precise vertex detection

cannot be used or will be very challenging. Figure 7.1 shows number of proton-proton interactions per bunch crossing for two energies and indicates the future issue.

7.2 4 jets

The second MPI process measured in the past is the multi-jet production. The most reasonable choice of 4 jets in the final state, where always two jets come from one scatter, was considered, while the 2-jet and 3-jet cases were found to contain too small fractions of DPS. Left plot in Figure 3.1 sketches the DPS 4-jet production. The very high production rate of this process, from the MPI point of view, allowed the first measurement already in 80's in the 20^{th} century and is therefore the most promising process for the MPI measurement. However, background processes resulting in 4 jets in the final state also have very high cross section. The primary goal of such a feasibility study is to find such a kinematical variables that will be sensitive to the topology of individual contributions and that will provide the minimal ambiguity in distinguishing double parton scattering from the background. Such a competing processes are double bremsstrahlung (DB) and several di-jet productions in the multiple proton interactions (pile-up), where primary vertex reconstruction is not able to filter these events off.

The investigation of the 4-jet inclusive production at ATLAS closely follows the kinematics suggested by CDF [64] and D0 [49], only with respect to the specific phase space available at the ATLAS detector:

$$p_T(jet) > 10 \text{ GeV} , \qquad |\eta(jet)| < 2.0.$$

The jet algorithm used by the whole ATLAS collaboration is always the anti-kt algorithm [108]. Both values of jet radius 0.4 and 0.6 are investigated. The data sample obtained using these cuts is labeled as "all events".

The four jets satisfying above criteria are paired for the minimal momentum imbalance S defined in Eq. (3.30). This variable is calculated for all three possible jet pairings and the combination with the minimal S is further considered. The meaning of this choice consists in the tendency of DPS to produce p_T balanced jets. In other words, jets stemmed from DPS are expected to be statistically much more back-to-back oriented than jets from one parton-parton interaction. The distribution of momentum imbalance S is shown in Fig. 7.2, where Tevatron and LHC predictions are compared.

Moreover, additional criteria are applied on i and j jets in each jet-pair:

$$\Delta\phi_{ij} > 160^\circ , \qquad p_T^i/p_T^j > 0.8.$$

The first condition emphasize the demand of back-to-back orientation of both pairs, while the second condition requires the jets in a pair to be p_T balanced. The specific choice of these cuts is also the subject of the investigation and Figure 7.3 demonstrates a high sensitivity to the chosen value which varies from 0.8 to 0.5. Also the minimal required azimuthal angle between jets in a pair has to be investigated. Currently, the value of 150° and 160° is under the study. These "selected events" very well model the double parton scattering and offer a promising direction of the further investigation but one has to always keep in mind that their fraction in the all events sample is not equal

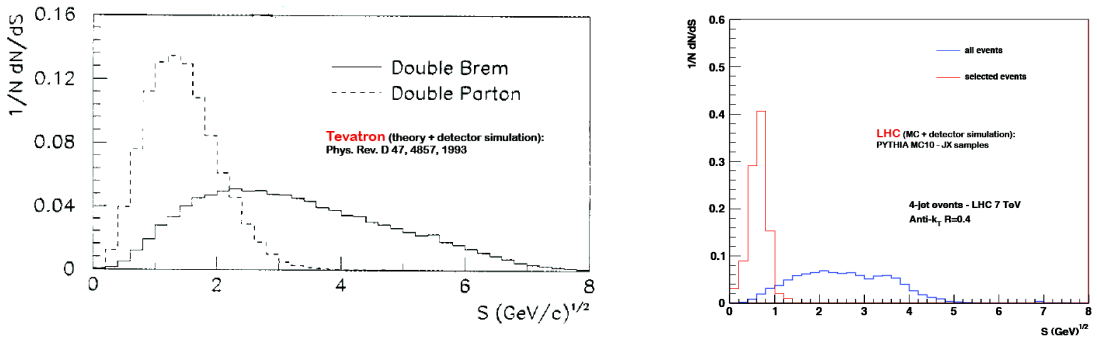

Figure 7.2: Momentum imbalance distributions for all 4 jet events divided into selected events modeling double parton scattering and double bremsstrahlung events. Left: Tevatron theoretical prediction, Right: MC for 7 TeV.

to the true fraction of the DPS. SPS background events and pile-up events will have to be subtracted on the basis of Monte Carlo estimation. Such simulations always carry a significant uncertainty, especially in the low p_T region which is the domain of MPI.

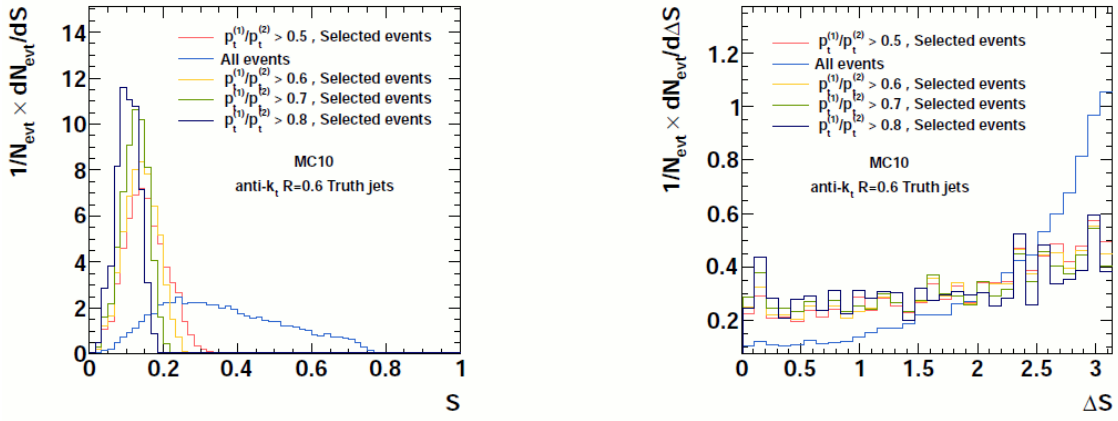

Figure 7.3: Influence of the jet pair p_T balance cut demonstrated on MC data. Left: momentum imbalance for four jet system S, Right: difference in azimuthal angles of jet pairs. The tighter cut are applied the higher purity of the selected events is reached. However, the decrease in the number of selected events is significant.

Besides the already mentioned imbalances S, variable Δ_S defined as a difference in azimuthal angles of jet pairs for minimal imbalance S:

$$\Delta_S = \Delta\phi\left(\vec{p}_T(i,j)\vec{p}_T(k,l)\right).$$

can also be used for the signal selection. Δ_S is supposed to be larger for single parton interactions, where the 4 jets are more-or-less correlated with each other, and goes often up to π value. On the other hand, DPS should embody the flat distribution of Δ_S, assuming that the formed pairs correspond truly to the two uncorrelated parton interactions.

Results shown in this section are only illustrative. There is an ongoing analysis working on the trigger selection and other technical issues. There is a high sensitivity of the fraction of the selected events on the choice of the transverse momentum balance cut, on the jet size and definition (track vs calorimeter jets) and on the Monte Carlo used which require further work.

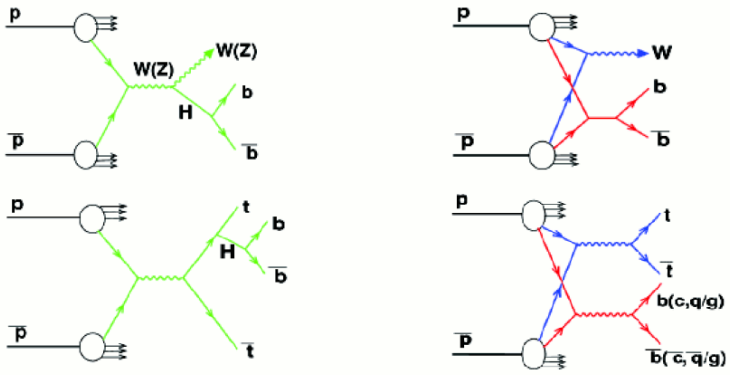

Figure 7.4: Example diagrams for bbjj production via Higgs production and DPS.

A special case of four jet production is a heavy flavor production. A wide spectra of processes should be investigated in the context of the precise measurement of Higgs boson properties. Multiple parton scattering would play a role of small background that could be filtered off with reasonably high jet p_T cut. Nonetheless, this background should be precisely measured and its influence quantified. Two example processes are shown in Figure 7.4. These are always $b\bar{b}$ production either followed by hadronic W decay or coming from Higgs decay created in $t\bar{t}$ production.

7.3 W + 2 jets

The most advanced study searching for double parton scattering at ATLAS deals with the exclusive production of W boson decaying leptonically accompanied by an additional QCD di-jet production. In this section, the method of the measurement is described and is followed by the brief summary of results reached so far [130]. These results were preliminary and are now significantly updated and still under development. However, shape of the distributions remains very similar and describe the main points of the analysis very well.

The W + 2 jets analysis is based on very careful choice of the most suitable Monte Carlo program, whose results serve for DPS identification within the 2010 ATLAS data. The data sample used in the analysis corresponds to an integrated luminosity of 33 pb^{-1}. For the purpose of the best kinematic behavior investigation and systematics determination, all main full-event generators Pythia [29], Sherpa [75], and Herwig [104] were studied. Herwig was used together with Alpgen [131] matrix element generator and Jimmy package.

Final state under study consists of one isolated charged lepton, electron or muon, and of exactly two jets. Transverse mass of the secondary lepton pair is reconstructed using missing transverse energy (MET) that is identified with the p_T of the invisible secondary neutrino. All events have to satisfy additional cuts:

$$\begin{array}{lllllllll} p_T(l) & > & 25 \text{ GeV}, & |\eta(l)| & < & 2.5, & \text{MET} & > & 25 \text{ GeV}, \quad M_T(l\nu) > 40 \text{ GeV}, \\ p_T(j) & > & 20 \text{ GeV}, & |y(j)| & < & 2.8, & \Delta R(jl) & > & 0.5. \end{array}$$

Background processes resulting in the same final state are studied at MC level. These are single parton production of multi-jets, where a random isolated lepton can appear, single Drell-Yan Z boson production, where the two jets come from initial state radiation or from irreducible pile-up, $t\bar{t}$ production, and tau decays from single W production. The single parton interaction (SPI) and double parton interaction (DPI) W + 2 jets production kinematics is studied and their combination should fit the measured W + 2 jets data. Feynman diagrams of both competitive processes are shown in Fig. 7.5. The DPI process consists of two independent parton interactions, where one is W + 0 jets (W_0) production and the second is a QCD di-jet production. In the following, two templates are defined in order to simplify the notation. Template A represents SPI W + 2 jets production and template B denotes the DPI contribution. σ^{tot}_{W+2j} contains all selected events for either Monte Carlo or real data, where all mentioned background was removed.

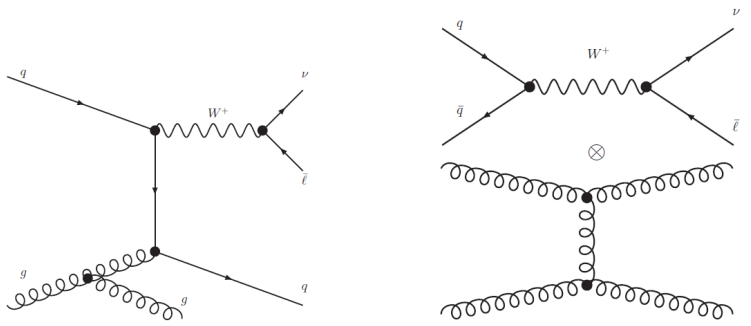

Figure 7.5: Example LO diagrams for the single parton (left) and double parton (right) scattering contributions to W + 2 jets production.

Therefore, one may write

$$\sigma^{tot}_{W+2j} = \sigma_{(W+2j)_{SPI}} + \sigma_{W_0+2j_{DPI}}, \tag{7.1}$$

where

$$\sigma_{W_0+2j_{DPI}} = \frac{\sigma_{W_0}\sigma_{2j}}{\sigma_{eff}}. \tag{7.2}$$

A simple factorization of double parton distribution functions was used in Eq. (7.2). Contribution from double parton process, where the W boson would be accompanied by one jet from the same scatter and the additional QCD process would produce only one jet in the considered kinematical region or would not be reconstructed at all, is neglected.

The authors argue in favor of neglecting this process and support their assumption by MC-level analysis. One may still wonder, if such simplification remains reasonable also for the real data. Also triple parton scattering possibility is neglected.

The σ_{eff} extraction procedure itself stems from Eq. (7.2), where cross sections are replaced by event numbers divided by factors including luminosity, geometrical acceptance, unfolding and trigger efficiency. Most of the coefficients cancel in the ratio and the very final formula

$$\sigma_{eff} = \frac{1}{f_{DP}} . \frac{N_{W_0}}{N_{W+2j}} . \frac{1}{\epsilon_{2j}} . \frac{N_{2j}}{\mathcal{L}_{2j}} \tag{7.3}$$

contains only the di-jet sample luminosity and the appropriate trigger efficiency. N_0 is the number of events with one lepton and zero jets, N_{2j} is the number of pure di-jet events, and N_{W+2j} is the number of all W + 2 jets events. The variable f_{DP} is defined as

$$f_{DP} = \frac{N_{W_0+2j_{DPI}}}{N_{W+2j}} \tag{7.4}$$

and represents the fraction of double parton events against single parton events in the background-subtracted data sample. This is actually the crucial point of the whole analysis. Fraction f_{DP} is obtained from the fit of two MC or data-driven sub-samples for pure DPI and pure SPI contributions to the whole measured sample:

$$N_{W+2j} = (1 - f_{DP}) . N_{(W+2j)_{SPI}} + f_{DP} . N_{W_0+2j_{DPI}} . \tag{7.5}$$

This equation used for some kinematical variable distributed into bins serves for the search of the minimal χ^2/ndf fit. The most suitable variable seems to be

$$\Delta^n_{jets} = \frac{|\vec{p}_T^{\,j1} + \vec{p}_T^{\,j2}|}{|\vec{p}_T^{\,j1}| + |\vec{p}_T^{\,j2}|} \tag{7.6}$$

that reflects directions of the two jets. The more back-to-back jets are the lower Δ^n_{jets} becomes.

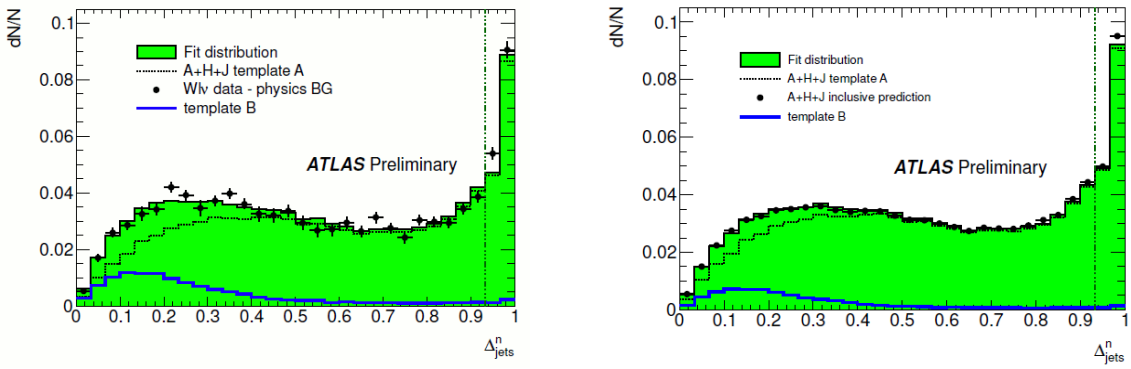

Figure 7.6: Linear combination of normalized SPI (Alpgen+Herwig+Jimmy) and DPI (data driven) sub-samples fitted to background-subtracted ATLAS data (left) and Alpgen+Herwig+Jimmy reconstructed MC data (right).

Two sub-samples on the right hand side in Eq. (7.5) are modeled using Monte Carlo generators and are studied in details. Here, only a few points are pointed out. First, the DPI sub-sample is replaced by SPI di-jet sample, because Δ^n_{jets} variable depends only on jets in the final state. Full sample W_0 + 2 jets is not necessary to be constructed. Only a small correction is applied to the di-jet sample to model the jet veto for jets that would be too close to the isolated lepton. Second, the DPI sub-sample is modeled using Monte Carlo generators, where the MPI generation is switched off.

The final fit, see Fig. 7.6, is performed at full W + 2-jet MC level sample (including ATLAS detector simulation) for real data. Alpgen+Herwig+Jimmy was used only for comparison and validation. Both distributions for SPI and DPI sub-samples are normalized to 1. Final result also contains correction for pile-up contamination and is re-calculated to the hadron level using a Bayesian unfolding procedure. Preliminary results referred in [130] are

$$f_{DP} = 0.16 \pm 0.01(\text{stat}) \pm 0.03(\text{syst}), \tag{7.7}$$

$$\sigma_{eff} = 11 \pm 1(stat)^{+3}_{-2}(syst) \text{ mb}. \tag{7.8}$$

The measured σ_{eff} value (7.8) is nicely put into the context of the previous measurements in Fig. 7.7. Assuming the high uncertainties of all the measurements, the new value is reasonably placed within the expected interval. One may expect a little higher value as the effect of the energy scale dependence.

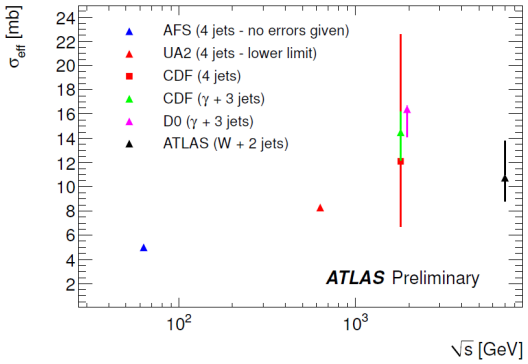

Figure 7.7: Dependence of σ_{eff} on the energy scale $\sqrt{s}$ in different processes and different experiments.

The further development of the method embodies several issues that significantly change the result. The task of SPI modeling appears to be a little problematic, since every generator has a different parton-level p_T^{max} cut set on additional parton processes. Sherpa has this cut set to 3.5 GeV, while Jimmy does not have such a threshold. One has to filter events according to the generator record and set this cut by hands. Influence of this cut on the f_{DP} fraction is shown in Fig. 7.8. Points with the error band represent f_{DP} values for different p_T^{max} cuts at hadron level (MC lvl). The closest point to the true parton-level fraction (broken line) is chosen for the final fit and corresponds to the 10 GeV.

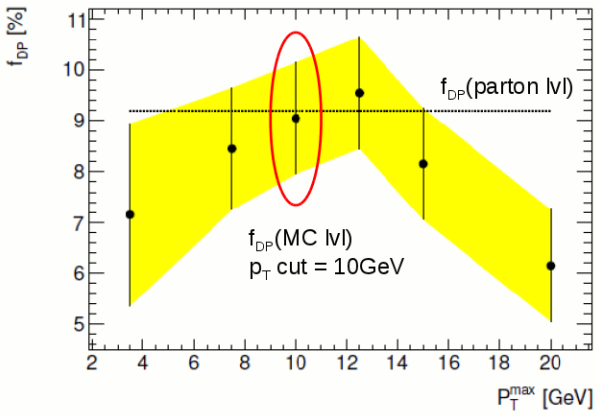

Figure 7.8: Variation of extracted f_{DP}^{MC} value (black points) as a function of p_T^{max}. The statistical uncertainty is shown (yellow band). The value of $f_{DP}^{parton\ lvl}$ is also shown (broken line). The smallest difference is for value of 10 GeV and this cut was chosen for the analysis.

Moreover, the change of the jet radius used for anti-kt algorithm can affect the σ_{eff} value, within approximately 1 mb. Sensitivity of this analysis to pile-up leads also to the significant dependence on the jet offset correction for the primary vertex position. Contemporary preliminary prediction for σ_{eff} is approximately 15 mb after application of all above mentioned corrections.

7.4 ll + 2 jets

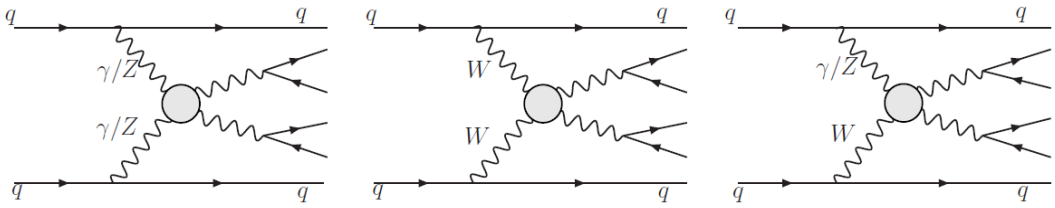

Figure 7.9: W boson pair production as an example of vector boson scattering process.

One short note belong also to the vector boson scattering. This class of processes produces any pair of vector bosons in one parton interaction as shown in Fig. 7.9. One can therefore wonder, how big contribution to the given final state might come from the two independent single vector boson creations occurring in one double parton scattering event. An arbitrary charge combination of di-lepton events is investigated at ATLAS as a result of W boson pair production. Both, Herwig++ [56] and Pythia8 [29] are used to determine the DPS contribution. Investigation at this stage shows very minor fraction of DPS events in di-lepton sample. Especially the requirement of two forward jets, that are always present in vector boson scattering events, rejects most of the possible DPS background.

8 Physics Objects

An intermediate step between theory and further analysis of either real or Monte Carlo simulated data is discussed in this section. Two types of physics objects, jets and muons, are described with respect to the ATLAS detector construction, see Chapter 6. Direct transition from Monte Carlo objects to detector level objects is straightforward and both terms tightly correspond. Thus, one can easily compare theoretically predicted results with the future measurements.

8.1 Muons

High energy proton-proton collisions at the LHC produce mostly a vast amount of hadron particles whose identification and momentum reconstruction have a significant uncertainty. The electroweak processes and decays are generally considered as much cleaner signals for the physics analyses and the best object for the reconstruction is a muon. Muons are detected by the inner detector and by the outer muon spectrometer while the energy losses in the calorimeter are not of great importance. Electrons suffer from being dissolved in the electromagnetic calorimeter and their identification is harder. Therefore, the high purity requirements set to this double parton scattering study prefer to study muon final state. The simplicity of the muon selection at the hadron level of the Monte Carlo generator record compress the whole problematics into the appropriate PDG ID condition. Therefore, the further description concerns reconstructed muons at the detector level.

8.1.1 Muons at ATLAS

The two complementary muon measurements by the inner detector (ID) and the muon spectrometer (MS) offer several muon objects at the reconstructed level. The final muon candidate is then given by a set of selection criteria that reflect most of the available information. In this sub-section, the STACO muon reconstruction algorithm is introduced. It is followed by a description of additional conditions usually placed on the reconstructed muons in addition. These conditions will be used at the appropriate stage of the analysis.

The STAtistical COmbination (STACO) muon reconstruction algorithm attempts to statistically merge the independent ID and MS tracks reconstructed separately in ID and MS sub-systems. The merging is done by combining the 5x5 covariance matrices of the two tracks to obtain the benefit of two independent measurements and the χ^2/NDF

of the MS-ID track match at the perigee is required to be less than 20. Further identification selection uses different informations about reconstructed tracks and calorimeter energy loss in order to distinguish several reconstruction quality levels. The highest quality level is called *tight*.

The following criteria can be added to the muon selection afterwards in order to increase the significance of the muon candidate. To reject muons from charged π or K decays and charged particles from the beam-induced backgrounds, the ID and MS track consistency check can be applied:

$$\frac{|p_T^{ID} - p_T^{MS}|}{p_T^{ID}} < 0.5. \tag{8.1}$$

The ID muon tracks should fulfill a further set of requirements, in addition to the conditions given by the reconstruction algorithm, that take into consideration numbers of hits in the inner detector layers and the numbers of known dead regions. The strategy is that if the detector module is known to be dead, it is added to the hit count and ignored in the hole count. It can be mathematically abbreviated to

$$\begin{aligned} \text{B-layer}_{hits} &> 0, \text{if expected hits}, \\ \text{Pixel}_{hits} &+ \text{Pixel}_{dead} > 1, \\ \text{SCT}_{hits} &+ \text{SCT}_{dead} > 5, \\ \text{Pixel}_{holes} &+ \text{SCT}_{holes} < 3, \end{aligned} \tag{8.2}$$

where *holes* are points of the reconstructed track in the active material of the detector but without any response. TRT requirements depend on the pseudorapidity of the track and they take into considerations hits in the detector which most likely do not belong to the track (outlying hits). One of the following conditions has to be fulfilled:

$$\begin{aligned} \eta_{track} < 1.9 \quad \& \quad N > 5 \quad \& \quad TRT_{outlying\ hits}/N < 0.9, \\ \eta_{track} \geq 1.9 \quad \& \quad N > 5 \quad \& \quad TRT_{outlying\ hits}/N < 0.9, \\ \eta_{track} \geq 1.9 \quad \& \quad N \leq 5, \end{aligned} \tag{8.3}$$

where $\text{N} = \text{TRT}_{hits} + \text{TRT}_{outlying\ hits}$.

The kinematical selection applied to the muon candidate includes a cut on the minimal transverse momentum and reflects the η coverage range of the muon trigger chambers:

$$p_T^{\mu} > 5\ GeV, \qquad |\eta^{\mu}| < 2.4. \tag{8.4}$$

The minimal transverse momentum cut at detector level analysis then reflects the requirements by the individual triggers applied.

The study in the next chapter searches for the same-sign di-muon events and therefore the muon electric charge plays its role in the reconstruction selection. The hardest muon in the event decides which electric charge is the desired one for the second searched muon and these signal muons are further processed by the isolation and primary vertex impact parameter cuts. On the other hand, isolation and vertex related cuts are not applied on the opposite-sign muons. Since the single parton scattering di-boson production acts as

the most serious physics background, it is desired to detect a most of the opposite-sign muons.

There are two isolation methods depending on what sub-detector is used. Calorimeter based isolation calculates total transverse energy deposited in the calorimeter cells in the cone around the reconstructed muon trajectory except the muon contribution. This cone points from the reconstructed muon production vertex and its radius in the $\eta - \phi$ plane is chosen to 0.3. The calorimeter isolation selection will be applied in the form of

$$\frac{\sum E_T^{cone}}{p_T^{\mu}} < 0.14. \tag{8.5}$$

Similarly, the ID based isolation calculates the total transverse momenta of all reconstructed tracks in the cone around the muon, except the muon track. The size of the cone is the same as for the calorimeter isolation and the final condition

$$\frac{\sum p_T^{cone}}{p_T^{\mu}} < 0.15 \tag{8.6}$$

will be applied. The factors on the right hand side can be interpreted as a maximal allowed transverse momentum accompanying the muon. In the case of ID isolation, tracks around the muon can carry at most 15% of the muon transverse momentum. The threshold is set to 14% for the calorimeter isolation. The purpose of the isolation cuts is to suppress muons from hadronic jets.

In addition, only prompt muons pass the selection criteria. The perigee of the reconstructed muon track with respect to the primary vertex can be calculated. Restrictions on its longitudinal (z_0) and transverse (d_0) impact parameters will be placed:

$$|z_0| < 1.0 \text{ mm}, \qquad |d_0/\sigma(d_0)| < 3.0. \tag{8.7}$$

Values of muon cuts follow the muon selection used in the similar ATLAS study concerning W pair analysis for 2011 LHC run [132].

8.1.2 Primary vertex

A short note is placed here in order to properly define the above mentioned impact parameters and the term of the primary vertex, see Sec. 10.2 in [120] and Sec. 4 in [124]. Proton-proton collisions at the LHC proceed within an intersection of two colliding bunches of accelerated protons. Figure 7.1 shows distributions of relatively large number of proton-proton interactions per bunch crossing for two energies. The inner detector is supposed to measure charged tracks and to extrapolate their production vertex. A group of tracks with vertices suspiciously close to each other are grouped and a fitting procedure finds their common interaction vertex. The goal is to find a vertex with small number of tracks with high transverse momentum and filter vertices with many small p_T tracks. Therefore, $\sum p_T^2$ of the associated tracks is calculated for each reconstructed interaction vertex. The one with the largest sum is then declared as the primary vertex. In this analysis, at least 3 tracks are required to be associated with the primary vertex. Otherwise, the event is rejected.

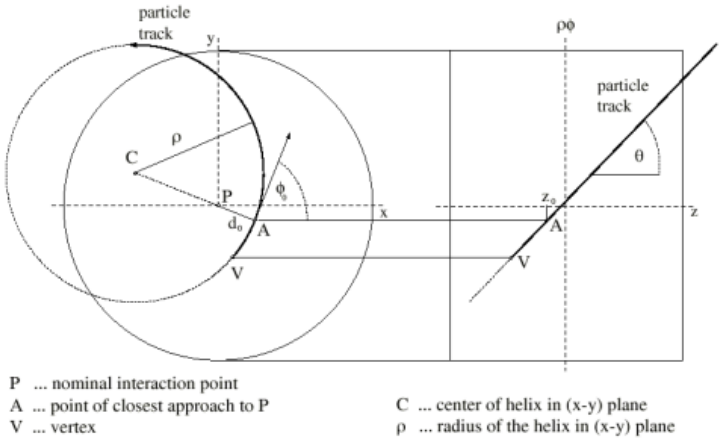

Figure 8.1: Graphical representation of the ATLAS perigee parameters [133].

The origin of the detector coordinate system is shifted into the primary vertex position for the track perigee determination. Since the charged track in the magnetic field of the inner detector has the shape of a helix, the point of the closest approach of each reconstructed track to the primary vertex (assumed to be the interaction point) is described in two projections. The transversal impact parameter (d_0) is defined as the closest distance of the track to the z-axis. The longitudinal impact parameter (z_0) is the z-coordinate of the perigee. The whole situation is illustrated in Fig. 8.1. The projection of the helix to the x-y plane has a shape of a circle with a radius of ρ. The z-coordinate of the perigee is nicely shown in the z-ϕ plane, where the helix profile is a straight line under a fixed polar angle Θ.

8.2 Jets

Although jets are not of the primary interest in the same-sign di-muon signal searches, they are very important for the event topology determination. Jets help to quantify hadronic energy flow in the proton-proton collisions and allow us to distinguish higher order single parton processes, heavy flavor QCD production, and multiple hadron interactions (pile-up) from the signal. Moreover, a special attention to jets is paid in case of effective cross section evaluation. The value of this MPI scale factor is taken from the $\gamma + 3$ jets measurement and a correction factor is applied in Section 5. For this reason, three jet clustering algorithms are described and compared, while only one algorithm is used by the ATLAS collaboration.

In the general meaning, jets are defined as a spray of more-or-less collinear particles with relatively large momenta emerging from the collision of two energetic particles, whether hadrons or leptons. Every specific jet definition according to jet formation slightly differs and satisfies specific conditions and requirements of the appropriate experiment. At the beginning, only visual check of the final state picture was satisfactory to find jets. Nowadays, high jet multiplicities per event and high event production rates require sophisticated algorithms that can be quickly run over the data. These jet algo-

rithms have to deal with the large number of final state particles, whether real or from detector noise, and form a reasonable number of jets. The algorithms can be applied on both real or Monte Carlo simulated data.

8.2.1 Ideal algorithm properties

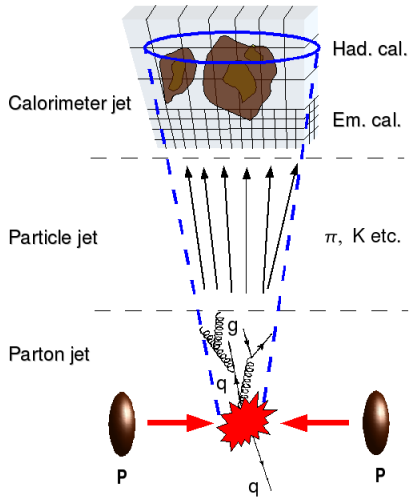

Figure 8.2: Different levels of final state that may be used for jet clustering algorithms [134].

An ideal jet algorithm have to satisfy both theoretical and experimental conditions and should provide same results at every stage of the final state. In the QCD improved parton model of the hard scattering between two hadrons, a pair of partons interact and produce a pair of other partons (or leptons) outgoing from the interaction point. This stage is marked as *parton* level, see Fig.8.2, and correspond to the desired true information about the interaction. However, these partons cannot be detected directly and create the shower of many virtual particles. These showers are modeled by parton evolution, where generation starts from the parton from the final state of the matrix element with known virtual mass and longitudinal momentum fraction and further steps of the time-like cascade lead to the set of partons with the higher virtuality. Partons from the final-state shower are still undetectable and have to be arranged into hadrons. Hadronization models, string model and cluster model developed so far, combine partons from final-state shower together with partons from initial-state shower and with partons from hadron remnants and provide a set of detectable color-less hadrons. This stage is referred as *particle* level in Fig. 8.2. Theoretical models end here and further stage depends only on the detector layout. Jets at this *calorimeter* level are formed mostly from the energy deposition in the electromagnetic and hadronic calorimeter cells but can be also studied at the level of charged tracks in the inner track detector.

Every serious jet definition has to be fully specified. All kinematical variables, particle selection, and corrections have to be completely defined and cannot allow any ambiguities, even when running at the different stages of the final state. The definition should not introduce any additional procedures on either theoretical or experimental side. New algorithms are also required to be infrared and collinear safe. Not only infrared and collinear divergences in the perturbative calculations of the cross sections should be avoided. Jet algorithm should also be insensitive to soft and collinear radiations in the context of the jet multiplicity. In other words, addition of a soft particle or splitting one particle into two collinear ones should not change the result of the algorithm. Other attributes of the ideal algorithm are invariance under longitudinal boost, detector independence, stability for pile-up rate, insensitivity to hadronization model, stability for resolution smearing and so on. Processing time consumption is also an important parameter.

In this thesis, three jet algorithms are used as implemented in the FastJet [109] package and are briefly characterized in the following.

8.2.2 Cone algorithms: PxCone and CDF JetClue

The CDF JetClu [71] algorithm was used by CDF collaboration as a main jet definition during Run I and was also used during RunII. The choice of this algorithm for the effective cross section correction estimation, see Chapter 5, is therefore straightforward, even though the authors of the measurement [26] do not specify their cone algorithm. Both PxCone [107] and CDF JetClu algorithms belong to the class of iterative cone algorithms, for which the main motivation is to find a dominant energy flow within the list of final state particles (four-momenta). The physics motivation is to approximate the four-momentum of the original parton giving rise of the parton shower. Most of the parton emissions propagate close to the original direction and larger angle radiations are highly suppressed. Cone algorithms therefore search for these centers of energy flow and build a virtual geometrical cone whose axis goes from the interaction point and the size of the cone is decided in advance. The cone size is usually defined as the circle radius R of the cone projection in the η-ϕ space:

$$R = \sqrt{(\Delta\eta)^2 + (\Delta\phi)^2}, \tag{8.8}$$

and has the meaning of the angular resolution.

Both above mentioned algorithms have several steps in common. They use all particles from the input list as a seed for a stable cone search. At first, the algorithm creates a predefined cone around the axis given by the seed four-momentum and calculates the total jet four-momentum from all particles within this cone. If the new jet four-momentum differs from the seed direction, jet direction is taken as a new seed and the first step is repeated. The iteration continues until a stable position is reached. Such a stable cone is declared as a protojet and the original seed is removed from the input list. After the algorithm reiterates over all seeds, the output list contains several different protojets (the same stable cones are recorded only once) that might be overlapping among each other.

Note that there are several ways how to re-combine individual particle four-momenta into the total jet four-momentum. The most suitable method is the so called E-scheme recombination. Here, complete four-momenta of all items (i) in the cone are summed up:

$$p_{jet} = (E_{jet}, \vec{p}_{jet}) = \sum_i (E_i, \vec{p}_i). \tag{8.9}$$

Besides the E-scheme, there are other recombination schemes, e.g. p_t scheme called Snowmass, where only transverse momenta of two combined objects is summed. In this case, the resulting jets are massless four-vectors, which disfavors this scheme for many analysis.

Both studied algorithms deal with the protojes in a little different ways. CDF JetClu algorithm uses the so called split and merge method, where always two overlapping protojets are split or merged according to the amount of the shared energy. The threshold

of the energy overlap is usually set to 75%. At the end of this step, the output list contains final disjoint jets. A big disadvantage of this algorithm is its infrared instability, marked as IR_{2+1} unsafety.

The PxCone algorithm tries to increase the infrared stability by addition of midpoints between all protojets. Midpoints are taken as additional set of seeds and the search for the stable cones repeats all over. This trick is supposed to model the situation where the soft underlying event could modify the algorithm output. After the algorithm deals with all the seeds and finds new set of overlapping protojets, the split-drop procedure is called. It consists of several steps:

- Protojets with lower transverse energy than the pre-set threshold are dropped from the list (deleted). FastJet implementation of the PxCone algorithm has this cut (EPSLON) set to 5 GeV as default but the threshold of 1 GeV is used in Chapter 5 in order to study low E_T jets as they were measured at CDF. Fig. 8.3 shows a nice comparison of the threshold influence on the final jets.

- Remaining overlapping protojets are split in the case when the fraction of shared transverse energy is lower than a pre-set value. Otherwise, the protojet with the lower transverse energy is deleted. The algorithm is set to take 50% as a default threshold.

- Particles that are contained in more than one protojet are assigned to the protojet whose axis is the nearest in the $\eta - \phi$ plane.

- The protojet four-momenta are recalculated using new particle assignment.

- Again, all protojets with lower transverse energy than the EPSLON threshold are deleted.

All the remaining protojets are classified as final jets. Even though the PxCone algorithm uses the midpoints, it still suffers from being infrared unsafe of order IR_{3+1}. PxCone was chosen for the comparison with the CDF JetClu as the middle step between simple cone algorithm and the fully IR safe recombination anti-k_t algorithm described in the following.

8.2.3 Sequential recombination algorithm: anti-k_t

One of the newest algorithms is the anti-k_t algorithm [108]. It belongs to the family of sequential recombination algorithms but behaves like a standard cone. Cone-like shape of the jet is more intuitive and one can easily talk about the jet radius R of the circular cross section in the y-ϕ plane. The underlying idea of the algorithm is also to merge the outgoing particles in order to get closer to the original parton four-momenta before the shower. Particles with nearly parallel momenta are joined together and form a new momentum which re-enters the check again. These steps are repeated still on and on until all four-momenta are well separated.

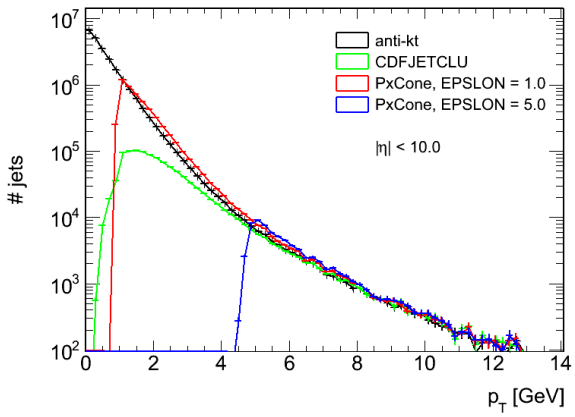

Figure 8.3: Jet transverse momentum distributions for different clustering algorithms. Also the influence of the minimal transverse momentum cut applied on PxCone protojets is shown. Both cone algorithms are infrared unsafe while the anti-k_t algorithm is infrared safe. A sample of QCD $2 \to 2$ events was prepared using the Herwig++ generator [56].

Quantitatively spoking, the distance between two input particles i and j is defined as

$$d_{ij} = min(k_{ti}^{-2}, k_{tj}^{-2}) \frac{(y_i - y_j)^2 + (\phi_i - \phi_j)^2}{R}, \tag{8.10}$$

where k_{ti}, y_i and ϕ_i are the transverse momentum, rapidity and azimuth angle of particle i. Moreover, the distance of the individual particle to the beam (B) axis is defined:

$$d_{iB} = k_{ti}^{-2}. \tag{8.11}$$

A list of all the d values is compiled and the smallest one undergoes the further decision step. If this case concerns the distance of two particles, their four-momenta are recombined according the predefined scheme and the new sum replaces the two original momenta. If the smallest distance belongs only to one momentum which is closer to the beam than to any other item, this momentum is declared as a complete jet and is removed from the input list. In both cases, this algorithm step reduces number of input items by one and is repeated until all items are declared as final jets. The larger R value is chosen, the smaller d_{ij} distances are and thus more merging take place before jets are completed.

Transverse momentum distributions of jets created using three different jet algorithms in Fig. 8.3 reflect the infrared and collinear safety of the anti-k_t algorithm against the two cone algorithms. The distribution of anti-k_t jets continues smoothly with decreasing jet p_T down to zero, while both cone algorithms have some artificial threshold protecting them against the soft underlying event.

Using the anti-k_t algorithm, also the influence of the jet parameter R is studied at Monte Carlo level. Figure 8.4 demonstrates that the larger radius R of the cone-like jets is chosen, the fewer jets are present in the event but carry larger part of the total transverse energy. One event from the double parton scattering production of positively charged di-muon pair at 14 TeV proton-proton interaction is shown. Every analysis has

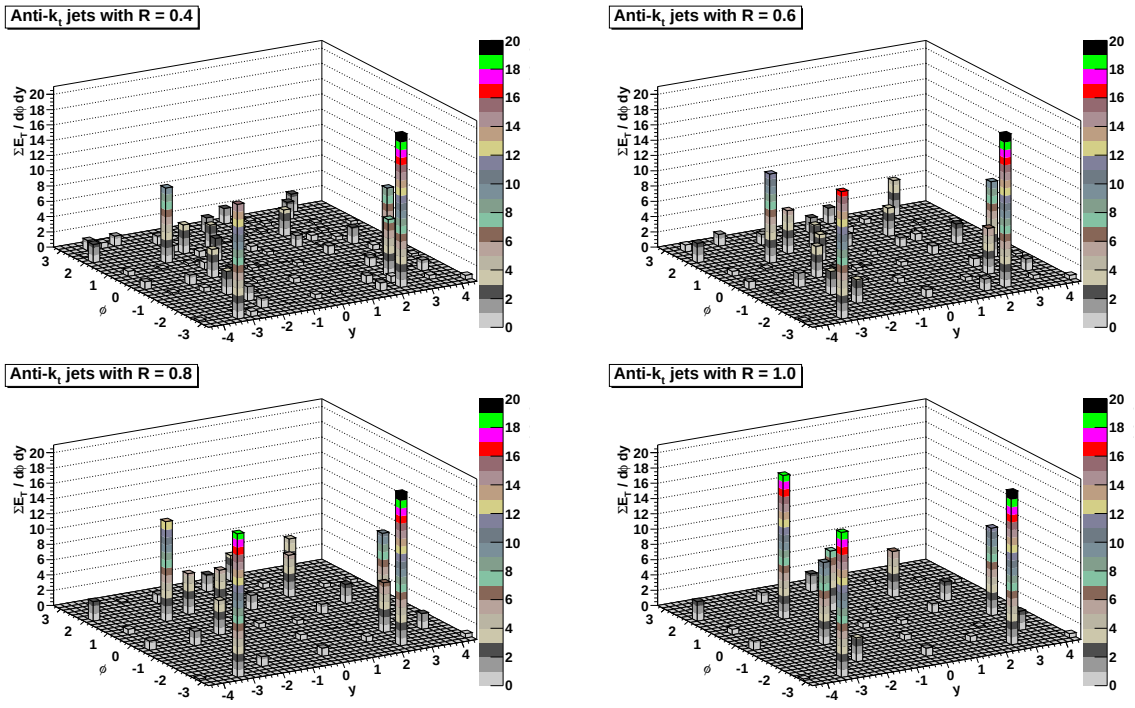

Figure 8.4: Distributions of the jet transverse energy in the y-ϕ plane for four values of the jet size parameter, from 0.4 to 1.0. With the increasing radius-like parameter the more jets are merged together and so increase their chance to be detected and reconstructed. On the other hand, the resolution of the jet reconstruction decreases.

to investigates its own dependence on the jet size. Because of the ATLAS restriction to the values of 0.4 and 0.6 of the ATLAS anti-k_t jet size, the differences between only these two values are described in Section 9.4.2. Jet radius of 0.6 was found to be the most suitable choice for this double parton scattering research.

8.2.4 Jets at ATLAS

The ATLAS collaboration [124] decided to adopt only the anti-k_t algorithm after some tests at the beginning. The very same procedure as in the above described FastJet implementation is used with the E-scheme for momentum recombination. The choice of the distance parameter R is restricted to the values of 0.4 and 0.6. The additional information about the ATLAS jets concerns the detector read-out method that has to take into account also detector effects like non-compensating calorimeter, dead regions, passive material, calorimeter noise etc. Several types of jets are distinguished according to the different input to jet finder [135]: calorimeter towers, topological clusters or charged tracks, and according to the jet calibration method [136]: global scale or local calibration.

Topological energy clusters are three-dimensional objects representing field of energy deposited in the calorimeter cells. Every cluster is formed dynamically around a seed,

which is a calorimeter cell containing energy larger than $4\sigma_{cell}$ above the noise. Neighbor cells to the seed cell are successively included to the cluster, if they carry energy above $2\sigma_{cell}$ of the noise. In a final step, all nearest-neighbor cells surrounding the cluster are added to the cluster. These clusters can then be split or merged depending on local maxima or minima within the clusters. Negative energy clusters are rejected.

An additional step might take place on top of the energy cluster formation. The calorimeter can be divided according to two orthogonal planes. The longitudinal division contains electromagnetic (EM) and hadronic parts of the calorimeter, the transversal division is taken as a fixed geometrical grid in the $\eta - \phi$ plane with one segment of size of 0.1×0.1. These parts of the detector are called calorimeter towers and the further jet reconstruction incorporates these towers separately. The energy of each tower is computed using its cells that belong to topological cluster. Therefore, the same noise suppression is used. Since the negative energy check is performed at the level of whole clusters, additional filter has to by applied on towers to ensure that only positive energy items enter the jet reconstruction.

There is also a possibility to reconstruct jets on the basis of the inner detector if desired. ATLAS implemented the so called 3D track jet method. It combines standard calo-jet algorithms applied on charged tracks and z-clustering. This tool clusters tracks from the input list by their impact parameter and so ensures that all tracks in the track jet come from the same interaction.

Atlas uses two jet energy calibration approaches: the global calibration, where jets are calibrated once built out of calorimeter object at EM scale, and the local calibration, where jets are build from hadronic-calibrated calorimeter clusters. The first approach is p_T and η dependent calibration scheme based on Monte Carlo simulations and converts the calibration of the ATLAS EM calorimeter to the calibration of the whole jet, i.e. EM + hadron calorimeter together. Global calibration therefore consists in the creation of the calibration constants, which are p_T and η dependent but still valid for the whole detector. Local cluster weighting calibration scheme uses Monte Carlo simulations and properties of clusters to calculate weights for individual cluster calibration. The current default ATLAS strategy uses the global EM scale factors.

In the experimental part of this thesis, globally EM calibrated jets from topological clusters are studied. First, the kinematical cuts

$$p_T^{jet} > 20GeV, \qquad |y^{jet}| < 4.4 \tag{8.12}$$

are applied to all jet candidates in order to model the detector acceptance and the ability of the detector to precisely and efficiently reconstruct detected jets. Since the jet mass can be calculated from the clusters the jet rapidity rather than pseudorapidity is determined. Second, additional cleaning conditions are required to reach the standard quality of reconstructed jets. Jets are classified in three categories: the bad, the ugly and the good.

The ugly jets correspond to real energy depositions in regions, where the energy measurement is known to be inaccurate, .e.g the transition regions between barrel and end-caps and problematic calorimeter regions.

The bad jet definition is more complicated and is based on several discriminating variables. One of the most important indicators of the jet quality is the fraction of energy

corresponding to liquid argon calorimeter cells. This factor takes into consideration also the shape of the measured pulse and compares it against the predicted shape. Another factor affecting the bad definition is the transverse momentum fraction of the charged tracks within the calibrated jet. Bad jet conditions also try to suppress the beam noise without collisions and cosmic radiation backgrounds. Generally speaking, different properties of all different types of the ATLAS detector are utilized in order to reach the best precision of the jet measurement.

Good jets are jets which are not bad neither ugly. Only good jets are used in the experimental part of this study.

The inner detector offers additional information about jets which are fully localized within its acceptance. The measuring of the individual tracks allows the reconstruction algorithm to evaluate the coefficient that characterizes the association of the given track to the reconstructed vertex. Based on the association tool, every jet in the tracking detector mat be assigned by the jet vertex fraction JVF(jet,vertex) discriminant which measures the probability that a jet originated from a particular vertex. In our case, the primary vertex is always taken and therefore the notation can be simplified for all jets just to JVF. The value of the jet vertex fraction is calculated using formula

$$JVF = \frac{\sum p_T(associated\ tracks)}{\sum p_T(all\ tracks\ in\ jet)}, \tag{8.13}$$

where the *associated tracks* are tracks associated with at least one vertex from the list of closest vertices to the primary one. The definition of the closeness of the vertex is related to the pre-defined window with sizes of longitudinal distance times sinΘ and transverse distance. If the jet has no matched track, it is pure calorimeter jet for instance, the JVF algorithm assigns a value of -1 to such a jet. In other cases, JVF value lies between 0 and 1. Jets with JVF = 1 are pure hard scatter jets and with the decreasing JVF value they are more and more affected by the pile-up. Jets with JVF = 0 are pure pile-up jets. It was found that jet selection based on JVF value is stable against the contributions from simultaneous uncorrelated soft collisions that occur during pile-up and is well behaved in a range of instantaneous luminosities. More details can be found in ATLAS internal note [137].

Moreover, the precise track reconstruction of charged particles in the inner detector, interaction vertex reconstruction and jet vertex association tool are very important for identifying jets containing b-hadrons. A detailed description of the algorithms which are supposed to gather all the necessary information and assign to all jets the probability of being initiated by the b-quark, the so called b-tagging algorithms, goes beyond the scope of this thesis and reader is rather referred to [138]. Generally speaking, the most important input information to all b-tagging algorithms is a distance of the reconstructed jet vertex to the primary vertex. The uncertainty of such a determination is highly affected by additional more-or-less soft pile-up events and every algorithm deals with it in a different way. This analysis uses the new MV1 algorithm based on a neural network training. This algorithm assigns to every jet a weight which is computed using three different weights IP3D, SV1 and IP3D+JetFitter and jet transverse momentum and pseudorapidity.

9 Analysis of the Same-Sign Muon Pairs

In the following, the analysis of DPS signal events together with relevant SPS background events is performed at the level of Monte Carlo simulated data, which were processed through the full chain of the standard ATLAS procedures simulating detector response [127, 128], briefly described in Chapter 6. The goal is to perform a feasibility study and provide relevant predictions for a future ATLAS measurement of proton-proton collisions at $\sqrt{s} = 14$ TeV. Even though the future high energy LHC runs as well as the ATLAS detector performance might differ from the designed expectations, the settings were chosen to model the situation reasonably well.

Monte Carlo generation of the hard processes is matched with the appropriate number of additional proton-proton interactions occurring in the same bunch crossing. These so called pile-up events are modeled using the Monte Carlo generation of minimum bias events, which represent the most probable case of soft QCD proton-proton interaction. Processes at harder scales are strongly suppressed, only few slightly harder QCD proton-proton interactions are taken into account. In the case of the pile-up simulation for this thesis, Pythia8 [139] was used to generate low and high p_T minimum bias events. Tune 4C [140, 141] and CTEQ6l1 [77] PDF was used. The redistribution of the minimum bias events added to the hard process obeys the Poisson distribution with the pre-set average number of proton-proton interactions per bunch crossing. The average number of pile-up interactions, $< \mu >$, is set to 40 and divides into two components according to the scale:

$$< \mu_{low\ p_T} >= 39.9547, \qquad < \mu_{high\ p_T} >= 0.0453. \tag{9.1}$$

One can compare this predicted $< \mu >$ value for future 14 TeV LHC run with the values of 9.1 and 19.5 in Fig. 7.1, which correspond to 7 and 8 TeV LHC runs. Before the LHC has started to operate, the predicted average number of pile-up interactions for 14 TeV at designed luminosity of 10^{34} cm^{-2}s^{-1} was 23, which substantially underestimated the real case. It is still an open question, if the predicted $< \mu > = 40$ models well the size of the real future pile-up.

Generated hard process as well as the pile-up minimum bias processes are simulated for the ATLAS detector response. The output from the simulation Geant4 program is in the form of set of hits in the detector volume. Hits are objects containing information about the location, where the generated particle intersects the active detector elements, about the amount of energy deposited at this point and about the time of the energy deposition. Hard process and pile-up hits are merged together and then

digitized. The output information about appropriate electric currents is transformed into the raw physics data and subsequently organized according to the reconstruction algorithms into physics objects, of which the previous chapter dealt. In the further text, the data samples corresponding to the full detector response simulation and containing pile-up events are labeled as *RECO*, while the data samples corresponding to the direct generator output record are labeled as *GEN*.

The studied processes will be described in details in the following sections. Here, only a brief summary of the data samples prepared using Hewig++ 2.5.1 [56] and MadGraph 5 [76] generators is given. CTEQ6l1 PDF set was used in both generators. Three categories of *GEN* data sets were prepared privately but via the same ATLAS software as used by the official ATLAS production later on. These three categories are distinguished by the energy of the proton-proton collision, $\sqrt{s} = 7$ or 14 GeV, and by the electric charge of the secondary muon pair, $\mu^+\mu^+$ or $\mu^-\mu^-$. The production of $\mu^+\mu^+$ at $\sqrt{s} =$ 14 GeV was avoided since these data sets were requested to be produced by the ATLAS collaboration.

Tables 9.1 and 9.2 offer the overview of the generated samples, generators used for the generation of the given parton process (the shower and hadronization steps are always managed by Herwig++ 2.5.1), the numbers of generated events and the appropriate cross sections[1]. ATLAS software release 16.6.7.16 was used for the generation.

Both *GEN* and *RECO* data sets for $\mu^+\mu^+$ production at $\sqrt{s} = 14$ GeV were produced by the ATLAS collaboration and are officially validated. These data sets correspond to the proton-proton collisions at $\sqrt{s} = 14$ TeV and to the production of the positively charged muons. The motivation for the restriction of the analysis of *RECO* data only to this choice is discussed in Section 9.9. Table 9.3 summarizes the same information for the officially prepared data samples as for the privately produced data. Releases of the ATLAS software differ according to the process and according to the stage of the full chain of generation-simulation-reconstruction. The DPS signal process and the $t\bar{t}$ process were prepared as the MC11 (Monte Carlo production for the year of 2011). These data sets were generated in release 16.6.8.2, simulated in 16.6.7.20 and reconstructed in 17.0.6.4. The generation, simulation and reconstruction tags were e1082, s1411, s1383, r3274 and r3109. The preparation of the remaining processes was delayed by the technical problems with the insertion of the LHE-files from MadGraph generator into Herwig++ in the framework of the computing grid. At the end, the generation of the di-boson processes was done within MC12, using ATLAS software release 17.2.4.7, but the HepMC output was converted into the MC11 format. Therefore, the other two steps, simulation and reconstruction, were done in the MC11-related releases. Simulation was done in 16.6.7.34 and reconstruction in 17.0.6.4. The generation, simulation and reconstruction tags were e1489, s1568, s1383, r3274 and r3109.

The set of steering parameters for Herwig++ Monte Carlo program used for the private generation are the same as for the official production, only the form of the job-option files is different. Appendix B shows the direct Herwig++ commands which are present in both versions.

[1]The statistical errors are negligible, therefore are suppressed in the Tables.

Process	Generator	# events	σ [fb]
DPS pp$\rightarrow$W$^+$W$^+ \rightarrow \mu^+\mu^+ +$ X	Herwig++ 2.5.1	100,000	0.81
SPS pp$\rightarrow$W$^+$W$^+jj \rightarrow \mu^+\mu^+ +$ X	MadGraph 5	100,000	1.02
SPS pp$\rightarrow$W$^+$Z$\rightarrow \mu^+\mu^+ +$ X	MadGraph 5	100,000	67.6
SPS pp$\rightarrow t\bar{t} \rightarrow \mu^+\mu^+ +$ X	Herwig++ 2.5.1	500,000	8.0×10^3
DPS pp$\rightarrow$W$^-$W$^- \rightarrow \mu^-\mu^- +$ X	Herwig++ 2.5.1	100,000	0.39
SPS pp$\rightarrow$W$^-$W$^-jj \rightarrow \mu^-\mu^- +$ X	MadGraph 5	100,000	0.35
SPS pp$\rightarrow$W$^-$Z$\rightarrow \mu^-\mu^- +$ X	MadGraph 5	100,000	47.8
SPS pp$\rightarrow t\bar{t} \rightarrow \mu^-\mu^- +$ X	Herwig++ 2.5.1	500,000	8.0×10^3
SPS pp$\rightarrow$ZZ$\rightarrow \mu^\pm\mu^\pm +$ X	MadGraph 5	100,000	27.3

Table 9.1: Overview of *GEN* data sets for proton-proton collisions at $\sqrt{s} = 7$ TeV from private production using ATLAS software.

Process	Generator	# events	σ [fb]
DPS pp$\rightarrow$W$^-$W$^- \rightarrow \mu^-\mu^- +$ X	Herwig++ 2.5.1	100,000	1.74
SPS pp$\rightarrow$W$^-$W$^-jj \rightarrow \mu^-\mu^- +$ X	MadGraph 5	100,000	1.46
SPS pp$\rightarrow$W$^-$Z$\rightarrow \mu^-\mu^- +$ X	MadGraph 5	100,000	118.5
SPS pp$\rightarrow t\bar{t} \rightarrow \mu^-\mu^- +$ X	Herwig++ 2.5.1	600,000	47.2×10^3
SPS pp$\rightarrow$ZZ$\rightarrow \mu^\pm\mu^\pm +$ X	MadGraph 5	100,000	62.7

Table 9.2: Overview of *GEN* data sets for proton-proton collisions at $\sqrt{s} = 14$ TeV from private production using ATLAS software.

Process	Generator	# events	σ [fb]
DPS pp$\rightarrow$W$^+$W$^+ \rightarrow \mu^+\mu^+ +$ X	Herwig++ 2.5.1	100,000	2.78
SPS pp$\rightarrow$W$^+$W$^+jj \rightarrow \mu^+\mu^+ +$ X	MadGraph 5	90,000	3.33
SPS pp$\rightarrow$W$^+$Z$\rightarrow \mu^+\mu^+ +$ X	MadGraph 5	90,000	148.3
SPS pp$\rightarrow t\bar{t} \rightarrow \mu^+\mu^+ +$ X	Herwig++ 2.5.1	1,000,000	47.2×10^3
SPS pp$\rightarrow$ZZ$\rightarrow \mu^\pm\mu^\pm +$ X	MadGraph 5	90,000	62.7

Table 9.3: Summary of data sets for proton-proton collisions at $\sqrt{s} = 14$ TeV obtained from the official production by the ATLAS collaboration. Both variants, *GEN* as well as further simulated and reconstructed data (*RECO*), were used in the analysis.

9.1 Double parton scattering signal generation

The motivation of this thesis is to perform a search for the multiple parton interaction effects in the new channel that has never been measured yet. The vector boson pair production offers a very straightforward test of the current stage of the MPI models. Specifically, the signal process is chosen to be the simultaneous and independent production of two W bosons within the same proton-proton interaction, as visualized in Fig. 9.1, where both bosons decay in the muon channel. The final state, as shown in Fig. 9.1, is thus formed by the pair of positively charged muons. In the further analysis, the signal process is referred in the abbreviated notation as $2 \times \mathrm{pp} \rightarrow \mathrm{WW}$. The *RECO* data based study is restricted to the $\mathrm{W^+W^+}$ charge combination and to $\sqrt{s} =$ 14 TeV, while the *GEN* data based analysis deals with both charge combinations and is also done for p-p collisions at $\sqrt{s} = 7$ TeV. It is assumed that this simplification is reasonable with respect to the parton distribution functions of interacting protons and that it demonstrates well the further measurability of such MPI process. However, a short comparison of kinematics for both charge combinations, $\mathrm{W^+W^+}$ and $\mathrm{W^-W^-}$ at the *GEN* data level, is outlined at the end of this chapter. Also a short comparison between the two energies of the proton-proton collisions will be shown.

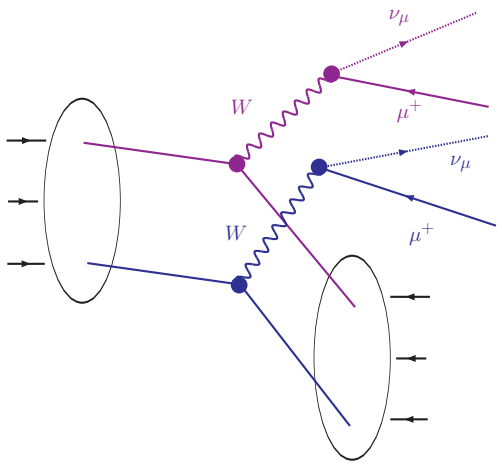

Figure 9.1: Schematic diagram of double parton scattering in pp collision. A pair of positively charged W bosons is produced via two independent parton annihilations.

In comparison to the γ^*/Z boson pair production, as example of another double Drell-Yan process, our signal process is better suited to the ATLAS detector measurement. The key factor for signal detection as well as for background suppression is the transverse momentum of secondary muons. W bosons statistically produce muons hard enough to be detected while the neutral boson suffers from low mass virtual photon propagator and its region of dominance contains significantly softer secondary muons. On the contrary, the restriction of the matrix element to the Z boson peak would reduce the total production cross section.

The signal process was generated using the Herwig++ program version 2.5.1. Unlike the QCD-type MPI processes measured up to now, the matrix element for the $\mathrm{W^+}$ creation allows only six flavor combinations of annihilating quark-antiquark pairs:

$$u\bar{d},\ u\bar{s},\ u\bar{b},\ c\bar{d},\ c\bar{s},\ c\bar{b} \rightarrow W^+ \rightarrow \mu^+\nu_\mu, \tag{9.2}$$

where the $u\bar{d}$ sub-process dominates over all other possibilities for the proton-proton interaction at $\sqrt{s} = 14$ TeV. The particular numbers of the percentage contributions of all individual combinations are summarized in Fig. 9.2 for the CTEQ6l1 PDFs. One

can see that the heavy quark contribution is still small even for such a high energy of the hadron collision.

Herwig++ is fully capable to generate this type of proton-proton events within its underlying event model only with one limitation. The generator does not calculate the production cross section for the whole desired event in order to stay as general as possible. For that reason, the normalization of the DPS production cross section is discussed a little bit more.

The formula for the double parton scattering inclusive cross section

$$\sigma_{WW}^{DPS} = \frac{\sigma_W^2}{2\sigma_{eff}}, \tag{9.3}$$

where two W productions take place in the same proton-proton collision. The simple factorization model is assumed.

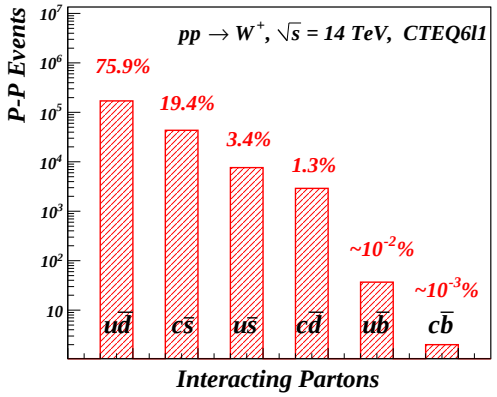

Figure 9.2: A relative fraction of parton flavor combinations producing W^+ boson demonstrating parton density distributions at $\sqrt{s} = 14$ TeV. The significant dominance of $u\bar{d}$ combination could allow to extract the information for valence-sea quark related geometrical coefficient. CTEQ6l1 PDF set is used.

There are two sources of the overall uncertainty for signal production cross section. First, the value of $12.0 \pm 1.3^{+1.3}_{-1.5}$ mb is taken for the σ_{eff} which corresponds to the corrected value of the CDF measurement [101]. This parameter could be calculated from the underlying event model of the Herwig++ generator using Eq. (2.52). However, the model is assumed to cover mostly the basic features of QCD multiple parton interactions and the intention is to leave the hard DPS cross section estimation rather independent on the underlying event activity.

Second, the evaluation of the SPS W production cross section depends on the choice of the parton distribution function and from the Monte Carlo used. Both theoretical uncertainties are studied for signal process. The purpose is to demonstrate a significant uncertainty in the signal cross section normalization which leads to the need of careful comparison between Monte Carlo and real data.

Since the matrix elements of background processes are generated using the MadGraph, the cross section value of the single parton $W^+(\rightarrow \mu^+)$ production calculated via MadGraph is compared here to the Herwig++ one. In addition, the influence of the parton distribution function (PDF) used during the generation for both programs is studied. One data sub-set was obtained using the CTEQ6l1 (CTEQ) and the other sub-set was gained using the MRST2007LOmod (MRST) [112]. Thus, four sets of SPS W events were prepared privately in order to study kinematic differences between muons produced via MadGraph and Herwig++ using two PDF sets. The cross sections for selection requiring muon with minimal transverse momentum of 5 GeV and within pseudorapidity range $|\eta| < 2.4$ are summarized in Table 9.4. One can see that the signal

production rate strongly depends on the Monte Carlo generator as well as on the PDFs. One should also note, that the DPS cross section for Herwig++ and CTEQ PDF, which is taken in the further analysis, is the lowest one from the studied options.

		σ_{SPS} [nb]	σ_{DPS} [fb]
HERWIG++	CTEQ6l1	5.76	1.38
	MRST2007LOmod	6.82	1.94
MadGraph	CTEQ6l1	7.07	2.08
	MRST2007LOmod	7.75	2.50

Table 9.4: Summary of the generated cross sections for single parton W^+ production for two different PDFs and two different generators. DPS W^+W^+ production cross sections were calculated using $\sigma_{eff} = 12.0$ mb.

The pseudorapidity and transverse momentum distributions for the hardest positively charged muon in the event at particle level are shown in Fig. 9.3. These results lead to the conclusion that there is no significant kinematic difference between the Herwig++ and MadGraph data and that the cross section calculations have a different sources like running coupling constants or other internal parameters of the Monte Carlo programs. Also PDF choice has only minimal influence on the final state muon kinematics, while the differences in the cross sections are large.

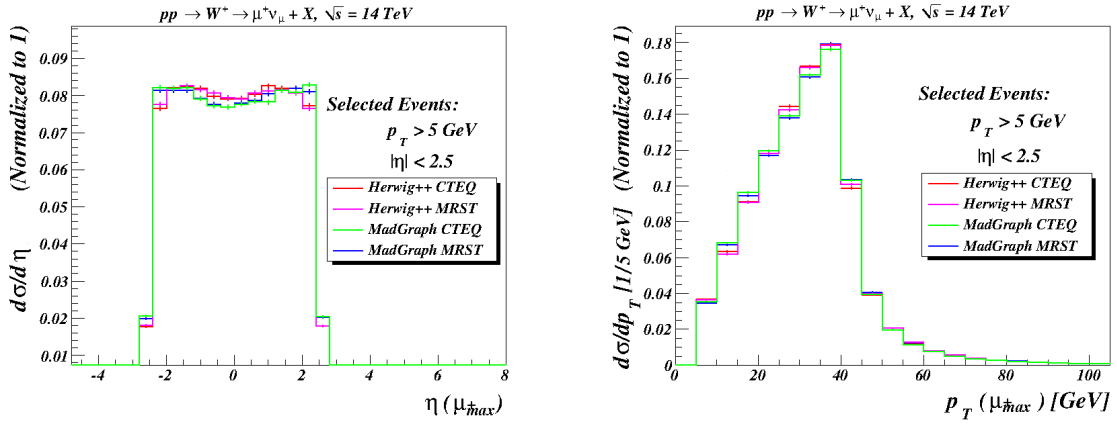

Figure 9.3: Differential cross section as a function of pseudorapidity (left) and transverse momentum (right) of the hardest positively charged muon, μ^+_{max}. Distributions are normalized in order to study their shapes depending on the Monte Carlo generator and PDF set used.

The last consideration belongs to the underlying event associated with any hard process generation. In order to satisfy the inclusiveness of this double parton process in the number of parton sub-interactions, Herwig++ continues to generate additional parton sub-processes according to the pre-sampled Poisson distribution. If any event

violates the momentum conservation, the event veto is called and the whole event is re-generated using the decreased number of additional parton interactions. The underlying event (UE) model steers the additional generation and assigns the simple QCD $2 \to 2$ matrix element to all sub-processes additional to the two W^+ creations.

The final state particles from the QCD underlying event contribute to the background jet activity together with the dominant component coming from the initial state radiation. In the following, fractions of the shower algorithm contribution and of the QCD MPI contribution to the jet formation are discussed. SPS W^+ production is used for this estimation since the DPS W^+W^+ cannot be generated when the main MPI switch is set to off. Plots in Fig. 9.4 display the transverse momentum distributions for the hardest (leading) and for the second hardest (sub-leading) jet assuming that the event contains at least one jet (two jets in the case of the sub-leading jet distribution) with the $p_T^{jet} > 20$ GeV and $|\eta^{jet}| < 2.8$. This threshold was set according to the expected performance of the ATLAS detector as an example of the sensible selection [142]. The anti-k_t clustering algorithm [108] implemented in the FastJet package version 3.0.1 [110] was applied on the non-lepton final state particles with the radius-like parameter $R = 0.4$.

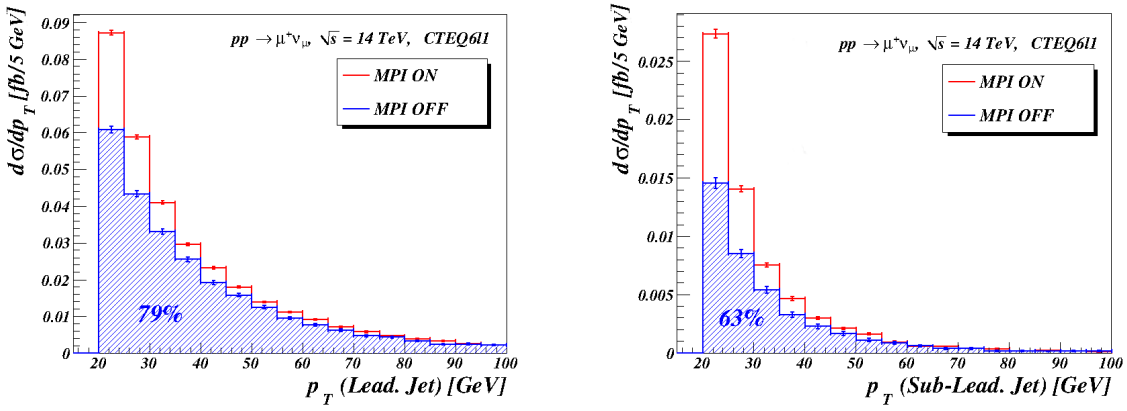

Figure 9.4: Comparison of transverse momentum distributions of the leading (left plot) and the sub-leading (right plot) jet using Herwig++ with MPI switched ON (red line) and OFF (blue line). The secondary scatters contribute to the leading jet in 21% of events and to the second leading (sub-leading) jet in 37% of events. The increase of the MPI fraction with decreasing jet mean p_T is given by relatively high number of additional QCD scatterings at semi-hard level while the radiations from the primary process decrease rapidly with p_T.

The histograms in Fig. 9.4 were obtained for the full event generation (red line) and for the generation where the MPIs were switched off (blue line). The expected behavior was confirmed. The production rate of $\mu^+ + 1$ jet events decreases only by 21% after the MPIs are switched off while the number of $\mu^+ + 2$ jets events dropped down by 37%. Although it is not so straightforward, one may argue that the jets from the MPIs are much softer than those coming from the initial state radiation but their number balances this disadvantage and their impact rises with the increasing number

of the required jets. A slightly smaller contribution from MPI is expected for the case of DPS W^+W^+ creation.

Settings of the underlying event generation in Herwig++ offers two free parameters which control the tune appropriate to the experiment. For the purpose of this study, the ATLAS UE tune for p-p collisions at $\sqrt{s} = 14$ TeV and for CTEQ6l1 PDF is used. This tune sets the threshold for the minimal transverse momentum of interaction products, p_T^{min}, to 3.16 GeV and the inverse proton radius squared, μ^2, to 1.35 GeV^2.

9.2 Single parton scattering background estimation

So far, issues associated with the double parton scattering signal process generation were discussed and with its production cross section normalization. The signal final state was defined as two positively charged muons. The two neutrinos should carry similar transverse energy as the detected muons and so the signal events are assumed to embody a significant missing transverse energy (MET). The muon pair may also be followed by several jets originating in the initial state radiation, in the additional QCD parton sub-interactions or in the pile-up proton-proton events within one bunch crossing. All the objects characteristic for the signal are important for the analysis and therefore all processes producing the same composition of the final state should be included into the background analysis. The analysis described in the following deals only with the physics background processes that result in the searched final state already at parton level, while the background stemming from the detector-related effects, like lepton misidentification, is only briefly outlined here.

Even though this thesis involves the full simulation of the ATLAS detector for the signal and main physics background processes, detector effects causing a random signal-like detector response from basically different interaction is not studied in details. It is expected that the kinematic specifics of the *Final Selection*, see Table 9.11, ensures a significant dominance of the studied processes over the other effects.

The biggest issue could probably be connected to the lepton misidentification, where the negatively charged muon is recorded by the detector as positively charged and vice versa. The single parton $pp \to W^+W^-$ process has the cross section of several orders of magnitude higher than the double parton scattering signal. Assuming the misidentification rate to be of the order of 10^{-3}, the fake di-muon rate would be comparable with the signal production rate. The misidentification probability rises with the energy of the muon because the magnetic field may not be able to bend the muon track enough. Fortunately, the transverse momentum of muons from the double parton scattering are very well distributed within the limited region approximately up to 60 GeV, unlike the muons from single parton gauge boson pair production. The same argument is valid for example, in the case of simple Drell-Yan creation of the neutral vector boson decaying leptonically, where one secondary lepton is reconstructed with the wrong charge. In this case, analysis of the lepton pair invariant mass could help to suppress such an abundance of events.

If one would like to search for the DPS WW production in the electron channel, he would have to face another problem. The direct photon might be misidentified by the calorimeter as the lepton. Such a fake rate is of order of several per cent and would make the $pp \to W^+Z$ and $pp \to ZZ$ SPS background processes even more problematic. On the other hand, electron channel offers the use of a wider acceptance region. The calorimeters are usually in more forward regions than the muon chambers. This might help to veto more background events containing negatively charged electron from the Z boson decay.

9.2.1 SPS di-boson production

The first type of the irreducible physics background is a SPS gauge boson pair production. Gauge bosons are considered to decay in the muon channel. All three combinations are possible: WW, WZ, and ZZ. Due to the notation simplification, Z denotes any neutral vector boson. However, the calculations contain also the off-shell effects: virtual gamma, Z peak, and their interference.

Matrix elements for the vector boson pair production were prepared using the MadGraph program [76]. These parton-level events were inserted in the form of LHE file into the Herwig++ and re-run in order to add the shower and hadronization steps into the full event generation. Also the generation of additional QCD multiple parton sub-processes were included.

Muons coming from the processes with virtual γ decays may propagate very close to each other, see Fig. 9.5. The ZZ and especially WZ productions thus had to be filtered at the parton level in order to avoid the divergences in the cross section for too many collinear muons. Parton level cuts were imposed on the outgoing leptons (l):

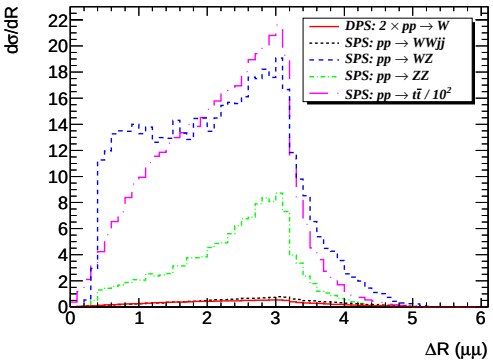

Figure 9.5: Differential cross section as the function of the relative distance of two hardest positively charged muons in the $\eta - \phi$ plane.

$$\hat{p}_T(l) > 3 \text{ GeV}, \qquad |\hat{\eta}(l)| < 5.0, \qquad \Delta\hat{R}(ll) > 0.4. \tag{9.4}$$

The edge of Δ R close to the zero is fuzzy-distributed due to the shower algorithm applied on the matrix element.

The production rate for same-sign WW is highly suppressed in comparison to opposite-sign W pair production because of the choice of the electric charge combination. The simplest tree level Feynman diagram for the single parton production of the same-sign WW contains also two outgoing quark lines in the final state and so the process looks like $pp \to W^+W^+jj$. After addition of the lepton lines, the leading order cross section is of $\mathcal{O}(\alpha_S^2\alpha_{EW}^4)$ or $\mathcal{O}(\alpha_{EW}^6)$ and is comparable to the double parton scattering production rate. The former case, drawn in Fig. 9.6 is restricted QCD 2→2 process to which two W emissions are attached to the initial or final state quark line. The restriction consists in the electroweak character of the W emission connected to the up-quark line. The assigned up has the meaning of the SU(2) doublets.

One of the most important consequences of this restriction, valid for $\mathcal{O}(\alpha_S^2\alpha_{EW}^4)$ processes same as for $\mathcal{O}(\alpha_{EW}^6)$ ones, is that the gluon component of the proton at the LHC energies does not contribute to this process at the LO and the overall dominant parton process is $uu \to dd\mu^+\mu^+\nu\nu$ (around 57%).

Example Feynman diagrams in Fig. 9.7 demonstrate well the main categories of the individual contributions to the pure electroweak processes of $\mathcal{O}(\alpha_{EW}^6)$. Graph 1 shows how the external quark lines may be directly connected by neutral vector boson propagator and W bosons are radiated from the initial or final state quark lines. Graph 2 represents wider spectra of interactions among vector bosons and/or lepton internal

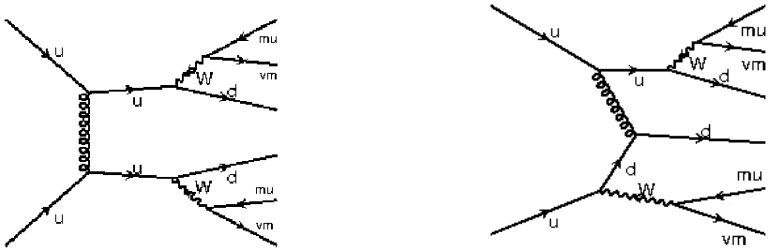

Figure 9.6: Example of leading order diagrams for semi-QCD interaction producing two positively charged muons in association with two jets.

lines, whether the Z boson is stretched between quark line and secondary lepton from W boson decay or anyhow else. Graph 3 and graph 4 illustrate the triple and quadruple interaction vertices for gauge bosons.

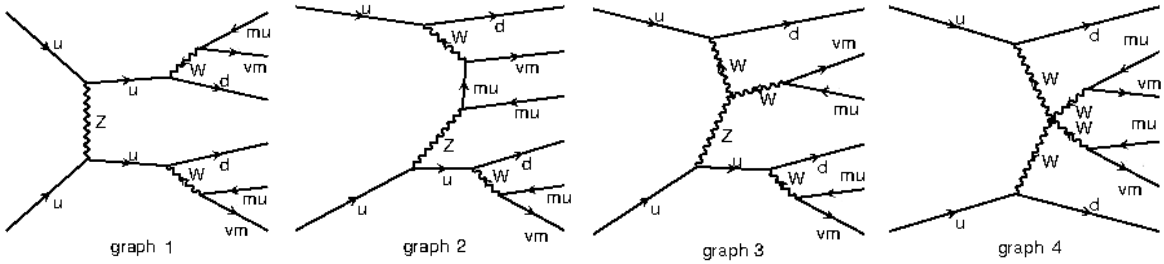

Figure 9.7: Typical leading order diagrams for pure electroweak interaction producing two positively charged muons in association with two jets.

The vector boson pair production processes where one ($pp \to W^+Z$) or both bosons are electrically neutral ($pp \to ZZ$) are considered as physics backgrounds too, since the negatively charged muon (OS muons; opposite sign with respect to the searched muon charge) from the neutral boson decay may not be found. Such an OS muon can fall outside the studied pseudorapidity acceptance, can have an insufficient transverse momentum to be distinguishable from underlying event muons present in all events, its track reconstruction quality parameters may not be sufficient for our selection or the muon track may not be reconstructed at all. Otherwise, events containing OS muon can be easily vetoed.

The production of $pp \to W^+Z$ events may proceed only through the three types of diagrams shown in Fig. 9.8. The first two graphs represent Drell-Yan creation of gauge boson, where one of the final state lepton lines emits the second gauge boson (graph 1) or where the created boson exhibit in the triple gauge vertex and so the desired boson pair is produced (graph 2). Graph 3 reflects the possibility of the presence of t-channel quark internal line with boson emissions in both vertices.

The single parton production of neutral vector boson pairs, $pp \to ZZ$, is highly suppressed by requiring that no OS muon can be present in the event. Although, the production rate still keeps this process among the physics backgrounds. There are many diagrams similar to each other reflecting the interference of the neutral bosons. Figure 9.9 shows two topologically different diagrams, the t-channel fermion exchange (graph

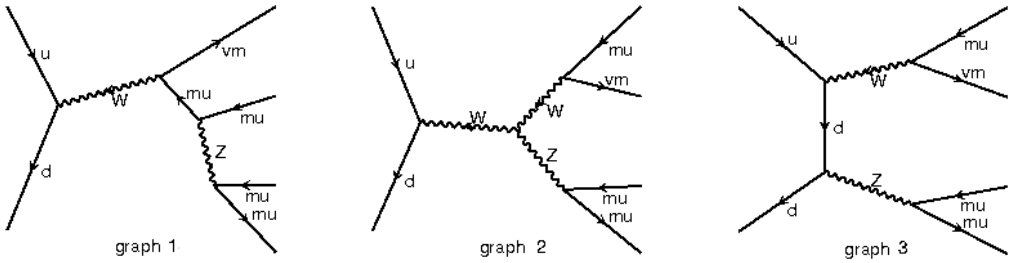

Figure 9.8: Leading order Feynman graphs for $pp \to W^+Z$ scattering process.

1) and the s-channel gauge boson creation (graph 2). The triple gauge boson vertex for two neutral bosons is not permitted in the standard model.

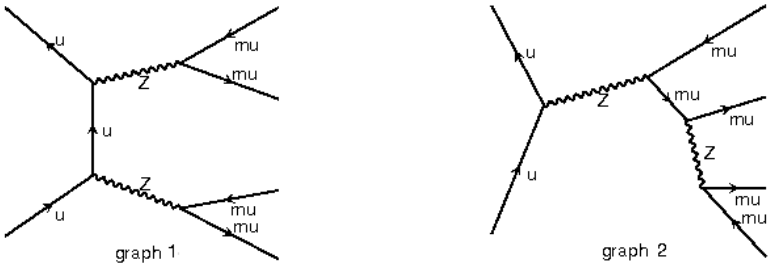

Figure 9.9: Leading order Feynman diagrams for neutral gauge boson pair production.

9.2.2 SPS $t\bar{t}$ production

The second source of the same-sign muon pairs in the final state is a heavy quark pair production, where the huge cross section leaves a lot of space for the muon radiation from short-living hadrons together with the heavy quark decay to the hard muon. The bulk of all possible final states coming from QCD $2 \to 2$ processes may form a challenging background at the first sight. The cross section of few hundreds of micro-barns means that even a tiny fraction of these events would overwhelm the double parton scattering signal. However, muons are generally produced with much different transverse momenta than in the case of muons coming from single W production. Especially the second muon has a very low chance to be produced hard enough to contribute to the irreducible background. The generation within the Herwig++ would be highly inefficient in order to generate the same-sign di-muon events for the general $QCD2 \to 2$ matrix element. Therefore, we use the $pp \to t\bar{t}$ process to demonstrate the kinematics that one should expect from the heavy quark production, which is practically the only QCD process capable to produce the studied di-muons. These events were generated directly using Herwig++.

The generation proved the fact that one of the muons (usually the hardest one) always originates in the top quark decay through the lepton decay of the W radiated during the top transition into bottom quark:

$$t \to W^+b \to \mu^+\nu_\mu b, \qquad BR = 0.108059 \tag{9.5}$$

while the second muon is generally much softer and comes from short-living hadrons, e.g. $B0, B^+, D0, D_S^+$. Such a production of the muon pair is always followed by jets that may serve as a very useful handle for the background suppression.

9.3 Event selection

Before turning to analysis itself, all the information about data samples and requirements applied on the studied proton-proton collisions at $\sqrt{s} = 14$ TeV are summarized in this section. One data set of the DPS WW pair production and four data sets of physics background processes were prepared to investigate the kinematic differences among the individual processes contributing to the searched di-muon final state. Background processes are SPS productions of WWjj, WZ, ZZ, and $t\bar{t}$. Symbol Z represents full matrix element for neutral vector boson, where no minimal invariant mass was required. The muon decay channel was set for all the stated gauge bosons. In the $t\bar{t}$ production, the gain of two positively charged muons was optimized by forcing the t quark to end up its decay cascade with μ^+. Such a branching ratio was taken to be 0.108059. Physics objects and terms defined in Chapter 8 will be used in the following analysis without explicit individual references.

The analysis searches for events containing at least two positively charged muons in the final state. For the DPS signal events, the two hardest muons always belong to the studied W decays. Therefore, two objects are distinguished to be analyzed. The hardest μ^+ is labeled as leading, μ_{lead}, while the second hardest μ^+ is marked as trailing, μ_{trail}. Note that the hardest muon in the event is always required to be positively charged and therefore has to satisfy conditions applied on the leading muon, while the trailing positively charged muon does not need to be the second hardest muon (any charge) in the event. The muon pairs coming from the DPS WW process are distributed in the phase space in such a way that the standard isolation cone of radius $\Delta R \equiv \sqrt{\Delta\eta^2 + \Delta\phi^2} = 0.3$ would be sufficient condition just from the detection point of view. However, generation of SPS WZ and ZZ background processes required internal parton level ΔR cut at 0.4, as discussed in previous section. The particle-level distribution of ΔR in Fig. 9.5 shows that the reasonable choice of the minimal relative distance of the two hardest muons in the $\eta - \phi$ plane is 0.6.

As a starting point, the *Base Selection* is determined in order to extract an event sample which will serve as a starting point for further investigation of the kinematics of the studied processes. Except the above mentioned Δ R separation of the two muons, the *Base Selection* requires also some minimal transverse momentum and maximal pseudorapidity on leading and trailing muons:

$$\mathrm{p}_T(\mu) > 5 \text{ GeV}, \qquad |\eta(\mu)| < 2.4, \qquad \Delta \text{ R}(\mu_{lead}\mu_{trail}) > 0.6. \tag{9.6}$$

where the transverse momentum p_T is defined in relation to the beam axis. The pseudorapidity η cut is chosen on the basis of the ATLAS detector performance [120]. The ATLAS muon spectrometer cover $|\eta| < 2.7$ but combined information about hits also from both the inner tracker ($|\eta| < 2.5$) and the muon trigger system ($|\eta| < 2.4$) is expected. Therefore, the pseudorapidity cut is restricted to their common acceptance. One should emphasize that no quality requirements are placed on the reconstructed muon tracks at this point.

Few other physics objects are analyzed in addition: the hardest negatively charged muon (opposite sign (OS) against the searched muons), OS μ_{lead}, and four hardest jets in the event. The same minimal transverse momentum and maximal pseudorapidity

requirements are applied on negatively charged muons as on the positively charged ones:

$$\mathrm{p}_T(\mathrm{OS}\ \mu_{lead}) > 5\ \mathrm{GeV}, \qquad |\eta(\mathrm{OS}\ \mu_{lead})| < 2.4. \tag{9.7}$$

Jets are reconstructed from globally EM calibrated topological clusters and formed using Anti-k_t algorithm with distance parameter R = 0.6. Accepted jets have to be *good* jets satisfying

$$\mathrm{p}_T(\mathrm{jet}) > 20\ \mathrm{GeV}, \qquad |\mathrm{y}(\mathrm{jet})| < 4.4. \tag{9.8}$$

These cuts ensure that jets lie well within the high trigger efficiency plateau region and that the jet energy scale is well understood for this region [142].

9.4 Background suppression

In this section, specific properties of all the five considered processes are investigated in order to find a set of selection criteria that could help us to maximize the signal-to-background ratio. Considering that the signal DPS process has the production cross section of $\mathcal{O}(1\ fb)$, this task requires a very careful approach. In the following, the lepton and jet analysis are separated but their impact on the studied *Base Selection* data samples has a cumulative effect.

9.4.1 Lepton analysis

At first, a comparison between data from chain of full detector simulation, hits digitization and physics object reconstruction (the *RECO* data) and data from generator record (the *GEN* data) is shown in Table 9.5, where only the *Base Selection* was applied. Muons at the *RECO* level are required only to be STACO muons with no further quality criteria. Technical details and nomenclature used are discussed in Chapter 8. One can see, that almost all cross sections decreased by around 1-4% when switched from the *GEN* to *RECO* level data. There is only one exception, the QCD $t\bar{t}$ production, where the number of accepted events increased by approximately 12%. QCD production of heavy flavor quarks is simply accompanied by larger amount of final state particles which might be misidentified as muons or anyhow else fake the signal in the detector. Influence of the simulated pile-up is improbable, since the additional QCD interactions are statistically the same in every process.

σ [fb]	DPS signal	SPS background			
	W^+W^+	W^+W^+jj	W^+Z	ZZ	$t\bar{t}$
GEN data	1.38	1.75	46.00	13.40	$4.20{\cdot}10^3$
RECO data	1.34	1.73	44.38	13.18	$4.70{\cdot}10^3$

Table 9.5: Comparison of cross sections obtained for the *RECO* and *GEN* data by application of the *Base Selection* cuts.

This comparison is meaningful only for the evaluation of the detection and reconstruction efficiency. From the physics point of view, the detector response simulation and addition of pile-up proton-proton interactions make the final picture of the interaction event at the *RECO* level more complicated than it is at level of the generator record. A series of quality requirements are involved to the analysis in addition to the default settings for the chosen STACO algorithm:

- $N^{PV}_{tracks} \geq 3$; Number of tracks in the inner detector associated with the primary vertex (PV) has to be at least 3 in order to set a minimal quality requirements to the reconstructed primary vertex.
- *Combined muons*; All muons have to be well detected by both inner tracker (ID) and muon spectrometer (MS) so the two independent tracks are reconstructed.

- *Tight muons*; All reconstructed muon tracks have to fulfill a set of detector-based quality criteria that are common to every analysis. The tight quality keyword was chosen as the highest quality level among the loose-medium-tight option. Moreover, the ID muon track is demanded to be reconstructed from the certain amount of hits in the ID summarized in Eq. (8.3) and (8.4).

- $\chi^2_{(ID-MS\ match)} < 20$; The value of the χ^2/NDF of the MS-ID track match at the perigee is required to be less than 20 for all muons.

- $|p_T^{ID} - p_T^{MS}|/p_T^{ID} < 0.5$; The relative difference of the transverse momentum between muon ID and MS tracks is required to be less than 0.5 for all muons.

- $Isolation_{calo}$; Positively charged muons have to be isolated with respect to the energy deposited in the calorimeters.

- $Isolation_{track}$; Positively charged muons have to be isolated also with respect to the charged tracks reconstructed in the inner detector.

- $z/d_{(\mu-PV)}$; Longitudinal and transverse impact parameter of the positively charged muons with respect to the PV have to indicate the promptness of the muon.

The gradual influence of requirements on the muon quality reconstruction is summarized in Table 9.6. The fraction of survived events expressed in percentage below the appropriate cross section is related to the number of events in the *Base Selection*, which creates the input 100%. One can see, that the PV quality condition has a minimal effect on the selected events. As expected, processes directly producing jets, SPS WWjj and $t\bar{t}$, have even slightly higher chance to have at least 3 reconstructed tracks associated to the PV. The pure boson production at matrix element level is accompanied by additional hadron activity that cannot be separated. This is also reflected in the results for muon isolation requirements. Almost 7% of signal events is lost by requiring muons to be combined. The additional tight reconstruction quality requirement with combination of ID-MS consistency conditions suppress another 3% of the signal events. Very similar fractions of background events are rejected and the size of the remaining data sample is around 90% of the input *Base Selection* sample.

Further conditions are placed only at positively charged muons since the presence of oppositely charged muons in the event is studied without restriction on their isolation or promptness. The combined calorimeter- and track detector- based muon isolation suppress another 11% of signal events and around 20% of SPS di-boson background events. The key role of the isolation lies in the suppression of the most of the QCD background. In the case of $t\bar{t}$ production, around 77% of events are rejected since they do not contain two isolated positively charged muons. One could expect that when the heavier quark is produced the smaller effect of isolation could be observed since the muon can be radiated at statistically larger angle from the outgoing jet. Therefore, even large suppression of another QCD background events is assumed. Limitations set on the longitudinal and transversal impact parameters of the muon track with respect to the PV have only small effect on DPS signal and SPS di-boson background processes but suppress about 50% of the remaining $t\bar{t}$ events.

σ [fb]	DPS signal	SPS background			
	W^+W^+	W^+W^+jj	W^+Z	ZZ	$t\bar{t}$
Base Selection	1.34	1.73	44.38	13.18	$4.70 \cdot 10^3$
	(100%)	(100%)	(100%)	(100%)	(100%)
$N^{PV}_{tracks} \geq 3$	1.34	1.73	44.33	13.17	$4.70 \cdot 10^3$
	(99.9%)	(100%)	(99.9%)	(99.9%)	(100%)
Combined muons	1.25	1.61	41.81	12.45	$4.13 \cdot 10^3$
	(93.1%)	(92.6%)	(94.2%)	(94.4%)	(88.0%)
Tight muons	1.22	1.57	40.87	12.22	$3.96 \cdot 10^3$
	(90.8%)	(90.4%)	(92.1%)	(92.7%)	(84.3%)
$\chi^2_{(ID-MS\ match)} < 20$	1.21	1.56	40.71	12.18	$3.93 \cdot 10^3$
	(90.3%)	(89.9%)	(91.7%)	(92.4%)	(83.7%)
$\lvert p_T^{ID} - p_T^{MS} \rvert / p_T^{ID} < 0.5$	1.20	1.54	39.75	11.77	$3.68 \cdot 10^3$
	(89.7%)	(88.6%)	(89.6%)	(89.3%)	(78.4%)
$Isolation_{calo}$	1.15	1.35	36.56	10.87	229.01
	(85.8%)	(78.0%)	(82.4%)	(82.5%)	(4.9%)
$Isolation_{track}$	1.05	1.22	31.01	8.85	53.18
	(78.3%)	(70.4%)	(69.9%)	(67.2%)	(1.1%)
$z/d_{(\mu-PV)}$	1.04	1.20	30.52	8.69	23.94
	(77.1%)	(69.3%)	(68.8%)	(65.9%)	(0.5%)

Table 9.6: Summary of the gradual influence of the reconstruction quality requirements applied on final state muons in the *RECO* data sample. Every condition contains also the above cuts.

In order to model the analysis of real data, a trigger decision has to be taken into consideration. Event filter (EF) triggers containing all levels of the decision algorithm are considered. Four single muon triggers and one di-muon trigger with the highest rates of the triggered DPS signal events are studied. Even though the future triggers might be somewhat different, the current stage of the detector simulation and contemporary triggers provide a consistent and reasonable prediction of the future situation. Table 9.7 shows appropriate cross sections for the triggered events from the *Base Selection*, to which all above studied quality requirements are applied. Therefore, the triggered events can be compared among each other since the selected muons already satisfy our isolation and quality conditions and do not rely on the trigger settings. The trigger nomenclature contains the trigger level (EF) and transverse momentum required for at least one muon in the event. Trigger name may also contain an i as a reference to the muon isolation, quality key word for muon track reconstruction (loose, medium, tight) or an EFFS shortcut as a signature for the full scan of calorimeter at event filter trigger level.

However, settings for the listed triggers differ in more aspects and technical details, like muon reconstruction algorithm and fit procedures, which description goes beyond the scope of this study. One can especially observe different dependencies on trigger for two groups of processes. DPS WW and SPS WWjj processes exhibit the same

σ [fb]	DPS signal	SPS background			
	W^+W^+	W^+W^+jj	W^+Z	ZZ	$t\bar{t}$
EF_mu15	0.84	0.96	25.77	7.88	17.90
	(80.8%)	(80.0%)	(84.4%)	(90.7%)	(74.8%)
EF_mu20i_medium	0.93	1.08	24.91	7.44	17.38
	(89.4%)	(90.0%)	(81.6%)	(85.6%)	(72.6%)
EF_mu24_MG_tight	0.90	1.06	23.80	7.13	17.33
	(86.5%)	(88.3%)	(78.0%)	(82.0%)	(72.4%)
EF_mu30_tight	0.88	1.06	24.54	7.19	17.38
	(84.6%)	(88.3%)	(80.4%)	(82.7%)	(72.6%)
EF_mu15_mu10_EFFS	0.97	1.12	27.00	8.07	16.96
	(93.3%)	(93.3%)	(88.5%)	(92.9%)	(70.8%)

Table 9.7: Muon trigger overview. The relative percentage numbers are with respect to the last line in Table 9.6, where all quality requirements are satisfied. One can therefore see only the trigger influence.

behavior and also SPS WZ, ZZ and $t\bar{t}$ processes have very similar dependence on the single muon trigger. For the case of signal events, the simplest single muon trigger, the EF_mu15, provides the minimal efficiency for our selection, while all the other triggers fulfill the intuitive expectation. The accepted number of events decreases with the increasing transverse momentum cut and decreases also for stricter quality word for track reconstruction. The di-muon trigger EF_mu15_mu10_EFFS was chosen to be the most suitable trigger for this analysis with respect to the DPS signal kinematics and will be applied on data further on.

The input data for the further analysis is labeled as *Trigger Selection* and accommodates all the above discussed quality requirements, EF_mu15_mu10_EFFS di-muon trigger and the following conditions on transverse momentum of the studied muons:

$$\mathrm{p}_T(\mu_{lead}) > 17 \text{ GeV}, \qquad \mathrm{p}_T(\mu_{trail}) > 12 \text{ GeV}, \tag{9.9}$$

since the trigger p_T cuts at 15 and 10 GeV are not as reliable as cuts applied after full reconstruction and the shift of about 2 GeV is recommended and standard method how to avoid the possible inconsistencies. It was also checked that it should be possible to find unprescaled di-muon triggers planed for the future high-luminosity LHC runs of type 2MU11 (i.e. trigger searching for two muons with $\mathrm{p}_T > 11$ GeV).

Eventually, the kinematics of the studied muons can be finally investigated. One DPS signal and four SPS background sub-samples are kept divided in order to study their differences and to search for an appropriate kinematic selection allowing a further signal enhancement in the context of the whole data sample.

First, there are significant differences among the transverse momentum distributions for the leading and trailing positively charged muons, see Figure 9.10. One can easily localize peaks for the signal distributions and so establish the muon transverse momentum cuts for both μ_{lead} and μ_{trail}:

$$(\ 20 < p_T(\mu_{lead}) < 60\ ) \text{ GeV}, \qquad (\ 12 < p_T(\mu_{trail}) < 45\ ) \text{ GeV}. \tag{9.10}$$

These cuts are selected in a most signal conserving way with no respect to the signal significance for now.

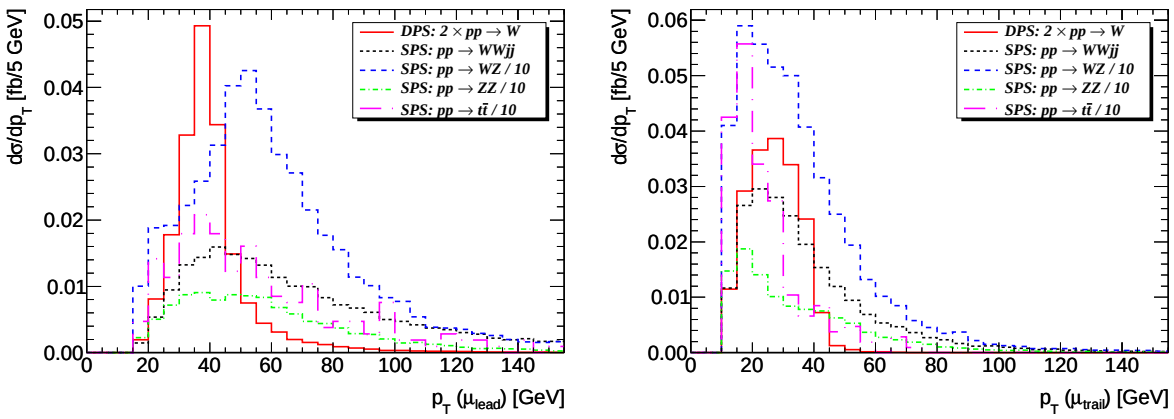

Figure 9.10: Differential cross section as a function of the transverse momentum of the leading (left) and trailing (right) positively charged muon. Distributions for SPS WZ, ZZ and $t\bar{t}$ processes are rescaled by factor of 0.1.

The second step is to investigate the transverse momentum distribution of negatively charged muons satisfying (9.7). Left plot in Fig. 9.11 compares transverse momentum distributions of the hardest oppositely charged muon, OS μ_{lead}, for all studied processes. One should emphasize that the OS muons do not have to be isolated and prompt. For the *RECO* data, the lowest reasonable p_T threshold for accepting reconstructed muon object as a real muon is around 5 GeV, which is given by the ATLAS detector performance. This threshold is adopted for this analysis in order to accept the opposite sign muon as real and its presence in the reconstructed event is used for the event rejection. The signal events contain practically only OS muons from extra radiation or secondary decays which usually do not exceed few GeV in p_T, while the di-boson events containing neutral gauge boson exhibit the opposite behavior. Most of these background events contain at least one OS muon with $p_T > 5$ GeV and thus they can be filtered off the data sample.

The right plot in Fig. 9.11 shows number of extra positively charged muons which were found in the event besides the two hardest muons. Distributions are normalized to unity in order to compare processes among each other. The expectation that hard QCD $t\bar{t}$ might produce statistically higher number of muons is not confirmed and no background process embodies any extraordinary behavior.

The third step is to check the muon pair variables which may help to isolate the signal contribution. Figure 9.12 shows distributions of invariant and transverse mass of the searched muon pair. There is no extra difference in the shape of distributions among the studied processes. Minimal invariant mass of 10 GeV and minimal transverse momentum of 40 GeV are required to suppress contribution from random detector background, e.g. from low mass Drell-Yan process misidentified as same-sign muon pair production.

Influence of the above discussed muon cuts is summarized in Table 9.8. This cut flow table shows cross sections for the *Trigger Selection* creating the input sample and to which all other cut steps are related to. Relative number of survived events is evaluated

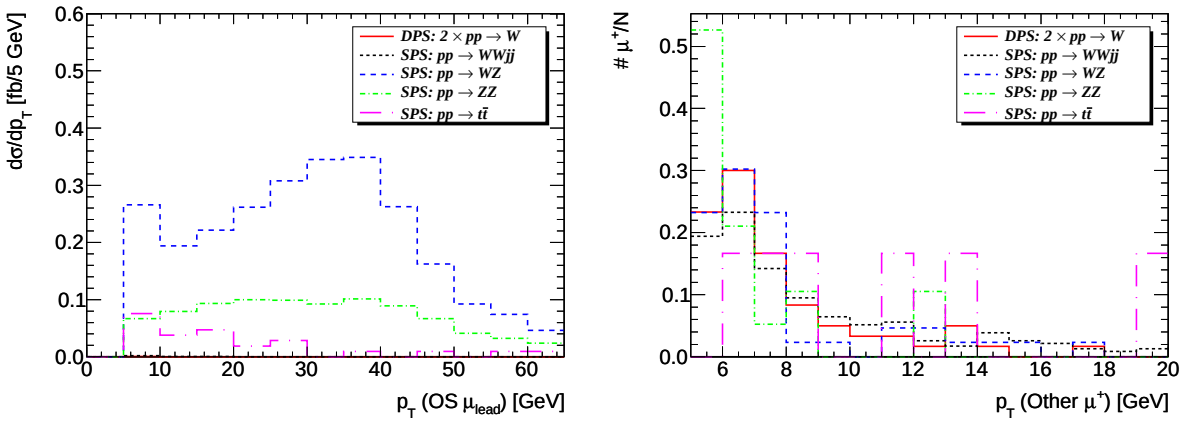

Figure 9.11: Left: Differential cross section as a function of the transverse momentum of the leading opposite-sign muon. Right: Relative numbers of positively charged muons additional to the two hardest ones as a function of muon transverse momentum (distributions are normalized to 1).

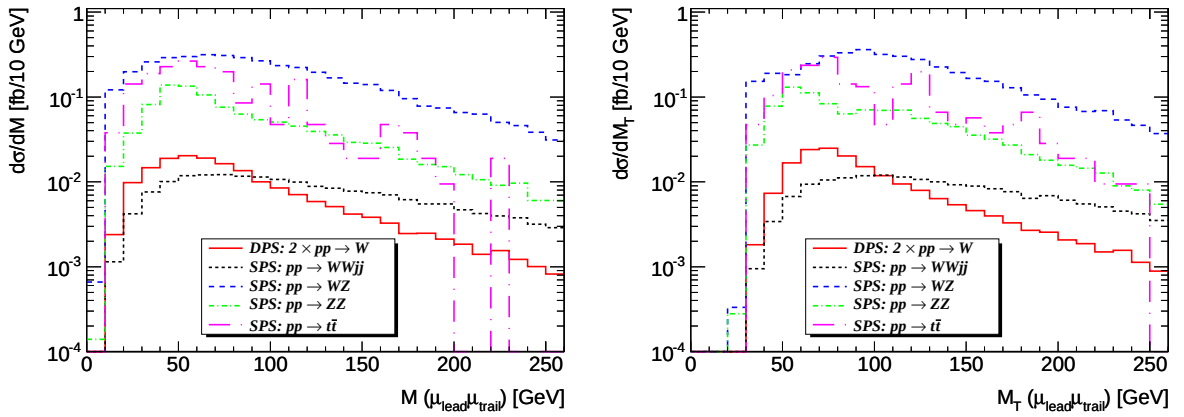

Figure 9.12: Differential cross section as a function of the invariant mass (left) and transverse mass (right) of the searched muon pair.

in percentage below the appropriate cross section. All shown cuts together applied on data forms the final *Lepton Selection*.

σ [fb]	DPS signal	SPS background			
	W^+W^+	W^+W^+jj	W^+Z	ZZ	$t\bar{t}$
Trigger Selection	0.92	1.06	21.76	5.54	9.97
	(100%)	(100%)	(100%)	(100%)	(100%)
$(20 < p_T(\mu_{lead}) < 60)$ GeV					
$(12 < p_T(\mu_{trail}) < 45)$ GeV	0.84	0.46	10.89	2.92	5.95
	(88.4%)	(43.4%)	(50.0%)	(52.7%)	(59.7%)
$p_T(OS\ \mu_{lead}) < 5$ GeV	0.84	0.46	4.87	0.47	5.15
	(88.4%)	(43.4%)	(22.4%)	(8.5%)	(51.7%)
$M(\mu_{lead}\mu_{trail}) > 10$ GeV					
$M_T(\mu_{lead}\mu_{trail}) > 40$ GeV	0.83	0.45	4.67	0.45	5.01
	(87.4%)	(42.5%)	(20.5%)	(8.1%)	(50.3%)

Table 9.8: Muon cut flow table summarizing the influence of three sets of cuts applied on the final state muons. Every sub-selection contains also above cuts too. The combination of all three sets of cuts listed here form the *Lepton Selection*.

9.4.2 Jet analysis

In this section, an extensive study of jets contained in the *RECO* data is performed. Jets associated with the DPS signal and SPS di-boson background muon pairs may stem from the initial state radiation, proton remnants, additional soft QCD multi parton interactions and from additional proton-proton collisions (pile-up). The SPS WWjj and $t\bar{t}$ processes may produce jets directly from the hard interaction. During the signal generation description, jets coming from radiation and MPI were discussed and their fractions were evaluated. Here, the influence of pile-up jets is mostly discussed.

The *Lepton Selection* creates the input data sample for the further analysis. Since the lepton analysis cuts suppressed the SPS di-boson background processes to reasonable level, the QCD $t\bar{t}$ production remains the largest physics background. The goal is to find such a set of jet cuts that would suppress the remaining (low) number of QCD background events to minimum. The SPS WWjj process exhibits very similar jet behavior as $t\bar{t}$ process but its influence on the the final data selection is already very suppressed and thus the further comparisons are focused on the DPS signal and SPS $t\bar{t}$ processes. Also the SPS WZ and ZZ processes are not shown since their hadron component is very similar to the signal case.

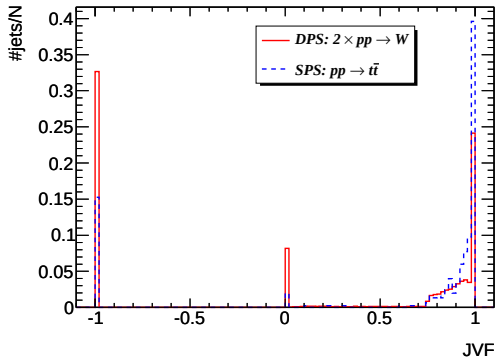

Figure 9.13: Values of JVF coefficient for all jets with $p_T > 20$ GeV and $|y| < 4.4$. Jets in $t\bar{t}$ events originates more likely from the primary vertex than the ones in signal events.

The coefficient Jet Vertex Fraction (JVF), described in Chapter 8, is investigated in order to suppress the pile-up influence on the final state jets. On the basis of reconstruction of charged tracks in the inner detector, this coefficient determines the fraction of tracks associated with the given jet which are matched with the primary vertex. Values of JVF for all jets in the DPS WW and SPS $t\bar{t}$ events are shown in Fig. 9.13. Here, anti-k_T jets with R = 0.6 and satisfying

$$|y(j)| < 4.4, \qquad p_T(j) > 20 \text{ GeV} \tag{9.11}$$

are considered. Distributions are normalized to unity and thus one can see that jets in $t\bar{t}$ events originates in the primary vertex more often than jets in signal events. The JVF value of -1 signs that jet does not contain any track matched with the primary vertex.

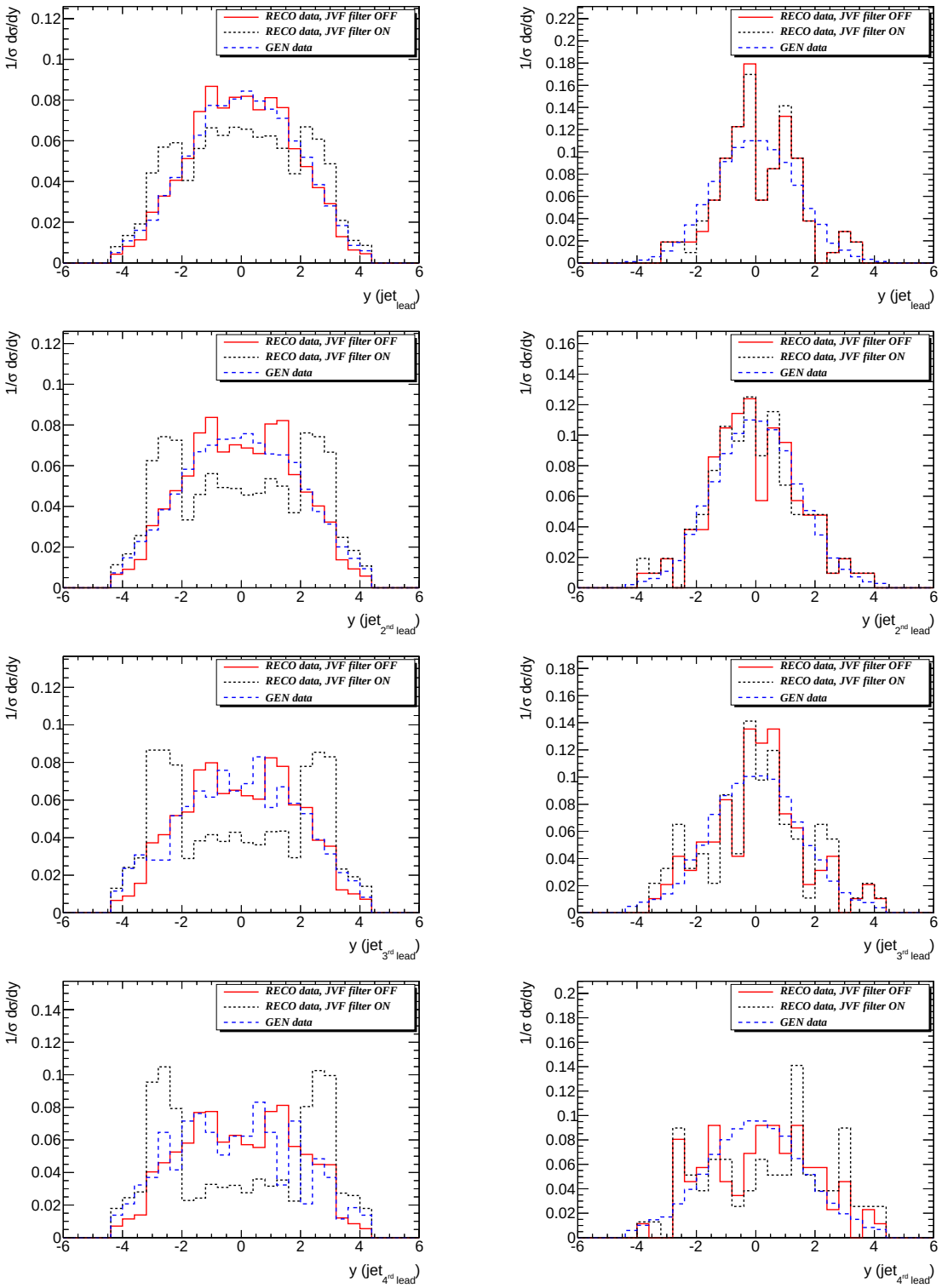

Figure 9.14: Jet rapidity distributions for four hardest jets, if present in the event. DPS WW production (left plots) is compared to the QCD $t\bar{t}$ production (right plots). Jets with $|y| < 4.4$ are considered.

It might happen when a jet is localized outside the inner detector acceptance or simply when the jet is reconstructed in the calorimeter and does not contain any charged track. In order to minimize the fraction of the unwanted jets coming from pile-up interactions, every jet localized well in the inner detector is required to have its JVF coefficient above some threshold. Specifically, jets have to satisfy the condition

$$\text{JVF} > 0.75 \qquad \text{if} \qquad |y| < 2.0, \tag{9.12}$$

which is labeled as JVF filter. If the jet has rapidity larger than 2.0, no JVF condition is applied. The efficiency of JVF filter is defined here as the ratio of the number of suppressed jets by this filter and the number of all jets for the given data sample. This efficiency will be further evaluated and then will be taken into consideration for the determination of suitable kinematic selection. The influence of the JVF filter on the final state jets and its efficiency in suppressing pile-up jets are investigated in details in the following paragraphs. After that, the kinematic selection is studied. In the following, jets are ordered according to their transverse momenta in the descending order: the first leading jet (j1), the second leading jet (j2), the third leading jet (j3) and the fourth leading jet (j4).

At first, one can look at rapidity distributions for the four hardest jets in the event. Such a separation demonstrates the influence of the JVF filter on the individual order of the jet in the event. Fig. 9.14 shows all the rapidity distributions, left plots correspond to DPS WW events and right plots to SPS $t\bar{t}$. The main attention should be paid to the comparison between distributions obtained by applying (9.12) (JVF filter ON) or not applying (9.12) (JVF filter OFF) on the *RECO* data. The distributions for the *GEN* data are shown just for illustration, how the distributions might look if there would be no pile-up. One can clearly see that the central jets are considerably rejected by the JVF filter while forward jets cannot be suppressed at all. If there would be essentially no difference between distributions for DPS signal and SPS $t\bar{t}$ background events, no rapidity restriction would be needed. However, the efficiency of the JVF filter to veto jets coming from pile-up is larger for DPS signal rather than for SPS $t\bar{t}$ and therefore the first step towards the $t\bar{t}$ background suppression is to limit the jet rapidity acceptance to

$$|y(j)| < 2.0. \tag{9.13}$$

This restriction suppresses the jet content in the signal events much more than in the $t\bar{t}$ background events. This leads to the more effective background suppression using jet transverse momentum cuts afterwards.

Another important behavior of JVF filter is that its jet suppression power rises with the order of the jet in the event. It is given by the jet multiplicity and by the dependence of JVF coefficient on jet transverse momentum. Both effects are discussed now.

The jet suppression power of JVF filter depends on the specific order of jet in the event. Table 9.9 shows the differences between relative numbers of events containing at least the given number of jets for data sets where the JVF filter was ON and OFF (two columns for both rapidity intervals). These differences rise with the number of jets required. It is given by the fact that rejected n^{th} jet by the JVF filter can be replaced by the softer jet in the event which satisfies the JVF filter condition. Thus the number

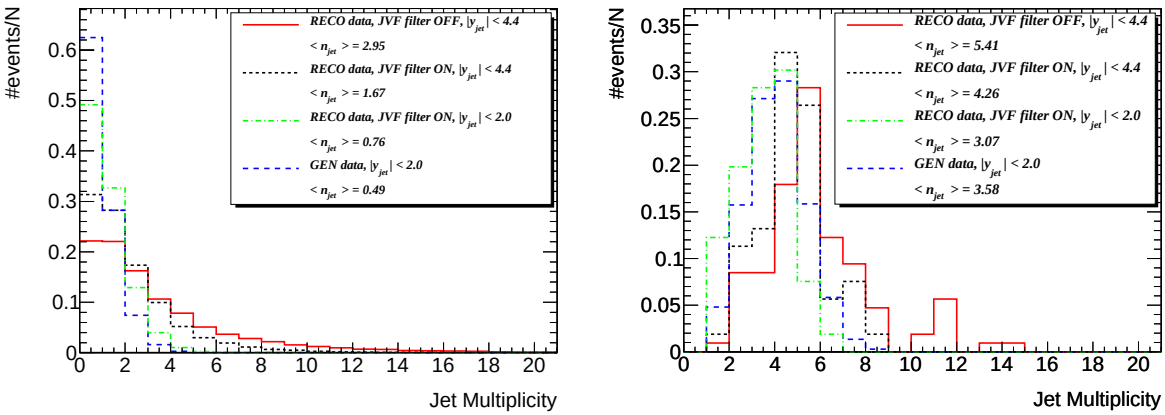

Figure 9.15: Jet multiplicity distributions for DPS WW (left) and SPS $t\bar{t}$ (right) processes. Distributions for the *RECO* data are compared to distribution obtained for the *GEN* data. All distributions are normalized to unity.

of $t\bar{t}$ events, which generally contain much more jets than the signal DPS events, exhibit much weaker dependence on the JVF filter for the given number of jets in the event. Figure 9.15 shows jet multiplicity distributions for signal and $t\bar{t}$ background process. One can see the gradual effect of JVF filter application on jets with $|y| < 4.4$ and of the rapidity range restriction from $|y| < 4.4$ to $|y| < 2.0$. The former condition decreased the average jet multiplicity by about 60%, from 2.95 to 1.67, for signal events and by about 20%, from 5.41 to 4.26, for $t\bar{t}$ events. The rapidity restriction rejects another sizable amount of jets from the event. The average jet multiplicity decreased to 0.76 for signal process and to 3.07 for $t\bar{t}$ background process. A very important fact is that $t\bar{t}$ events still contain at least one jet.

Comparison of average jet multiplicities for the *RECO* data after JVF filter and for the *GEN* data shows an opposite behavior for signal and for $t\bar{t}$ background processes. The average multiplicity for signal process is larger for the *RECO* data than for the *GEN* data. It can be explained mostly by additional contribution to jets from pile-up interactions. However, the average multiplicity for $t\bar{t}$ process is smaller for the *RECO* data than for the *GEN* data. The explanation consists in the different kinematics and also origin of the jets in the $t\bar{t}$ events. Pile-up hadron activity reshuffles the jet clustering in the way that the statistically harder would-be jets from hard interaction are much more affected than the softer would-be jets coming just from underlaying event. Therefore the final jets in $t\bar{t}$ events in the *RECO* data are softer and their p_T does not exceed 20 GeV in most cases.

The dependence of the suppression power of the JVF filter on the jet transverse momentum is investigated in two manners: JVF as a function of the jet transverse momentum and JVF as a function of the order of the jet in the event. Both questions are closely related but both dependencies have to be checked in order to test the consistency of the further conclusions. Figure 9.16 shows distributions of number of jets in the event with respect to its JVF value. If the JVF > 0.75, the distribution corresponds to the jets surviving JVF filter. One can see, that the fraction of jets surviving JVF filter

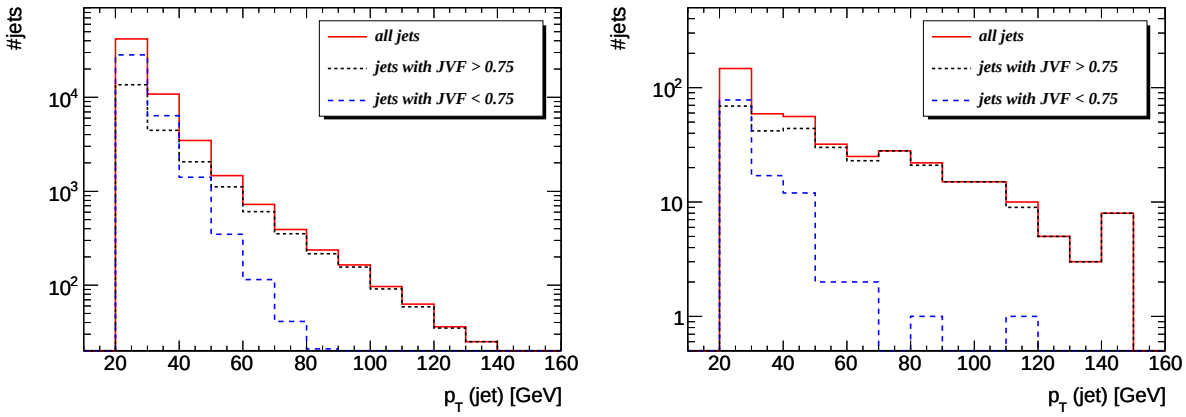

Figure 9.16: Jet transverse momentum distributions for three jet selections. Comparison between DPS WW (left) and SPS $t\bar{t}$ processes is shown. Jets with $|y| < 2.0$ are considered.

increases with the increasing jet transverse momentum. This fraction is even larger for $t\bar{t}$ events.

This property of the JVF filter propagates to its dependence on the order of the jet in the event. Even though one can find an event with the hardest jet softer than the third hardest jet in another event, the hardest jets are statistically more probable to pass the JVF filter. Figure 9.17 shows distributions of JVF values for four hardest jets separately.

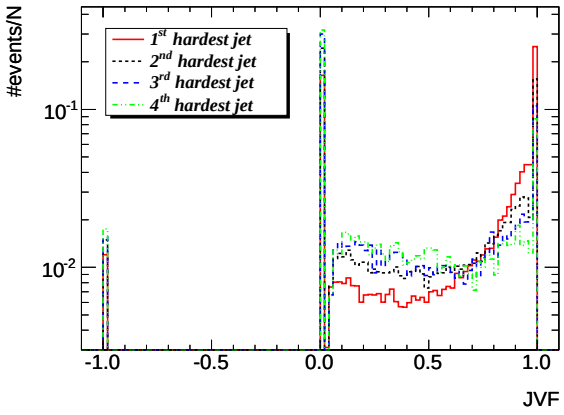

Figure 9.17: Normalized JVF distributions for four hardest jets in DPS WW events. One can see that relative fraction of jets satisfying JVF filter statistically increases with the mean value of the jet transverse momentum. Jets with $|y| < 2.0$ are considered.

Results of this investigation is summarized in Table 9.9, where relative number of events are evaluated in percentage for given selections with respect to the total number of events in the *Lepton Selection* sub-sample. Also the mean values of the given nth jet transverse momentum is given.

A general conclusion is that pile-up contribution can be filtered off by applying JVF

	RECO data					*GEN* data
Anti-k$_t$	R = 0.6				R = 0.4	R = 0.6
Events [%]	$\|y\| < 4.4$ JVF OFF	$\|y\| < 4.4$ JVF ON	$\|y\| < 2.0$ JVF OFF	$\|y\| < 2.0$ JVF ON	$\|y\| < 2.0$ JVF ON	$\|y\| < 2.0$
DPS: 2 x pp $\rightarrow$ WW						
1 jet	77.8	68.7	70.8	50.9	32.2	37.5
$< p_T >$ [GeV]	37.6	37.2	26.3	37.0	38.0	37.6
2 jets	55.8	40.5	45.1	18.2	6.9	9.3
$< p_T >$ [GeV]	28.9	28.1	27.9	27.6	28.8	28.6
3 jets	39.6	23.1	28.9	5.3	1.2	1.9
$< p_T >$ [GeV]	26.4	25.4	25.6	24.8	25.8	25.4
4 jets	28.9	13.2	18.6	1.3	0.2	0.3
$< p_T >$ [GeV]	25.3	24.4	24.6	23.0	24.1	23.5
SPS: pp $\rightarrow t\bar{t}$						
1 jet	100.0	100.0	100.0	100.0	98.1	99.3
$< p_T >$ [GeV]	100.7	100.0	97.6	96.9	90.2	98.8
2 jets	99.1	98.1	89.6	87.7	84.0	94.6
$< p_T >$ [GeV]	70.2	68.5	67.6	66.1	60.0	66.1
3 jets	90.6	86.8	81.1	67.9	58.5	78.9
$< p_T >$ [GeV]	44.2	42.0	40.8	40.0	37.6	46.4
4 jets	82.1	73.6	66.0	39.6	33.0	52.0
$< p_T >$ [GeV]	32.5	31.9	30.0	32.0	30.7	35.5

Table 9.9: Relative number of events containing at least the given number of jets with respect to the all events. Event selections differ in the rapidity range for jets and in the application of the JVF filter. Comparison between results obtained using two values for jet radius, 0.4 and 0.6, is also shown. The last column corresponds to the similar event selection for the *GEN* data.

filter more effectively for softer jets, represented here by an order of jet in the event. This behavior is favorable with respect to the fact that signal events contain mostly softer jets while the harder jets are present mostly in $t\bar{t}$ events. For instance, the relative fraction of the signal *RECO* events containing at least 4 jets decreased from 29% to 1.3%, which is comparable to value of 0.3% obtained for the *GEN* events. The appropriate fraction for the *RECO* $t\bar{t}$ events dropped also by about 30% but the remaining fraction of 4 jet events in the whole sample is still about 52%.

Table 9.9 also contains results for jets formed using anti-k$_T$ algorithm with R = 0.4. The comparison should demonstrate that the more narrow jets are considered the smaller is the difference between jets from signal and $t\bar{t}$ background events. The desired selection favors jets from signal events to be as soft as possible while jets from QCD background are supposed to be as hard as possible. Therefore, the jet radius R = 0.6 is chosen as the more suitable option than the R = 0.4, which produce jets with the opposite properties.

The efficiency of the JVF filter is calculated from the ratio of number of jets surviving

JVF condition and the number of all jets in the given rapidity region. The ratio is then subtracted from the unity in order to express the fraction of jets filtered off the sample. The JVF filter efficiency for both processes in two rapidity regions is:

- $|y| < 4.4$:

$$\epsilon_{JVF}^{WW} = 1 - \frac{50054}{88567} = 43.5\%, \qquad \epsilon_{JVF}^{t\bar{t}} = 1 - \frac{452}{573} = 21.1\% \tag{9.14}$$

- $|y| < 2.0$:

$$\epsilon_{JVF}^{WW} = 1 - \frac{22828}{59485} = 61.6\%, \qquad \epsilon_{JVF}^{t\bar{t}} = 1 - \frac{325}{439} = 26.0\% \tag{9.15}$$

One should note, that this efficiency is analysis dependent, since we study effect of JVF filter on pre-selected events, which are of our interest, and not overall jet measurement.

Eventually, jet transverse momentum distributions are studied in order to find such cut selections which would maximally suppress the $t\bar{t}$ contribution and leave the signal as much as possible. Figure 9.18 shows the normalized transverse distributions for all four studied jets. These jets are ordered according to their transverse momenta in the descending order: the first leading jet (j1), the second leading jet (j2), the third leading jet (j3) and the fourth leading jet (j4).

In all four cases, SPS WZ and ZZ exhibit almost the same shapes of the distributions and are very similar to the given signal DPS WW distribution. Though, one can see that the lowest bin has always maximum for the signal process and that the difference turns vise versa for the higher bins. Therefore the appropriate cuts may emphasize signal against these backgrounds as well as against the WWjj and $t\bar{t}$ processes, where the differences are obvious. The cuts for the further event selection were chosen mostly according to the relative event fractions for signal and $t\bar{t}$ background and with a certain respect to the other backgrounds.

Specifically, the number of signal events with at least four jets with $p_T > 20$ GeV was found almost negligible and therefore veto on such events was adopted. Events containing a third hardest jet create approximately 5% of the signal sample and cannot be completely filtered off. The maximal value of the third jet transverse momentum is allowed to be 25 GeV. This value corresponds to the point, where signal relative fraction meets the $t\bar{t}$ event fraction and also begun to be below the SPS WZ and ZZ fractions. The same criteria was set upon the second hardest jet transverse momenta which leads to the maximal p_T threshold of 30 GeV. A little less strict cut was placed on the leading jet transverse momentum since the QCD background suppression is already substantial and because the pile-up effect can be expected even stronger in the future measurement. As shown, the JVF filter has the most significant effect on the higher jet multiplicities while the fraction of the events with one jet remains to be a very important component of the signal events. All the considerations lead to the maximal p_T threshold of 50 GeV. Note that also cut on 40 GeV was studied and the resulting selection was found to suppress another 30% of the remaining $t\bar{t}$ events but for the price of the 5% losses of the signal events, which is not acceptable.

Above described jet selection can be summarized as:

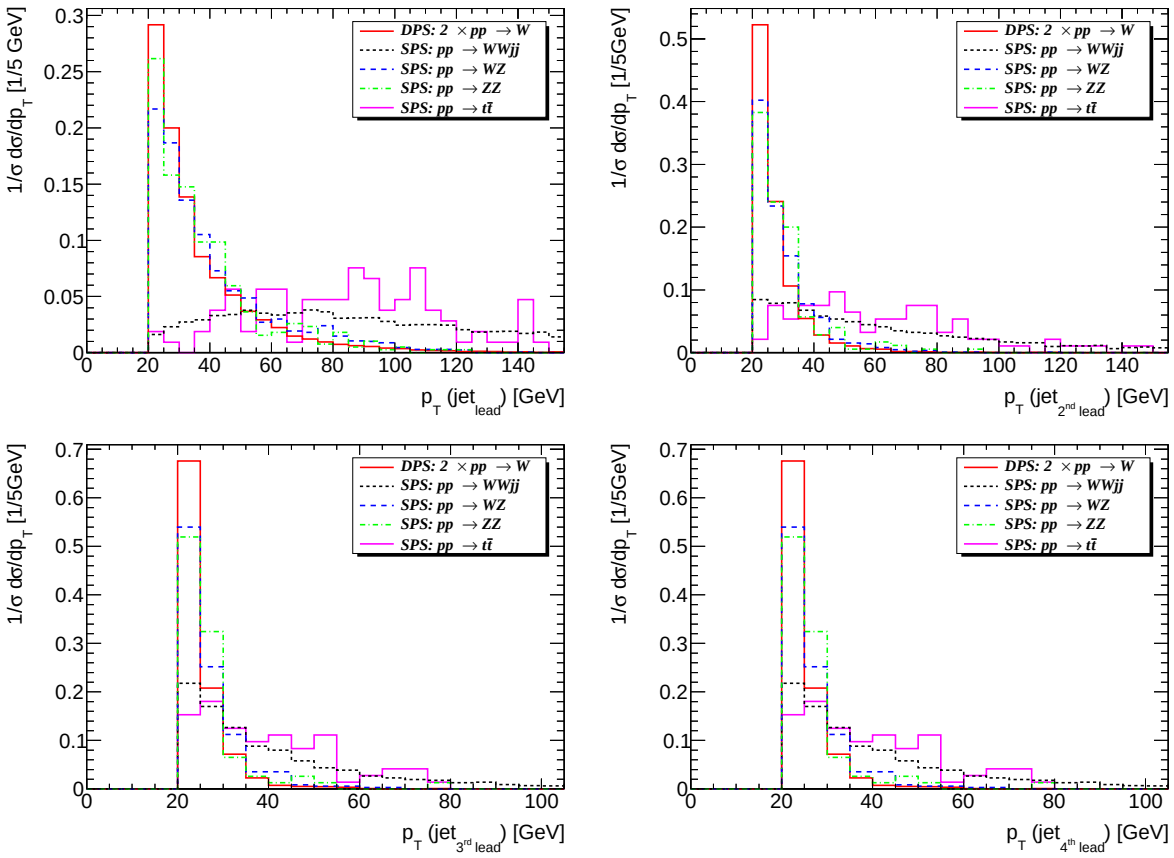

Figure 9.18: Transverse momentum distributions for four hardest jets in event. Distributions are normalized to unity. Jets with $|y| < 2.0$ and JVF > 0.75 are considered.

$$|y| < 2.0 \qquad \text{JVF} > 0.75 \qquad p_T^{j1} < 50 \text{ GeV}$$
$$p_T^{j2} < 30 \text{ GeV} \qquad p_T^{j3} < 25 \text{ GeV} \qquad p_T^{j4} < 20 \text{ GeV}$$

σ [fb]	DPS signal	SPS background			
	W^+W^+	W^+W^+jj	W^+Z	ZZ	$t\bar{t}$
Lepton Selection	0.83 (100%)	0.45 (100%)	4.67 (100%)	0.45 (100%)	5.01 (100%)
$p_T^{j4} < 20$ GeV	0.82 (99%)	0.32 (71%)	4.43 (95%)	0.43 (96%)	3.02 (60%)
$p_T^{j3} < 25$ GeV	0.81 (98%)	0.25 (55%)	4.33 (93%)	0.42 (93%)	2.08 (42%)
$p_T^{j2} < 30$ GeV	0.79 (95%)	0.13 (29%)	4.06 (87%)	0.39 (87%)	0.95 (19%)
$p_T^{j1} < 50$ GeV	0.74 (89%)	0.06 (13%)	3.74 (80%)	0.37 (82%)	0.33 (7%)
no jet veto	0.41 (49%)	0.01 (3%)	1.87 (40%)	0.18 (40%)	0.00 (0%)

Table 9.10: Jet cut flow table summarizing the influence of the individual cuts on the jet transverse momenta in an ascending order from the 4^{th} leading jet to the 1^{th} leading jet. Every cut contains also the above cuts too. The last line offers an ultimate jet veto on all events containing at least one jet with $p_T > 20$ GeV.

For completeness, note that the jet selection deals with the anti-k_T jets with radius-like

parameter R = 0.6 and that only jets with $p_T > 20$ GeV are considered.

The cuts on the transverse momenta of the appropriate jets are applied on the studied data sample one by one in order to follow the gradual impact of the individual cuts, see Table 9.10. One can observe that signal suppression increases in the relative manner from 1% for the j4 cut to 6% for the j1 cut. The very opposite behavior can be seen for the $t\bar{t}$ events, where the suppression is biggest for the j4 cut (40%) and smallest for j1 cut (12%). The overall fraction of the remaining signal events is 89%. The corresponding fractions of the remaining background events are 13% for SPS WWjj, 80% for SPS WZ, 82% for SPS ZZ and 7% for the $t\bar{t}$ productions.

Moreover, one extra selection is shown in Table 9.10 in order to demonstrate a complete (or at least maximal) suppression of the QCD heavy flavor production background. In this selection, labeled as no jet veto, every event containing at least one anti-k_t jet with R = 0.6 and with transverse momentum above 20 GeV is rejected. Unfortunately, the signal suppression would be also huge would lead to the signal sample with the half of event population.

9.5 Final selection

This section summarizes the results of the previous lepton and jet analyses, whose contain the detailed discussions about the application of several detector-related conditions. The list of technical requirements, like muon reconstruction quality, muon isolation or the relation of the jet to the primary vertex, is not repeated but is part of the selection. The main attention is paid to the restrictions on kinematic characteristics of the accepted muons and jets, which are put together in Table 9.11 and labeled as *Final Selection*.

$\lvert\eta(\mu)\rvert$	$<$	2.4	p_T(OS μ_{lead})	$<$	5 GeV
$p_T(\mu_{lead})$	$>$	20	$p_T(\mu_{lead})$	$<$	60 GeV
$p_T(\mu_{trail})$	$>$	12	$p_T(\mu_{trail})$	$<$	45 GeV
$M(\mu_{lead}\mu_{trail})$	$>$	10 GeV	$M_T(\mu_{lead}\mu_{trail})$	$>$	40 GeV
$\lvert y(j)\rvert$	$<$	2.0	JVF(j)	$>$	0.75
p_T^{j1}	$<$	50 GeV	p_T^{j2}	$<$	30 GeV
p_T^{j3}	$<$	25 GeV	p_T^{j4}	$<$	20 GeV

Table 9.11: *Final Selection* cuts.

This kinematic selection is considered to be the very final set of cuts suitable for the double parton scattering search in the same-sign di-muon final state. Four stacked histograms are shown in order to demonstrate the contribution of the signal process to the appropriate differential cross section. These histograms represent transverse momentum distribution for the leading and trailing muon in the event, see Fig. 9.19, and invariant or transverse mass distributions of the same-sign muon pair, see Fig. 9.20.

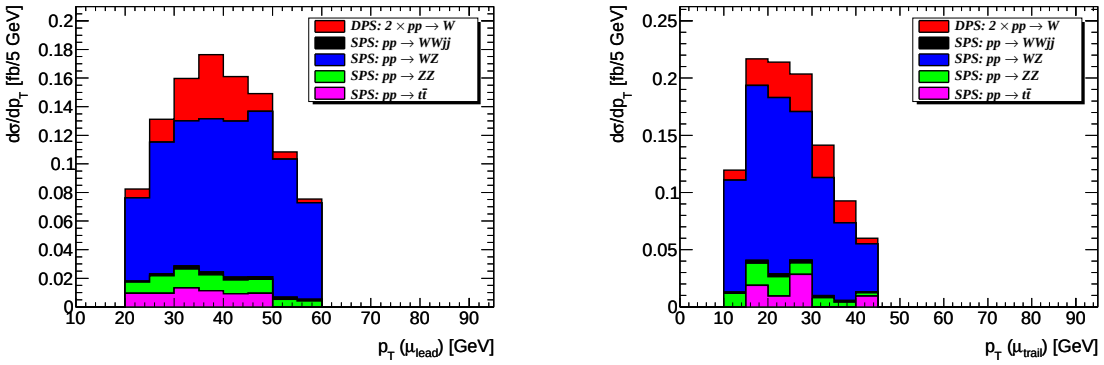

Figure 9.19: Differential cross section as a function of transverse momentum of leading (left) and trailing (right) muon for the *Final Selection* data sample.

Predicted cross section obtained from the LO calculations using Herwig++ and MadGraph programs are summarized in Table 9.12. Cross sections are identical to those from the final jet cut selection. Only the additional information about the signal fraction within the total sample, S/(S+B), and the ratio $S/\sqrt{B}$ is given. A conclusion can be drawn that the suggested *Final Selection* provides the data sample, where 14.1% of events are created by the double parton scattering contribution. Moreover, Figure

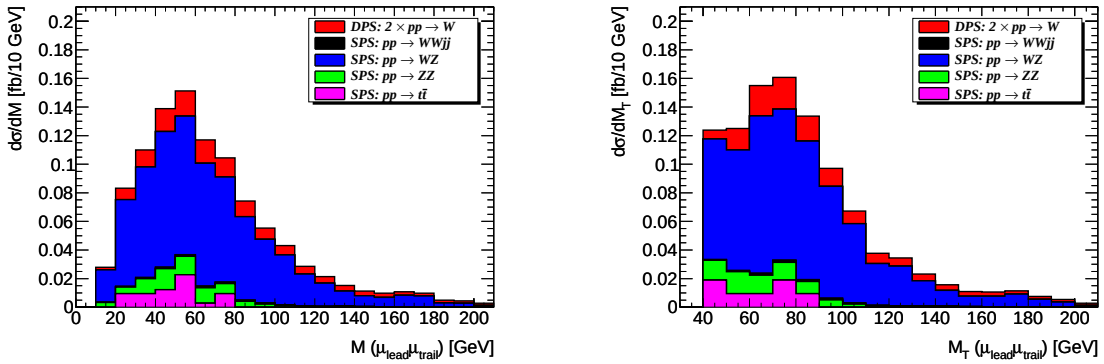

Figure 9.20: Differential cross section as a function of invariant mass (left) and transverse mass (right) of the same-sign muon pair for the *Final Selection* data sample.

9.21 shows the dependence of the DPS signal significance as a function of the amount of data recorded by an experiment in units of integrated luminosity. Numbers show that the LHC would have to deliver an integrated luminosity of 205.4 fb^{-1} to reach the 5σ significance of the DPS signal over the background. The level of integrated luminosity of $\mathcal{O}(100\ fb^{-1})$ recorded can be reached by the LHC experiments approximately withinfour months of non-stop running with full designed luminosity $\mathcal{L} = 10^{34}\ cm^{-2}s^{-1}$. Even with respect to the NLO K-factors and other signal enhancement effects not involved in the analysis, it is obvious that the DPS WW measurement will require a long-term analysis.

σ [fb]	DPS signal	SPS background					
	W^+W^+	W^+W^+jj	W^+Z	ZZ	$t\bar{t}$	S/(S+B) [%]	$S/\sqrt{B}$
Final Selection	0.74	0.06	3.74	0.37	0.33	14.1	0.349

Table 9.12: Summary of production cross sections for five processes contributing to same-sigh di-muon production. The fraction of double parton scattering signal in the *Final Selection* data sample was found to be 14.1%.

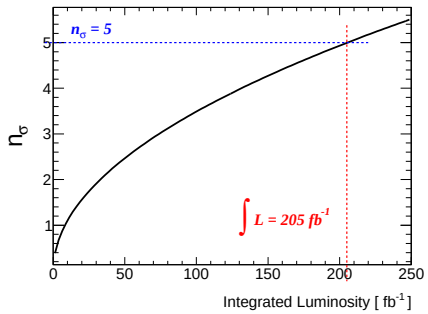

Significance	$\mathcal{L}$ [fb^{-1}]	DPS events	All events
1σ	8.2	6.1	43.0
2σ	32.9	24.3	172.4
3σ	74.0	54.8	387.8
4σ	131.5	97.3	689.1
5σ	205.4	152.0	1076.3

Figure 9.21: Signal significance expressed in units of the standard deviations as a function of the integrated luminosity of the measured data sample.

9.6 Further di-boson background suppression

This section suggests five further kinematic selections, whose purpose is to demonstrate the differences among event topologies for the individual contributions to the studied final state. As will be shown, the relative position of the two searched same-sign muons depends on their origin. Generally speaking, SPS background processes produce muons from the same parton interaction and thus the muon four-momenta should be appropriately correlated. On the other hand, multiple parton interactions in Herwig++ are modeled more-or-less as independent processes and the secondary muons should propagate in random directions with respect to each other. The connection between two hard parton interactions is set only through the total longitudinal momentum conservation requirement and through the color reconnection algorithm. Both tools should have a minimal effect on hard parton processes.

However, the real situation is much more smeared than at the parton level and the differences are not as sharp as expected. The suggested selections slightly increase the signal purity of the studied data sample but their application on signal data sub-sample reduces the event production rate by about 20 to 40%. Such a reduction of the signal cross section is kind of undesirable from the experimental point of view. At the end, selection resulting in the highest signal significance is shown more in details but the *Final Selection* remains to be the main result of this analysis.

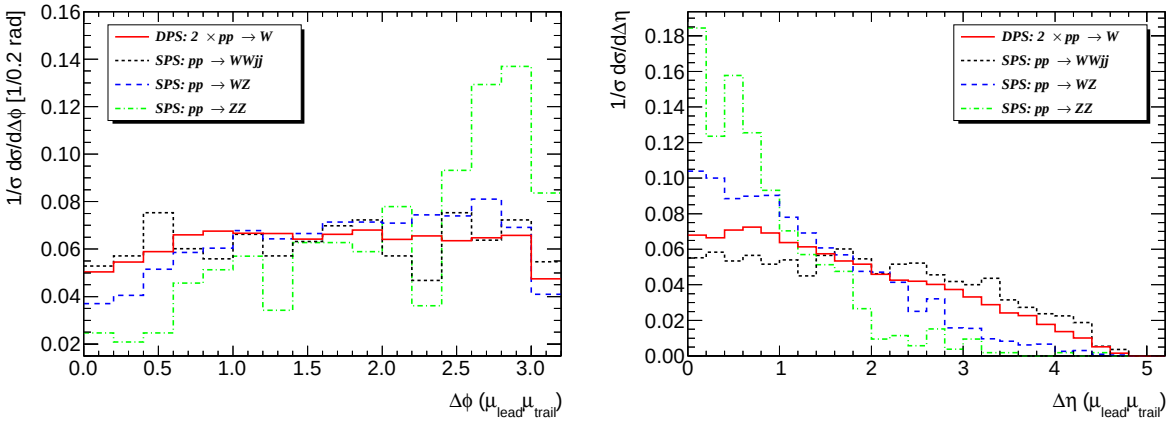

Figure 9.22: Normalized distributions of differences between muon azimuthal angles (left) and between muon pseudorapidities (right) for the *Final Selection* data sample.

A first look may be taken to the differences between the azimuthal angles and pseudorapidities of the secondary muons. First plot in Fig. 9.22 displays almost flat distribution of the difference between the azimuthal angles, $\Delta\phi$, of the studied muons for the DPS signal, while the background processes WZ and ZZ tend to slightly prefer the back-to-back topology in the ϕ-plane projection. The opposite behavior for the pseudorapidity difference distributions, $\Delta\eta$, can be seen in the second plot in Fig. 9.22. The distribution for the DPS signal drops slower than for SPS WZ and ZZ contributions when the $\Delta\eta$ value approaches the maximum threshold for the given acceptance.

One can conclude that the scale of the processes plays its statistical role. Whereas

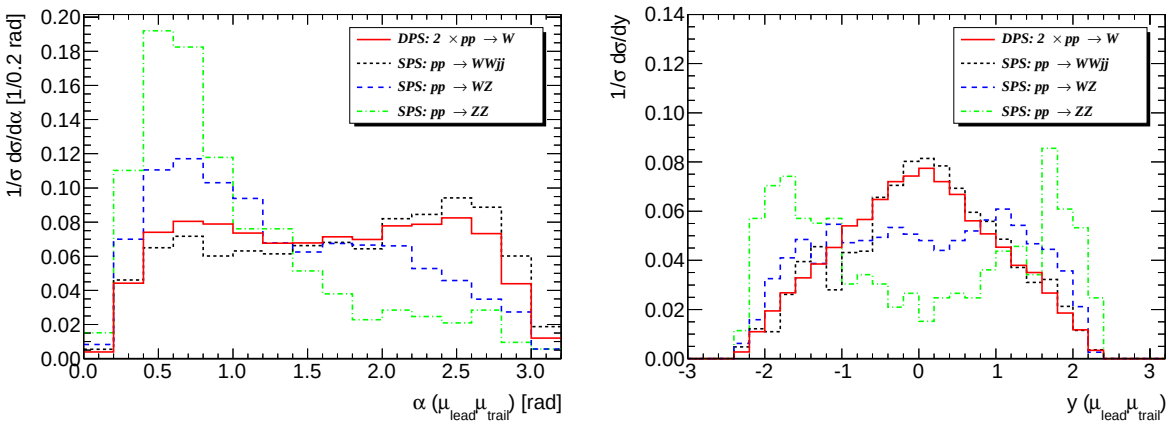

Figure 9.23: Normalized distributions of direct angle between the two muons (left) and of muon pair rapidity (right) for the *Final Selection* data sample.

both SPS WWjj distributions are even more flat than distributions for DPS WW process, distributions for SPS WZ and ZZ processes tend to prefer more correlated dependence. Thanks to the full matrix element taken for the γ^*/Z boson production, distributions for ZZ production creates sharper peaks at low $\Delta\eta$ and high $\Delta\phi$ values than distributions for WZ process.

The combined information from both projections can be seen in Fig. 9.23. Left plot demonstrates the relative angle between the muon tracks. Again, the uncorrelated DPS is confirmed while especially the SPS WZ and ZZ processes tend to produce much more collinear muons. SPS WWjj process is not here as flat as in Fig. 9.22 and tend to slightly prefer larger angles between secondary muons.

Figure 9.23 shows the distributions of the muon pair rapidity, where on can see an interesting relative abundance of signal events over the SPS WZ and ZZ events around the zero rapidity.

All distributions in Figures 9.22 and 9.23 are normalized to unity in order to simplify the comparison of the fractional contributions from individual processes.

Except for the direct angle between the secondary muons, one can also look at relative position of the two muons in the 3D look at their pseudorapidities. Whilst the individual pseudorapidity distributions for both leading and trailing muon do not indicate any specific differences, see Fig. 9.24, the combined two-dimensional distributions in Fig. 9.25 demonstrate the searched correlations well. One can see that 2D distributions for SPS WZ and even more for ZZ processes are maximal for the two muons having the similar pseudorapidities. On the contrary, distributions for DPS WW and SPS WWjj processes are almost flat, with respect on the lack of muons in the very central region of η, or maybe even prefer the arrangement, where the two muons have opposite sign of their pseudorapidities.

Considering that the pseudorapidity signs divide the ATLAS detector into two hemispheres, the multiplication of the pseudorapidities of the two muons with each other, $\eta_{\mu_{lead}} \cdot \eta_{\mu_{trail}}$, provides an information about their relative spatial orientations in terms of the detector hemispheres. It was suggested in [48] to investigated this feature for dif-

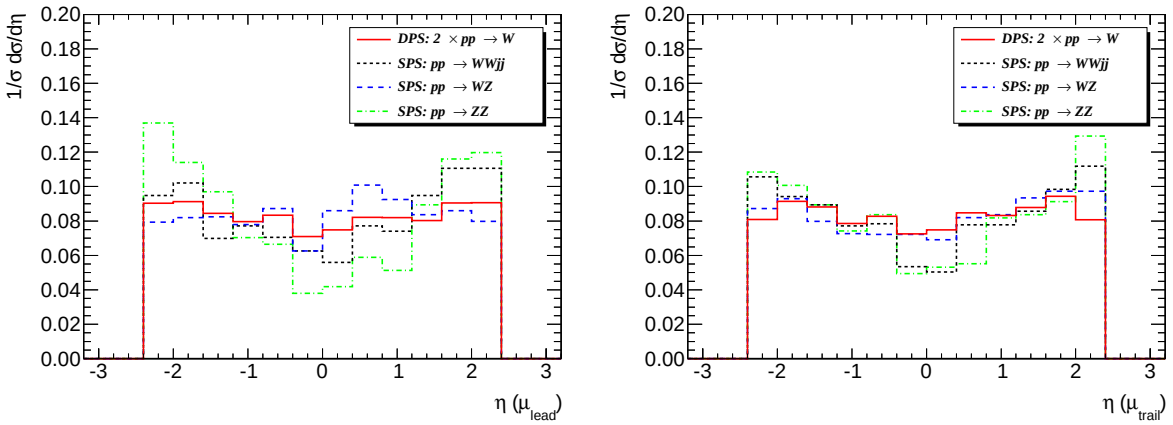

Figure 9.24: Normalized distributions of pseudorapidities for individual searched muons. Shapes of all distributions are very similar, except the one for leading lepton pseudorapidity for SPS ZZ production.

ferent η ranges in order to see the gradual increase of the asymmetry between same- and opposite-hemisphere orientation of the muon pair. Such a pseudorapidity asymmetry can be defined as

$$\eta_{Asym} = \frac{\sigma(\eta_{\mu_{lead}} \cdot \eta_{\mu_{trail}} < 0) - \sigma(\eta_{\mu_{lead}} \cdot \eta_{\mu_{trail}} > 0)}{\sigma(\eta_{\mu_{lead}} \cdot \eta_{\mu_{trail}} < 0) + \sigma(\eta_{\mu_{lead}} \cdot \eta_{\mu_{trail}} > 0)}. \tag{9.16}$$

This variable quantifies the difference between numbers of events with muons going into the opposite η hemispheres and events with muons going into the same hemispheres. The asymmetry is positive for data sub-samples where the muon pseudorapidities have mostly the opposite signs and vice-versa. The left top plot in Fig. 9.26 shows the η_{Asym} values for the individual data sub-samples in five bins according to the minimal absolute value of the pseudorapidity η_{min} required for both the μ_{lead} and μ_{trail}. The bin for η_{min} = 0.0 corresponds to the entire considered detector acceptance. The $\eta_\mu \cdot \eta_\mu$ distribution for the entire η acceptance is shown in the right top plot in Fig. 9.26. Higher values of η_{min} gradually cut off the central regions of the detector in order to increase the difference among the data sub-samples. The appropriate $\eta_\mu \cdot \eta_\mu$ distributions are shown in the remaining plots in Fig. 9.26. One can conclude that the more forward muons are, the more significant differences in η_{Asym} values for the investigated processes can be observed.

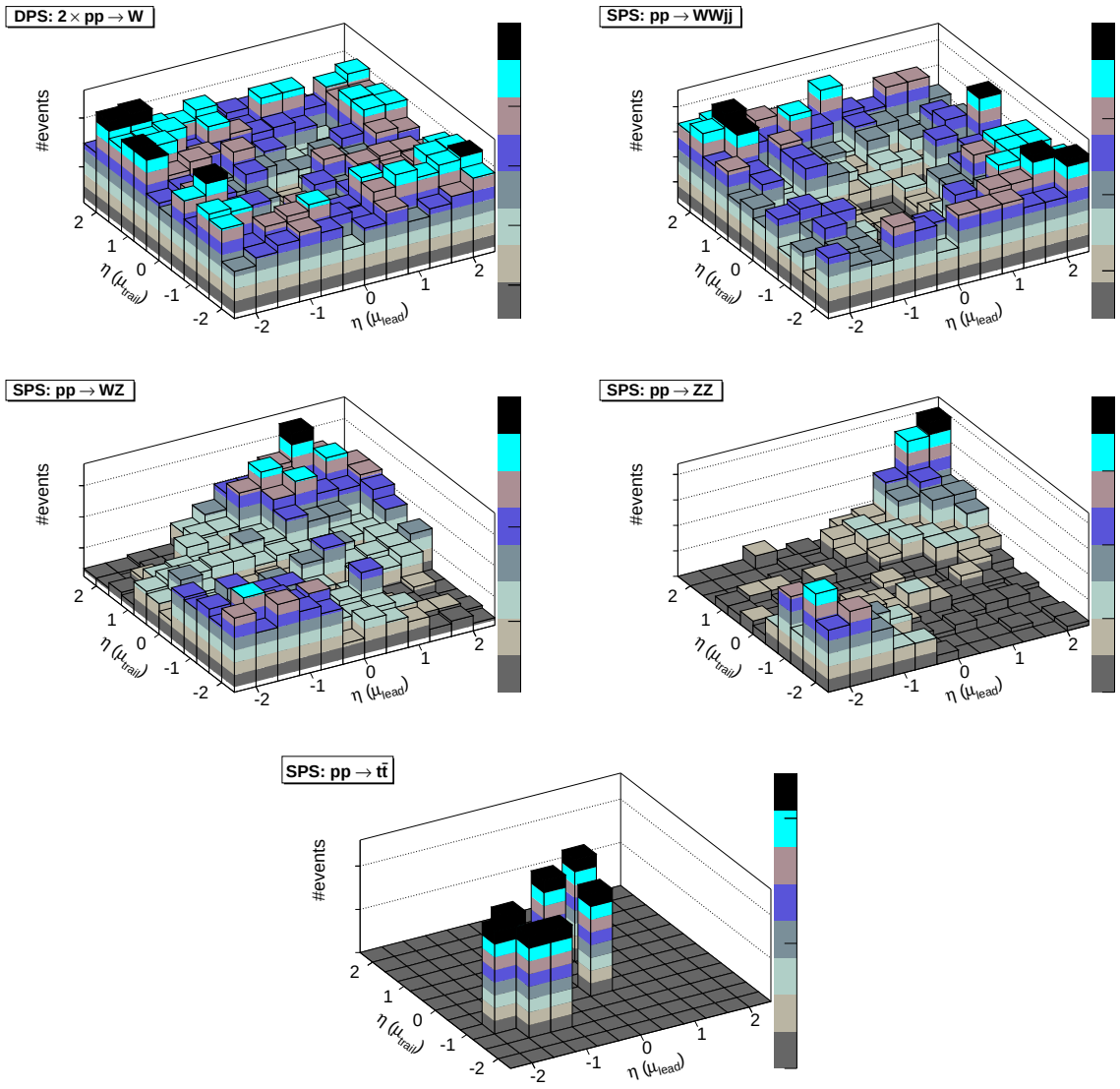

Figure 9.25: Two-dimensional distributions of pseudorapidities for both leading and trailing muons. Except the lack of events in the central region for all processes, significant differences can be seen. Distributions for DPS WW and SPS WWjj processes are more-or-less flat or tend slightly to prefer the opposite signs of muon pseudorapidities. On the contrary, distributions for SPS WZ and ZZ processes peak for the same pseudorapidity signs of both muons. SPS $t\bar{t}$ events were suppressed so effectively that only 7 events remained and no special behavior can be observed.

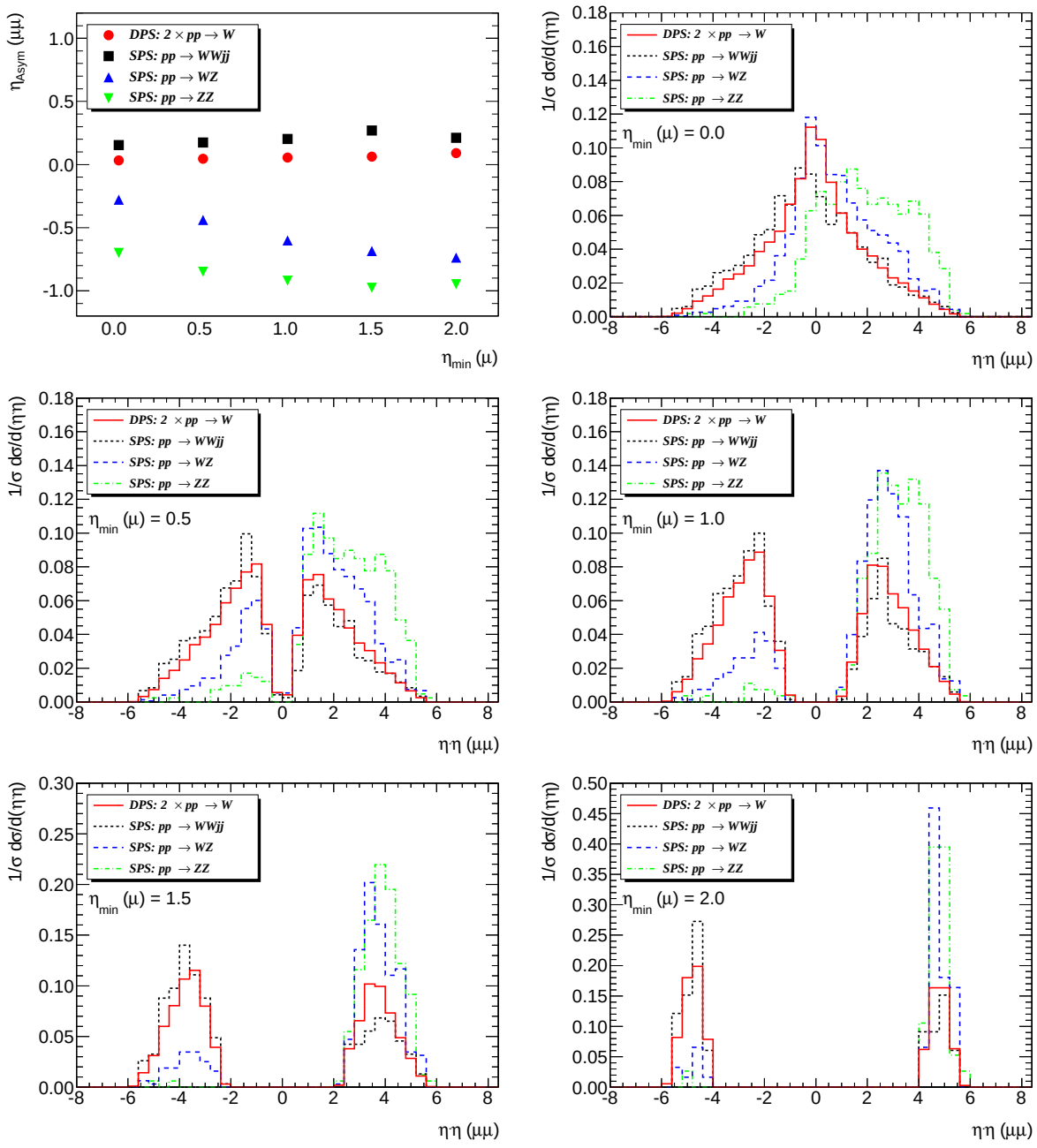

Figure 9.26: Pseudorapidity asymmetry η_{Asym} as a function of the minimal muon pseudorapidity required. $\eta_{min} = 0.0$ means that the whole ATLAS acceptance is taken. The larger η_{min} is used the bigger central part of the detector is excluded. One can see that the more forward region of the detector is taken the larger asymmetry can be observed. The multiplication of the two pseudorapidities in the remaining plots demonstrate how many events have both muons in the same (positive multiplication) or in the opposite (negative multiplication) detector hemispheres.

On top of the *Final Selection*, few more cuts are studied in order to reach the highest signal purity of the total data sample. The influence of the muon transverse momentum and pseudorapidity cuts on the final cross sections was found to be more-or-less independent on each other. Both variables can be further restricted in order to increase the fraction of the signal events in the final data sample. First, one can see from Fig. 9.19 that transverse momentum distributions for both leading and trailing muons form sharper peaks for the DPS signal process than for the most serious background, the SPS WZ production, and that the narrowing of both p_T windows leads to the enhancement of the signal fraction in the resulting data sample. Second, the connected restrictions on pseudorapidities of the leading and trailing muons provide further increase of the signal fraction in the final data sample. Such a selection filters off events containing muons with certain minimal pseudorapidity and which are located in the same detector hemisphere.

Both above discussed groups of cuts are classified as:

- Selection A: Events satisfying

$$(25 < p_T\ (\mu_{lead}) < 50)\ \text{GeV}, \qquad (15 < p_T\ (\mu_{trail}) < 40)\ \text{GeV}. \tag{9.17}$$

  pass the selection.

- Selection B: Events complying with

$$\eta(\mu_{lead}) \cdot \eta(\mu_{trail}) > 0 \quad \& \quad \eta\ (\mu) > 1.0 \tag{9.18}$$

  are rejected from the sample.

- Selection C: Events fulfilling

$$\eta(\mu_{lead}) \cdot \eta(\mu_{trail}) > 0 \quad \& \quad \eta\ (\mu) > 0.5 \tag{9.19}$$

  are rejected from the sample.

σ [fb]	DPS signal	SPS background			
	W^+W^+	W^+W^+jj	W^+Z	ZZ	$t\bar{t}$
Final Selection	0.74 (100%)	0.06 (100%)	3.74 (100%)	0.37 (100%)	0.33 (100%)
Selection A	0.61 (82%)	0.04 (67%)	2.14 (57%)	0.23 (62%)	0.24 (73%)
Selection B	0.61 (82%)	0.05 (83%)	2.68 (72%)	0.18 (49%)	0.19 (58%)
Selection C	0.51 (69%)	0.04 (67%)	1.99 (53%)	0.10 (27%)	0.09 (27%)
Selection A+B	0.51 (69%)	0.03 (50%)	1.56 (42%)	0.11 (30%)	0.09 (27%)
Selection A+C	0.42 (57%)	0.03 (50%)	1.16 (31%)	0.06 (16%)	0.09 (27%)

Table 9.13: Summary of cross sections for further possible kinematic selections causing a significant signal reduction (18 - 43% with respect to the *Final Selection*).

Results for individual selections A, B and, C are given in Table 9.13 same as for their combination A+B and A+C. Selections are characterized by the cross sections

and by the appropriate fractions of events survived the given selection in comparison to the *Final Selection* data sample. One should note that the fraction of survived signal events is truly very low, approximately between 80 and 60 per cent.

The fractions of signal events in comparison to the sum of all events (signal plus all background) and the corresponding $S/\sqrt{B}$ ratio are summarized in Table 9.14. One can see, that the selections are ordered by their power to suppress all the background processes and that the fraction of DPS events within the total data sample increases from 14.1% to 23.9%. However, the signal fraction is not only one parameter that determines the convenience of the given selection. For such a rare process, one should bare in mind that the signal significance and the available statistics plays an important role. Table 9.14 clearly demonstrates that the $S/\sqrt{B}$ ratio does not follow the increasing signal fraction and that the most suitable selection in that manner is the A+B combination.

Selection	*Final*	A	B	C	A+B	A+C
S/(S+B) [%]	14.1	15.8	16.4	18.7	22.2	23.9
$S/\sqrt{B}$	0.349	0.338	0.346	0.342	0.381	0.363

Table 9.14: Summary of signal fractions for individual further possible selections together with the $S/\sqrt{B}$ ratios.

Figure 9.27 shows the event numbers and the integrated luminosity necessary for the given significances for the Selection A+B. Even though the signal cross section for this selection decreased by 42% in comparison to the *Final Selection*, the luminosity corresponding to the 5 standard deviations decreased slightly, see Fig. 9.21.

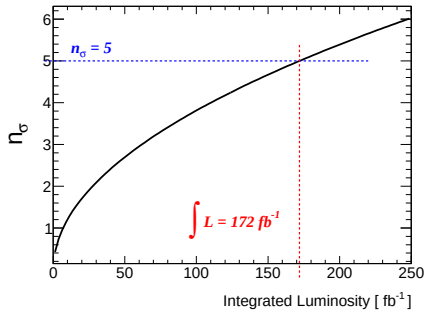

Significance	$\mathcal{L}$ [fb^{-1}]	DPS events	All events
1σ	6.9	3.5	15.9
2σ	27.6	14.1	63.5
3σ	62.0	31.6	142.6
4σ	110.2	56.2	253.5
5σ	172.2	87.8	396.1

Figure 9.27: Signal significance for selection A+B expressed in units of the standard deviations in dependence on the integrated luminosity of the measured data sample.

In summary for this section, one can conclude that the observed differences in the event topologies for the studied processes can be used to further suppress the physics background and thus the signal significance can be increased. Specifically, the selection A+B was found to correspond to the lowest estimated integrated luminosity of 172.2 fb^{-1} necessary for the 5σ signal significance. However, the fraction of the physics background events in the sample is still very high. It is very difficult to find a set of cuts which would mitigate further contribution from background processes. The common strategy is thus to make the analysis as simple as possible. The more kinematical cuts are required in

the analysis the higher is the uncertainty that may stem from the comparison between Monte Carlo and real data. Moreover, this analysis aims mostly to the DPS searching measurement, where the higher event statistics is preferred. For these reasons, the *Final Selection* is kept to be the most suitable definition of the fiducial region for the measurement of the DPS contribution.

9.7 Cross section measurement

Since the uncertainty on the absolute value of the production cross sections evaluation at leading order is high, see Sec. 9.1, the future measurement cannot rely on it. The method of the DPS cross section evaluation in the signal dominance phase space region defined by the *Final Selection* (FS), see Table 9.11, is proposed in the following. The basis idea is that one has to evaluate the cross sections of all background processes and then subtract it from the total same-sign di-muon production cross section measured from data. In other words, one should search for the abundance of desired events with respect to the expected single parton scattering production rate. Mathematically, it can be expressed as

$$\sigma_{FS}^{real}(DPS) = \sigma_{FS}^{real}(\mu^+\mu^+) - \sigma_{FS}^{real}(WWjj) - \sigma_{FS}^{real}(WZ) - \sigma_{FS}^{real}(ZZ) - \sigma_{FS}^{real}(t\bar{t}), \quad (9.20)$$

where the subscript *FS* refers to the kinematic region defined by the *Final Selection* and the superscript *real* signs that the cross sections correspond to the real measurement. The type of the process is marked in the brackets, where $(\mu^+\mu^+)$ stands for all possible processes producing this same-sign di-muon final state.

The procedure suggests to rescale the calculated background production cross sections σ_{FS}^{MC} separately for all background processes using rescaling factors (RF) in order to obtain the real values:

$$\sigma_{FS}^{real} = \sigma_{FS}^{MC} \times RF. \quad (9.21)$$

One of the main assumptions for this method is a declaration that these rescaling factors are still the same for the given process in every kinematic region. In other words, there is always RF-times more (or less) real events than predicted by Monte Carlo generation in every phase space selection. This assumption is supported by the Monte Carlo prediction of the obtained distributions of the studied differential cross sections which should model the real situation reasonably well, since the shower and hadronization models are (or will be) tuned for the given energies of the collisions. Thus, the kinematics found is predicted to be very close to the future measurements at the ATLAS detector.

The second assumption is based on the fact that it is not possible to distinguish final states coming from the WWjj process or from the $t\bar{t}$ production. Both processes are characterized by the presence of at least two hard jets and almost no opposite-sign muons additional to the desired same-sign muon pair in the final state. Thus, one cannot define such a control region, where one of these background processes would be suppressed, and one has to declare the rescaling factors for WWjj and $t\bar{t}$ processes to be equal. Let's denote them as

$$RF^{WWjj} = RF^{t\bar{t}} = RF^{\mu^+\mu^+jj}. \quad (9.22)$$

This simplification is also motivated by the low statistics of $t\bar{t}$ events at disposal. Therefore, the systematical uncertainty introduced here is within the statistical uncertainty for $t\bar{t}$ cross section evaluation.

At the end, there are only three unknown rescaling factors RF^{WZ}, RF^{ZZ} and $RF^{\mu^+\mu^+jj}$ requiring three control phase space regions (C_1 to C_3). These regions differ

from the *Final Selection* in order to emphasize always a different background process. Mathematically spoking, one has three unknown variables and three linear equations, which have an unambiguous solution. Each equation can be written as

$$\sigma_{C_i}^{real}(\mu^+\mu^+) = \sigma_{C_i}^{MC}(WZ) \times RF^{WZ} + \sigma_{C_i}^{MC}(ZZ) \times RF^{ZZ} + \\ + \left(\sigma_{C_i}^{MC}(WWjj) + \sigma_{C_i}^{MC}(t\bar{t})\right) \times RF^{\mu^+\mu^+jj} \quad (9.23)$$

for the control selection C_i. The individual cross sections at the Monte Carlo level are summarized in Table 9.15. The contribution from the signal process was neglected for every selection.

$\sigma_{C_i}^{MC}$ [fb]	DPS signal	SPS background			
	W^+W^+	W^+W^+jj	W^+Z	ZZ	$t\bar{t}$
C_1 selection	0.00	0.00	0.00	1.50	0.00
C_2 selection	0.00	0.00	9.02	3.39	0.24
C_3 selection	0.02	0.65	0.34	0.02	5.20

Table 9.15: Production cross sections obtained using LO Monte Carlo generators for three different kinematic selections applied on the *RECO* events of proton-proton collisions at $\sqrt{s} = 14$ TeV.

Control selections C_1, C_2, and C_3 are defined in the following and are based on the definition of the *Final Selection*. Control selections cancel the upper bounds on the leading and trailing muon transverse momenta. Moreover, certain conditions are inverted in order to suppress signal events and enhance the desired background process events. These selections serves not only for the background rescaling in this particular study but might also serve as a good guide to the other selections whose aim would be to deal with DPS process as with the unwanted background. For instance, the requirement of a hard jet ($p_T > 50$ GeV) or requirement of hard opposite-sign muon ($p_T > 10$ GeV) in the final state almost completely suppresses the DPS contribution. Control selections are:

- C_1 selection, see Table 9.16, is suggested to require at least two negatively charged muons with transverse momentum greater than 12 GeV.
- C_2 selection, see Table 9.17, is designed to require at least one negatively charged muon with transverse momentum greater than 12 GeV.
- C_3 selection, see Table 9.18, is chosen to require at least two hard jets with transverse momentum greater than 50 GeV (leading jet) and 40 GeV (sub-leading jet). Restrictions on transverse momenta of the third and fourth hardest jet in the event present in the *Final Selection* are avoided.

$\lvert\eta(\mu)\rvert$	$<$	2.4	p_T(OS $\mu_{2^{nd}lead}$)	$>$	12 GeV
$p_T(\mu_{lead})$	$>$	20 GeV	$p_T(\mu_{trail})$	$>$	12 GeV
$M(\mu_{lead}\mu_{trail})$	$>$	10 GeV	$M_T(\mu_{lead}\mu_{trail})$	$>$	40 GeV
$\lvert y(j)\rvert$	$<$	2.0	JVF(j)	$>$	0.75
p_T^{j1}	$<$	50 GeV	p_T^{j2}	$<$	30 GeV
p_T^{j3}	$<$	25 GeV	p_T^{j4}	$<$	20 GeV

Table 9.16: Control selection C_1. Selection is suggested for cross section rescaling for SPS ZZ process.

$\lvert\eta(\mu)\rvert$	$<$	2.4	p_T(OS μ_{lead})	$>$	12 GeV
$p_T(\mu_{lead})$	$>$	20 GeV	$p_T(\mu_{trail})$	$>$	12 GeV
$M(\mu_{lead}\mu_{trail})$	$>$	10 GeV	$M_T(\mu_{lead}\mu_{trail})$	$>$	40 GeV
$\lvert y(j)\rvert$	$<$	2.0	JVF(j)	$>$	0.75
p_T^{j1}	$<$	50 GeV	p_T^{j2}	$<$	30 GeV
p_T^{j3}	$<$	25 GeV	p_T^{j4}	$<$	20 GeV

Table 9.17: Control selection C_2. Selection is designed for cross section rescaling for SPS WZ process.

$\lvert\eta(\mu)\rvert$	$<$	2.4	p_T(OS μ_{lead})	$<$	5 GeV
$p_T(\mu_{lead})$	$>$	20 GeV	$p_T(\mu_{trail})$	$>$	12 GeV
$M(\mu_{lead}\mu_{trail})$	$>$	10 GeV	$M_T(\mu_{lead}\mu_{trail})$	$>$	40 GeV
$\lvert y(j)\rvert$	$<$	2.0	JVF(j)	$>$	0.75
p_T^{j1}	$>$	50 GeV	p_T^{j2}	$>$	40 GeV

Table 9.18: Control selection C_3. Selection is chosen for cross section rescaling for both SPS $t\bar{t}$ and WWjj processes together.

9.8 Data reconstruction efficiency for $\mu^+\mu^+$ production at $\sqrt{s} = 14$ TeV

The topic of data reconstruction efficiency was shortly touched in the beginning of Sec. 9.4.1, where the comparison between cross sections for the *GEN* and *RECO* data were shown for the *Base Selection* final state cuts. Here, results for three other selections are shown in addition in order to demonstrate the source of gradually decreasing reconstruction efficiency for the signal events. On the other hand, efficiencies of background events reconstruction are not monotonously distributed and may even exceed the 100 per cent level. These values are connected to the detector-related effects, like misidentification of the muon charge, which may lead to the significant increase of number of searched events.

The comparison of results for more advanced selections than is the *Base Selection* requires to introduce the muon isolation condition into the *GEN* data analysis. Muon isolation condition for the *GEN* data

$$\frac{\sum p_T^{cone}}{p_T^{\mu}} < 0.15, \tag{9.24}$$

looks formally the same as the condition for the charged tracks found in the inner detector, see Eq. 8.6. The difference is that all final state particles are considered at the *GEN* data level and not only the charged ones. Therefore, the *GEN* level isolation filters generally more events off the sample than the combination of track and calorimetric isolations at the *RECO* level. There is no way how to apply quality reconstruction-like conditions on the *GEN* data and thus the *RECO* level cross sections become smaller than the *GEN* level cross sections at the end.

Table 9.19 shows cross sections for both data levels for four different kinematic selections. All selections were defined in the previous text: the *Base Selection* cuts are in Eq. (9.6), the *Trigger Selection* cuts are in Eq. (9.9), the *Lepton Selection* criteria are listed in Table 9.8 and the *Final Selection* conditions are summarized in Table 9.11.

Data reconstruction efficiencies for the individual processes and different selections are represented by the percentage numbers in brackets in Table 9.19. Efficiencies for the *RECO* data are always with respect to the *GEN* data for the given kinematic selection. The signal reconstruction efficiency begins at 97% for the *Base Selection* and drops down to 78% for the *Final Selection*. The highest efficiency (220%) for the *Final Selection* is found for the $t\bar{t}$ and reflects not only the detector effects but is affected also by the low statistics of theses events in this selection.

Observation of differences between distributions of kinematic variables obtained from analysis of the *GEN* and *RECO* data also brings an interesting result. It demonstrates the systematic effects of detector on observable characteristics, which will be the subject of the correction unfolding after the real measurement. Figure 9.28 shows distributions of transverse momenta of the leading and trailing muons, of the hardest opposite-sign muon, and of the leading jet in the DPS signal events for the *Trigger Selection*. Distributions for the SPS background processes are shown in Fig. E.3 in appendix.

One can read from the distributions that all transverse momenta are slightly shifted towards the higher values for the *RECO* data, except the case of $p_T(\mu_{lead})$ for SPS WZ

σ [fb]	data	DPS signal	SPS background			
		W^+W^+	W^+W^+jj	W^+Z	ZZ	$t\bar{t}$
Base Selection	*GEN*	1.38	1.75	46.00	13.40	$4.20 \cdot 10^3$
	RECO	1.34 (97%)	1.73 (99%)	44.38 (96%)	13.18 (98%)	$4.70 \cdot 10^3$ (112%)
Trigger Selection	*GEN*	1.12	1.36	26.66	6.88	4.04
	RECO	0.92 (82%)	1.06 (78%)	21.76 (82%)	5.54 (81%)	9.97 (247%)
Lepton Selection	*GEN*	1.02	0.58	4.74	0.37	1.72
	RECO	0.83 (81%)	0.45 (78%)	4.67 (99%)	0.45 (122%)	5.01 (291%)
Final Selection	*GEN*	0.95	0.11	4.27	0.34	0.15
	RECO	0.74 (78%)	0.06 (55%)	3.74 (88%)	0.37 (109%)	0.33 (220%)

Table 9.19: Cross sections for $\mu^+\mu^+$ production at $\sqrt{s} = 14$ TeV for four different selections. Numbers in percentage represent data reconstruction efficiencies for the given selection.

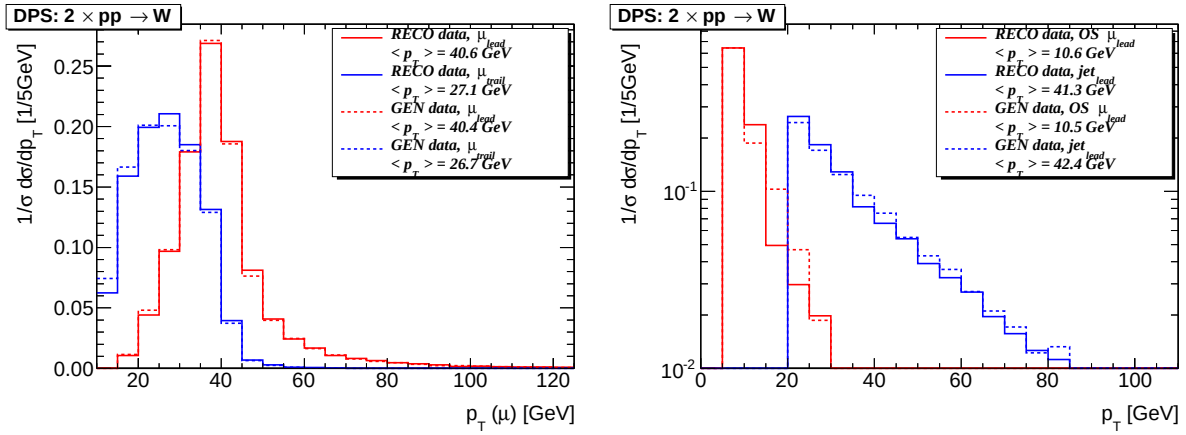

Figure 9.28: Example of distributions for the signal process as the demonstration of differences between the *RECO* and *GEN* data for the *Trigger Selection* of events. Left: normalized distributions of the leading and trailing muon transverse momentum. Right: normalized distributions of the transverse momenta of the leading opposite-sign (OS) muon and of the leading jet.

process. The smaller shift is for the leading muons, slightly larger shift can be observed for the trailing muons. For instance, these shifts in the mean values of the transverse momentum are 0.2 and 0.4 GeV for the DPS signal process. The largest shifts can be seen for the transverse momentum distributions of the leading and trailing muons for $t\bar{t}$ process, by 2.9 and 6.2 GeV. All these kinematic differences between the *GEN* and *RECO* data contribute to the differences between calculated cross sections.

9.9 Generalization to the same-sign di-muon production in pp collisions at $\sqrt{s} = 7$ and 14 TeV

So far, the analysis was restricted to study the production of two positively charged muons in the case of proton-proton collisions at $\sqrt{s} = 14$ TeV. The further generalization consists in the inclusion of processes producing two negatively charged muons into consideration. The analysis includes also events of proton-proton collisions at $\sqrt{s} = 7$ TeV in order to study dependence of the calculated differential and total cross sections on the energy. Two energies of 7 and 14 TeV were chosen to cover a full range of the LHC energies already run or designed to be run in the future.

All data shown in this section are from the direct generator record (the *GEN* level data). Results reached in the analysis of the detector simulated Monte Carlo data (the *RECO* data) for the production of the positively charged muon pair are used in this section only as an estimation of the general detection and reconstruction efficiencies for all the studied physics processes for 14 TeV collisions and for the given kinematic selections. From the detector point of view, there should be no difference between detecting positively and negatively charged muons and an appropriate underlying event. However, one has to describe also the differences in kinematics of the positively and negatively charged muons stemming from the parton distribution functions for different flavors of initial state partons, whose interaction produces either positively or negatively charged W boson.

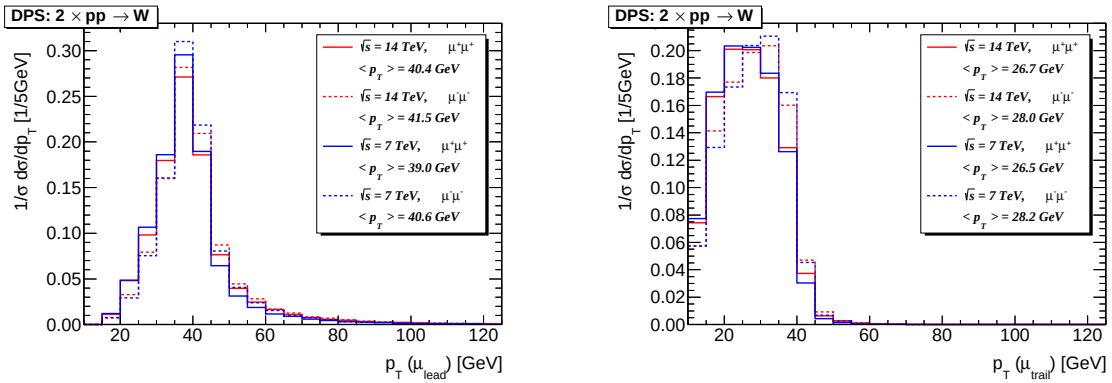

Figure 9.29: Normalized distributions of the transverse momentum of the leading (left) and trailing (right) muon for the signal events passing the *Trigger Selection*. One can compare between two energies of the proton-proton interactions (red lines correspond to $\sqrt{s} = 14$ TeV, blue lines to $\sqrt{s} = 7$ TeV) and between two charge combinations for the final same-sign muon pair (solid lines correspond to ++ charge combination, dashed lines to – – combination).

Figure 9.29 shows distributions of transverse momentum of the leading and trailing muons for the DPS signal process, while the distributions for all the background processes are moved to Fig. E.4 in appendix. One can see that the negatively charged muons produced via the DPS signal process are statistically slightly harder than the positively charged ones. The mean value of the transverse momentum of the leading

μ^- is 41.5 GeV, while the same mean value for leading μ^+ is 40.4 GeV. This difference grows slightly if one take a look at the trailing muons. Muons produced via all physics background processes together do not exhibit any general property. SPS WWjj process produces significantly harder negative muons than positive ones, SPS WZ process produces slightly softer μ^-'s than μ^+'s and SPS ZZ process offers both charge variants according to the very similar distributions. Figures E.1 and E.2 summarize the joint transverse momentum distributions for both positively and negatively charged muons for the two energies.

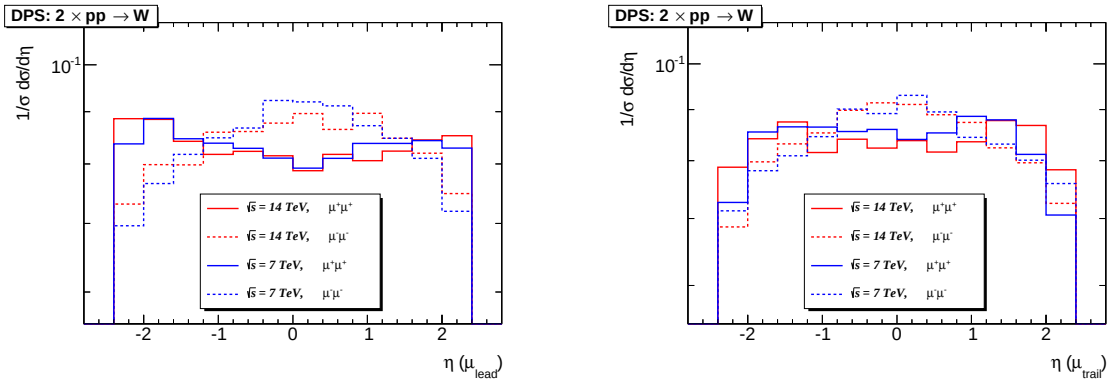

Figure 9.30: Normalized distributions of the pseudorapidity of the leading (left) and trailing (right) muon for the signal events passing the *Trigger Selection*. One can compare between two energies of the proton-proton interactions (red lines correspond to $\sqrt{s} = 14$ TeV, blue lines to $\sqrt{s} = 7$ TeV) and between two charge combinations for the final same-sign muon pair (solid lines correspond to ++ charge combination, dashed lines to $--$ combination).

Muon pseudorapidity distributions for the signal process exhibit also an interesting behavior. The distribution for positively charged muons have convex shapes, while distributions for negatively charged muons are concave functions of the muon pseudorapidity. Figure 9.30 shows pseudorapidity distributions for the leading and trailing muons for the DPS signal process. The described effect is better visible for the leading muon but the trend remains also at the trailing muon, where the convex shape of the distribution for positive muon is localized in more central region. The appropriate distributions for the background processes are shown in Fig. E.5 in appendix.

The analysis of the underlying event present in the accepted DPS signal events is represented here by the jet multiplicity distribution and by the distribution of the transverse momentum of the leading jet, see Fig. 9.31. One can see that both characteristics do not depend on the charge combination and the differences are at the level of statistical fluctuations. Only the dependence on the energy of the collision is visible. In order to show the differences in leading jet transverse momentum for two energies and for all processes, Figure 9.32 contains joint distributions of leading jet transverse momentum for all studied processes. These joint distributions were obtained by merging the given distributions for the positively and negatively charged muon pair productions. The transverse momentum distributions for the second, third and fourth leading jet are

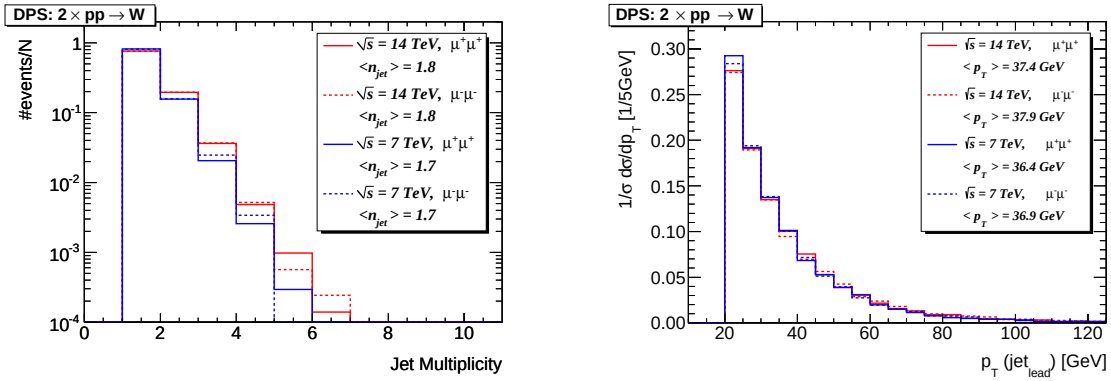

Figure 9.31: Left: Normalized distributions of the jet multiplicity for the DPS events. Right: Normalized distributions of the leading jet transverse momentum for the DPS events. In both plots, one can compare distributions for two interaction energies and two charge combinations of the searched same-sign muon pair. All events passed the *Lepton Selection*.

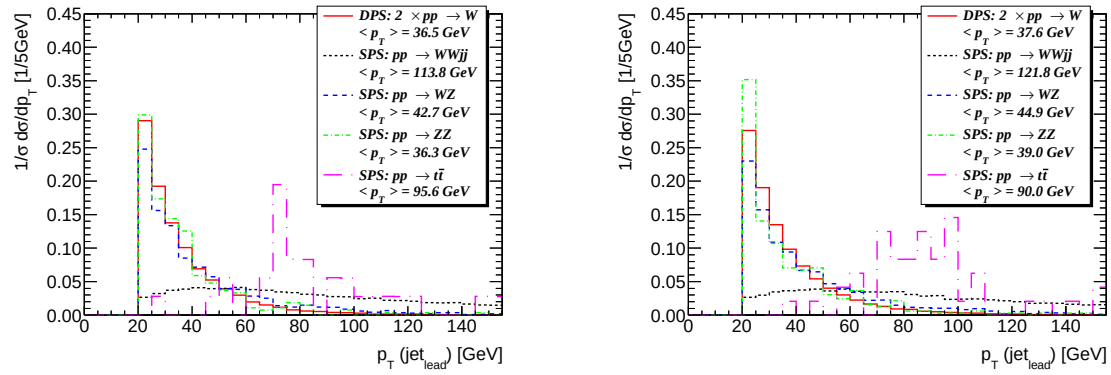

Figure 9.32: Normalized distributions of the leading jet transverse momentum for all studied processes. Distributions correspond to the events of proton-proton collisions at $\sqrt{s} = 7$ TeV (left) and $\sqrt{s} = 14$ TeV (right). All events passed the *Lepton Selection*.

shown in Fig. E.6 in the appendix. When comparing the mean values of the individual transverse momenta for the two energies, one should bear in mind the small numbers of jets present in di-boson events stemming just from the gluon radiation. Therefore the statistical fluctuations have a non-negligible influence.

One should emphasize that the shape of the differential cross sections corresponding to the production of two positively or two negatively charged muons at the *GEN* data level are almost the same and do not exhibit any extreme differences in kinematics. Moreover, the dependence of the studied differential cross sections on the energy of the collision is very small. This property of the studied processes leads to two statements. First, the signal enhancing fiducial region defined by the *Final Selection* has turned out to be universal and can be applied on data for both charge combinations as well as for both energies. Second, the data reconstruction efficiencies found in Sec. 9.8 for positively charged muon pair production can be considered valid also for the negatively

σ [fb]	Charges	DPS signal	SPS background			
		WW	WWjj	WZ	ZZ	$t\bar{t}$
Base Selection	$\mu^+\mu^+$	0.47	0.69	24.64	6.69	$0.75 \cdot 10^3$
	$\mu^-\mu^-$	0.17	0.22	16.53	6.43	$0.74 \cdot 10^3$
	Sum	0.63	0.91	41.17	13.12	$1.49 \cdot 10^3$
Trigger Selection	$\mu^+\mu^+$	0.39	0.55	14.00	3.30	0.56
	$\mu^-\mu^-$	0.14	0.20	8.28	3.19	0.66
	Sum	0.53	0.74	22.28	6.50	1.22
Lepton Selection	$\mu^+\mu^+$	0.36	0.27	2.41	0.17	0.26
	$\mu^-\mu^-$	0.13	0.06	1.34	0.15	0.29
	Sum	0.49	0.33	3.75	0.32	0.54
Final Selection	$\mu^+\mu^+$	0.34	0.05	2.23	0.17	0.02
	$\mu^-\mu^-$	0.13	0.01	1.26	0.14	0.00
	Sum	0.47	0.07	3.49	0.31	0.02

Table 9.20: The *GEN* data level cross sections for same-sign muon pair production at $\sqrt{s} = 7$ TeV for four different cut selections. Two possible charge combinations are shown in separated lines as well as together in the Sum line.

σ [fb]	Charges	DPS signal	SPS background			
		WW	WWjj	WZ	ZZ	$t\bar{t}$
Base Selection	$\mu^+\mu^+$	1.38	1.75	46.00	13.40	$4.20 \cdot 10^3$
	$\mu^-\mu^-$	0.71	0.75	36.45	12.94	$4.19 \cdot 10^3$
	Sum	2.09	2.50	82.46	26.33	$8.39 \cdot 10^3$
Trigger Selection	$\mu^+\mu^+$	1.12	1.36	26.66	6.88	4.04
	$\mu^-\mu^-$	0.60	0.64	18.97	6.61	3.74
	Sum	1.73	1.99	45.63	13.49	7.77
Lepton Selection	$\mu^+\mu^+$	1.02	0.58	4.74	0.37	1.72
	$\mu^-\mu^-$	0.55	0.18	3.18	0.33	1.94
	Sum	1.57	0.77	7.93	0.69	3.66
Final Selection	$\mu^+\mu^+$	0.95	0.11	4.27	0.34	0.15
	$\mu^-\mu^-$	0.50	0.04	2.90	0.31	0.07
	Sum	1.45	0.15	7.16	0.65	0.22
Final Selection (rescaled)	$\mu^+\mu^+$	0.74	0.06	3.76	0.37	0.33
	$\mu^-\mu^-$	0.39	0.02	2.55	0.34	0.15
	Sum	1.13	0.08	6.31	0.71	0.48

Table 9.21: The *GEN* data level cross sections for same-sign muon pair production at $\sqrt{s} = 14$ TeV for four different cut selections. Two possible charge combinations are shown in separated lines as well as together in the Sum line.

charged muon pair production at 14 TeV.

Tables 9.20 and 9.21 summarize the calculated cross sections obtained for the *GEN* data for 7 and 14 TeV proton-proton collisions. Both possible charge combinations of final state muons are shown separately as well as summed up. The latter case thus rep-

resents the general same-sign di-muon production cross section for the given kinematic selection. There are no reconstruction efficiencies for the 7 TeV data to be applied. These cross sections serve only for illustration, how problematic would the measurement be at lower energies than the designed one. The signal production cross section at 7 TeV is 0.47 fb, which is about one third of the cross section at 14 TeV. The sum of the cross sections for the physics background processes is 3.89 fb, which is about one half of the same cross section for the 14 TeV collisions.

The cross sections for 14 TeV *GEN* data corresponding to the *Final Selection* are 1.45 fb for the signal DPS process and 8.18 fb for the sum of all background processes, see Table 9.19. These pure Monte Carlo cross sections were rescaled using the data reconstruction efficiencies evaluated in Section 9.8 to 1.13 fb for the signal DPS process and 7.58 fb for the sum of all background processes. The data reconstruction efficiencies can be found in the last line in Table 9.21. They are: 0.78, 0.55, 0.88, 1.09 and 2.20. The order of the efficiencies is the same at the order of the processes in Table 9.19.

Table 9.22 evaluates fractions of the DPS signal events within the complete same-sign di-muon samples, which include all physics background processes and correspond to the *Final Selection*. It also contains values of the $S/\sqrt{B}$ ratios representing the magnitude of the signal significance over the considered background. One can see that the $S/\sqrt{B}$ ratio for 14 TeV data decreased remarkably from 0.51 to 0.41 after rescaling *GEN* cross sections using the set of reconstruction efficiencies. Similar rescaling of the LO cross sections for 7 TeV data would decrease the theoretical $S/\sqrt{B}$ ratio 0.24 to very small value. Therefore, one of the conclusions of this study is the recommendation to measure this process at the highest possible energy of the proton-proton collisions.

	$\sqrt{s} = 7$ TeV			$\sqrt{s} = 14$ TeV					
	GEN data			*GEN* data			*GEN* data; rescaled		
	++	−−	Sum	++	−−	Sum	++	−−	Sum
S/(S+B) [%]	12.1	8.4	10.8	16.3	13.1	15.1	14.1	11.3	13.0
$S/\sqrt{B}$	0.216	0.109	0.238	0.430	0.274	0.507	0.348	0.223	0.410

Table 9.22: Summary of signal fractions for individual contributions to the *Final Selection* event sample together with the $S/\sqrt{B}$ ratios. All data are taken at *GEN* level. First two parts for 7 and 14 TeV data correspond to the generator-level results. The last part for 14 TeV data correspond to the cross sections rescaled according to the *RECO* results from $\mu^+\mu^+$ analysis.

Significance	$\mathcal{L}$ [fb^{-1}]	DPS events	All events
1σ	5.9	6.7	51.8
5σ	148.7	168.0	1295.2

Table 9.23: Signal significance expressed in units of the standard deviation in dependence of the integrated luminosity of the measured data sample for the general same-sign di-muon production at 14 TeV collisions.

In summary, the same-sign muon pair production cross section is estimated to be 8.71 fb in the fiducial region defined by the *Final Selection* for the 14 TeV proton-proton collisions at the ATLAS experiment. This cross section accounts for all the signal and physics background processes. The fraction of the DPS signal events is expected to be around 13%. This fraction corresponds to the cross section of 1.13 fb. As shown in details in Table 9.23, the integrated luminosity necessary for the signal significance of 5 standard deviations above the physics background is 148.7 fb^{-1}. Such a luminosity is remarkably smaller than 205.4 fb^{-1}, which would correspond to the same signal significance, if the measurement would be restricted to the positively charged muons.

10 Summary and Conclusions

Recent LHC measurements of charged track multiplicities and other minimum bias or underlying event characteristics demonstrate the increasing importance of the multiple parton interactions in the description of the hadron-hadron collisions. These processes proceed at soft or semi-hard scales and their investigation is mostly restricted to the statistical comparison between real and Monte Carlo data obtained for different tunes of generator parameters. This thesis deals with the special class of the multiple parton interactions (MPI), with the double partons scattering (DPS), where at least two parton processes within one hadron-hadron collision proceed at hard scale and which may produce the final state identical to the hard single parton scattering (SPS). The specific process under study is the production of a pair of same-sign W bosons, where both gauge bosons decay to a muon and an appropriate neutrino.

This thesis begins with a brief introduction to the theoretical descriptions of the studied phenomena, with a special attention paid to the underlying event model in Herwig++. Since all the MPI theories suffer from being still at preliminary level of our knowledge of the phenomena, the thesis focus its attention to set this particular analysis into the context of the contemporary stage of the ongoing theoretical studies and experimental measurements performed up to now. The thesis emphasizes the importance of the wide spectra of studied DPS processes from the point of view of the internal hadron structure investigation. So far, one can already state that the DPS measurements revealed the picture of the hadron, described as a composite object full of sea quark and gluon constituents, as a non-uniformly filled out object. The measurements of the DPS scaling factor clearly sign that the effective area of the hadron contributing to the hard scattering is much smaller than the total cross section for proton-proton collision. The picture of hadron is nowadays described using a two-components model, in which the "hard" core is surrounded by a sphere of partons, which can contribute only to the soft component of the collision.

The goal of this study is to prepare a comprehensive analysis of the final state containing same-sign muon pair, which might be produced whether via single or double parton scattering at the ATLAS experiment. This thesis contains the analysis of Monte Carlo simulated data. One part of the data was simulated for the detector response and exhibits the main core of the study. This thesis aims to predict the measurability of this process in high energy proton-proton collisions (at $\sqrt{s} = 14$ TeV) designed for the future runs of the LHC. The experimental part of the study contains analysis of the signal DPS process as well as the analysis of four types of SPS physics background processes also producing same-sign muon pair. These are production of a same-sign W

pair accompanied at LO by two jets, WZ and ZZ di-boson productions and a $t\bar{t}$ QCD production.

Throughout the analysis, several selections of kinematic cuts are designed in order to study the kinematic differences among the five studied processes and in order to evaluate the contribution of the double parton scattering to the given final state. The analysis starts from the *Base Selection*, which is very close to the region corresponding to the measurement of the total cross section of the studied process. In this selection, the DPS process is completely overwhelmed by the SPS background. The analysis continues towards the definition of the *Final Selection*, which is based on the final state muon isolation and restrictions of the transverse momentum interval allowed. This selection also reflects the analysis of all expected jets, whether they may come from the hard or pile-up collisions. Even though that the analysis offers further selections, based on the event topology considerations, the *Final Selection* is suggested as the most suitable fiducial region for the measurement of the double parton scattering contribution to the same-sign muon pair production. The appropriate cross section for the DPS signal process was evaluated at LO using Herwig++ event generator and was found to be 1.13 fb. The fraction of these DPS events in the final fiducial region is 13% with respect to all events including the studied physics background generated using MadGraph and Herwig++ programs. The $S/\sqrt{B}$ ratio is around 0.41 and one can therefore expect to reach 5σ signal significance for data at around 150 fb^{-1} of integrated luminosity.

The LO cross sections obtained from Monte Carlo programs serve as an approximate predictions for the real measurement. In addition to the *Final Selection*, the thesis suggests three other selections, where always a different type of the physics background process dominates. The real measurement of the appropriate cross sections in these regions could be used for rescaling of the predicted LO cross sections. After the rescaling of the background processes cross sections, assuming that the ratios between real and generated values remains still the same in the whole kinematic region, one can measure the abundance of the same-sign di-muon events in the *Final Selection* and so evaluate the true DPS cross section searched.

The combination of the DPS signal and SPS W boson production cross section measurements would provide an information about the σ_{eff} scaling factor, which is assumed to be process and cut independent at the parton level. Its measurement was performed only for 4 jets and γ + 3 jets up to now and thus the result for completely different process would be especially valuable. Moreover, a precise measurement of the differential cross sections as a function of transverse momenta and pseudorapidities of the searched muons could resolve, which theoretical approach of MPI phenomena description is more appropriate and what kind of parton distribution functions should be further developed. Specifically, how large effects of the internal parton correlations take place in different kinds of processes, if the convolution of the two single parton distribution functions models accurately the double parton distribution function or if the factorization of the longitudinal and transversal part of the 3D generalized parton distribution function is valid.

A σ_{eff} Analysis Results

A.1 Intrinsic k_T dependence

	Herwig++		Herwig		Pythia	
σ [mb]	Hard	Soft	Hard	Soft	Hard	Soft
σ_{1jet}	5.13	1.40	5.33	6.61	4.79	0.06
σ_{2jets}	0.65	0.26	0.54	0.70	0.66	0.00
σ_{jets}	8.67	2.05	8.72	8.31	8.04	0.06
σ [nb]						
$\sigma_{\gamma+1jet}$	5.38	0.06	3.41	0.16	4.46	0.08
$\sigma_{\gamma+2jets}$	1.39	0.01	1.02	0.04	0.92	0.15
$\frac{\sigma_{2jets}}{\sigma_{1jet}}$	0.139		0.103		0.136	
$\frac{\sigma_{jets}}{\sigma_{1jet}}$	1.641		1.426		1.668	
$\frac{\sigma_{\gamma+2jets}}{\sigma_{\gamma+1jet}}$	0.256		0.300		0.236	
f	0.648		0.575		0.620	

Table A.1: The calculated cross sections, their ratios and the final correction factors for the intrinsic k_T RMS = 0.0 GeV for three MC generators. CDFJetClu jet algorithm was used.

	Herwig++		Herwig		Pythia	
σ [mb]	Hard	Soft	Hard	Soft	Hard	Soft
σ_{1jet}	5.72	0.86	5.60	6.96	4.78	0.10
σ_{2jets}	0.64	0.08	0.54	0.72	0.75	0.00
σ_{jets}	9.37	1.11	9.01	8.88	8.01	0.10
σ [nb]						
$\sigma_{\gamma+1jet}$	5.50	0.09	3.46	0.11	4.48	0.08
$\sigma_{\gamma+2jets}$	1.43	0.01	1.13	0.06	0.92	0.07
$\frac{\sigma_{2jets}}{\sigma_{1jet}}$	0.109		0.100		0.136	
$\frac{\sigma_{jets}}{\sigma_{1jet}}$	1.591		1.424		1.668	
$\frac{\sigma_{\gamma+2jets}}{\sigma_{\gamma+1jet}}$	0.257		0.335		0.218	
f	0.582		0.619		0.590	

Table A.2: The calculated cross sections, their ratios and the final correction factors for the intrinsic k_T RMS = 1.0 GeV for three MC generators. CDFJetClu jet algorithm was used.

	Herwig++		Herwig		Pythia	
σ [mb]	Hard	Soft	Hard	Soft	Hard	Soft
σ_{1jet}	9.73	3.79	6.23	10.74	6.93	2.51
σ_{2jets}	0.65	0.13	0.72	0.81	0.72	0.00
σ_{jets}	14.73	4.38	10.87	12.99	10.54	2.52
σ [nb]						
$\sigma_{\gamma+1jet}$	5.51	0.05	3.43	0.17	4.47	0.08
$\sigma_{\gamma+2jets}$	1.48	0.03	1.08	0.05	1.05	0.07
$\frac{\sigma_{2jets}}{\sigma_{1jet}}$	0.058		0.090		0.076	
$\frac{\sigma_{jets}}{\sigma_{1jet}}$	1.414		1.404		1.383	
$\frac{\sigma_{\gamma+2jets}}{\sigma_{\gamma+1jet}}$	0.271		0.312		0.246	
f	0.465		0.564		0.445	

Table A.3: The calculated cross sections, their ratios and the final correction factors for the intrinsic k_T RMS = 2.0 GeV for three MC generators. CDFJetClu jet algorithm was used.

A.2 Jet algorithm dependence

	CDFJetClu		PxCone		anti-k$_t$	
σ [mb]	Hard	Soft	Hard	Soft	Hard	Soft
σ_{1jet}	9.16	3.16	10.90	3.91	8.89	3.21
σ_{2jets}	0.62	0.15	0.88	0.24	0.70	0.24
σ_{jets}	13.87	3.70	16.02	4.56	13.38	3.98
σ [nb]						
$\sigma_{\gamma+1jet}$	5.66	0.03	5.28	0.04	2.89	0.01
$\sigma_{\gamma+2jets}$	1.46	0.01	1.53	0.02	0.83	0.00
$\frac{\sigma_{2jets}}{\sigma_{1jet}}$	0.063		0.076		0.078	
$\frac{\sigma_{jets}}{\sigma_{1jet}}$	1.426		1.390		1.434	
$\frac{\sigma_{\gamma+2jets}}{\sigma_{\gamma+1jet}}$	0.258		0.292		0.288	
f	0.458		0.512		0.525	

Table A.4: The calculated cross sections, their ratios and the final correction factors in dependence on the jet clustering algorithm using Herwig++ generator.

	CDFJetClu		PxCone		anti-k$_t$	
σ [mb]	Hard	Soft	Hard	Soft	Hard	Soft
σ_{1jet}	5.33	6.61	6.18	8.30	5.73	9.58
σ_{2jets}	0.54	0.70	0.78	1.25	0.71	1.96
σ_{jets}	8.72	8.31	9.85	10.72	9.27	13.84
σ [nb]						
$\sigma_{\gamma+1jet}$	3.41	0.16	3.07	0.11	1.64	0.02
$\sigma_{\gamma+2jets}$	1.02	0.05	1.05	0.06	0.45	0.03
$\frac{\sigma_{2jets}}{\sigma_{1jet}}$	0.103		0.140		0.175	
$\frac{\sigma_{jets}}{\sigma_{1jet}}$	1.426		1.421		1.510	
$\frac{\sigma_{\gamma+2jets}}{\sigma_{\gamma+1jet}}$	0.300		0.348		0.291	
f	0.575		0.693		0.704	

Table A.5: The calculated cross sections, their ratios and the final correction factors in dependence on the jet clustering algorithm using Herwig generator.

	CDFJetClu		PxCone		anti-k_t	
σ [mb]	Hard	Soft	Hard	Soft	Hard	Soft
σ_{1jet}	9.62	2.88	11.41	3.98	8.84	2.50
σ_{2jets}	1.17	0.00	1.51	0.00	1.16	0.00
σ_{jets}	15.04	2.92	17.20	4.02	13.81	2.55
σ [nb]						
$\sigma_{\gamma+1jet}$	4.47	0.08	4.21	0.07	1.90	0.02
$\sigma_{\gamma+2jets}$	1.05	0.07	1.04	0.07	0.45	0.07
$\frac{\sigma_{2jets}}{\sigma_{1jet}}$	0.076		0.085		0.075	
$\frac{\sigma_{jets}}{\sigma_{1jet}}$	1.383		1.338		1.378	
$\frac{\sigma_{\gamma+2jets}}{\sigma_{\gamma+1jet}}$	0.246		0.258		0.270	
f	0.445		0.459		0.475	

Table A.6: The calculated cross sections, their ratios and the final correction factors in dependence on the jet clustering algorithm using Pythia generator.

A.3 PDF dependence

	MRST98		CTEQ6L1		MRST LO**	
σ [mb]	Hard	Soft	Hard	Soft	Hard	Soft
σ_{1jet}	5.54	1.71	6.39	1.73	9.16	3.16
σ_{2jets}	0.36	0.07	0.41	0.07	0.62	0.15
σ_{jets}	8.46	1.98	9.59	1.98	13.87	3.70
σ [nb]						
$\sigma_{\gamma+1jet}$	3.77	0.06	4.21	0.04	5.66	0.03
$\sigma_{\gamma+2jets}$	1.00	0.04	1.06	0.03	1.46	0.01
$\frac{\sigma_{2jets}}{\sigma_{1jet}}$	0.060		0.059		0.063	
$\frac{\sigma_{jets}}{\sigma_{1jet}}$	1.440		1.423		1.426	
$\frac{\sigma_{\gamma+2jets}}{\sigma_{\gamma+1jet}}$	0.271		0.255		0.258	
f	0.477		0.447		0.458	

Table A.7: The calculated cross sections, their ratios and the final correction factors in dependence on the parton distribution function used in Herwig++ generator.

	CTEQ5L		MRST LO**	
σ [mb]	Hard	Soft	Hard	Soft
σ_{1jet}	9.62	2.88	9.62	2.88
σ_{2jets}	1.17	0.00	1.17	0.00
σ_{jets}	15.04	2.92	15.04	2.92
σ [nb]				
$\sigma_{\gamma+1jet}$	4.47	0.08	6.32	0.09
$\sigma_{\gamma+2jets}$	1.05	0.07	1.29	0.19
$\frac{\sigma_{2jets}}{\sigma_{1jet}}$	0.076		0.094	
$\frac{\sigma_{jets}}{\sigma_{1jet}}$	1.383		1.436	
$\frac{\sigma_{\gamma+2jets}}{\sigma_{\gamma+1jet}}$	0.246		0.232	
f	0.445		0.468	

Table A.8: The calculated cross sections, their ratios and the final correction factors in dependence on the parton distribution function used in Pythia generator

A.4 Order of α_S dependence

	1-loop α_S		2-loops α_S	
σ [mb]	Hard	Soft	Hard	Soft
σ_{1jet}	13.99	5.23	9.16	3.16
σ_{2jets}	0.95	0.24	0.62	0.15
σ_{jets}	20.96	6.19	13.87	3.70
σ [nb]				
$\sigma_{\gamma+1jet}$	6.53	0.05	5.66	0.03
$\sigma_{\gamma+2jets}$	1.77	0.04	1.46	0.01
$\frac{\sigma_{2jets}}{\sigma_{1jet}}$	0.062		0.063	
$\frac{\sigma_{jets}}{\sigma_{1jet}}$	1.412		1.426	
$\frac{\sigma_{\gamma+2jets}}{\sigma_{\gamma+1jet}}$	0.275		0.258	
f	0.476		0.458	

Table A.9: The calculated cross sections, their ratios and the final correction factors in dependence on the order of α_S used in Herwig++ generator.

B Steering of the Generation

B.1 Common settings of Herwig++

```
cd /Herwig/Generators
set LHCGenerator:EventHandler:LuminosityFunction:Energy 14000
# Intrinsic pT tune extrapolated to LHC energy
set /Herwig/Shower/Evolver:IntrinsicPtGaussian 2.2*GeV
# Use 2-loop αS
create Herwig::O2AlphaS /Herwig/AlphaQCD_O2
set LHCGenerator:StandardModelParameters:QCD/RunningAlphaS /Herwig/AlphaQCD_O2
# Set CTEQ6L1.LHpdf
cd /Herwig/Partons
create ThePEG::LHAPDF PDFset ThePEGLHAPDF.so
set PDFset:PDFName cteq6ll.LHpdf
set PDFset:RemnantHandler HadronRemnants
set /Herwig/Particles/p+:PDF PDFset
# Set QED pT cutoffs to match PHOTOS
cd /Herwig/QEDRadiation/
set QEDRadiationHandler:RadiationGenerator:FFDipole:MinimumEnergyRest 10.0*MeV
set QEDRadiationHandler:RadiationGenerator:IFDipole:MinimumEnergyRest 10.0*MeV

# minimal pT cut-off
set /Herwig/UnderlyingEvent/KtCut:MinKT 3.16*GeV
set /Herwig/UnderlyingEvent/UECuts:MHatMin 6.32*GeV
# inverse hadron radius
set /Herwig/UnderlyingEvent/MPIHandler:InvRadius 1.35*GeV2
# Colour reconnection settings
set /Herwig/Hadronization/ColourReconnector:ColourReconnection Yes
set /Herwig/Hadronization/ColourReconnector:ReconnectionProbability 0.61
# Colour Disrupt settings
set /Herwig/Partons/RemnantDecayer:colourDisrupt 0.75
# inverse hadron radius
set /Herwig/UnderlyingEvent/MPIHandler:InvRadius 1.35
# Soft UE
set /Herwig/UnderlyingEvent/MPIHandler:twoComp Yes
set /Herwig/UnderlyingEvent/MPIHandler:DLmode 2
```

B.2 DPS $W^+W^+ \to \mu^+\mu^+$ generation in Herwig++

```
cd /Herwig/MatrixElements
insert SimpleQCD:MatrixElements[0] MEqq2W2ff
set MEqq2W2ff:Wcharge 1 # for W+
set MEqq2W2ff:Process 4 # for muon decay

cd /Herwig/Cuts
set WBosonKtCut:MinKT 0.0*GeV
set MassCut:MinM 0.*GeV
set MassCut:MaxM 14000.*GeV
set QCDCuts:MHatMin 0.0*GeV
set LeptonKtCut:MinKT 0.001*GeV
set LeptonKtCut:MaxEta 10.
set LeptonKtCut:MinEta -10.
set JetKtCut:MinKT 0.0*GeV

cd /Herwig/UnderlyingEvent
create ThePEG::SimpleKTCut DPKtCut SimpleKTCut.so
set DPKtCut:MinKT 0.001
set DPKtCut:MaxEta 10.
set DPKtCut:MinEta -10.
create ThePEG::Cuts DP1Cuts
set DP1Cuts:MHatMin 0.002
insert DP1Cuts:OneCuts 0 DPKtCut
create ThePEG::SubProcessHandler DP1
# the same ME to the secondary interaction
insert DP1:MatrixElements 0 /Herwig/MatrixElements/MEqq2W2ff
set DP1:PartonExtractor /Herwig/Partons/QCDExtractor
insert MPIHandler:SubProcessHandlers 1 DP1
insert MPIHandler:Cuts 1 DP1Cuts
insert MPIHandler:additionalMultiplicities 0 1
```

B.3 Di-boson ME's hadronization in Herwig++

```
set /Herwig/Shower/Evolver:HardVetoMode 1
set /Herwig/Shower/Evolver:HardVetoScaleSource 1
set /Herwig/Shower/Evolver:MECorrMode 0

# Create and set the Handler and Reader
library LesHouches.so
cd /Herwig/EventHandlers/
create ThePEG::LesHouchesFileReader LHEReader
create ThePEG::LesHouchesEventHandler LHEHandler
set LHEReader:IncludeSpin Yes
insert LHEHandler:LesHouchesReaders 0 LHEReader
set LHEReader:MomentumTreatment RescaleEnergy
set LHEReader:WeightWarnings 0
set LHEHandler:WeightOption VarNegWeight
set LHEHandler:PartonExtractor /Herwig/Partons/QCDExtractor
set LHEHandler:CascadeHandler /Herwig/Shower/ShowerHandler
set LHEHandler:HadronizationHandler /Herwig/Hadronization/ClusterHadHandler
set LHEHandler:DecayHandler /Herwig/Decays/DecayHandler
set /Herwig/Generators/LHCGenerator:EventHandler LHEHandler
set /Herwig/Shower/KinematicsReconstructor:ReconstructionOption General
set /Herwig/Shower/KinematicsReconstructor:InitialInitialBoostOption LongTransBoost
create ThePEG::FixedCMSLuminosity /Herwig/Generators/FCMSLuminosity
set LHEHandler:LuminosityFunction /Herwig/Generators/FCMSLuminosity
insert LHEHandler:PreCascadeHandlers 0 /Herwig/NewPhysics/DecayHandler

# Set the PDF for the LHE reader.
set LHEReader:PDFA /Herwig/Partons/AtlasPDFsetLO
set LHEReader:PDFB /Herwig/Partons/AtlasPDFsetLO
set /Herwig/Particles/p+:PDF /Herwig/Partons/AtlasPDFsetLO
# Shower/MPI always use the LO PDF.
set /Herwig/Shower/ShowerHandler:PDFA /Herwig/Partons/AtlasPDFsetLO
set /Herwig/Shower/ShowerHandler:PDFB /Herwig/Partons/AtlasPDFsetLO
# Even more PDF setup explicitness!
set /Herwig/Partons/MPIExtractor:FirstPDF /Herwig/Partons/AtlasPDFsetLO
set /Herwig/Partons/MPIExtractor:SecondPDF /Herwig/Partons/AtlasPDFsetLO

# Set default filename and cuts
set LHEReader:FileName lhefilename
create ThePEG::Cuts /Herwig/Cuts/NoCuts
set LHEReader:Cuts /Herwig/Cuts/NoCuts
```

B.4 $t\bar{t} \to \mu^+\mu^+$ generation in Herwig++

```
cd /Herwig/MatrixElements
insert SimpleQCD:MatrixElements[0] MEHeavyQuark
set MEHeavyQuark:TopMassOption OnMassShell
set MEHeavyQuark:Process 0
set MEHeavyQuark:QuarkType 6
set /Herwig/Particles/t/t->b,bbar,c;:OnOff Off
set /Herwig/Particles/t/t->b,c,dbar;:OnOff Off
set /Herwig/Particles/t/t->b,c,sbar;:OnOff Off
set /Herwig/Particles/t/t->b,sbar,u;:OnOff Off
set /Herwig/Particles/t/t->b,u,dbar;:OnOff Off
set /Herwig/Particles/t/t->nu_e,e+,b;:OnOff Off
set /Herwig/Particles/t/t->nu_mu,mu+,b;:OnOff On
set /Herwig/Particles/t/t->nu_tau,tau+,b;:OnOff Off

cd /Herwig/Cuts
set MassCut:MinM 0.*GeV
set MassCut:MaxM 14000.*GeV
set QCDCuts:MHatMin 0.0*GeV
set LeptonKtCut:MinKT 0.001*GeV
set LeptonKtCut:MaxEta 10.
set LeptonKtCut:MinEta -10.
set JetKtCut:MinKT 10.0*GeV
```

C Missing Transverse Energy

A missing transverse energy (MET) was studied as an additional detector-related variable with possible power to distinguish physics or detector background from the studied signal process. Missing transverse energy at ATLAS is calculated from calibrated calorimeter cells with $|\eta| < 4.9$ and from muons ($|\eta| < 2.4$) and it is supposed to represent the opposite vector sum of momenta of all particles within this pseudorapidity acceptance interval. This vector sum should be close approximation to the transverse energy carried by escaped neutrinos. Missing E_T distributions for all studied processes are shown in Fig. C.1. This plot confirms the expectation and only the SPS ZZ production is characterized by smaller MET values. No other background processes can be suppressed by minimal MET requirement. The similarity in MET distributions for WW and WZ productions is caused by the randomness of the neutrino directions and thus the muons might more or less balance the total momentum. Therefore, one missing neutrino embodies the similar MET distribution as distributions for two missing neutrinos.

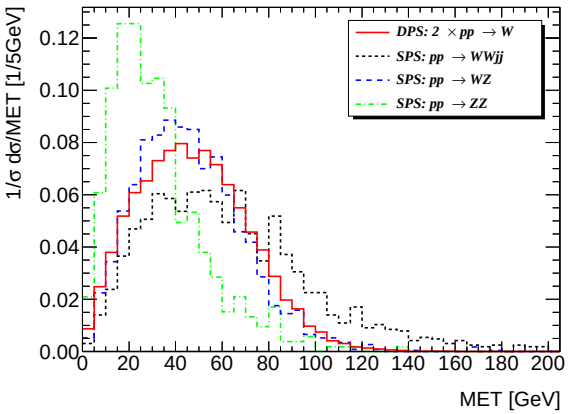

Figure C.1: Missing transverse energy reconstructed by the ATLAS detector on the basis of full simulation of detector response. No significant differences among processes producing one or two neutrinos. SPS ZZ production embodies smaller missing E_T as expected.

D B - tagging

If someone would be interested in results from a b-tagging of the remaining jets in the events corresponding to the *Final Selection*, MV1 weight was evaluated for all the jets. B-tagged jet is defined to be a jet satisfying

$$\text{MV1 weight} \; > \; 0.90. \tag{D.1}$$

Values of the MV1 weight are shown in Fig. D.1 for the leading jets in the selected signal and QCD background events.

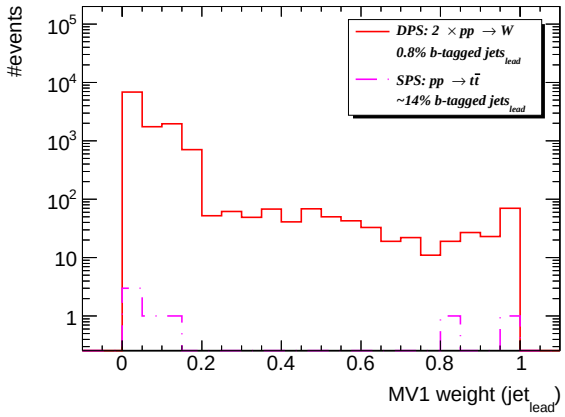

Figure D.1: MV1 weight distributions for the leading jet in DPS WW and SPS $t\bar{t}$ events. The threshold of 0.9 is required for tagging a jet as originating from bottom quark.

Even though there are only few remaining ttbar events and no statistically reliable conclusion can be drawn, the fact that at least one event contains b-tagged jet points towards the expectation that there is a high chance to filter heavy flavor QCD events off the selection using the b-tagging even at low jet pT (20 - 50 GeV).

For the signal process, and similarly for other non-QCD background processes, there is a non-zero chance to find a b-tagged jet and therefore to loose few events. In the given selection, 0.4% of signal events contain at least one b-tagged jet.

However, b-tagging generally subsides from the usage in the ATLAS analyses due to the growing impact of the pile-up interactions and increasing mis-tagging. Therefore the b-tagging is not involved in our final selection.

E Analysis Plots

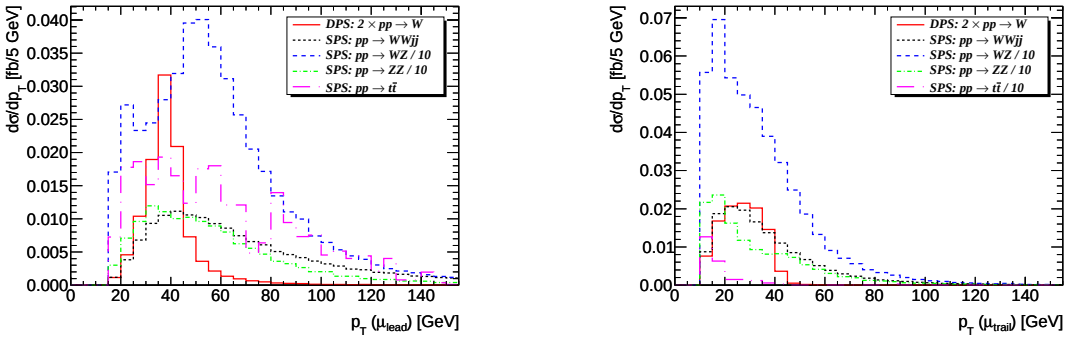

Figure E.1: Differential cross section as a function of the transverse momentum of the leading (left) and of the trailing (right) muon for all studied processes at the *GEN* level for proton-proton interactions at $\sqrt{s} = 7$ TeV. Both charge combinations are taken into consideration. All events passed the *Trigger Selection*.

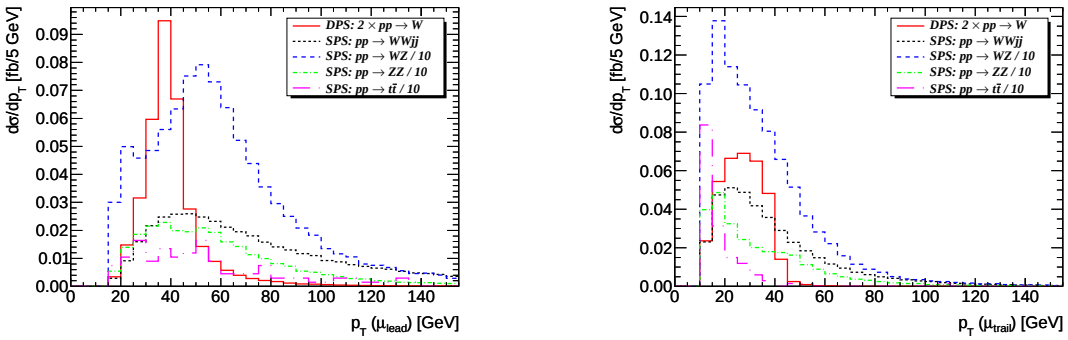

Figure E.2: Differential cross section as a function of the transverse momentum of the leading (left) and of the trailing (right) muon for all studied processes at the *GEN* level for proton-proton interactions at $\sqrt{s} = 14$ TeV. Both charge combinations are taken into consideration. All events passed the *Trigger Selection*.

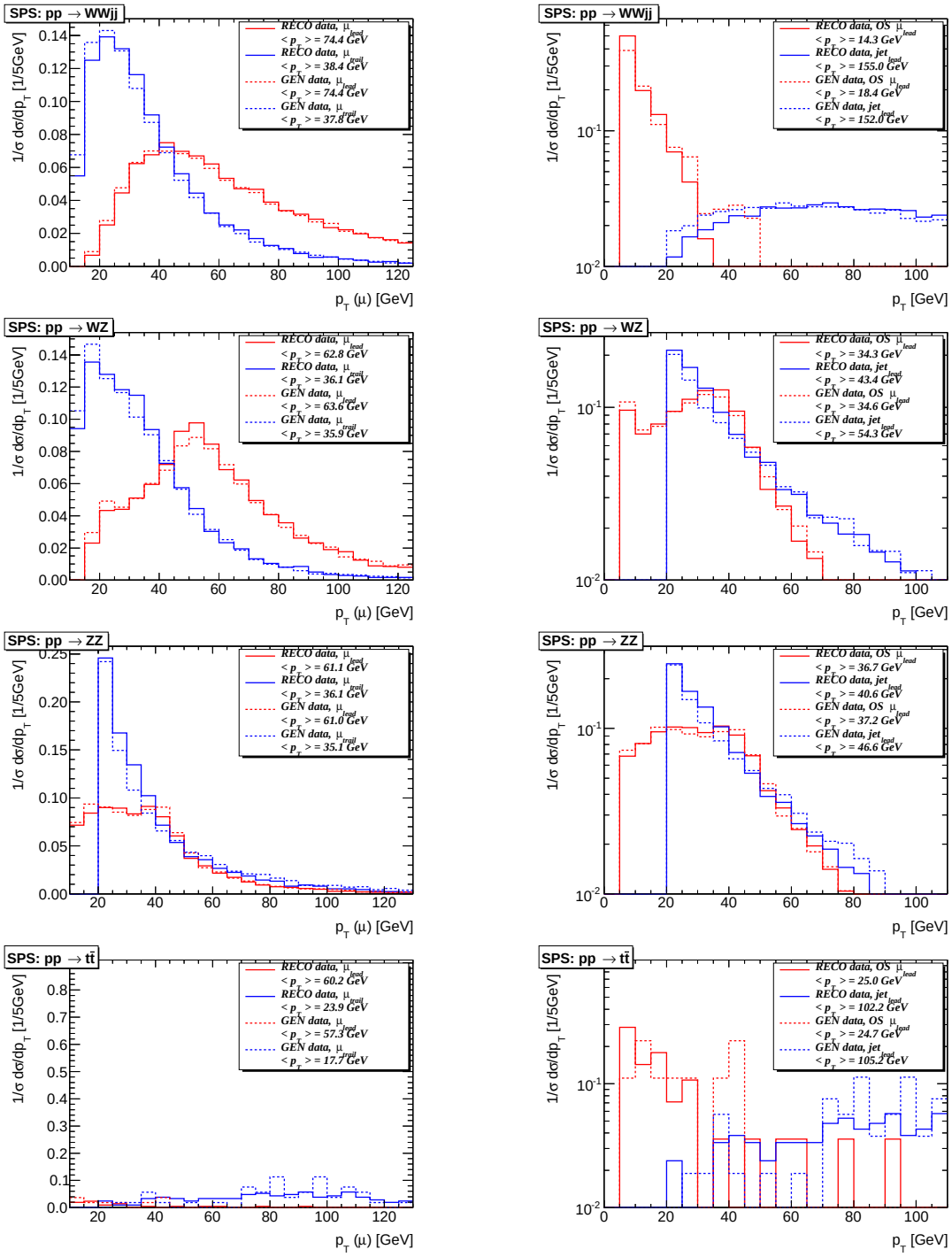

Figure E.3: Distributions for all the physics background processes as a demonstration of differences between the *RECO* and *GEN* data. Left: normalized distributions of the leading and trailing muon transverse momentum. Right: normalized distributions of the transverse momenta of the leading opposite-sign (OS) muon and of the leading jet.

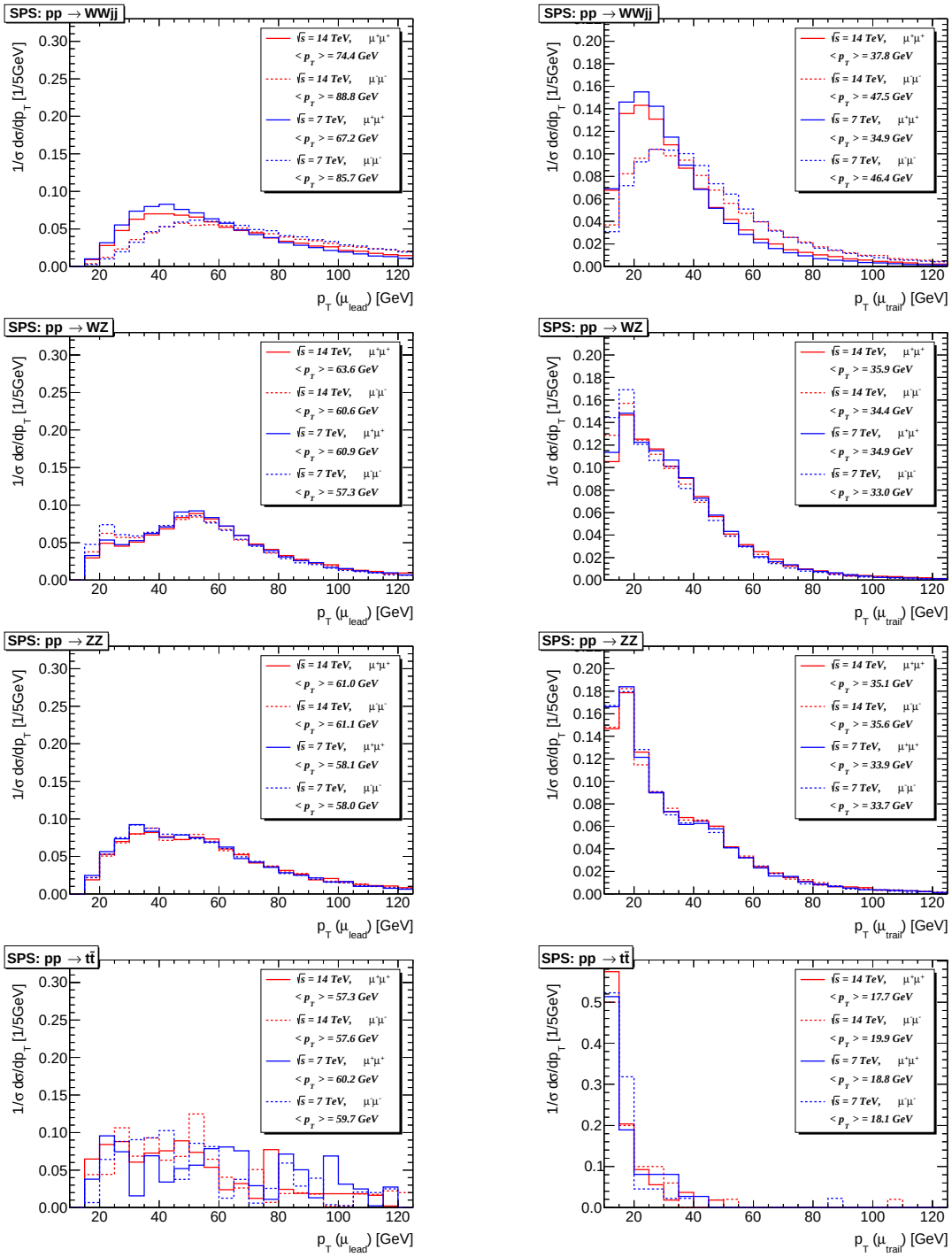

Figure E.4: Normalized distributions of the transverse momentum of the leading (left) and trailing (right) muon for all the physics background processes. One can compare between two energies of the proton-proton interactions and between two charge combinations for the final same-sign muon pair.

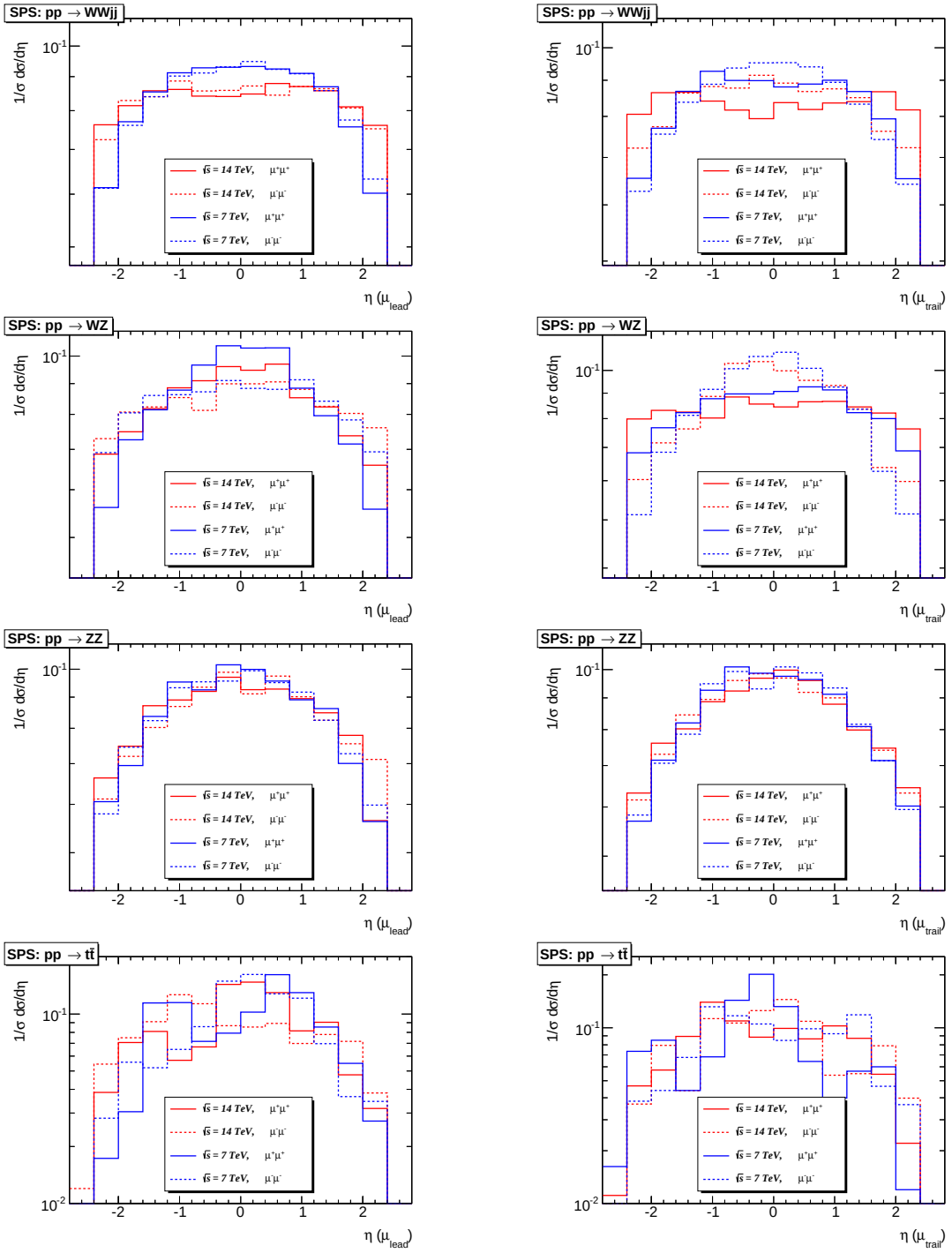

Figure E.5: Normalized distributions of the pseudorapidity of the leading (left) and trailing (right) muon for all the physics background processes. One can compare between two energies of the proton-proton interactions and between two charge combinations for the final same-sign muon pair.

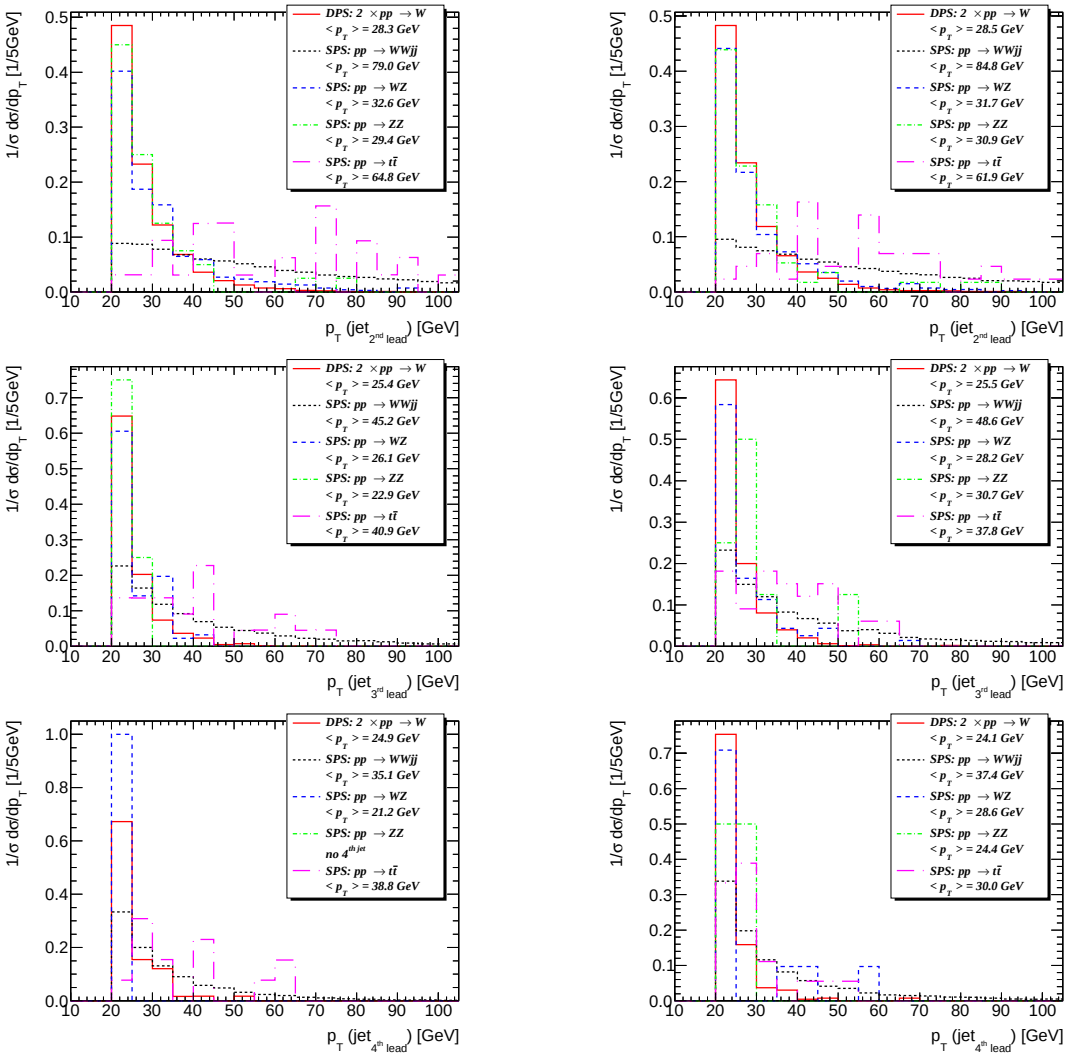

Figure E.6: Normalized distributions of the transverse momentum of the 2^{nd}, 3^{rd} and 4^{th} leading jet for all studied processes. Distributions correspond to the events of proton-proton collisions at $\sqrt{s} = 7$ TeV (left) and $\sqrt{s} = 14$ TeV (right).

References

[1] T. Sjöstrand and M. van Zijl, Phys. Rev. D **36** (1987) 2019.

[2] G. J. Alner et al. [UA5 Collaboration], Phys. Lett. B **138** (1984) 304.

[3] T. Akesson *et al.* [AFS Collaboration], Z. Phys. C **34** (1987) 163.

[4] A. Del Fabbro and D. Treleani, Phys. Rev. D **63** (2001) 057901.

[5] C. Goebel, D. M. Scott and F. Halzen, Phys. Rev. D **22** (1980) 2789.

[6] M. Mekhfi, Phys. Rev. D **32** (1985) 2371.

[7] F. Halzen, P. Hoyer and W. J. Stirling, Phys. Lett. B **188** (1987) 375.

[8] P. D. B. Collins, A. D. Martin, *Hadron interactions (Graduate Student Series In Physics)*, Published in Bristol, Uk: Hilger (1984).

[9] R. Field, Ann. Rev. Nucl. Part. Sci. **62** (2012) 453.

[10] $http://www.phys.ufl.edu/\sim rfield/cdf/CDF\_minbias.html$.

[11] A. A. Affolder *et al.* [CDF Collaboration], Phys. Rev. D **65** (2002) 092002.

[12] A. Capella, J. Tran Thanh Van and J. Kwiecinski, Phys. Rev. Lett. **58** (1987) 2015.

[13] A. Donnachie and P. V. Landshoff, Phys. Lett. B **296** (1992) 227.

[14] A. Donnachie and P. V. Landshoff, Phys. Lett. B **595** (2004) 393.

[15] B. Humpert, Phys. Lett. B **131** (1983) 461.

[16] B. Humpert and R. Odorico, Phys. Lett. B **154** (1985) 211.

[17] N. Paver and D. Treleani, Phys.Lett. B **146** (1984) 252.

[18] L. Ametller, N. Paver and D. Treleani, Phys. Lett. B **169** (1986) 289.

[19] N. Brown, Mod. Phys. Lett. A **4** (1989) 2447.

[20] J. M. Butterworth, J. R. Forshaw, T. Sjöstrand and J. K. Storrow, J. Phys. G **22** (1996) 883.

[21] G. Calucci and D. Treleani, Phys. Rev. D **57** (1998) 503.

[22] E. Cattaruzza, A. Del Fabbro and D. Treleani, Phys. Rev. D **72** (2005) 034022.

[23] E. Maina, JHEP **1101** (2011) 061.

[24] E. Maina, JHEP **0909** (2009) 081.

[25] E. Maina, JHEP **0904** (2009) 098.

[26] F. Abe *et al.* [CDF Collaboration], Phys. Rev. D **56** (1997) 3811.

[27] N. Paver and D. Treleani, Z. Phys. C **28** (1985) 187.

[28] R. Corke and T. Sjöstrand, JHEP **1001** (2010) 035.

[29] T. Sjöstrand, S. Mrenna and P. Skands, JHEP **0605** (2006) 026.

[30] D. Treleani, Phys. Rev. D **76** (2007) 076006.

[31] N. Paver and D. Treleani, Nuovo Cim. A **70** (1982) 215.

[32] B. Blok, Yu. Dokshitzer, L. Frankfurt and M. Strikman, Phys.Rev. D **83** (2011) 071501.

[33] M. Strikman, Acta Phys. Polon. B **42** (2011) 2607.

[34] L. Frankfurt, M. Strikman, and C. Weiss, Phys. Rev. D **83** (2011) 054012.

[35] R. Corke and T. Sjöstrand, JHEP **1105** (2011) 009.

[36] G. Calucci and D. Treleani, Phys. Rev. D **60** (1999) 054023.

[37] M. Diehl and A. Schäfer, Phys. Lett. B **698** (2011) 389.

[38] M. Diehl, D. Ostermeier and A. Schäfer, arXiv:1111.0910 [hep-ph].

[39] B. Blok, Yu. Dokshitzer, L. Frankfurt and M. Strikman, arXiv:1206.5594 [hep-ph].

[40] B. Blok, Yu. Dokshitzer, L. Frankfurt and M. Strikman, Eur. Phys. J. C **72** (2012) 1963.

[41] X. Artru and M. Mekhfi, LPTHE-ORSAY-89-11.

[42] M. Mekhfi, Phys. Rev. D **32** (1985) 2380.

[43] A. M. Snigirev, Phys. Rev. D **68** (2003) 114012.

[44] J. R. Gaunt and W. J. Stirling, JHEP **1003** (2010) 005.

[45] V. L. Korotkikh and A. M. Snigirev, Phys. Lett. B **594** (2004) 171.

[46] J. R. Gaunt and W. J. Stirling, JHEP **1106** (2011) 048.

[47] J. R. Gaunt, PoS DIS2010 (2010) 030.

[48] J. R. Gaunt, C. H. Kom, A. Kulesza and W. J. Stirling, Eur. Phys. J. C **69** (2010) 53.

[49] V. M. Abazov *et al.* [D0 Collaboration], Phys. Rev. D **81** (2010) 052012.

[50] T. Sjöstrand and P. Z. Skands, JHEP **0403** (2004) 053.

[51] G. Calucci and D. Treleani, Phys. Rev. D **79** (2009) 034002.

[52] G. Calucci and D. Treleani, Phys. Rev. D **79** (2009) 074013.

[53] A. Capella, U. Sukhatme, C.-I. Tan and J. Tran Thanh Van, Phys. Lett. B **81** (1979) 68.

[54] A. Capella and J. Tran Thanh Van, Phys. Lett. B **93** (1980) 146.

[55] A. Capella and J. Tran Thanh Van, Z. Phys. C **10** (1981) 249.

[56] M. Bähr *et al.*, Eur. Phys. J. C **58** (2008) 639.

[57] J. M. Butterworth, J. R. Forshaw and M. H. Seymour, Z. Phys. C **72** (1996) 637.

[58] I. Borozan and M. H. Seymour, JHEP **0209** (2002) 015.

[59] M. Bähr, S. Gieseke and M. H. Seymour, JHEP **0807** (2008) 076.

[60] M. Bähr, J. M. Butterworth and M. H. Seymour, JHEP **0901** (2009) 065.

[61] S. Gieseke, C. A. Röhr and A. Siódmok, arXiv:1110.2675 [hep-ph].

[62] R. S. Fletcher, T. K. Gaisser and F. Halzen, Phys. Rev. D **45** (1992) 377.

[63] J. Alitti *et al.* [UA2 Collaboration], Phys. Lett. B **268** (1991) 145.

[64] F. Abe *et al.* [CDF Collaboration], Phys. Rev. D **47** (1993) 4857.

[65] F. Paige and S. Protopopescu, BNL 31987 (1982).

[66] Z. Kunszt and W. J. Stirling, Phys. Lett. B **171** (1986) 307.

[67] F. Berends, W. Giele and H. Kuijf, Nucl. Phys. B **333** (1990) 120.

[68] H. U. Bengtson and T. Sjöstrand, Comput. Phys. Commun. **46** (1987) 43.

[69] I. Hinchliffe, Conf. Proc. C 930602 (1993) 679.

[70] Z. Kunszt and W. J. Stirling, Phys. Rev. D **37** (1988) 36.

[71] F. Abe *et al.* [CDF Collaboration], Phys. Rev. D **45** (1992) 1448.

[72] F. Abe *et al.* [CDF Collaboration], Phys. Rev. D **55** (1994) 5550.

[73] G. C. Blazey *et al.*, arXiv:hep-ex/0005012.

[74] V. M. Abazov *et al.* [D0 Collaboration], Phys. Rev. D **83** (2011) 052008.

[75] T. Gleisberg *et al.*, JHEP **0902** (2009) 007.

[76] J. Alwall *et al.*, JHEP **0709** (2007) 028.

[77] J. Pumplin *et* al., JHEP **0207** (2002) 012.

[78] A. D. Martin, W. J. Stirling, R. S. Thorne and G. Watt, Eur. Phys. J. C **63** (2009) 189.

[79] O. Éboli, F. Halzen and J. K. Mizukoshi, Phys. Rev. D **57** (1998) 1730.

[80] R. M. Godbole, S. Gupta and J. Lindfors, Z. Phys. C **47** (1990) 69.

[81] E. L. Berger, C. B. Jackson, S. Quackenbush and G. Shaughnessy, ANL-HEP-CP-11-61.

[82] D. Bandurin, G. Golovanov and N. Skachkov, FERMILAB-PUB-10-428-E.

[83] M. Y. Hussein, arXiv:0710.0203 [hep-ph].

[84] M. Y. Hussein, Nucl. Phys. B, Proc. Suppl. **174** (2007) 55.

[85] A. Del Fabbro and D. Treleani, Phys. Rev. D **61** (2000) 077502.

[86] M. Y. Hussein, arXiv:0612078 [hep-ph].

[87] M. Y. Hussein, Nucl. Phys. B, Proc. Suppl. **152** (2006) 296.

[88] The ATLAS Collaboration, Phys. Lett. B **716** (2012) 1.

[89] A. Kulesza and W. J. Stirling, Phys. Lett. B **475** (1999) 168.

[90] C. H. Kom, A. Kulesza and W. J. Stirling, Eur. Phys. J. C **71** (2011) 1802.

[91] The LHCb Collaboration, CERN-LHCb-CONF-2010-010.

[92] The LHCb Collaboration, CERN-LHCb-CONF-2011-009.

[93] C. H. Kom, A. Kulesza and W. J. Stirling, Phys. Rev. Lett. **107** (2011) 082002.

[94] A. Novoselov, arXiv:1106.2184 [hep-ph].

[95] A. V. Berezhnoy, A. K. Likhoded, A. V. Luchinsky and A. A. Novoselov, Phys. Rev. D **84** (2011) 094023.

[96] S. P. Baramov, A. M. Snigirev and N. P. Zotov, arXiv:1105.6276 [hep-ph].

[97] M. Strikman and W. Vogelsang, Phys. Rev. D **83** (2011) 034029.

[98] The LHCb Collaboration, JHEP **1206** (2012) 141.

[99] M. Luszczak, R. Maciula and A. Szczurek, arXiv:1111.3255 [hep-ph].

[100] A. Del Fabbro and D. Treleani, Phys. Rev. D **66** (2002) 074012.

[101] M. Bähr, M. Myska, M. H. Seymour, A. Siódmok, JHEP **1303** (2013) 129.

[102] G. Calucci and D. Treleani, Nucl. Phys. Proc. Suppl. **71** (1999) 392.

[103] S. Gieseke *et* al., arXiv:1102.1672 [hep-ph].

[104] G. Corcella *et al.*, JHEP **0101** (2001) 010.

[105] G. Corcella *et* al., arXiv:0210213 [hep-ph].

[106] A. Buckley *et* al., arXiv:1003.0694 [hep-ph].

[107] M. H. Seymour and C. Tevlin, JHEP **0611** (2006) 052.

[108] M. Cacciari, G. P. Salam, and G. Soyez, JHEP **0804** (2008) 063.

[109] M. Cacciari, G. P. Salam and G. Soyez, Eur. Phys. J. C **72** (2012) 1896.

[110] M. Cacciari and G. P. Salam, Phys. Lett. B **641** (2006) 57.

[111] A. D. Martin, R. Roberts, W. J. Stirling, and R. Thorne, Eur.Phys.J. C **4** (1998) 463 (1998).

[112] A. Sherstnev and R. S. Thorne, Eur. Phys. J. C **55** (2008) 553.

[113] O. S. Bruening *et al.*, CERN-2004-003-V-1.

[114] O. S. Bruening *et al.*, CERN-2004-003-V-2.

[115] M. Benedikt *et al.*, CERN-2004-003-V-3.

[116] L. Evans and P. Bryant, JINST **3** (2008) S08001.

[117] A. Breskin and R. Voss, The CERN Large Hadron Collider: Accelerator and Experiments, CERN, Geneva, 2009.

[118] http://www.lhcportal.com.

[119] The CMS Collaboration, JINST **3** (2008) S08004.

[120] The ATLAS Collaboration, JINST **3** (2008) S08003.

[121] The ALICE Collaboration, JINST **3** (2008) S08002.

[122] The LHCb Collaboration, JINST **3** (2008) S08005.

[123] M. Bajko *et al.*, CERN-LHC-PROJECT-REPORT-1168.

[124] The ATLAS Collaboration, CERN-OPEN-2008-020.

[125] *http* : *//www.nikhef.nl/pub/pr/eATLAS.html*.

[126] The ATLAS Collaboration, CERN-LHCC-97-22 (1997).

[127] The ATLAS Collaboration, Eur. Phys. J. C **70** (2010) 823.

[128] S. Agostinelli *et al.*, Nucl. Instrum. Meth. A **506** (2003) 250.

[129] The ATLAS Collaboration, Eur. Phys. J. C **71** (2011) 1630.

[130] E. Dobson, ATLAS-CONF-2011-160.

[131] M. L. Mangano *et al.*, JHEP **0307** (2003) 001.

[132] The ATLAS Collaboration, arXiv:1210.2979 [hep-ex].

[133] $https://twiki.cern.ch/twiki/pub/Atlas/PicturesInDoxygen/PerigeeExample.png$.

[134] $http://www.kip.uni-heidelberg.de/atlas/projects/analysis/index.php?lang=en$.

[135] W. Lampl *et al.*, ATL-LARG-PUB-2008-002.

[136] The ATLAS Collaboration, Eur. Phys. J. C **71** (2011) 1512.

[137] The ATLAS Collaboration, ATL-COM-PHYS-2008-008.

[138] The ATLAS Collaboration, ATLAS-CONF-2011-102.

[139] T. Sjöstrand, S Mrenna and Peter Skands, Comput. Phys. Commun. **178** (2008) 852.

[140] R. Corke and T. Sjöstrand, JHEP **1103** (2011) 032.

[141] The ATLAS Collaboration, ATL-PHYS-PUB-2011-009.

[142] The ATLAS Collaboration, Eur. Phys. J. C **71** (2011) 1.